THE UNIVERSITY OF
WARWICK

AUTHOR: **Stylianos Pyrzas** DEGREE: **Ph.D.**

TITLE: **Physical properties of eclipsing white dwarf binaries**

DATE OF DEPOSIT: .....

I agree that this thesis shall be available in accordance with the regulations governing the University of Warwick theses.

I agree that the summary of this thesis may be submitted for publication.

I **agree** that the thesis may be photocopied (single copies for study purposes only).

Theses with no restriction on photocopying will also be made available to the British Library for microfilming. The British Library may supply copies to individuals or libraries. subject to a statement from them that the copy is supplied for non-publishing purposes. All copies supplied by the British Library will carry the following statement:

> "Attention is drawn to the fact that the copyright of this thesis rests with its author. This copy of the thesis has been supplied on the condition that anyone who consults it is understood to recognise that its copyright rests with its author and that no quotation from the thesis and no information derived from it may be published without the author's written consent."

AUTHOR'S SIGNATURE: .....

USER'S DECLARATION

1. I undertake not to quote or make use of any information from this thesis without making acknowledgement to the author.
2. I further undertake to allow no-one else to use this thesis while it is in my care.

DATE SIGNATURE ADDRESS

.....

.....

.....

.....

.....

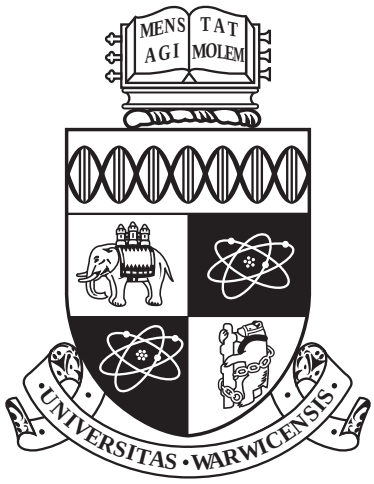

Physical properties of eclipsing white dwarf binaries

by

Stylianos Pyrzas

Thesis

Submitted to the University of Warwick

for the degree of

Doctor of Philosophy

Department of Physics

July 2011

THE UNIVERSITY OF
WARWICK

“…υποτιθεται γαρ τα μεν απλανεα των αστρων και τον αλιον μενειν ακινητον, ταν δε γαν περιφερεσθαι περι τον αλιον κατα κυκλου περιφερειαν, ος εστιν εν μεσω τω δρομω κειμενος…”

Αρισταρχος ο Σαμιος [310 − 230 πΧ]

“…[where] it is assumed that the fixed stars and the Sun remain unmoving, and that the Earth revolves about the Sun on the circumference of a circle, and the Sun lies in the centre of this track…”

Aristarchus of Samus [310 − 230 BC]

Contents

List of Tables

List of Figures

Acknowledgments

I am grateful to Prof. Boris Gänsicke for his supervision and guidance during my PhD. His door was always open for me and he was ever-willing to answer any question, simple or not, and clarify any theoretical or observational aspect of my work that I could not fathom. His comments, suggestions, ideas and (the much needed) constructive criticism have kept me motivated and helped me immensely to improve as a researcher. I thank him for getting me interested in and involved with white dwarfs, for giving me the opportunity to work on this subject and for encouraging (and endorsing) my eagerness for observations. He has put me on the path I'm currently walking and for that I will always be deeply thankful.

I would like to thank all my collaborators for their efforts and contributions to my work.

I would also like to thank Prof. Tom Marsh, Dr. Danny Steeghs, Dr. John Southworth, Dr. Alberto Rebassa-Mansergas, Dr. Chris Copperwheat, Dr. Elmé Breedt and Steven Parsons for many enlightening discussions over the years.

Dr. Pablo Rodríguez-Gil deserves a special mention, for his supervision during my one-year stay on La Palma and for teaching me how to use a spectrograph.

I owe much to the late Dr. Emilios Harlaftis, thanks to whom I took my first steps in the field of Cataclysmic Variables. May he rest in peace.

Last, but certainly not least, my deepest gratitude goes to my parents and to those I hold dear, for their unconditional love and unlimited understanding.

Declarations

I, Stylianos Pyrzas, hereby declare that this thesis has not been submitted in any previous application for a higher degree. This thesis represents my own work, except where references to other works are given, and where contributions made by my collaborators are referenced and acknowledged. In particular, details on observations and data reduction carried out by my collaborators are given in Chapter 3.

The following Chapters are based on refereed publications that I either submitted during my period of study or will submit in due course:

Chapter 4 is based on: Pyrzas, S.; Gänsicke, B. T.; Marsh, T. R.; Aungwerojwit, A.; Rebassa-Mansergas, A.; Rodrguez-Gil, P.; Southworth, J.; Schreiber, M. R.; Nebot Gomez-Moran, A. and Koester, D., "Post-common-envelope binaries from SDSS - V. Four eclipsing white dwarf main-sequence binaries", MNRAS, 394, 978 (2009).

Chapter 5 is based on: Pyrzas, S.; Gänsicke, B. T.; Brady, S.; Parsons, S. G.; Marsh, T. R.; Koester, D.; Breedt, E.; Copperwheat, C. M.; Nebot Gómez-Morán, A.; Rebassa-Mansergas, A.; Schreiber, M. R. and Zorotovic, M., "Post Common Envelope Binaries from SDSS. XV: Accurate stellar parameters for a cool $0.4\,M_{\odot}$ white dwarf and a $0.16\,M_{\odot}$ M-dwarf in a 3 h eclipsing binary", accepted for publication in MNRAS.

Chapter 6 is based on: Pyrzas, S.; Gänsicke, B. T.; Thorstensen, J. R.; Aungwerojwit, A.; Boyd, D.; Brady, S.; Casares, J.; Hickman, R. D. G.; Marsh, T. R.; Miller, I.; Ögmen, Y.; Pietz, J.; Poyner, G.; Rodríguez-Gil, P. and Staels, B, "HS 2325+8205 - an ideal laboratory for accretion disc physics", due to be submitted to MNRAS.

Chapter 7 is based on an ongoing collaboration between Pyrzas, S.; Gänsicke, B. T.; Mukadam, A.; Szkody, P.; Tovmassian, G. and Townsley, D.; it is work in progress, which is envisioned to lead to a referred publication in MNRAS.

Abstract

Close binaries containing compact objects come in many different forms, but have one thing in common: their evolution involves at least one common envelope phase and angular momentum losses. However, many aspects of these two fundamental processes are still poorly understood. Ample observational input holds the key to improving our understanding, as only then can theoretical models be properly calibrated and tested. Close binaries containing a white dwarf are perhaps the best-suited class of objects to provide such input, due to their ubiquity. White dwarf binaries that additionally display eclipses are of added interest, as accurate and model-independent determinations of fundamental stellar parameters, such as the masses and radii of the binary components, can only be obtained in such systems.

In this thesis, I present a study of eclipsing white dwarf binaries. I identify SDSSJ 0110+1326, SDSSJ 0303+0054, SDSSJ 1210+3347, SDSSJ 1435+3733 and SDSSJ 1548+4057 as new eclipsing, detached, post-common-envelope, white dwarf + M-dwarf binaries. I use follow-up photometric and spectroscopic observations, as well as a light curve fitting technique to measure their orbital periods, and derive the masses, radii and radial velocities of the binary components. These five systems have been identified as part of the first dedicated search for eclipsing post-common-envelope binaries and almost double the existing population. The measurements of the stellar parameters, and others obtained from similar systems, are of great value both for the calibration of the common envelope equations and for testing the mass-radius relations of white dwarfs and low-mass main sequence stars. I also identify HS 2325+8205 as a new eclipsing and very frequently outbursting dwarf nova. Combined constraints from photometric and spectroscopic observations are used to infer the binary and stellar parameters. The combination of eclipses, frequent outbursts, brightness range and high declination make HS 2325+8205 an ideal laboratory for detailed studies of accretion discs and accretion processes in close binaries. Finally I study the cataclysmic variable V455 And, in an attempt to verify the presence of non-radial pulsations in the white dwarf primary. This is achieved by analysing ten-years worth of photometric observations using time-series analysis techniques and Fourier transforms. The results are indeed consistent with white dwarf pulsations, although a very complex behaviour of the power spectra is revealed, most likely a result of the rapid rotation of the accreting white dwarf primary.

Chapter 1

Introduction

1.1 Prelude

Most people have, at one point or another, marvelled at the magnificence of the star-studded night-sky. Few realise, however, that those tiny, twinkling sparks of light do not necessarily lead solitary existences. In fact, most of them are part of binary or multiple systems [Iben, 1991]. Bound together by gravity in an eternal waltz around their common mass centre, the majority of the stars in binary systems are nevertheless far enough apart that they do not interact in any other way. Thus, these stars spend their lives on the main sequence and eventually evolve off it, to meet their fate in a final state that is governed solely by their initial mass, much like single stars. This process can be explained and described in detail by the theory of stellar evolution, one of the most established fields in modern astrophysics.

However, $\sim$ 25% of the binary population is expected to interact in one (or more) stages during its evolution [Willems & Kolb, 2004]. This interaction comes mainly in the form of mass transfer/exchange episodes. In the context of binary evolution, the cases where the interaction leads to the formation of a *common-envelope* (CE) are of particular interest. The CE process is believed to give birth to the most exotic objects in the Galaxy, such as cataclysmic variables (CVs), low-mass X-ray binaries, Supernovae Type-Ia progenitors, double degenerates (e.g. white dwarf + white dwarf binaries), short-GRB progenitors and millisecond pulsars. The theory of single-star evolution is often employed to study these objects, but does not always yield answers. *Binary* evolution is still not as well understood as single star evolution and is under-constrained by observations.

White dwarfs and low-mass stars represent the most common types of stellar remnant and main sequence star, respectively, encountered in our Galaxy. Therefore, binary systems consisting of a white dwarf (WD) primary and a low-mass main-sequence (MS) secondary star are ideal candidates to remedy the lack of observational input. Despite being very common, few white dwarfs and/or low-mass stars have accurately determined radii and masses. Consequently, the finite temperature mass-radius relation of white dwarfs [e.g. Wood, 1995; Panei et al., 2000] remains largely untested by observations [Provencal et al., 1998]. In the case of low mass stars, the empirical measurements consistently result in radii up to 15% larger and effective temperatures 400 K or more below the values predicted by theory [e.g. Ribas, 2006; López-Morales, 2007]. This is most clearly

demonstrated using low-mass eclipsing binary stars [Bayless & Orosz, 2006], but is also present in field stars [Berger et al., 2006; Morales et al., 2008] and the host stars of transiting extra-solar planets [Torres, 2007].

This thesis presents a study of white dwarf binaries. All the systems presented here are observed at an angle such that eclipses occur. Eclipsing binary systems offer the best opportunity of measuring fundamental stellar properties such as masses, radii, surface gravities, effective temperatures and luminosities [e.g. Andersen, 1991; Southworth & Clausen, 2007]. Geometric constraints, obtained from photometric studies of the eclipses, coupled with dynamical constraints, obtained from spectroscopic measurements of radial and rotational velocities, can yield direct and model-independent determinations of the stellar properties with exquisite accuracy (in some cases better than 1%). The thesis captures three snapshots of binary evolution at different stages, which in a somewhat simplified manner could be considered as the adolescence, the mid-age and the retirement-age of a white dwarf binary.

1.2 Post-Common-Envelope Binaries

1.2.1 The Roche Geometry

In a binary system consisting of a primary star with mass M_1 and a secondary star with mass M_2 ($M_1 > M_2$), at positions $\vec{r_1}$ and $\vec{r_2}$ from an arbitrary origin, under the assumptions that the orbit is circular and that the mass of each star is concentrated at its centre, the total gravitational potential at a point $\vec{r}$ is the sum of the potentials of the two stars and the rotational potential of the system [e.g. Frank et al., 1985]

$$\Phi(\vec{r}) = -\frac{GM_1}{|\vec{r}-\vec{r_1}|} - \frac{GM_2}{|\vec{r}-\vec{r_2}|} - \frac{1}{2}(\vec{\omega}\times\vec{r}) \tag{1.1}$$

where G is the gravitational constant and ω the angular frequency of the orbit.

Surfaces over which $\Phi(\vec{r}) = $const are called *equipotentials*. Near each stellar centre, the equipotentials are spherical (circular in cross-section), but on scales comparable to the separation tidal forces distort them into "pear" shapes pointing towards the companion. As Φ increases, the equipotentials of the two stars first touch and then merge. A sketch of the equipotential surfaces in the plane of the orbit of a binary system, calculated with Equation 1.1, is given in Figure 1.1.

The *shapes* of the equipotentials are functions only of the mass ratio q, defined as $q = M_2/M_1$, while their *scale* is determined by the binary separation a, defined as the distance between the centres of the two stars.

The volumes contained inside the critical surfaces, where the equipotentials of the two stars first cross, are called the *Roche lobes*. The cross-point of the critical equipotentials is called *the inner Lagrangian point* L_1. The Roche lobe of a star is the volume enclosed by the largest closed equipotential that can contain the star's mass. Any further expansion of the star's radius will result in Roche lobe-overflow and the onset of mass transfer from the Roche-lobe-filling star to the companion, through the L_1 point.

In order to find a spherical approximation for a Roche-lobe-filling star, it is convenient to

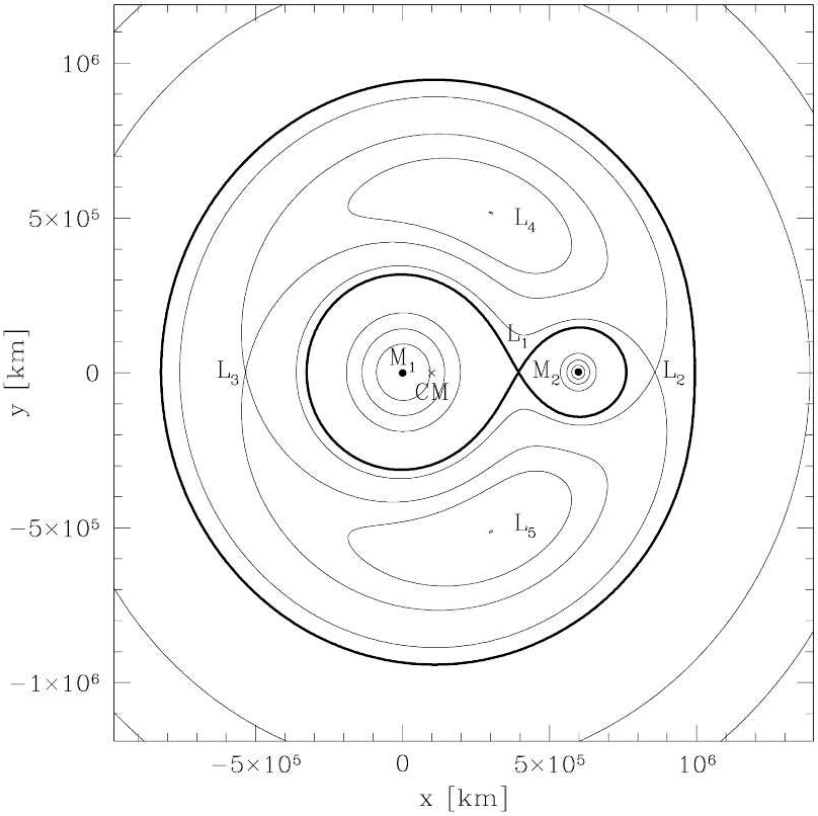

Figure 1.1: A cross section in the orbital plane of a binary with orbital period $P_{\rm orb} = 2\,\mathrm{h}$ and mass ratio $q = 0.2$ depicting the equipotential surfaces of the Roche geometry. The positions of the two stars and the centre of mass of the binary are labelled M_1, M_2 and CM respectively. Also shown are the Lagrangian points L_1 to L_5, which are equilibrium points of Equation 1.1. The bold "figure-8" line represents the largest closed equipotentials of each star, that make contact in the inner Lagrangian point L_1. The volumes enclosed by these equipotentials are the Roche lobes of the two stars. Figure courtesy of B. Gänsicke.

define the *volume radius* R_L, i.e. the radius of a sphere containing the same volume as the Roche lobe, as [Eggleton, 1983]

$$\frac{R_L}{a} = \frac{0.49\,q^{2/3}}{0.6\,q^{2/3} + \ln\left(1 + q^{1/3}\right)} \qquad 0 < q < \infty \tag{1.2}$$

which is accurate to better than 1%. In this definition, R_L is given in units of the binary separation and is a function only of the mass ratio q. The separation of a binary system with components of mass M_1 and M_2 and with an orbital period $P_{\rm orb}$ is given by Kepler's Third Law

$$a^3 = \frac{G\,(M_1 + M_2)}{4\pi^2}\,P_{\rm orb}^2 \tag{1.3}$$

Depending on the size of the star relative to its Roche lobe, a binary system is considered *detached*, when both stars lie well within their Roche lobes, *semi-detached*, when one of the stars fills its Roche lobe or *in contact*, when both stars fill their Roche lobes.

1.2.2 The formation of the common-envelope

About 25% of the MS+MS binaries have separations that are too short to allow the more massive star to evolve without overfilling its Roche lobe and initiating mass transfer [de Kool & Ritter, 1993; Willems & Kolb, 2004]. The binary's response to mass transfer depends strongly on the initial masses of the component stars.

Let us assume a binary system with component star masses of M_1 and M_2 and that $M_1 > M_2$. Let us assume further that the binary separation is such, that when the more massive star departs from the MS and begins expanding, it overfills its Roche lobe. As explained in Section 1.2.1 mass will be transferred to the companion through the L_1 point. To better understand the binary's response, we should consider the conservation of total angular momentum in the system. Material is moving from the more massive to the less massive star. This means that the material is gaining angular momentum, as it is moving away from the centre of mass. In order to compensate and conserve the total angular momentum, the binary separation must decrease. This, however, also leads to a decrease in the size of the Roche lobe, Equation 1.2. The stability of the mass transfer depends on the evolutionary status of the mass losing star. If the star is ascending the first giant branch or the asymptotic giant branch and has developed a deep convective envelope, its radius will *increase* as a response to mass loss; coupled with the shrinking Roche lobe, this leads to *dynamically unstable* mass transfer [Hjellming & Webbink, 1987; de Kool, 1992; Iben & Livio, 1993]. As a result the mass transfer rate increases considerably, on time scales shorter than the thermal time scale of the mass-receiving star (*thermally unstable* mass transfer). The companion cannot adjust to this increased inflow of material and is driven out of thermal equilibrium, consequently overfilling its Roche lobe as well. Thus, the binary comes into contact and plunges into the CE [e.g Webbink, 1977].

The envelope is not necessarily co-rotating with the binary. Friction within the envelope causes the two stars to spiral-in, drastically reducing the binary separation. Energy and angular momentum are extracted from the binary orbit and, eventually, the envelope is expelled to reveal the post-common-envelope binary, consisting of a WD (the core-remnant of the evolved star, assuming that initially $M_1 < 10\,{\rm M}_\odot$) and the MS companion. Current understanding suggests that the CE-

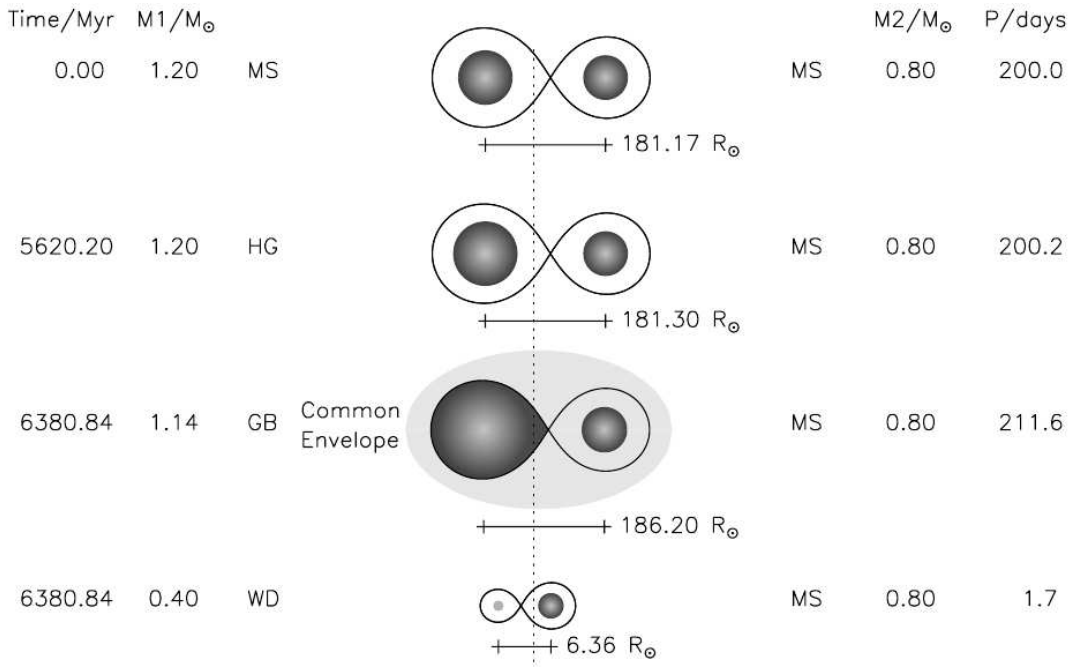

Figure 1.2: Schematic representation of the main evolutionary phases leading to the formation of a post-common-envelope binary. HG stands for Hertzsprung gap, GB for giant branch. Notice the mass of the resulting WD, the drastically reduced binary separation and the fact that the secondary star's mass remains constant. Also notice the very short timescale for the formation and ejection on the envelope. Figure adapted from Willems & Kolb [2004].

phase is probably short-lived, $\lesssim 10^3\,\mathrm{yr}$, and that the spiral-in begins rapidly after the onset of the CE [see e.g. Taam & Sandquist, 2000, and references therein, for a review of common envelope models]. The CE leads to the formation of short-period ($P_{\mathrm{orb}} \sim$days) binary systems and is believed to be the main mechanism for the creation of low-mass WDs [Rebassa-Mansergas et al., 2011]. The above process is illustrated in Figure 1.2.

The core composition of the emerging WD at the end of the CE-phase depends on the evolutionary status of the progenitor star (the more massive star in the initial MS+MS binary) at the onset of mass transfer [Iben & Livio, 1993; Willems & Kolb, 2004]. If the progenitor had not started the He-burning phase, the resulting WD will have a He-core with $M_{\mathrm{WD}} \lesssim 0.5\,\mathrm{M}_{\odot}$. If the progenitor had initiated the He $\rightarrow$ C/O-burning and a substantial amount of He had been converted, then the emerging WD will have a C/O-core with $0.5\,\mathrm{M}_{\odot} \lesssim M_{\mathrm{WD}} \lesssim 1.1\,\mathrm{M}_{\odot}$. Similarly, if a substantial amount of C/O had been converted to O/Ne, the WD will have an O/Ne-core, with $1.1\,\mathrm{M}_{\odot} \lesssim M_{\mathrm{WD}} \lesssim 1.38\,\mathrm{M}_{\odot}$.

Throughout this thesis we will be referring to all detached binaries consisting of a WD and a MS-star as WD+MS binaries; to those WD+MS binaries that have undergone a CE-phase as post-common-envelope binaries or PCEBs; and to WD+MS binaries that have not undergone a CE as WDMS binaries. Strictly speaking, other systems that have undergone CE evolution such as

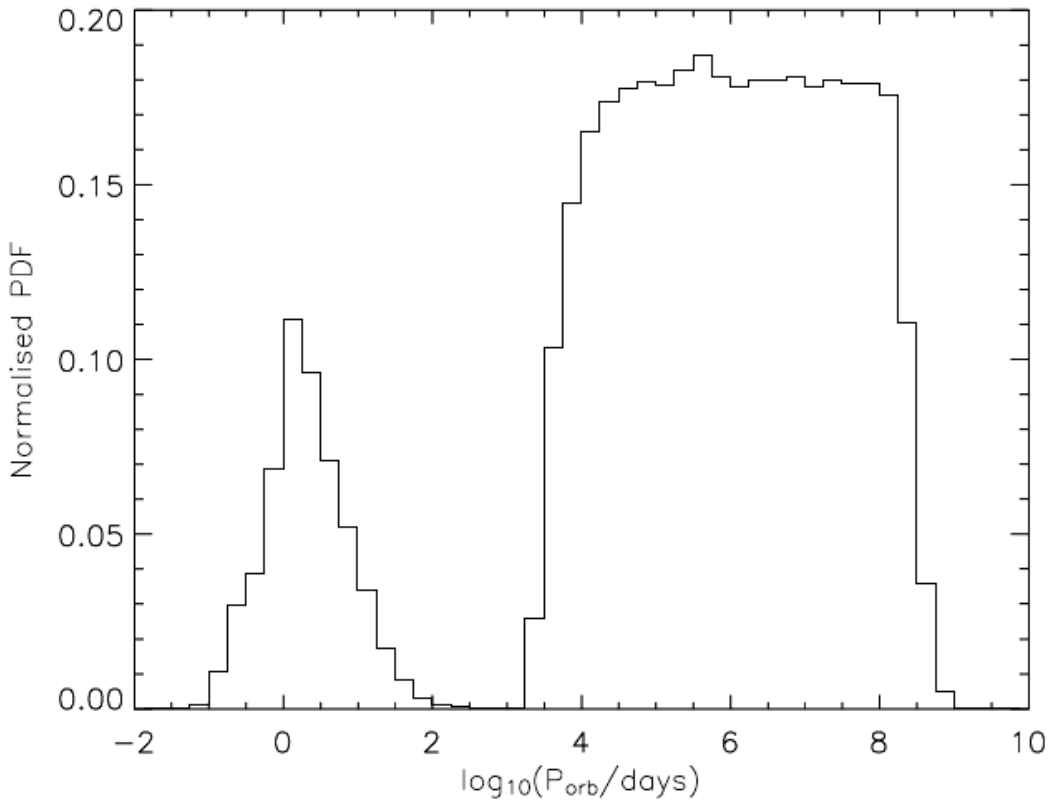

Figure 1.3: The distribution of orbital periods of WD+MS binaries. The distribution is clearly bimodal, with PCEBs occupying the lower end and WDMS binaries having longer orbital periods. Figure adapted from Willems & Kolb [2004].

cataclysmic variables (CVs) or double degenerate systems are also post-common-envelope binaries. When using the term PCEB we will *only* be referring to *detached* WD+MS binaries. From an (astro)physical point of view, the necessary parameter to tell apart PCEBs from WDMS binaries is the orbital period, as demonstrated by Willems & Kolb [2004] and shown in Figure 1.3. Binaries that interact through the CE-phase end up with reduced separations and shorter orbital periods than the original configuration; on the other hand, binaries that undergo mass transfer episodes without entering a CE-phase (dynamically and thermally stable mass transfer), and binaries that do not interact at all (but with mass loss from the evolving star leading to a weaker gravitational pull) will end up with larger binary separation/orbital period than the original. Thus, the orbital period distribution is expected to show a clear dichotomy, as is indeed the case in Figure 1.3.

1.2.3 The common-envelope phase

It was Paczynski [1976] who first considered the movement of the binary components inside the non-co-rotating envelope, a movement that reduces the binary separation and extracts energy and angular momentum from the orbit. This orbital energy could in turn be deposited on the envelope

and help expel it, before the merging of the binary components. It becomes evident that the slower the envelope is expelled, the shorter the orbit will become. On the other hand, the time required to expell the envelope depends on how efficient the process of extracting and depositing orbital energy is.

All the above led to the introduction of a parameter called *common envelope ejection efficiency* α_{ce} [see e.g. Tutukov & Yungelson, 1979; Iben & Tutukov, 1984; Webbink, 1984; Livio & Soker, 1988, and references therein] which can be defined as

$$\alpha_{ce} = \frac{\Delta E_{bind}}{\Delta E_{orb}} \tag{1.4}$$

where ΔE_{orb} is the change in the orbital energy of the binary between the beginning and the end of the spiral-in phase and ΔE_{bind} is the binding energy of the *ejected* material.

It is evident from Equation 1.4 that α_{ce} depends only on the orbital energy and every other energy source is neglected. However, it is believed that other physical processes could influence the efficiency of energy deposition [e.g. Livio, 1989; Iben & Livio, 1993]. Over the years there has been considerable theoretical work on these processes, including the efficiency of energy transport, non-spherical effects and the effect of recombination in the ionisation zones [see e.g. Meyer & Meyer-Hofmeister, 1979; Soker et al., 1984; Livio & Soker, 1988; Taam & Bodenheimer, 1989] and the effect they have on α_{ce}.

The α-formalism

The change in the orbital energy of the binary ΔE_{orb} can be approximated as the difference in gravitational energy between the start and the end of the CE-phase [e.g. Podsiadlowski et al., 2003]

$$\Delta E_{orb} = \frac{GM_2M_C}{2a_f} - \frac{GM_2M_G}{2a_i} = \frac{GM_2M_C}{2a_f} - \frac{GM_2\left(M_C + M_E\right)}{2a_i} \tag{1.5}$$

where G is the gravitational constant, M_2 is the mass of the secondary, a_i and a_f are the initial and final binary separations respectively, M_G is the mass of the giant, M_C is the mass of the giant's core and M_E is the mass of the envelope. Since the mass of the envelope is approximately the mass lost by the giant, we can write $M_G \approx M_C + M_E$. In Equation 1.5 it is assumed that the companion mass does not change during the CE-phase.

Based on the formalism proposed by Webbink [1984], several authors [e.g. Nelemans et al., 2000; Podsiadlowski et al., 2003; Nelemans & Tout, 2005] express the binding (or gravitational) energy ΔE_{bind} as

$$\Delta E_{bind} = \frac{G\left(M_C + M_E\right)M_E}{\lambda R_G} \tag{1.6}$$

where again G is the gravitational constant, M_C is the mass of the giant's core, M_E is the mass of the envelope, R_G is the radius of the giant and λ is the *structural parameter*, depending exclusively on the structure of the giant. The quantities that appear on the right hand side of Equation 1.6 for the binding energy are still a matter of debate in published literature and slight variations of this equation are used by different authors. A recent example is the approach presented in De Marco et al. [2011] who give the binding energy as

$$\Delta E_{\rm bind} = \frac{G\left(M_{\rm C} + \frac{M_{\rm E}}{2}\right)M_{\rm E}}{\lambda R_{\rm G}} \tag{1.7}$$

after a detailed calculation that includes the effect of self-gravity on the envelope, i.e. the attraction of the envelope onto itself.

Regarding the structural parameter, earlier work assumed λ to be constant, e.g. $\lambda = 0.5$ [de Kool et al., 1987]. More recently, Webbink [2008] provided a formula to approximate λ as

$$\lambda^{-1} \approx 3.000 - 3.816m_{\rm e} + 1.041m_{\rm e}^2 + 0.067m_{\rm e}^3 + 0.136m_{\rm e}^4 \tag{1.8}$$

where $m_{\rm e} = M_{\rm E}/M_{\rm G}$ is the ratio of envelope mass to total mass of the giant.

With the help of Equations 1.5 and 1.6, we can re-write Equation 1.4 as

$$\frac{GM_{\rm G}M_{\rm E}}{\lambda R_{\rm G}} = \alpha_{\rm ce}\left(\frac{GM_2M_{\rm C}}{2a_{\rm f}} - \frac{GM_2M_{\rm G}}{2a_{\rm i}}\right) \tag{1.9}$$

which is usually referred to as *the standard* α*-formalism*. Equation 1.9 represents the energy balance between the binding and orbital energies and defines the outcome of the CE-phase (implicitly assuming angular momentum conservation). A value of $\alpha_{\rm ce}$ close to unity implies a very efficient process, where the envelope is ejected quickly. On the other hand, low values of $\alpha_{\rm ce}$ lead to the formation of short $P_{\rm orb}$ binaries, as the process is much less efficient.

No definite answer has been given whether $\alpha_{\rm ce}$ really is a constant or its value depends on parameters such as the masses of the binary components, the evolutionary stage of the primary and the nature of the secondary. We should note that published values of $\alpha_{\rm ce}$ differ significantly from each other [Livio & Soker, 1988; Taam & Bodenheimer, 1989; de Kool, 1990; Maxted et al., 2006]. However, Zorotovic et al. [2010] have recently published a study, where the CE-phase is reconstructed using values for $\alpha_{\rm ce}$ over a small range only, $\alpha_{\rm ce} = 0.2 - 0.3$.

The γ-algorithm

Based on the fact that they were unable to explain some of the observed orbital periods of WD+WD binaries using the α-formalism, Nelemans et al. [2000] and Nelemans & Tout [2005] provided a different approach to predicting the outcome of the CE-phase. Instead of treating the matter from an energy point of view, they looked at it from the perspective of angular momentum balance, assuming energy conservation. Two further assumptions are made, that the envelope of the giant is lost completely, i.e. M_2 remains constant before and after the CE, and that this mass loss reduces the total angular momentum in a linear fashion. Thus,

$$J_{\rm i} - J_{\rm f} = \gamma J_{\rm i}\frac{\Delta M_{\rm tot}}{M_{\rm tot}} \Rightarrow \frac{\Delta J}{J} = \gamma\frac{M_{\rm E}}{M_{\rm G} + M_2} \tag{1.10}$$

where $J_{\rm i}$ and $J_{\rm f}$ stand for the initial and final angular momentum respectively, $M_{\rm tot}$ is the total mass of the system, γ is a parameter describing the loss of the angular momentum of the system and the rest of the symbols have been explained previously. This method is referred to as the γ-algorithm and, although Nelemans et al. [2000] and Nelemans & Tout [2005] managed to reconstruct the evolution

of the double degenerates with it, it still does not give a definite answer for the physical processes of the CE-phase (somewhat crudely, we can say that it changes one unknown parameter for another) and the matter is still open to debate [Webbink, 2008]

For completeness, we should mention that the change in binary separation is given by

$$\left(\frac{a_{\rm f}}{a_{\rm i}}\right)_{\alpha} = \frac{M_{\rm C}}{M_{\rm G}}\left(1+\frac{2M_{\rm E}}{\alpha_{\rm ce}\lambda R_{\rm L,G,i} M_2}\right)^{-1} \tag{1.11}$$

for the α-formalism, where $R_{\rm L,G,i}$ is the volume radius of the giant scaled by the initial binary separation (Equation 1.2) and

$$\left(\frac{a_{\rm f}}{a_{\rm i}}\right)_{\gamma} = \left(\frac{M_{\rm G}M_2}{M_{\rm C}M_2}\right)^2 \left(\frac{M_{\rm C}+M_2}{M_{\rm G}+M_2}\right)\left(1-\gamma\frac{M_{\rm E}}{M_{\rm G}+M_2}\right)^2 \tag{1.12}$$

for the γ-algorithm.

1.2.4 Challenges for the common-envelope theory

The theoretical treatment

Despite the fact that the broad physical mechanism of the CE-phase is clear, its exact workings remain elusive. Different treatments of the orbital and binding energies yield different results in explaining the existing population of PCEBs and their descendants. The commonest technique employed is population synthesis studies. In such studies, a population of binary stars is created, under specific assumptions, such as the mass distribution of the binary components and the orbital period distribution of the binaries. This population is subsequently allowed to evolve, a step that also requires assumptions regarding e.g. the input physics and the evolutionary models used. Using the results one can then draw conclusions and make predictions on the observed properties of such a population. Advances in the field of hydrodynamical simulations [Taam & Ricker, 2006; Ricker & Taam, 2008] have offered significant insight, but introducing these advances into a detailed model of the CE still poses a difficult challenge, mainly due to the three-dimensional nature of the problem and the required range of spatial and temporal scales to accurately model the binary. Hence, population synthesis studies rely on the simple treatment of Equations 1.11 and 1.12 to relate pre- and post-CE orbital parameters [Politano & Weiler, 2007, and references therein]. Although both the α-formalism and the γ-algorithm have their successes in various observed systems, they have their failures too, their possible values are only loosely constrained and a unified prescription is yet to be achieved.

The lack of observational input

Another substantial hurdle in our understanding of the CE-phase was the striking lack of observational input. To test the predictions of the theory and calculate $\alpha_{\rm ce}$ a large sample of systems that have undergone one or more CE phases and have well defined parameters (masses, binary separations, orbital periods etc) is needed. Cataclysmic variables are candidates for such work, however, as we will examine later, obtaining a full set of accurate parameters is notoriously difficult for CVs. Double degenerates (WD+WD binaries) have also been studied, but the evolution through two

common-envelope phases introduces additional complications and the population is still very small [$\sim$ 20 systems; Nelemans & Tout, 2005].

A few years ago, Schreiber & Gänsicke [2003] conducted a comprehensive study of the, then, known sample of well-studied PCEBs, which included only 30 systems. They concluded that the sample was heavily biased, due to the fact that most systems had been identified through observations of white dwarf candidates from blue-sensitive surveys. Therefore, the sample contained predominantly hot (young) WDs with late-type (spectral type M4 and later) companions. Early-type companions contribute a significant amount of the total system flux in the optical and, consequently, did not qualify as white dwarf candidates. Hence the sample could not be considered to be representative of either the general population of PCEBs or the progenitors of the observed population of CVs[1].

However, the field changed completely when the Sloan Digital Sky Survey [SDSS; York et al., 2000] began operations. The SDSS operates a dedicated 2.5-m telescope [Gunn et al., 2006] at the Apache Point Observatory in New Mexico, equipped with an imaging camera [Gunn et al., 1998] consisting of 30 2048 x 2048 pixel CCDs, and a pair a fibre-fed multi-object double spectrographs, covering the range $3800\mathring{A} - 9200\mathring{A}$ with a resolution of $\lambda/\Delta\lambda \simeq 2000$. Photometric observations are carried out using a new five-band u,g,r,i,z filter system [Fukugita et al., 1996]. Depending on their photometric properties, objects are then flagged for subsequent spectroscopic follow-up. In its decade of operations, SDSS has become the most influential ground-based survey in astronomy so far. The latest Data Releases (DR), DR7 and DR8 are presented in Abazajian et al. [2009] and Aihara et al. [2011]. The SDSS has been extremely successful in identifying large numbers of PCEBs. Further details will be given in Section 2.2.1.

1.2.5 The importance of eclipsing PCEBs

In Chapters 4 and 5 of this thesis, I will be presenting the analysis of five eclipsing PCEBs identified in the SDSS. There are multiple rewards to be enjoyed from such studies. Precise and model-independent masses and radii can help test the mass-radius (M-R) relations of both white dwarfs and low-mass main-sequence stars. In fact, one of the very few (to date) such measurement for a white dwarf comes from the eclipsing PCEB NN Ser [Parsons et al., 2010a]. Masses and radii of the secondary stars could help calibrate the low-mass end of the main-sequence M-R relation, which remains largely untested. Eclipsing PCEBs provide ultra-accurate orbital periods. Given a long baseline, orbital period changes in PCEBs can be used to track potential angular momentum losses [Parsons et al., 2010b] and even detect the presence of third-bodies in the binary [Beuermann et al., 2010]. The combination of accurate masses and orbital periods provides, of course, an accurate determination of the binary separation. These measurements form the much-needed observational input for testing the predictions of CE theory and the envelope ejection efficiency.

Given enough time, the PCEBs discussed previously will evolve into the configuration of a cataclysmic variable (CV). In what follows, I will first provide an overview of the broad context of CV

[1] As Schreiber & Gänsicke [2003] show, PCEBs with late-type ($M_{\rm sec} \lesssim 0.4\,{\rm M}_{\odot}$) companions evolve into short-period CVs. Long-period CVs ($P_{\rm orb} > 3\,{\rm h}$) come from PCEBs with earlier-type companions, which were missing from the sample.

theory and then study specific aspects of it in more detail.

1.3 Cataclysmic Variables

1.3.1 Overview

Cataclysmic variables are semi-detached binary systems consisting of an accreting white dwarf primary star and a late-type, mass-transferring, (near-)main sequence secondary star [Patterson, 1984; Warner, 1995]. In CVs, the secondary star overfills its Roche lobe and material is transferred through the L_1 point into the Roche lobe of the WD. The outcome of mass-transfer depends on the strength of the magnetic field of the white dwarf.

In most cases, the WD possesses a weak magnetic field, $B < 1\,\mathrm{MG}$, so the stream of material slingshots around the WD[2], and settles into a ring around it, which eventually is broadened by viscosity to form an *accretion disc* [Paczyński, 1971]. A *bright spot* is often formed at the outer edge of the disc, where the incoming mass-stream from the donor impacts onto the disc.

On the other hand, in systems where the WD has a strong magnetic field, $10\,\mathrm{MG} \lesssim B \lesssim 200\,\mathrm{MG}$, disc formation is disrupted by the magnetosphere of the WD. Instead of settling into a ring around the white dwarf, material is forced to flow along the magnetic field lines and is accreted on one (or both) poles of the (assumed) dipolar magnetic field of the WD. Another consequence of the strong magnetic field in these systems is that, through interaction with the weaker magnetic field of the secondary, the WD's rotational period P_{spin} is "locked" with the orbital motion of the binary P_{orb}, so $P_{\mathrm{spin}} = P_{\mathrm{orb}}$. These systems are known as *polars* or AM Herculis systems [see Cropper, 1990, for a comprehensive review].

An interesting scenario arises when the WD has an intermediate strength magnetic field, $1\,\mathrm{MG} \lesssim B \lesssim 10\,\mathrm{MG}$. Such systems are known as *intermediate polars* or DQ Herculis stars and, as their name suggests, the result of mass-transfer lies somewhere inbetween the other two cases: an accretion disc may form, but gets disrupted near the WD's magnetosphere, where material again flows along the magnetic field lines forming *accretion curtains*. Intermediate polars are not synchronised, $P_{\mathrm{spin}} < P_{\mathrm{orb}}$, and both stream-dominated- and disc-dominated-accretion systems are known [see Patterson, 1994, for a review].
Figure 1.4 illustrates the three cases analysed above.

A fundamental physical parameter when studying CVs is the orbital period, P_{orb}. Figure 1.5 shows the distribution of orbital periods of the observed CV population. The distribution has three remarkable features: (i) the dwindling number of systems at long orbital periods, $P_{\mathrm{orb}} \gtrsim 12\,\mathrm{h}$, (ii) the lack of observed systems with $2\,\mathrm{h} \lesssim P_{\mathrm{orb}} \lesssim 3\,\mathrm{h}$, commonly referred to in the literature as the *period gap* and (iii) the sharp cut-off at $P_{\mathrm{orb}} \sim 80\,\mathrm{min}$. We will take a closer look at these features in Section 1.3.4. As a final note, we add that a common way to segregate CVs is based on their orbital period. Systems are then divided into those above the period gap, $P_{\mathrm{orb}} \gtrsim 3\,\mathrm{h}$, and those below the period gap, $P_{\mathrm{orb}} \lesssim 2\,\mathrm{h}$.

[2] As the material carries substantial angular momentum, it cannot accrete directly onto the WD.

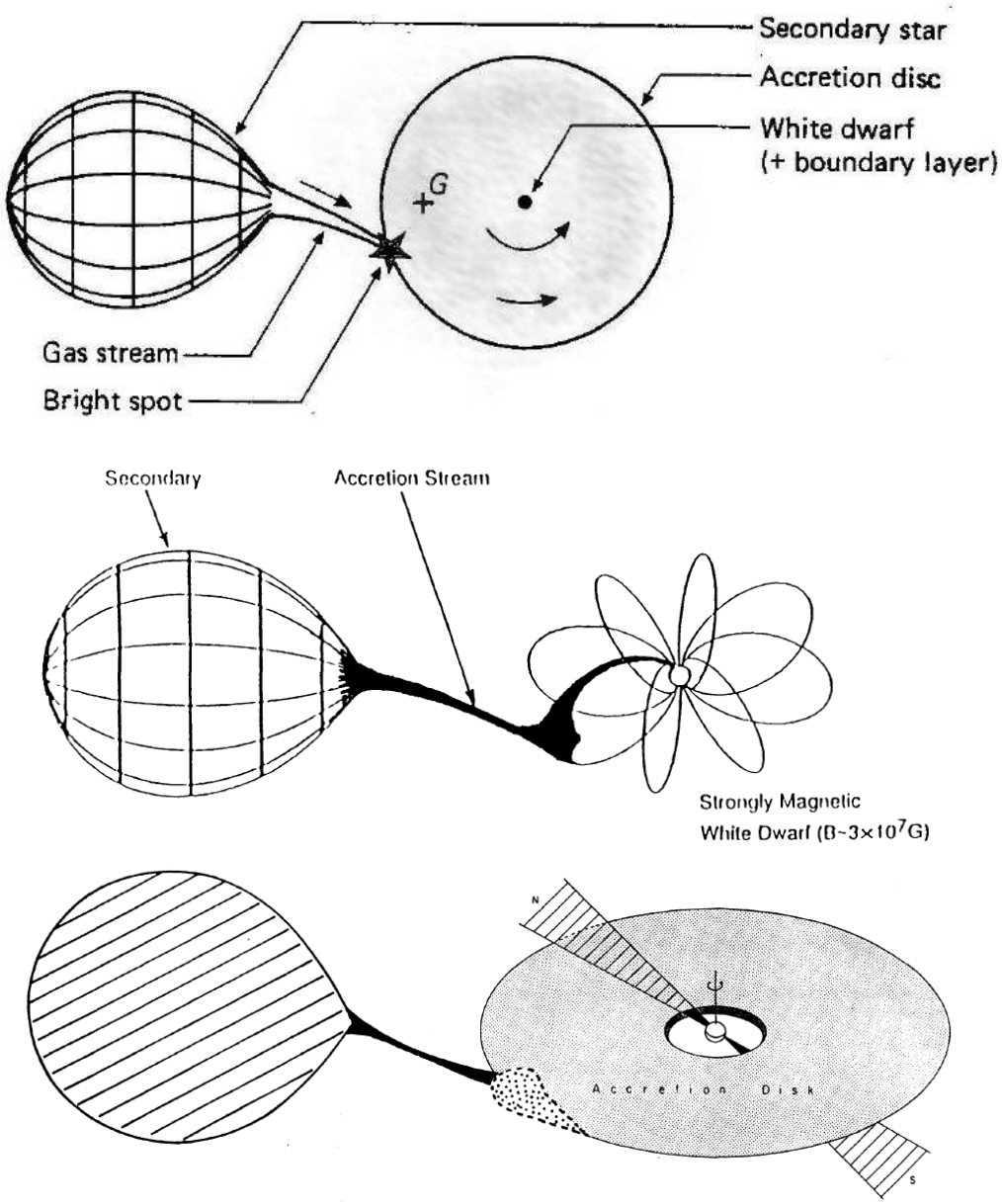

Figure 1.4: Schematic representations of cataclysmic variables. Components and features of interest are noted. Top: A typical CV with a non- or weakly-magnetic white dwarf. The mass transferred from the secondary is accreted onto the WD via an accretion disc. Adapted from Pringle, J. E. & Wade, R. A. [1985]. Middle: A polar. The mass-stream is channelled along the magnetic field lines onto the magnetic pole(s) of the WD, preventing accretion disc formation. Adapted from Cropper [1990]. Bottom: An intermediate polar. The transferred mass forms a disc, which gets disrupted near the centre, due to interaction with the WD's magnetosphere. The accretion curtains are not shown. Adapted from Patterson [1994].

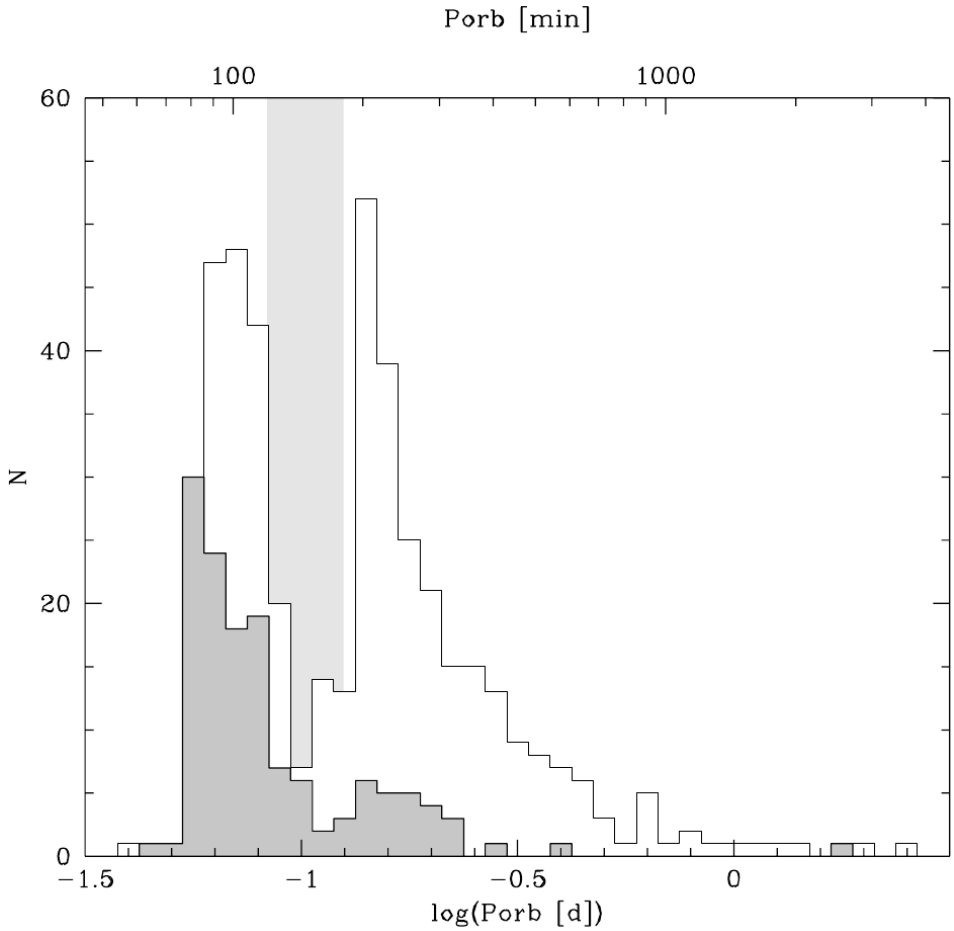

Figure 1.5: Orbital period distribution of the observed population of cataclysmic variables. The number of systems per bin is indicated on the left y-axis, while the bin width is 0.05 $\log(\mathrm{d})$. Shown in white is the distribution of 454 CVs from Ritter & Kolb [2003], catalogue edition 7.6, with no SDSS (DR6) spectroscopy. Depicted in dark grey is the distribution of 137 CVs identified in SDSS. It is evident that SDSS has revealed a population clustering around the period minimum. The period gap is highlighted in light grey. Figure adapted from Gänsicke et al. [2009].

1.3.2 The formation of cataclysmic variables

Before we probe deeper into the realm of CVs, we should take a step back and examine their formation scenarios. It has already been hinted in Section 1.2.4 that PCEBs evolve into CVs[3], a process which is estimated to take place on a timescale of $\sim 2\,\mathrm{Gyr}$ [Schreiber & Gänsicke, 2003].

In order to reach the semi-detached configuration of CVs, the secondary star in the PCEB needs to fill its Roche lobe. This can be achieved either with the secondary departing from the MS or with its Roche lobe shrinking. The former is highly unlikely for late-type secondaries, as their nuclear burning lifetime is longer than the age of the Galaxy. The latter is plausible, but requires the binary separation to be shrinking, implying that angular momentum is somehow removed from the system.

A similar conclusion can be reached if we consider the mass transfer stage. In systems with late-type companions, the mass of the white dwarf is greater than the mass of the secondary, $M_{\mathrm{WD}} > M_{\mathrm{sec}}$, so material leaving the secondary moves closer to the centre of mass and loses angular momentum. Under the assumption of angular momentum conservation, the binary expands in order to compensate, so the Roche lobe of the secondary becomes larger. What is more, the secondary itself is expected to shrink, in order to adjust to its lower mass and return to equilibrium. With its radius becoming smaller and that of the Roche lobe becoming larger, the secondary detaches from its Roche lobe. Thus, mass transfer ceases immediately after its onset. However, CVs are observed in a state of sustained mass transfer, again implying that angular momentum is not conserved, but continuously being removed from the system.

It is exactly this process of angular momentum loss (AML) that drives the evolution of PCEBs into the CV configuration and the subsequent CV evolution from longer to shorter orbital periods, so understanding the mechanisms that drive the AML is of paramount importance for binary evolution.

1.3.3 Angular momentum loss mechanisms

The first mechanism proposed to be responsible for AML was *gravitational radiation* (GR) [e.g. Kraft et al., 1962; Paczyński, 1967]. The rate of AML due to GR is given by Einstein's quadrupole formula [Taylor et al., 1979]

$$\dot{J}_{\mathrm{GR}} = -\frac{32\,G^{7/3}}{5\,c^2}\,\frac{{M_1}^2 {M_2}^2}{(M_1+M_2)^{2/3}}\left(\frac{2\pi}{P_{\mathrm{orb}}}\right)^{7/3} \tag{1.13}$$

where c is the speed of light and the rest of the symbols have been explained elsewhere.

Despite the fact that GR was successful in explaining some of the observed CV properties [Paczynski, 1981; Paczynski & Sienkiewicz, 1981; Rappaport et al., 1982], many other properties remained unexplained [see e.g. Patterson, 1984] and it was apparent that another, much more *efficient* mechanism of AML was required.

The said mechanism is believed to be *magnetic braking* (MB), AML in a stellar wind magnetically coupled to the tidally-locked secondary. The idea existed as a potential mechanism for

[3] PCEBs with very early-type companions, such as A- and F-stars, evolve into super-soft X-ray binaries or (after a second CE-phase) into double degenerates. This evolutionary channel will not be discussed.

slowing the rotation of single stars [Weber & Davis, 1967] and was suggested to be applicable to binary systems as well [e.g. Huang, 1966; Mestel, 1968; Eggleton, 1976]. Verbunt & Zwaan [1981] calculated the AML rate due to MB to be

$$\dot{J}_{\rm VZ} = -3.8 \times 10^{-30} M_2 \, {\rm R}_\odot{}^4 \left(\frac{R_2}{{\rm R}_\odot}\right)^\gamma \left(\frac{2\pi}{P_{\rm orb}}\right)^3 \tag{1.14}$$

where γ is a constant. In the work of Verbunt & Zwaan [1981] $\gamma = 4$, but $\gamma = 2$ is also frequently used [Schreiber & Gänsicke, 2003].

1.3.4 The standard scenario of CV evolution

Angular momentum loss through MB and GR explained, in principle, the evolution of PCEBs to CVs and the sustainability of mass transfer in CVs, and resulted in the understanding that CVs evolve from longer to shorter orbital periods. However, a more comprehensive theoretical treatment was required to fully explain the observed properties of the CV population, in particular the three distinct features of the orbital period distribution.

It is convenient to link the orbital period of a CV $P_{\rm orb}$ with the mean density of the Roche-lobe filling secondary. The density is of course

$$\bar{\rho} = \frac{M_{\rm sec}}{\frac{4}{3}\pi R_L^3} \tag{1.15}$$

with R_L^3 the volume radius, defined in Equation 1.2. Combining these two Equations, coupled with Kepler's third law, Equation 1.3, we find

$$\bar{\rho} = 107 P_{\rm orb}^{-2}\,({\rm h}) \quad \left[{\rm g\,cm^{-3}}\right] \tag{1.16}$$

Late-type main-sequence stars have densities of the order of $1 - 100\,{\rm g\,cm^{-3}}$ [Allen, 1976]. For $P_{\rm orb} \gtrsim 12\,{\rm h}$, Equation 1.16 requires densities lower than this value, indicating that such a late-type secondary needs to be evolved. However, the evolution timescales for late-type MS stars are longer than the Hubble time, and thus, such stars cannot fulfil this requirement. Early-type main-sequence stars can in principle fulfil the requirement, as they have lower densities, consistent with $\bar{\rho}$ from Equation 1.16 for long orbital periods, and also have shorter evolution timescales. However, to ensure stable mass transfer the secondary needs to be less massive than the white dwarf $M_{\rm sec} < M_{\rm WD}$ (to be precise, $q \lesssim 2/3$). White dwarfs must be below the Chandrasekhar limit of $M_{\rm WD} \lesssim 1.4\,{\rm M}_\odot$, which imposes a limit on the mass of the secondary, a limit that is not met by early-type stars. Few systems are expected to simultaneously meet the constraints of Equation 1.16 and $q \lesssim 2/3$, resulting in the dwindling number of systems at long orbital periods.

The abrupt cut-off at short orbital periods, $P_{\rm orb} \sim 80\,{\rm min}$, could be explained through a "transition" of the secondary from a MS star to a degenerate state. At such short orbital periods the mass of the secondary has become so low ($M_{\rm sec} < 0.08\,{\rm M}_\odot$) that hydrogen fusion terminates and the secondary becomes degenerate. The immediate consequence is that its radius *increases* with decreasing mass. This means that $\bar{\rho}$ also decreases, thus the orbital period must increase.

This is a fundamental prediction of CV evolution. CVs evolve from longer to shorter orbital

periods until a *minimum* $P_{\rm orb}$, when the secondaries become degenerate and the systems *bounce* back and evolve towards longer orbital periods. This also implies an accumulation of systems around the minimum orbital period, referred to as *the period minimum spike* [4].

The largest obstacle in forming a complete theory for CV evolution was to explain the statistically significant lack of systems with $2\,{\rm h} \lesssim P_{\rm orb} \lesssim 3\,{\rm h}$, the period gap. To reconcile theory with observation, Rappaport et al. [1983] proposed the *disrupted magnetic braking* (DMB) scenario, which has become the standard paradigm describing CV evolution [see Patterson 1984; King 1988; Howell et al. 2001 for reviews and see also Knigge et al. 2011].

Disrupted magnetic braking

In the DMB prescription, CV evolution is divided in two main phases, depending on the prevailing AML mechanism. For CVs above the gap, $P_{\rm orb} \gtrsim 3\,{\rm h}$, the secondary star still possesses a radiative core, leading to a magnetic field topology involving large scale fields with open field lines. Such a topology allows angular momentum to be carried away on the open field lines making magnetic braking the dominant form of AML above the gap. Magnetic braking can achieve mass loss rates of $\dot{M} \sim 10^{-9} - 10^{-8}\,{\rm M}_{\odot}{\rm yr}^{-1}$. Such high $\dot{M}$ values drive the secondary out of thermal equilibrium resulting in a slight expansion. Once the secondaries lose their radiative zone and become fully convective, $M_{\rm sec} \sim 0.3\,{\rm M}_{\odot}$, which corresponds to an orbital period of $P_{\rm orb} \simeq 3\,{\rm h}$, the topology of the magnetic field is believed to change to small scale fields with closed loops. Magnetic braking is thought to get *disrupted* and cease as a result of this change. The mass loss rate decreases significantly, allowing the secondary to relax back to its equilibrium radius, which is smaller than its Roche lobe radius. Hence, the secondary detaches from its Roche lobe, mass transfer shuts-off and the CV enters the period gap "masquerading" as a detached WD+MS binary [see Davis et al., 2008, for a study of "genuine" PCEBs vs "detached" CVs in the period gap]. The subsequent evolution of the system is governed by the emission of GR. Angular momentum loss through GR continues to decrease the separation, and the size of the Roche lobes, until contact is made again at $P_{\rm orb} \simeq 2\,{\rm h}$, mass transfer is resumed, the binary exits the gap and is observed as a CV once more. As GR is considerably less efficient than MB, mass loss rates are correspondingly lower, $\dot{M} \sim 10^{-11} - 10^{-10}\,{\rm M}_{\odot}{\rm yr}^{-1}$. A direct consequence of the above is that the evolution of CVs above (below) the gap is driven on much faster (slower) timescales. These timescales were calculated by Kolb & Stehle [1996] to be

$$\tau_{\rm MB} = -\left(\frac{J}{\dot{J}}\right)_{\rm MB} = 2.2\times10^{9}\,\frac{M_1}{(M_1+M_2)^{1/3}}\,{R_2}^{-4}\,{P_{\rm orb}}^{10/3}\,({\rm d}) \quad {\rm yr} \tag{1.17}$$

for magnetic braking and

$$\tau_{\rm GR} = -\left(\frac{J}{\dot{J}}\right)_{\rm GR} = 3.8\times10^{11}\,\frac{(M_1+M_2)^{1/3}}{M_1M_2}\,{P_{\rm orb}}^{8/3}\,({\rm d}) \quad {\rm yr} \tag{1.18}$$

for gravitational radiation. Figure 1.6 summarises the discussion above.

[4] As such an accumulation of systems will show up as a "spike" in a $P_{\rm orb}$ distribution diagram.

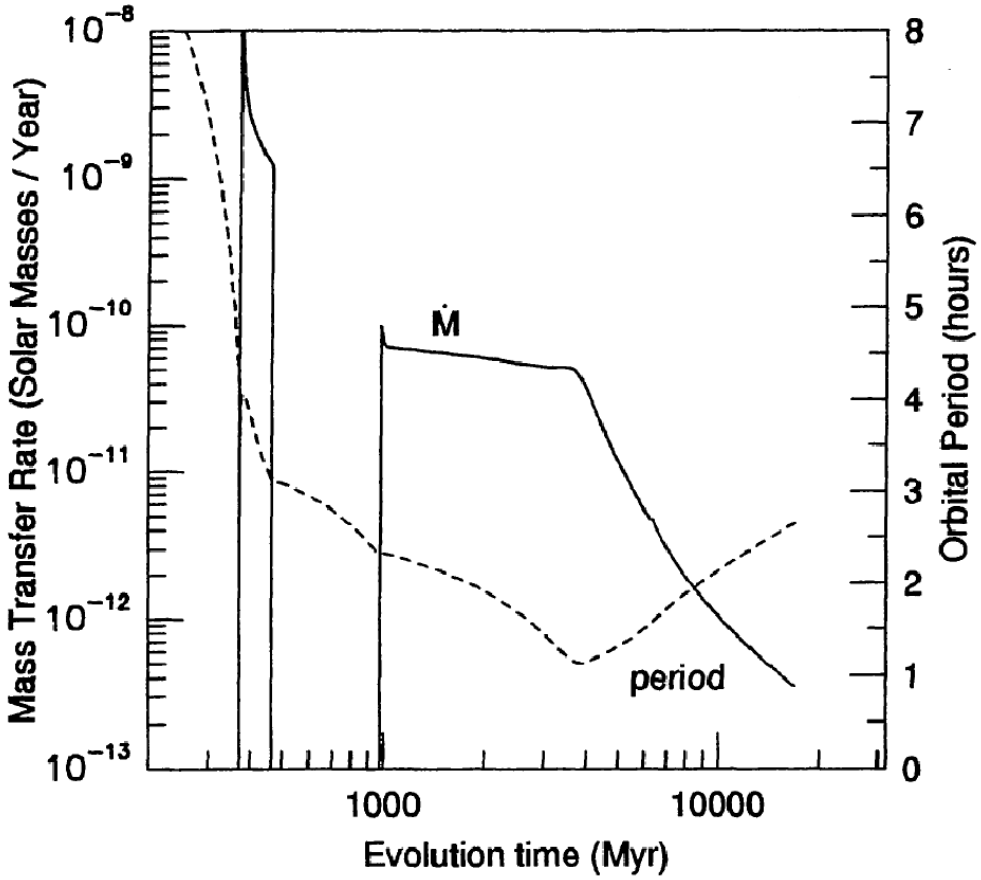

Figure 1.6: The evolution of the mass transfer rate and the orbital period of a CV, in the context of the disrupted magnetic braking theory. The system comes into contact for the first time at $P_{\rm orb} \simeq 4$h. Magnetic braking is the dominant AML mechanism, until it ceases at $P_{\rm orb} \simeq 3$h, and mass transfer stops completely. Contact is resumed when $P_{\rm orb} \simeq 2$h, and the mass transfer rate is now driven by the less effective GR. Note the timescales on which the system reaches the gap, crosses the gap and evolves until the period minimum. Figure adapted from Howell et al. [1997].

Contradictions between theory and observations

Despite the fact that DMB successfully explained the presence of the orbital period gap, allowing a unified treatment of CV evolution, some serious contradictions between theoretical predictions and observational reality remained. First, population synthesis studies predicted a space density for CVs in the range of $\rho \sim 10^{-5} - 10^{-4}\,\mathrm{pc}^{-3}$ [e.g. Politano, 1996; Howell et al., 1997], whereas the observed space density was an order of magnitude lower $\rho \sim 10^{-6} - 10^{-5}\,\mathrm{pc}^{-3}$ [e.g. Schreiber & Gänsicke, 2003; Pretorius et al., 2007]. Second, the calculated period minimum $P_{\mathrm{min}} \sim 70\,\mathrm{min}$ differed from the observed one $P_{\mathrm{min}} \sim 80\,\mathrm{min}$ [e.g. Howell et al., 1997; Patterson, 1998; Kolb & Baraffe, 1999; Howell et al., 2001]. In addition, due to the evolutionary timescales (Equations 1.17 and 1.18) of objects above and below the gap, it was expected that the majority of systems will be below the gap [e.g. Kolb, 1993] and, in fact, clustered around the period minimum. However, equal numbers of systems were found above and below the gap (Figure 1.5, white histogram). The assumed *period minimum spike* remained elusive for years, and has only recently been identified by Gänsicke et al. [2009] (Figure 1.5, grey histogram).

Politano & Weiler [2006] suggested a way of testing the DMB theory based on PCEBs. Essentially, their argument is that, under the assumption that DMB holds, magnetic braking should operate in PCEBs with secondary masses $M_{\mathrm{sec}} \gtrsim 0.3\,\mathrm{M}_{\odot}$ and, therefore, these PCEBs should quickly evolve into a semi-detached configuration. On the other hand, PCEBs with fully convective secondaries, $M_{\mathrm{sec}} \lesssim 0.3\,\mathrm{M}_{\odot}$, would rely only on GR as an AML mechanism, and consequently would evolve on much longer timescales. Thus, the observed population of PCEBs should predominantly consist of systems with low-mass secondaries and an abrupt cut-off should exist in the secondary mass distribution. The first evidence in support of this theory was presented by Schreiber et al. [2010].

Davis et al. [2008] suggested another test for DMB, also based on PCEBs. Their idea is that the orbital period distribution of PCEBs should show a significantly increased number of systems at orbital periods between 2 and 3 hours (the period gap), as the numbers of PCEBs are expected to be boosted by "detached" CVs, that have switched off mass transfer and are crossing the gap.

The successes of Gänsicke et al. [2009] in identifying the period minimum spike and Schreiber et al. [2010] in providing observational evidence supporting the DMB scenario (and see also Knigge 2010) illustrate the key role that observational input plays in testing (and potentially refining) the aspects of binary evolution theory under discussion, and also the necessity of properly evaluating and understanding the selection effects that are intrinsic to any observed population of CVs and PCEBs.

1.3.5 CV classification

The theoretical treatment of angular momentum loss and CV evolution described previously gives a unified description of CVs. However, as is often the case in astronomy, the reality is much more complicated. The observed population of CVs is diverse and presents a variety of features, so that a classification of systems, that share some basic characteristics, is required. Three physical parameters can be used to define classes of CVs: the orbital period, P_{orb}, the magnetic field of the white dwarf, B, and the mass-transfer rate, $\dot{M}$. Some of the divisions have been mentioned in

Section 1.3.1, but will be re-iterated for completion.

• The first division relies on $P_{\rm orb}$ and divides CVs into those above and those below the period gap.

• Based on the strength of B, CVs can be divided into magnetic and non-magnetic. Magnetic CVs are further sub-divided into polars (AM Her stars), where $B > 10\,$MG and are usually found below the period gap; and intermediate polars (IPs or DQ Her stars), where $1\,{\rm MG} \lesssim B \lesssim 10\,{\rm MG}$ and are usually found above the period gap.

• Based on $\dot{M}$, CVs are generally divided into dwarf novae (low $\dot{M}$, the majority being below the period gap) and nova-like variables (high $\dot{M}$, almost all above the period gap). Sub-divisions of dwarf novae include U Gem, Z Cam and SU UMa stars, with the latter including the groups of WZ Sge and ER UMa stars. Novalike variables are sub-divided into UX UMa, RW Tri, VY Scl and SW Sex stars.

The above classification with the groups and sub-groups may seem confusing and clearly illustrates the large diversity between CVs. The classification is not cast in iron and systems can belong to more than one class. An example of this is V455 And, the system that is presented in Chapter 7 of this thesis, which can be classified both as a WZ Sge and as a DQ Her star.

For the purposes of this thesis, I will now examine the class of dwarf novae in more detail.

1.3.6 Dwarf novae

Almost half of the known CV population belongs to the class of *dwarf novae* (DN), the dominant CV-type for systems with non- or weakly-magnetic white dwarfs. The most prominent feature of DN is the fact that they undergo quasi-periodical brightness changes of several magnitudes, lasting from days to weeks and with recurrence times that range from weeks to years. These brightenings are commonly known as *dwarf nova outbursts*[5]. The term *quiescence* is used to describe a dwarf nova in the state of minimum brightness.

Theoretical work has linked dwarf nova outbursts with a thermal instability in the accretion disc (see Section 1.3.7). In this context accretion discs undergo outbursts if the mass transfer rate is below a critical value, $\dot{M}_{\rm crit}$. For systems above the orbital period gap, accretion rates are usually larger than $\dot{M}_{\rm crit}$ and, as a result, only about a third of non-magnetic systems above the gap are dwarf novae; the rest belong to the novalike variables class. Only a handful of DN can be found directly above the gap, $3\,{\rm h} < P_{\rm orb} < 4\,{\rm h}$ [Shafter, 1992]. The situation is completely different below the period gap, as DN constitute the overwhelming majority among the short period non-magnetic systems [Shafter et al., 1986; Shafter, 1992].

Based on their observed outburst properties, see e.g. Szkody & Mattei [1984] and Ak et al. [2002] for related analyses, DN can be subdivided into three distinct groups:

[5]The term "dwarf nova" arose from the need to distinguish DN from their, much brighter, cousins the classical nova (CN) eruptions. The use of the term "nova" in both cases could be misleading, as the mechanisms driving DN and CN are completely different.

U Gem-type

The prototype star itself, U Gem (attracting attention since 1855, see Pogson [1857]), as well as another member of this class, SS Cyg [Pickering & Fleming, 1896], are among the best studied variable stars. This sub-class of CVs is somewhat loosely defined. U Gem-type systems are found above the period gap and comprise all systems that undergo DN outbursts, but do not show the, distinguished, characteristics of either Z Cam- or SU UMa-type CVs.

Z Cam-type

This sub-class consists of systems that are found above the orbital period gap. The hallmark of Z Cam-type stars are the *standstills*, periods interspersed between the (usually rapid) outbursts, when the system is found in an intermediate brightness level, between outburst maxima and minima. Standstills can last from a few days to years and are believed to be a result of the mass-transfer rate fluctuating about the critical value $\dot{M}_{\rm crit}$ [e.g. Buat-Ménard et al., 2001].

SU UMa-type

The vast majority of systems belonging to this sub-class are found below the period gap. SU UMa-type stars, in addition to normal outbursts, also exhibit *superoutbursts*, that are brighter and last longer than normal outbursts, but are less frequent. A feature that accompanies superoutbursts are the *superhumps*, a modulation of the light near the superoutburst-maximum, believed to be caused by tidal interactions between the accretion disc and the secondary star, which result in the disc becoming elliptical and precessing [e.g. Vogt, 1982; Whitehurst, 1988; Hirose & Osaki, 1990]. The sideband frequency between the orbital period of the system and the precession period of the accretion disc is known as the *superhump period*, $P_{\rm sh} > P_{\rm orb}$, and it is often used to obtain an estimate of the mass ratio of the system [Patterson, 2001].

1.3.7 Dwarf nova outbursts

During the 1970's a fierce theoretical contest over the mechanism responsible for DN outbursts was taking place. There were two competing theories. The *mass-transfer-burst* (MTB) model, advocated mainly by G. Bath [Bath, 1969, 1972, 1973], which suggested that DN outbursts are the result of liberation of energy in the accretion disc, following instabilities in the secondary star, resulting in enhanced mass-transfer episodes. On the other hand, Osaki [1974] proposed the *disc instability model* (DIM), which traced the cause of outbursts to intermittent accretion of matter onto the WD, due to (unknown at that time) instabilities in the accretion disc. Work by Hōshi [1979] and Meyer & Meyer-Hofmeister [1981] led to the discovery of the *thermal limit cycle* as the mechanism driving disc instabilities. In this context, a thermal instability is triggered in the disc, due to partial ionisation of hydrogen, which brings the disc in a high-viscosity hot state, greatly increasing the rate by which material is transferred through the disc and accreted on the white dwarf.

This work, together with the good agreement between the DIM model predictions and observed properties of DN outbursts, settled the argument in favour of Osaki's model and lead to its near-universal acceptance. However, it should be pointed out that the DIM model is not a panacea,

and that mass-transfer fluctuations still hold some merit in explaining certain aspects of the low-states[6] of VY Scl, AM Her and some SU UMa stars [see e.g. Schreiber et al., 2002, and references therein].

1.3.8 The importance of eclipsing CVs

Obtaining accurate parameters of the binary components in a CV is a key ingredient for the improvement of our understanding of binary evolution. Masses and radii of both the white dwarf and the secondary star are fundamentally important in quantifying the effects of accretion and mass-transfer on the structure of the white dwarf and the secondary respectively. However, the presence of the accretion disk in a CV complicates matters considerably. For example, measurements of radial velocities for the dynamical studies of white dwarf primaries are very uncertain, if not unobtainable in most cases [e.g. Shafter, 1983; Thorstensen, 2000]. In general, deriving masses of white dwarfs in CVs is a notoriously difficult task [Patterson, 1998].

Eclipsing systems are, practically, the only way of securely measuring the masses of the binary components, through geometric considerations alone [e.g. Wood et al., 1989]. In fact, the first confirmation of a brown dwarf secondary in a CV (predicted by the standard scenario of CV evolution) was made in an eclipsing system [Littlefair et al., 2006b]. Eclipsing CVs also allow the study of the size and structure of the accretion disc, through techniques such as *eclipse mapping* [Horne, 1985], providing a test-ground for the predictions of the disc-instability theory. We should note however that the detection of eclipses in a CV does not automatically mean that accurate parameters can be measured. We revisit this point in Chapter 6. Finally, we note that Southworth et al. [2009] list only 10 systems above the orbital period gap that have accurate parameter determinations.

The observational hurdles in determining stellar parameters mean that additional approaches need to be sought out, in order to study CVs in more detail. Nearly 14 years ago, a new avenue presented itself with the detection of pulsations in the white dwarf primary of a cataclysmic variable star. The final part of this chapter deals with the topic of white dwarf pulsations.

1.4 Pulsating white dwarfs

1.4.1 A census of white dwarfs

Before giving a general overview of the pulsating white dwarfs, it is useful to present a brief classification of white dwarf types. White dwarfs have traditionally been separated into two distinct families: those with a hydrogen-rich atmosphere composition and those with a helium-rich surface composition. Using the currently accepted nomenclature [e.g. McCook & Sion, 1999] white dwarfs can be classified in the following "spectral types":

- DA - only hydrogen (Balmer) lines; no He I or metals present

[6] Irregularly occurring phases, when a system is observed at a much fainter state than its typical quiescent brightness

- DB - He I lines; no H or metals present, $T_{\rm eff} \sim 12000 - 40000\,{\rm K}$
- DC - continuous, featureless spectrum; no lines deeper than 5% in any part of the spectrum
- DO - strong He II lines; He I or H present, $T_{\rm eff} \gtrsim 40000\,{\rm K}$
- DZ - metal lines only; no H or He lines
- DQ - atomic C I or molecular C_2 carbon features; $T_{\rm eff} \sim 4000 - 13000\,{\rm K}$

Recently, a number of white dwarfs with $T_{\rm eff} \sim 20000\,{\rm K}$ that showed atomic C II features have been identified in the SDSS. These objects have been dubbed as "hot DQ white dwarfs", although Dufour et al. [2008] speculate that they are fundamentally different from their cool DQ counterparts.

1.4.2 Overview of variable white dwarfs

More than forty years ago, Landolt [1968] reported on short-period light variations on the (suspected at the time) white dwarf HL Tau 76. Soon after, Lasker & Hesser [1969] discovered similar variations in G44-32, to be followed by the star Ross 548 (= ZZ Ceti) [Lasker & Hesser, 1971]. Shortly afterwards, Chanmugam [1972] and Warner & Robinson [1972] concluded that the observed timescales of these multiperiodic light variations were consistent with non-radial gravity mode oscillations (g-modes). The first unified treatment of the newly-emerged class of isolated, non-interacting, DA pulsating white dwarfs was achieved by McGraw [1977], who established that the pulsating DA white dwarfs were tightly grouped around a colour index of $B - V \sim +0.2$, corresponding to $T_{\rm eff} \sim 12000\,{\rm K}$.

The work of McGraw inspired many groups to come up with theoretical models able to drive pulsational instabilities in white dwarfs [e.g. Winget et al., 1981; Dziembowski & Koester, 1981; Dolez & Vauclair, 1981; Winget et al., 1982b], however it was the work of Winget [1982] that found the cause of pulsations to be linked with increased envelope opacity, which strangles the flow of radiation, attributed to the recombination of hydrogen in the WD atmosphere at the temperature of $T_{\rm eff} \sim 12000\,{\rm K}$. A better understanding of the driving mechanism, taking into account the presence of convection zones, was offered by Brickhill [1983]. This basic picture still holds very much true today.

In a direct analogy to the pulsating DA white dwarfs, predictions were made about the existence of pulsating DB white dwarfs, as the recombination of helium (albeit at higher effective temperatures, $T_{\rm eff} \sim 25000\,{\rm K}$) could potentially excite g-modes as well. These predictions were confirmed with the discovery of GD 358 (= V 777 Her) by Winget et al. [1982a].

In the meantime, McGraw et al. [1979] had discovered multiperiodic luminosity variations, reminiscent of white dwarf pulsations, in the star PG 1159-035 (= GW Vir), recognised today as a third class of pulsating white dwarfs. Stars of this class [see Werner & Herwig, 2006, for a review] have very high effective temperatures, of the order of 100000 K, atmospheres devoid of H showing a mixture of He, C and O, while also displaying strong N lines [Dreizler & Heber, 1998]. They are believed to be the product of the, so-called, *born-again scenario*, in which the progenitor experiences a late He thermal pulse in the post-asymptotic giant branch (post-AGB) phase, which

strips the hydrogen and mixes helium, carbon and oxygen in the envelope [e.g. Althaus et al., 2007, and references therein]. The $\kappa-$mechanism, the cyclic ionisation of the K-shell electrons of carbon and oxygen [see Quirion et al., 2007, for an account], is responsible for driving pulsations in these stars.

The latest addition to the classes of pulsating white dwarfs came in the form of four systems belonging to the "hot DQ" class [Montgomery et al., 2008; Barlow et al., 2008; Dunlap et al., 2010; Dufour et al., 2011].

From the brief discussion above, it is readily visible that pulsators are encountered among white dwarfs with different atmosphere/envelope composition and in different temperature regions along the WD cooling tracks. Hence, pulsations are believed to be an evolutionary stage in the life of every white dwarf [e.g. Fontaine et al., 2003]. This is visualised in Figure 1.7.

The study and understanding of white dwarf pulsations, using the methods and techniques of *asteroseismology*, presents a unique opportunity to advance our knowledge on matters of a wider astrophysical context. Each pulsational mode is an independent constraint on the stellar structure. With some modes, we can probe the stellar interior, even as far down as the core. Through asteroseismology we can determine fundamental stellar parameters such as masses, core compositions, ages, rotation rates and magnetic field strengths. If and once these parameters are known, the information obtained from pulsating white dwarfs can then be used to test a wide range of phenomena. Comparing rotation rates between different pulsating WD classes can give clues about the evolution of angular momentum. The carbon-oxygen ratio in WD cores depends on the rate of the important $^{12}\mathrm{C}\,(\alpha,\gamma)\,^{16}\mathrm{O}$ nuclear reaction [Metcalfe et al., 2002; Metcalfe, 2003]. Pulsating low-mass ($\log g \leq 7.6$)[7] He-core white dwarfs should allow us to probe their equation of state [Mukadam et al., 2004], while high-mass ($\log g \geq 8.5$) DA white dwarfs could be crystallised, offering an empirical test of the theory of crystallisation in stellar plasma [e.g. Winget et al., 1997]. Pulsating WDs could help calibrate the theoretical cooling tracks, thus providing better estimates for white dwarf ages, which in turn can be used to better determine the age of the Galactic disc and halo [e.g. Hansen et al., 2002].

Comprehensive reviews of pulsating white dwarfs and associated asteroseismology considerations are provided by Winget & Kepler [2008] and Fontaine & Brassard [2008].

1.4.3 The ZZ Ceti stars

White dwarfs with hydrogen-dominated atmospheres (DA) constitute the large majority of the white dwarf population [Fleming et al., 1986], hence the pulsating DAs, commonly referred to as DAVs or ZZ Ceti stars, are the most numerous class of pulsating white dwarfs, numbering almost 150 systems [e.g. Mukadam et al., 2006; Fontaine & Brassard, 2008; Castanheira et al., 2010, and references therein].

The observed pulsation periods range from ~ 100 to 1200 s and there is a distinct trend in periods and amplitudes with temperature. This trend allows a meaningful division of the ZZ Ceti pulsators into hot (hDAV) and cold (cDAV) ones [Clemens, 1994; Kanaan et al., 2002; Mukadam

[7] Throughout this thesis, $\log g$ is given by $\log g = \log\left(\mathrm{GM/R^2}\right)$, with G, M and R in the cgs-system, so $[\log g] = \left[\log\left(\mathrm{cm/s^2}\right)\right]$.

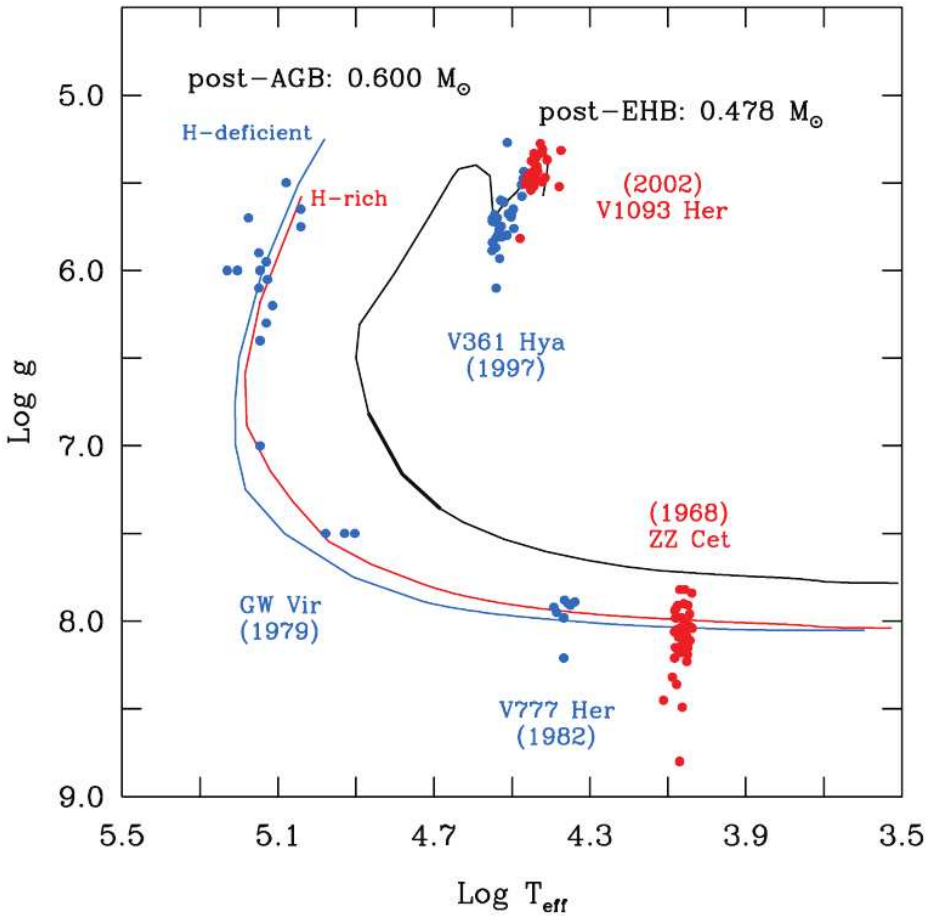

Figure 1.7: The $T_{\rm eff} - \log g$ diagram for compact pulsators. Each class is identified by its official name and year of discovery of the prototype. Included are also the two classes of pulsating hot B sub-dwarf (sdB) stars, the V 1093 Her and V 361 Hya systems,which are not discussed in the text. The newly emerged class of pulsating "hot" DQs is not shown, as accurate values of $T_{\rm eff}$ and $\log g$ are not yet known. Also plotted are typical evolutionary/cooling tracks for (i) a $0.6\,M_{\odot}$ post-AGB, H-rich star which will evolve into a DA white dwarf (red curve), (ii) $0.6\,M_{\odot}$ post-AGB, H-deficient star which will evolve into a DB white dwarf (blue curve) and (iii) a $0.478\,M_{\odot}$ post-extreme horizontal branch (EHB) star which will evolve into a low-mass DA white dwarf (black curve). Figure adapted from Fontaine & Brassard [2008].

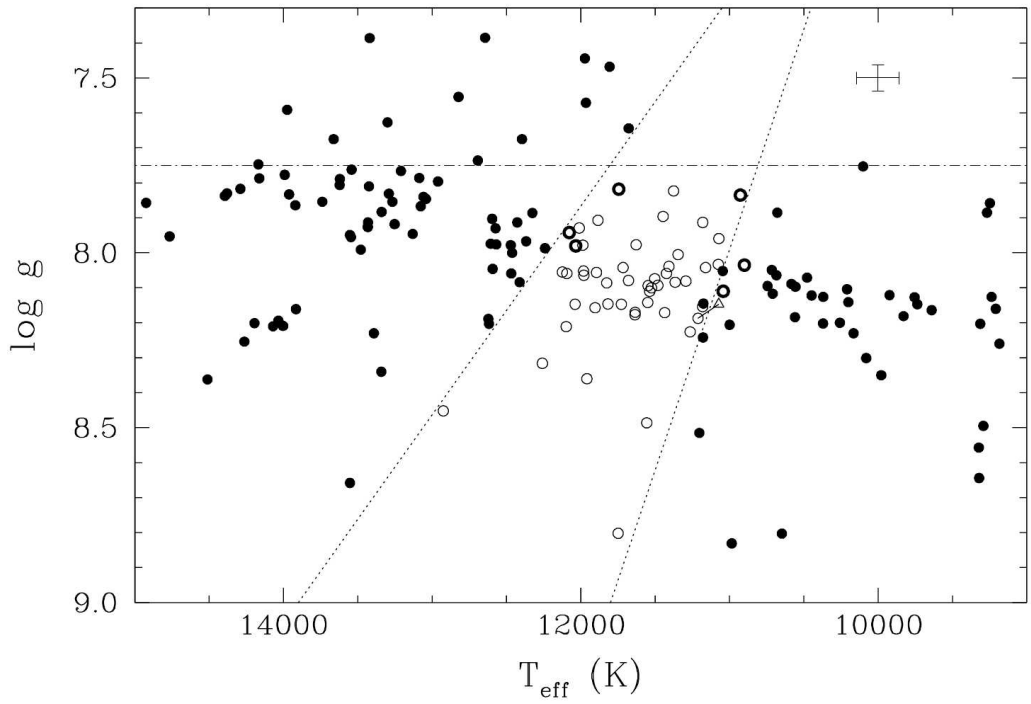

Figure 1.8: The current view of the empirical ZZ Ceti instability strip. Open circles correspond to pulsators, filled circles to non-variables. The error bars in the upper right corner show the typical errors in the $T_{\rm eff}$ and $\log g$ determinations. The dotted lines show the location of the strip. Systems above the dashed-dotted line at $\log g \sim 7.75$, which in this temperature range corresponds to $M_{\rm WD} \sim 0.47\,{\rm M}_{\odot}$, are the product of binary evolution. Figure adapted from Gianninas et al. [2007].

et al., 2006]. Hot DAVs show relatively few pulsation modes, with low amplitudes ($\sim 0.1\% - 3\%$) and periods around $100 - 300$ s. On the other hand, cold DAVs show longer periods, $600 - 1000$ s, larger amplitudes (up to 30%) and greater amplitude variability [Kleinman et al., 1998].

ZZ Ceti stars are located in a well defined region of the $T_{\rm eff} - \log g$ space, with $10500\,{\rm K} \lesssim T_{\rm eff} \lesssim 14000\,{\rm K}$ and $7.3 \lesssim \log g \lesssim 9$, known as the *ZZ Ceti instability strip* [e.g. Bergeron et al., 1995b; Koester & Allard, 2000]. Figure 1.8 illustrates the current view of the strip. Noteworthy is the fact that the width in $T_{\rm eff}$ of the strip depends on $\log g$, and it is only $\sim 1500\,{\rm K}$-wide for $\log g \simeq 8$.

Over the years there has been substantial theoretical work trying to determine the exact edges of the instability strip and confirm (or reject) the hypothesis that the strip is pure, i.e. there are no photometrically constant white dwarfs inside the strip [see e.g. Bergeron et al., 2004; Gianninas et al., 2005, 2006]. The direct implication of a pure strip is that *all* DA white dwarfs will become ZZ Ceti-type pulsators at some point, as they cross the strip during their evolution. This, in turn, means that results from asteroseismology on pulsating DAs can be used to infer the basic structural properties of the DA white dwarfs as a class.

1.4.4 Pulsating white dwarfs in CVs

Over a decade ago, an important and surprising discovery was made: the white dwarf primary in the cataclysmic variable GW Lib was found to exhibit g-mode pulsations, similar to a ZZ Ceti star [Warner & van Zyl, 1998; van Zyl et al., 2000].

This discovery was important, because it opened a new avenue for measuring masses of white dwarfs in CVs through application of asteroseismology. It was surprising, because the white dwarf in GW Lib *should not* be pulsating, as its $T_{\rm eff} \sim 14700\,$K and $\log g \sim 8$ measurements placed it nominally outside the ZZ Ceti instability strip [Szkody et al., 2002a]. In fact, most of the (non-magnetic) white dwarfs in cataclysmic variables are not expected to be pulsating, as accretion heats them to effective temperatures greater than 12000 K [Townsley & Gänsicke, 2009].

Townsley et al. [2004] studied GW Lib and speculated that the presence of pulsations could be attributed to a higher white dwarf mass than previously believed. They also stated that two factors could affect the pulsations and render their solution inaccurate: (i) the accretion of heavier elements, which lead to a solar composition or subsolar metal composition of the WD atmosphere and (ii) a rapid rotation of the WD, which could be an order of magnitude more rapid than single ZZ Ceti pulsators. A more detailed study was presented in Arras et al. [2006]. They concluded that the atmospheric composition of the accreting WD, especially the He abundance, plays an important role in determining the location of the instability strip. High He abundances (above solar) will in fact form an additional region at $T_{\rm eff} \sim 15000\,$K, where pulsations can be driven due to He II ionisation.

The diversity in $\log g$, $T_{\rm eff}$ and (accreted) atmosphere composition encountered in the WD primaries of CVs, is mirrored in the diversity of the observed variable and non-variable population of accreting WD pulsators. About a dozen pulsating WDs in CVs have been discovered [Szkody et al., 2010, and references therein] and, for simplicity, they can be divided in "hot" ($T_{\rm eff} \sim 15000\,$K e.g. GW Lib) and "cold" [$T_{\rm eff} \sim 12000\,$K e.g. V455 And; Araujo-Betancor et al., 2005] pulsators. However, both hot [WZ Sge, BC UMa, SW UMa; Sion et al., 1995; Gänsicke et al., 2005] and cold [EG Cnc, Szkody et al., 2002b] CV primaries are found to be non-variable. This is clearly illustrated in Figure 1.9.

It is unclear which of the two cases (if any) is the normal scenario for CV pulsators, if they could be considered as two distinct sub-classes of pulsating, accreting white dwarfs, or if pulsating WDs in CVs should be examined in a case-by-case manner. Observational input, in the form of accurate $\log g$, $T_{\rm eff}$, atmosphere compositions and rotation rates measurements, along with more detailed models incorporating the effects of accretion in the driving of g-modes are required in order to improve our understanding on this matter.

1.5 Thesis overview

In this first chapter I have presented a broad introduction on close compact binaries consisting of a white dwarf and a main-sequence companion. I have provided an overview of the current theoretical understanding of the common envelope phase and the formation of post common envelope binaries, I have discussed the class of cataclysmic variables and reviewed the mechanisms that drive their evolution and I have given a summary on pulsating white dwarfs. I have highlighted various issues

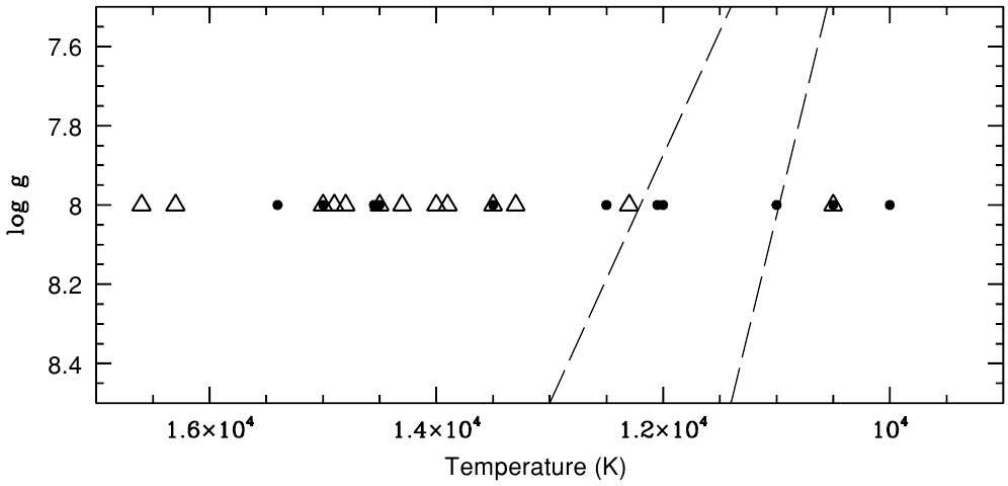

Figure 1.9: The current view of the instability strip for pulsating WDs in CVs. The limits of the ZZ Ceti strip from Gianninas et al. [2007] are shown as dashed lines. Pulsating WDs are indicated with filled circles, non-variable WDs with open triangles. A $\log g = 8$ is assumed for all systems, as the WD parameters are uncertain. Figure adapted from Szkody et al. [2010].

that remain unresolved and have emphasised the need for observational input in order to tackle these issues. The required observational input involves the determination of fundamental binary and stellar parameters, such as the orbital period of the binary and the masses and radii of the binary components.

The purpose of the work presented in this thesis is to identify systems where such measurements are (in principle) feasible and, when possible, perform said measurements. I will first provide a review of the observational techniques and the analysis methods used to obtain the desired measurements (Chapter 2) and then present the entire observational data set (Chapter 3). In Chapters 4 and 5 I will present the study of five new eclipsing post common envelope binaries. Building a large sample of such systems and measuring their orbital periods and the masses of their stellar components can provide significant insight in the efficiency of the ejection of the common envelope and the value of α_{ce}; furthermore, masses and radii determined from such systems can help calibrate the mass-radius relations of both white dwarfs and main-sequence stars. In Chapter 6 I will present the study of a new eclipsing cataclysmic variable. Obtaining the masses of the binary components in CVs (especially that of the white dwarf) is notoriously difficult and it is sad but true that only about 12% of the known CV population has a mass determination for the white dwarf [Zorotovic et al., 2011]. Identifying and studying eclipsing CVs is one way of alleviating the problem. Another avenue for obtaining white dwarf masses in CVs has recently opened up and involves the study of pulsating white dwarfs in CVs. This will be explored in Chapter 7, where I will present the study of such a white dwarf.

Chapter 2

Methods and Techniques

2.1 Introduction

In this Chapter I will present the various methods and techniques that can be employed in the study of binary systems in general and eclipsing systems in particular. I will start with a description of how we have selected the systems analysed in Chapters 4 to 7. I will then describe the process of collecting and reducing the necessary data and focus on the tools that will be used to achieve the goal of measuring fundamental system parameters.

2.2 Target selection

2.2.1 Post-Common-Envelope Binaries from the SDSS

The objects presented in Chapters 4 and 5 were originally identified as part of a large scale search for PCEBs in the SDSS. The SDSS was expected to be very prolific in identifying WD+MS binaries, due to the innovative five-band photometric system, which provides ample coverage of the parameter space [see Rebassa-Mansergas et al., 2010]. Indeed, this search, which selected candidates based on their spectroscopic appearance [Rebassa-Mansergas et al., 2010], has yielded more than 1600 WD+MS binaries. Intensive spectroscopic follow-up has provided radial velocity information for a considerable number of systems in this sample and orbital periods have been measured for some of them (a process detailed in Section 2.4.2). Systems that exhibited noticeable radial velocity variations and systems with short orbital periods were revealed to be PCEBs[1] [Rebassa-Mansergas et al., 2007; Schreiber et al., 2008; Rebassa-Mansergas et al., 2008].

As a separate project, we have begun searching for eclipsing PCEBs among the systems identified. Various methods have been employed to select eclipsing candidates. Some of candidates have been identified through discrepancies between their photometric and spectroscopic fluxes from SDSS, or from multi-epoch photometry performed by SDSS (Stripe 82). Another very successful method was the following: decomposing the binary spectrum into its constituents and studying them

[1] See again Figure 1.3.

individually can provide an initial estimate of the masses of the binary components [see e.g. Rebassa-Mansergas et al., 2007, for a description of how this is achieved]. Coupled with the knowledge of the orbital period and radial velocities (Section 2.4.2), obtained through spectroscopic follow-up, the binary's inclination angle can be constrained (Section 2.4.3). A review of the aforementioned methods used to identify eclipsing candidates is given in Pyrzas et al. [2010].

2.2.2 Cataclysmic Variables from the HQS

The objects presented in Chapters 6 and 7 were originally identified as CV candidates from the Hamburg Quasar Survey (HQS). The HQS is an objective-prism survey carried out with the 0.8 m Schmidt Telescope at the Calar Alto Observatory (Almeria, Spain), aiming to identify bright quasars at high galactic latitudes [Hagen et al., 1995]. Candidate CVs were selected based on their spectroscopic properties, specifically the presence of Balmer emission lines in their spectra, and subjected to follow-up spectroscopic observations to confirm their CV nature [Gänsicke et al., 2002]. More than 50 systems have been confirmed as CVs (or pre-CVs) and a dozen candidates still await confirmation. Summaries of the project and results are reported in Aungwerojwit et al. [2005, 2006]; Aungwerojwit & Gänsicke [2009], and references therein.

Having candidate systems at hand, we then proceed with the collection of the required photometric and spectroscopic data sets that will allow the determination of the binary and stellar parameters.

2.3 Observations and Reductions

2.3.1 Charge Coupled Devices

Astronomy is one of the scientific disciplines where *experiments*, in the traditional laboratory version, where the scientist has some degree of control over the system under study, cannot be conducted. Instead, researchers rely on *observations* gathered through telescopes in a multitude of ways. The painstaking combination of eye-pen-and-paper, photographic plates and photoelectric photometers are a few of the means that have been employed throughout the history of observational astronomy. The most important advance in the field came when astronomy entered the digital era and began using *charge-coupled devices*, CCDs.

A modern CCD is essentially an array of metal-oxide-semiconductor (MOS) capacitors, with the necessary electronics to measure and output the array contents. A MOS capacitor is a silicon substrate doped with boron (p-type-dopant) and phosphorous (n-type-dopant), with an overimposed thin oxide layer (e.g. SiO_2) and a conductive polysilicon gate atop. Henceforth, we will be referring to a MOS capacitor as a *pixel*.

During an exposure, incoming photons create free electrons via the photoelectric effect. Voltages applied on the gate of each pixel allow the pixel to act as a potential well and trap the generated electrons, until the exposure is finished.

At the end of the exposure, on-board electronic circuits begin the *readout* process: the purpose is to move the collected charge across the chip, through the *array transfer gate* (ATG),

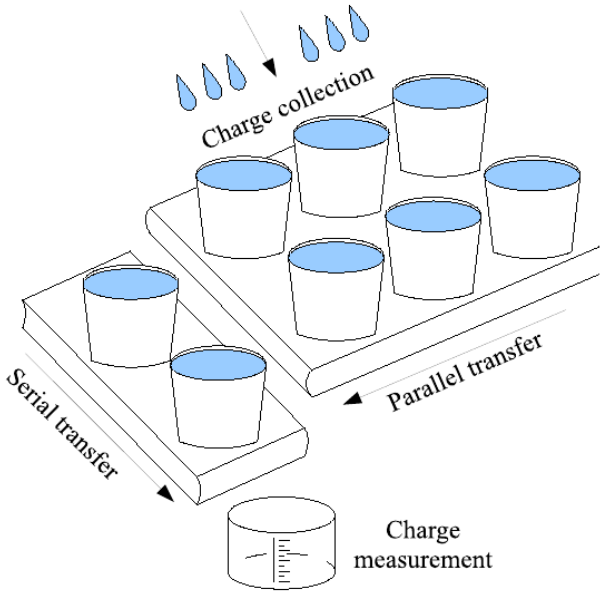

Figure 2.1: The bucket brigade analogy for the operation of a CCD. Each bucket (pixel) fills with rainwater (photo-electrons) during an exposure. After the exposure is finished, each row of buckets is moved via parallel transfer onto a serial register, before each bucket of a row is moved via serial transfer in order to have its charge measured. Figure courtesy of Richard Hickman.

a process usually called *parallel clocking*, onwards to the *output summing well* (OSW), a process called *serial clocking*, and subsequently move it through the *output transfer gate* (OTG) towards the *sense node*, where the charge measurement occurs. The operation of a CCD can be summarised in the *bucket brigade* analogy, illustrated in Figure 2.1.

Moving the charge across the chip is achieved by altering the voltages on the gate of each pixel. This is usually implemented using three different voltage configurations, as shown in Figure 2.2, and effectively transfers the collected charge from one pixel to another. It is exactly this *coupling* of charge from pixel to pixel that gives CCDs their name.

In the sense node, each analog charge is digitised by the *analog-to-digital converter* (ADC), according to the CCD's *gain*, i.e. the number of electrons required to produce a value of 1 *analog-to-digital unit* (ADU). Most modern CCDs have 16-bit ADCs, which means they can output ADU values ranging from 0 to 65535 ($= 2^{16} - 1$). ADCs can only produce integer values, which means some charge is inevitably uncounted. For example, assuming that 13 electrons have been collected and the CCD has a gain of $5\,\mathrm{e}^-/\mathrm{ADU}$, the output of the ADC will be 2 ADU and 3 electrons will be "lost".

The readout process can introduce some uncertainties in the final signal output. First, the conversion from analog to digital signal is not perfectly repeatable, which means that even in the hypothetical case of the same pixel being read out multiple times, each time with identical charge, a slightly different output may be produced. Second, the on-board CCD electronics themselves will

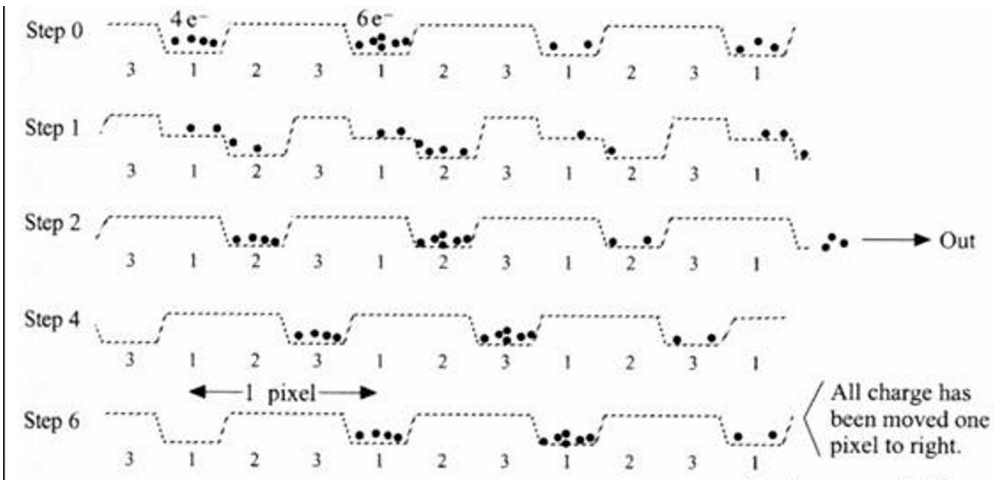

Figure 2.2: Read-out process in a CCD. A three-step alteration of the voltages applied at the gate of the pixels, allows the transfer of charge from one pixel to another. Figure courtesy of Boris Gänsicke.

introduce spurious electrons into the process, yielding unwanted random fluctuations in the output. The combined effect of these uncertainties is referred to as *readout noise*.

The readout process also introduces *dead time* in the observations, as the CCD needs to be read out before a new exposure can start. This dead time can be quite significant compared to the exposure time, which causes problems when high time-resolution is a requirement. For example, reading out the Wide Field Camera (WFC) on the 2.5 m Isaac Newton Telescope (INT) on La Palma (Canary Islands) can take up to 40 seconds. In order to reduce the readout time and readout noise, *binning* and *windowing* can be used. With binning, neighbouring pixels are grouped (at the OSW) and read out together, resulting in one "superpixel" being stored in the output, e.g. a binning mode of 2x2 will group 4 adjacent pixels together, ideally reducing the readout time and noise of the whole chip by a factor of ~ 4. With windowing, only a specific part of the CCD is read out, again resulting in reduced readout time. In most cases, binning and windowing can be used in conjunction. A different approach is applied in *frame transfer* CCDs (FT-CCDs). In an FT-CCD, only half of the chip is exposed. At the end of the exposure, the accumulated charge is transferred to the unexposed half to be read out, while a new exposure begins. As this transfer is very fast (of the order of milli-seconds) FT-CCDs have essentially zero dead-time.

In any case, the result of the readout phase is a two-dimensional array, consisting of digitised values of the charge of each pixel. A CCD image is a simple graphical representation of this 2D array. Measurements can then be performed on this array in a number of ways to extract information about the object of interest.

2.3.2 Photometry

Photometry is a fundamental observational technique, used to measure the (total) flux of a specific object over a range of wavelengths. Observations can be performed using a photometric filter, e.g.

observations in the SDSS *u*-band filter allow the measurement of the flux of an object in the range $3000\,\text{Å} - 4000\,\text{Å}$, or without one, usually called *filterless* or *white light* photometry. Time-series photometry, i.e. a long series of successive images of a specific target, is used to construct a *light curve*, depicting the variation of the target's luminosity with time. However, before a light curve can be obtained, the CCD data need to be properly calibrated and reduced. This involves the following steps.

Bias subtraction

The conversion of analog signal to a digital number in a CCD is not a perfectly repeatable process. In the digitisation phase, the ADC will produce a statistical distribution of possible answers, centred on a mean value. Upon read out of an unexposed pixel, the value of zero collected photoelectrons will translate into a mean value with a small distribution around zero. To avoid having to digitise negative numbers (which would require a "sign bit" to be used), CCDs have a built-in positive offset. This offset value, the mean "zero" level of a CCD, is called the *bias level*. The bias level can be estimated using *bias frames*, zero exposure-time frames - essentially, a read-out of the unexposed CCD chip. A mean bias frame, constructed from a large number of bias frames taken before (and/or after) the science images, should be subtracted from the science images, to remove the unnecessary extra ADUs.

Dark-current subtraction

Dark current is caused by electrons in the chip having enough thermal energy to make the transition from the valence to the conductivity band without the intervention of a photon. As the ADC cannot distinguish the source for any electron, these thermal electrons are counted along with the photoelectrons and introduce spurious ADUs in the final image. In practise, the problem is alleviated by cooling the CCD to very low temperatures using liquid nitrogen. However, in CCDs where less efficient cooling methods are used (peltier or water cooled CCDs), the dark current needs to be taken into account. This is achieved with the help of *dark frames*. Dark frames are long exposures (of the order of several minutes) with the CCD shutter closed. As the dark current is proportional to the exposure time, the dark frame can be scaled to match the exposure time of the science images, thus providing a measurement of the rate of thermal electrons in the science images. The usual practise is to combine a few dark frames in a mean frame, which is then scaled accordingly and subtracted from each science image and flat field (introduced below).

Flat-fielding

Each pixel on the CCD chip does not have the same response to incoming photons, i.e. the probability that a photon will create a photoelectron is different between pixels. In simple terms, some pixels are more sensitive than others. This results in a non-uniform spatial behaviour of the CCD chip, which must be corrected before measurements of any kind are performed on the science images. The correction is achieved through *flat fields*, exposures of the chip under a uniform source of light. The most common way to obtain flat fields is to take exposures of the twilight sky (sky flats),

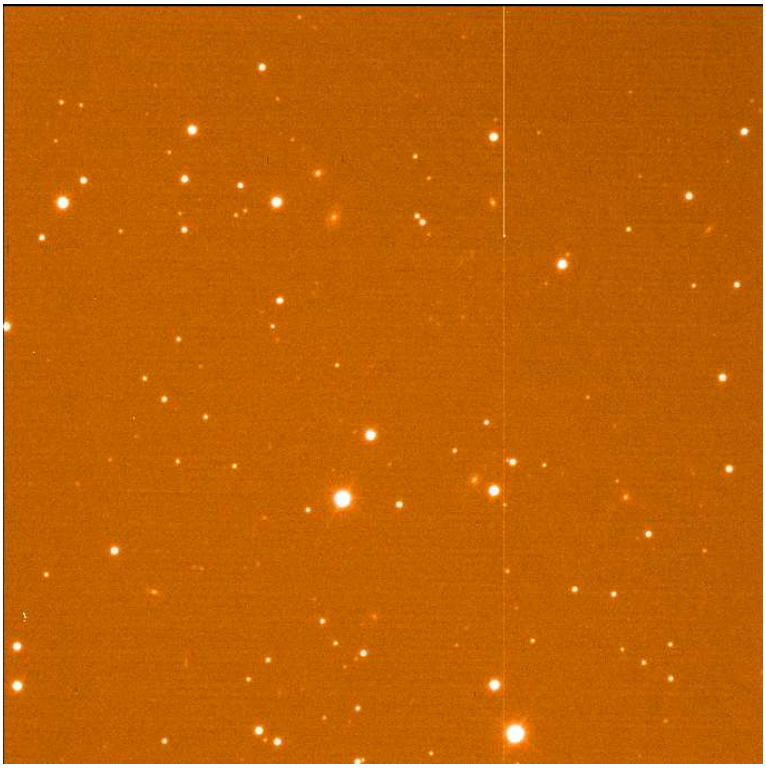

Figure 2.3: An example of a CCD image. The field is that of V 455 And (Chapter 7) and the image was obtained at the 1.20 m Mercator Telescope using the MEROPE CCD. The straight line to the right-hand side of the image is a defective CCD column.

or use special flat-field screens provided in many observatories (dome flats). Similarly to bias and dark frames, a number of flat fields is used to create a mean image, which is normalised to unity. Any deviations from unity will correspond to different pixel sensitivity. Dividing the science images with the mean flat frame results in "flattened" images.

Aperture photometry

An example of a CCD image of a stellar field is shown in Figure 2.3. The most common way to obtain the desired photometric signal is to employ *aperture photometry*.

As its name suggests, aperture photometry is the process of placing an aperture, usually circular with a radius $r_{\rm T}$ of a few pixels, around the target and summing all the counts contained within the aperture. This sum S is the total photometric signal, including the contribution from the target and also from background sources, such as the sky. In order to estimate the contribution of the sky, common practise is to use two more apertures, with radii $r_{\rm S1}$ and $r_{\rm S2}$, which define a sky annulus around the target, "sampling" the sky background in the immediate vicinity of the target (obviously $r_{\rm T} < r_{\rm S1} < r_{\rm S2}$). The estimated sky background B can then be subtracted from S, yielding the desired quantity, the photometric signal I of the target, which is usually given in *instrumental magnitudes*.

Care needs to be taken when choosing the size of the apertures. The target aperture needs to

be large enough, so that it encompasses the whole stellar profile, but not too large, so that it doesn't encompass a large background region. The same applies for the radii defining the sky annulus. They need to be large enough to adequately sample the sky around the target, but not too large, to avoid any potential inclusion of neighbouring stellar profiles, e.g. in crowded regions. Common practice is to employ variable apertures, scaled according to the *full width at half maximum* (FWHM) of the stellar profile in each image, to minimise aperture losses and maximise the signal-to-noise ratio.

Obtaining a light curve

Performing photometry on a long sequence of images allows us to measure the (instrumental) magnitude of the target, $\mathrm{MAG_T}$, with respect to time, i.e. construct the target's light curve. The common practise is to also measure the magnitude from a photometrically constant star, $\mathrm{MAG_C}$, called the *comparison* star, and calculate the light curve in *differential magnitude* ΔMag, where $\Delta\mathrm{Mag} = \mathrm{MAG_T} - \mathrm{MAG_C}$. This process, called *differential photometry*, preserves any intrinsic variability of the target but removes spurious/unwanted variations, e.g. drops of signal due to clouds. Another advantage of differential photometry is the ability to calculate the target's apparent magnitude, if the apparent magnitude of the comparison star is known. This can be achieved because CCDs operate in a linear fashion[2].

2.3.3 Spectroscopy

Spectroscopy is another fundamental observational technique, which allows us to measure how the flux of an object is distributed in wavelength, over a range of wavelengths. Observations are conducted using *spectrographs*, which contain CCDs to record the data, but are equipped additionally with a slit on the focal plane of the telescope, a dispersion element in the light path of the telescope and collimators, which allow an image on the slit to be dispersed and then re-imaged on the CCD.

Diffraction gratings are the most common dispersion elements used. A grating is characterised by a number measured in lines/mm. The *resolution* of a spectrum $\lambda/\Delta\lambda$, effectively the step in wavelength between pixels, depends on the grating used, and increases with increasing number of lines/mm. However, a higher resolution results in a narrower wavelength range (using the same CCD). For example, using the Intermediate dispersion Spectrograph and Imaging System (ISIS) on the 4.2 m William Herschel Telescope (WHT) on La Palma (Canary Islands) with the R600 grating (600 lines/mm) gives a resolution of $0.49\,\text{Å}/\text{pixel}$ over a range of $2054\,\text{Å}$, whereas the R1200 grating (1200 lines/mm) gives a resolution of $0.26\,\text{Å}/\text{pixel}$ over a range of $1055\,\text{Å}$[3] As with photometry, spectroscopic data need to be calibrated and reduced, before a usable spectrum is obtained.

[2]When high photometric accuracy is desired, the colour indices of the stars and the sensitivity of the CCD - which varies with wavelength - need to be taken into account.

[3]These resolutions also depend on the pixel size of the ISIS CCDs and assume a specific slit width. Changing the width of the slit, or changing the CCD for one with a different pixel size, will result in different spectral resolutions, when the same gratings are used.

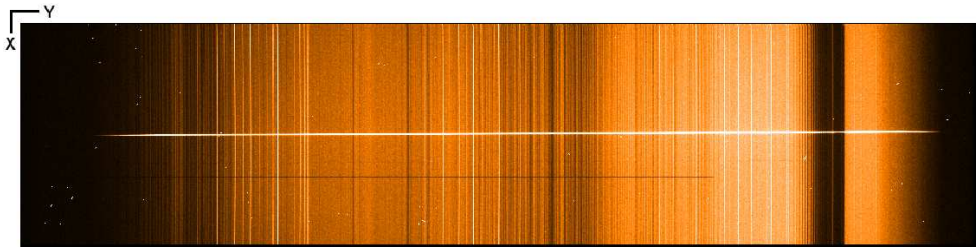

Figure 2.4: An example of a CCD spectrum. The X- and Y-directions (corresponding to columns and rows of the CCD) indicated are known as spatial and dispersion directions respectively. The bright horizontal line in the centre of the frame is the target spectrum, while the black horizontal line beneath the spectrum is a bad CCD row. The vertical lines (along the spatial direction) are sky lines. The white marks spread throughout the image are cosmic ray hits.

Bias and dark-current subtraction

As the bias level and the dark current are inherent properties of the CCD used, bias subtraction and, if required, dark-current subtraction are performed in the same way as for photometric data.

Flat-fielding

Although the idea behind flat-fielding remains the same, the mechanics of it change slightly for spectroscopic observations. Flat fields are usually obtained using Tungsten (W) lamps located inside the spectrograph. However, as the light from the lamp goes through the slit and the grating, the flat field that we obtain contains not only the slit response and the pixel-to-pixel variation of the CCD, but also the spectral distribution of the flat lamp, which must be removed from the mean flat field, before it is applied on the science data.

Obtaining a spectrum

Figure 2.4 shows a raw CCD image obtained with a spectrograph. Extracting the spectrum from the science images is the spectroscopic analogue of performing aperture photometry: we need to measure the total signal S and the background contribution B in order to obtain the target signal I.

We need to know the position of the spectrum through the image, so that we can define the regions from which the spectrum and the sky background are extracted. In an analogy to aperture photometry, these regions are equivalent to placing "rectangular apertures" on the image. The spectrum runs along the dispersion axis, but not necessarily parallel to it. Therefore, we need to *track* the spectrum, i.e calculate precisely where the spectrum lies on the CCD. For this, we measure the position of the spectrum along the spatial direction on each *column* of the image. A polynomial fit to these positions provides the trace of the spectrum along the dispersion direction. We then need to define the *rows* from which the spectrum and the sky brightness should be extracted. For example, along *one column i* of the image, we define the *rows* $j-1, j, j+1$ to contain the spectrum, and the rows $j-5,\ldots,j-2$ and $j+2,\ldots,j+5$ to contain the sky background. Using the trace of the spec-

trum obtained previously, we can extrapolate the position of these regions on each column along the dispersion direction. Subsequently, we calculate the sky level by fitting polynomials to the counts in the sky regions defined in the previous step. Finally, the spectrum itself is extracted from the image, again making use of polynomial fitting to the spectrum profile along the spectrum trace. However, our work is not done yet.

Wavelength calibration

The "raw" spectrum obtained at the previous stage, contains the distribution of counts along the pixels of the CCD. Each pixel corresponds to a wavelength bin according to the resolution of the spectrum, but *which* pixel corresponds to *which* wavelength exactly is unknown. To achieve this transformation from pixel-scale to wavelength-scale, we employ calibration frames called *arcs*. Arcs are exposures taken using emission line lamps within the spectrograph. The lamps usually contain a combination of CuNe, CuAr or ThAr, which have numerous spectral lines with precisely known wavelengths. Using these lines an arc map can be created relating pixel position to wavelength, which can then be applied on the science spectra to calibrate them.

2.4 Tools of the trade

2.4.1 Eclipses and the orbital period

In eclipsing systems the orbital period can be accurately determined by measuring the times of mid-eclipse. For the analysis presented in this thesis, mid-eclipse times have been determined in the following fashion: first, the observed eclipse profile was mirrored in time. The mirrored profile was then overplotted on the original eclipse profile and shifted against it, until the best overlap between the two profiles was found, yielding the desired mid-eclipse point. The process is illustrated in Figure 2.5.

Subsequently, orbital phases were computed for the measured times of mid-eclipse for a large set of test periods. The most likely period and the cycle count were determined by maximising the quantity $(\phi_0^{\text{observed}} - \phi_0^{\text{fit}})^{-2}$, where ϕ_0 is the phase corresponding to mid-eclipse. Then, a linear fit was done to the measured times of mid-eclipse versus the cycle count number. This fit provided the coefficients for the *ephemeris* of the binary, which is of the form $T = T_0 + E \times P_{\text{orb}}$, with P_{orb} the orbital period, E the cycle number and T_0 the zero-point of the ephemeris, i.e. essentially the first measured mid-eclipse time. Finally, the *observed minus calculated* (O-C) values were computed using the ephemeris. This procedure is illustrated in Figure 2.6.

2.4.2 Radial velocities and the orbital period

Time-resolved spectroscopy, a long series of consecutive spectra of an object, can be used to measure the radial velocities of the binary components and the orbital period of a binary system. As the binary components orbit around the mass centre, spectral lines will be shifted due to the Doppler effect. This spectral shift is translated in different values of radial velocity amplitudes (the projected

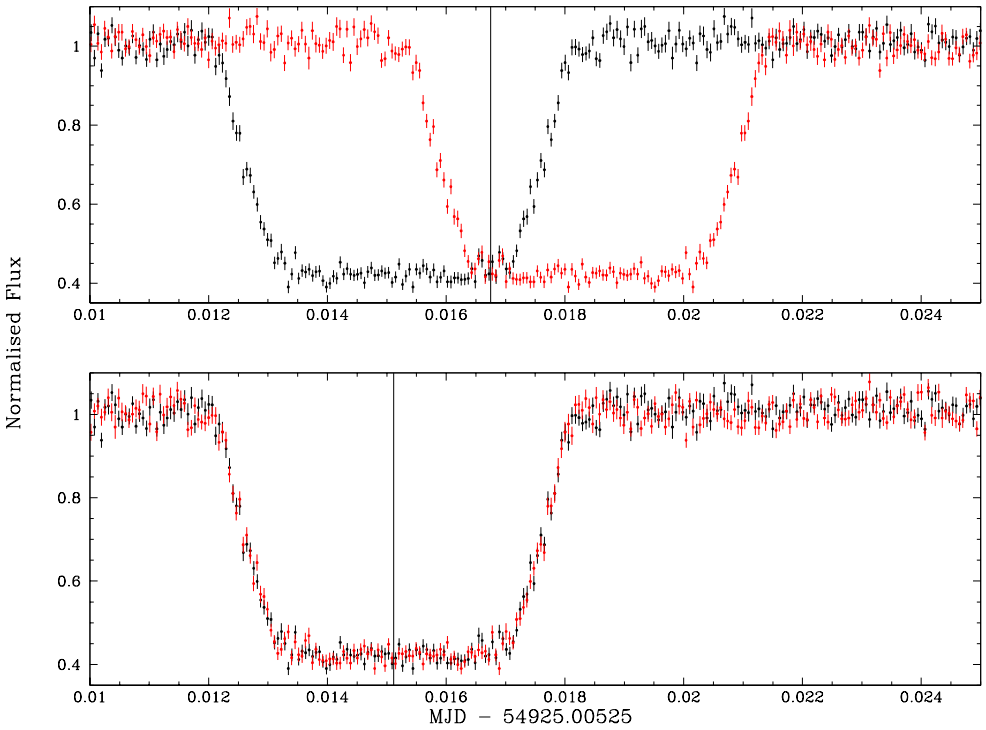

Figure 2.5: The mirroring method for measuring mid-eclipse times. Top panel: the observed eclipse (black points) is mirrored in time around an, initially, arbitrary axis (solid line) and the mirrored profile (red points) is overplotted and shifted against the original. Bottom panel: when the best overlap between the two profiles has been achieved, the mirroring axis corresponds to the mid-eclipse time (solid line).

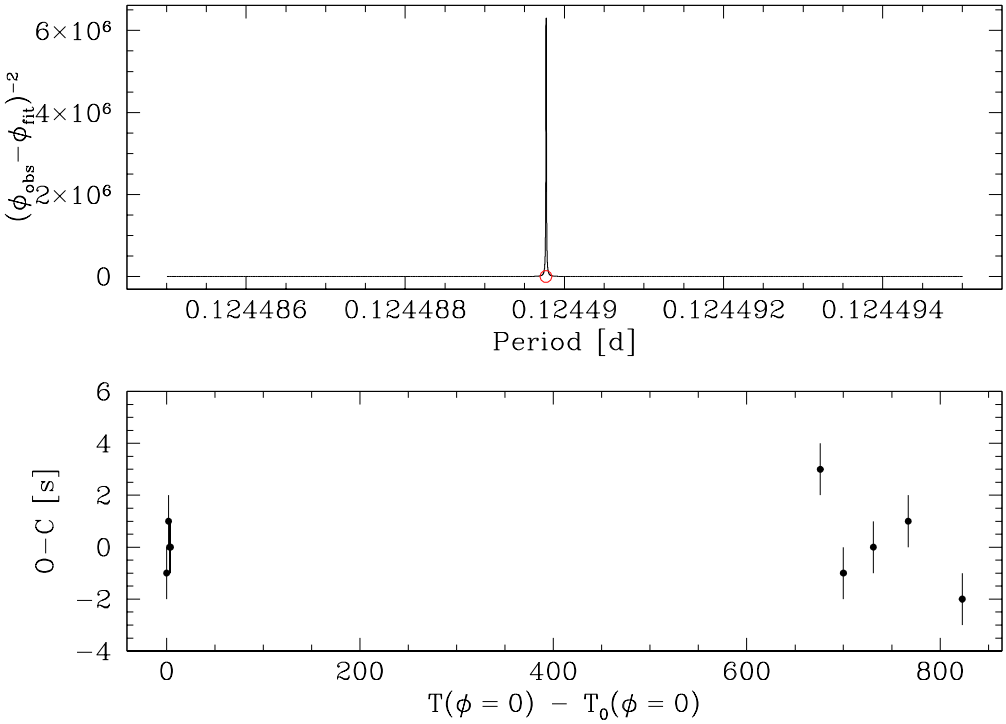

Figure 2.6: Top panel: using the mid-eclipse times and a large set of trial periods, the orbital period (red circle) is determined by maximising the quantity $(\phi_0^{\text{observed}} - \phi_0^{\text{fit}})^{-2}$. A linear fit to the mid-eclipse times versus cycle count produces an ephemeris of the form $T = T_0 + E \times P_{\text{orb}}$. Bottom panel: using the ephemeris observed minus calculated (O-C) values are computed for the mid-eclipse times.

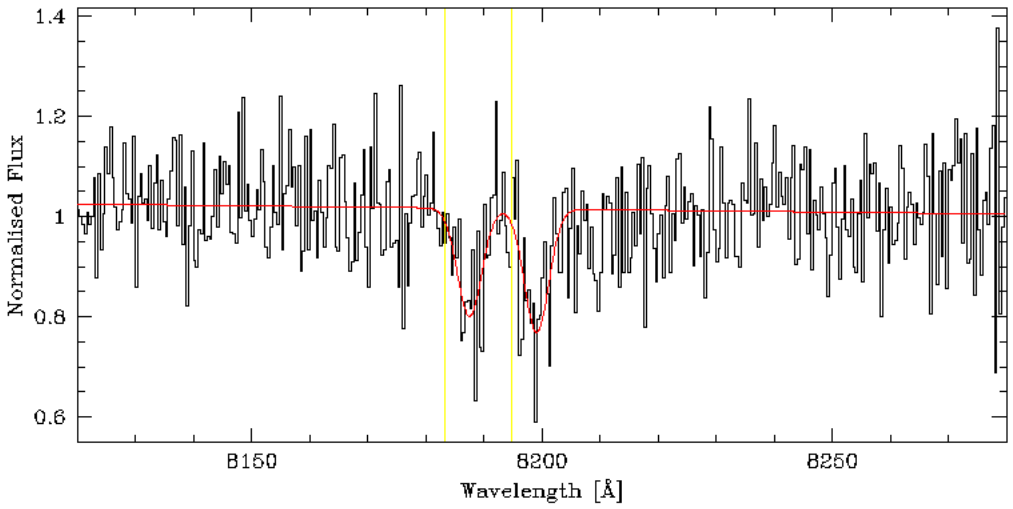

Figure 2.7: A double Gaussian of common width and fixed separation plus a second-order polynomial (red line) is fitted to the observed profile of the Na I λλ 8183.27,8194.81 absorption doublet (black line). The vertical yellow lines indicate the laboratory values. The shift of the line with respect to the laboratory value is obvious.

velocity in the line of sight) for each binary component. For circular orbits, the radial velocities will exhibit a sinusoidal variation over the course of an orbit, modulated at the orbital period of the binary[4].

One method of measuring radial velocities from spectra is to fit the profiles of the spectral lines. A fit to the line provides a measurement for the *observed* wavelength $\lambda_{\rm obs}$ of the line centre. Comparing with the corresponding laboratory values λ_0 yields the radial velocities as $V_{\rm rad} = c\,(\lambda_{\rm obs} - \lambda_0)\,/\lambda_0$. This is illustrated in Figure 2.7.

With the radial velocity measurements at hand we can obtain the orbital period of the binary by fitting a sine wave of the form $V_{\rm rad} = \gamma + K\sin\left[2\pi\,(t - T_0)\,/P_{\rm orb}\right]$, which yields the *systemic velocity* γ, the *radial velocity amplitude* K and the *orbital period* $P_{\rm orb}$. This is illustrated in Figure 2.8.

Measuring radial velocity variations of the stellar components needs sharp spectral features. In the case of WD+MS binaries, such features in the secondary star are the Na I λλ 8183.27,8194.81 doublet or the Ca II λλ 8498.02,8542.09,8662.14 triplet. Determining the radial velocity amplitude of the white dwarf, $K_{\rm WD}$, is notoriously difficult because of the width of the Balmer lines and the He I lines in DA and DB white dwarfs respectively. Measurements could be made if the data are of sufficient quantity and signal-to-noise ratio [see e.g. the approach outlined in Maxted et al., 2004], or in the case of DZ white dwarfs, where lines such as the Ca II H and K doublet (3968.5 Å and 3933.7 Å respectively), the Ca I λ 4226, the Mg I λ 3835 and the Fe I λ 3730 can be detected [see e.g. Dufour et al., 2007]. The white dwarf of SDSS 1210, presented in Chapter 5 is a DAZ white dwarf and measuring $K_{\rm WD}$ is possible. Ultraviolet spectroscopy allows accurate measurements of

[4] A striking exception of this rule is V455 And, the system presented in Chapter 7.

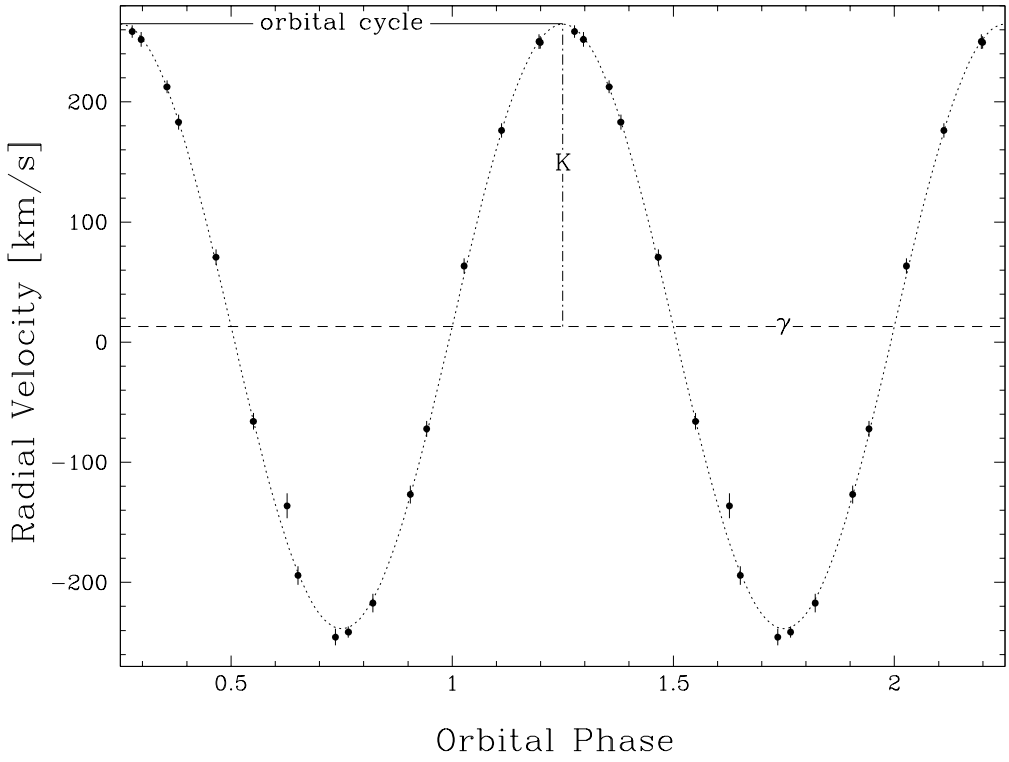

Figure 2.8: A sine fit (dotted line) of the form $V_{\rm rad} = \gamma + K\sin\left[2\pi\left(t - T_0\right)/P_{\rm orb}\right]$ to the radial velocities (black points) yields the orbital period $P_{\rm orb}$, the radial velocity amplitude K (dash-dot line) and the systemic velocity γ (dashed line). Two orbital cycles (solid line) are shown for clarity.

$K_{\rm WD}$ using narrow metal lines originating in the white dwarf photosphere, [O'Brien et al., 2001; O'Donoghue et al., 2003; Kawka et al., 2008], but at the cost of space-based observations.

2.4.3 Basic equations

Here, I will collect all the equations that can be used to combine the observational information and solve a binary system to determine its physical properties. In what follows the orbit of the binary is assumed to be circular.
The first fundamental equation is Kepler's third law,

$$a^3 = \frac{G\,(M_1 + M_2)\,P_{\rm orb}^2}{4\pi^2} \tag{2.1}$$

In a binary system with an orbital period $P_{\rm orb}$, with stars of mass M_1 and M_2, with a_1 and a_2 being the distance of star 1 and 2 respectively from the (common) mass centre, we have

$$a = a_1 + a_2 \tag{2.2}$$

for the binary separation, and also

$$a_1 M_1 = a_2 M_2 \tag{2.3}$$

Combining Equations 2.2 and 2.3 yields

$$a = a_1 \left(\frac{M_1 + M_2}{M_2}\right) \tag{2.4}$$

Observed at an inclination angle i, the orbital velocity of each star is

$$K_1 = \frac{2\pi a_1}{P_{\rm orb}} \sin i \quad \text{(a)} \qquad \text{and} \qquad K_2 = \frac{2\pi a_2}{P_{\rm orb}} \sin i \quad \text{(b)} \tag{2.5}$$

Using Equations 2.1 and 2.4, we can re-arrange the set of Equations 2.5 to yield

$$\frac{(M_1 \sin i)^3}{(M_1 + M_2)^2} = \frac{P_{\rm orb} K_2^3}{2\pi G} < M_1 \quad \text{(a)} \qquad \text{and} \qquad \frac{(M_2 \sin i)^3}{(M_1 + M_2)^2} = \frac{P_{\rm orb} K_1^3}{2\pi G} < M_2 \quad \text{(b)} \tag{2.6}$$

where the quantities on the right on both equations are functions of the observables $P_{\rm orb}$, K_1 and K_2 only. The quantities on the left are referred to as *mass functions* and provide strict lower limits for M_1 and M_2 respectively.
Taking the ratio of Equations 2.6b and 2.6a, we obtain the mass ratio q of the system

$$q = \frac{M_2}{M_1} = \frac{K_1}{K_2} \tag{2.7}$$

The mass functions can be used in various ways to provide constraints on the system parameters. Assuming for instance that we have measured the binary's $P_{\rm orb}$ and one of the radial velocities, e.g. K_2, and that we have an estimate for M_1 and M_2, for example from fitting the observed spectrum with

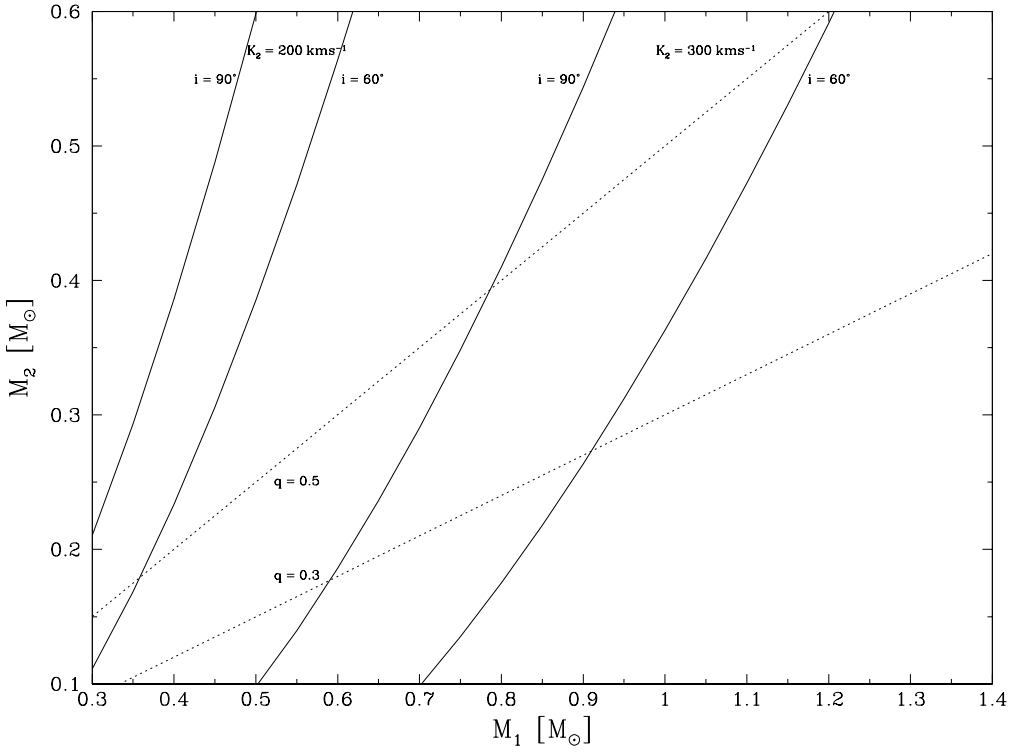

Figure 2.9: The mass function for a binary system with $P_{\rm orb} = 3$h. Plotted as solid curves are the results of Equation 2.6b over a wide range of M_1 and M_2 values for $K_2 = 200\,{\rm kms}^{-1}$ and $K_2 = 300\,{\rm kms}^{-1}$, and for $i = 60^\circ$ and $i = 90^\circ$. Also plotted, as dotted lines, are two cases of binary mass ratio $q = 0.3$ and $q = 0.5$. Knowledge of K_2 allows a given pair of (q,i) values to be uniquely linked to (M_1,M_2) values.

appropriate models, we can obtain an estimate for the binary's inclination angle, since Equation 2.6b can be solved for i as

$$\sin i = \left(\frac{P_{\rm orb} K_2^3}{2\pi G} \frac{(M_1+M_2)^2}{M_1^3} \right)^{1/3} \tag{2.8}$$

This equation is used to identify eclipsing PCEB candidates, as mentioned in Section 2.2.1.

In an eclipsing system, the mass functions can also provide accurate measurements of the stellar masses. If K_1 and K_2 are known from spectroscopy, then the mass ratio q is directly obtained from Equation 2.7. Eclipses provide an accurate $P_{\rm orb}$, as well as the value of the inclination angle i (see Section 2.4.4 for an account of how this is achieved). Masses can then be obtained using Equations 2.6

$$M_1 = \frac{P_{\rm orb} K_2^3}{2\pi G} \frac{(1+q)^2}{\sin^3 i} \quad \text{(a)} \qquad \text{and} \qquad M_2 = \frac{P_{\rm orb} K_1^3}{2\pi G} \left(\frac{1+q}{q}\right)^2 \frac{1}{\sin^3 i} \quad \text{(b)} \tag{2.9}$$

An illustration of the above Equations is given in Figure 2.9.

In the framework of our light curve fitting code, LCURVE, which will be presented in detail in the next Section, it is convenient to write the basic equations as functions of the code parameters. The subscript "1" will from now on be substituted by "WD" and the subscript "2" by "SEC".
First can define the sum of the unprojected orbital speeds of the two stars as

$$V_{\rm S} = V_{\rm WD} + V_{\rm sec} = \frac{K_{\rm WD}}{\sin i} + \frac{K_{\rm sec}}{\sin i} = \frac{(K_{\rm WD} + K_{\rm sec})}{\sin i} \tag{2.10}$$

and using Equations 2.2 and 2.5 we can write

$$V_{\rm S} = \frac{2\pi}{P_{\rm orb}} a \tag{2.11}$$

We can also combine Equations 2.7 and 2.10 to write the radial velocities as

$$K_{\rm WD} = \frac{q}{1+q} V_{\rm S} \sin i \quad \text{(a)} \qquad \text{and} \qquad K_{\rm sec} = \frac{1}{1+q} V_{\rm S} \sin i \quad \text{(b)} \tag{2.12}$$

Combining Equations 2.1, 2.7 and 2.11, we can write the masses as

$$M_{\rm WD} = \frac{P_{\rm orb}}{2\pi G} \frac{1}{1+q} V_{\rm S}^3 \quad \text{(a)} \qquad \text{and} \qquad M_{\rm sec} = \frac{P_{\rm orb}}{2\pi G} \frac{q}{1+q} V_{\rm S}^3 \quad \text{(b)} \tag{2.13}$$

Regarding the radii of the two stars, LCURVE includes both radii scaled by the binary separation $r_{\rm WD} = R_{\rm WD}/a$ and $r_{\rm sec} = R_{\rm sec}/a$. Turning this around and using Equation 2.11 we have

$$R_{\rm WD} = r_{\rm WD}\, a = \frac{P_{\rm orb}}{2\pi} r_{\rm WD} V_{\rm S} \quad \text{(a)} \qquad \text{and} \qquad R_{\rm sec} = r_{\rm sec}\, a = \frac{P_{\rm orb}}{2\pi} r_{\rm sec} V_{\rm S} \quad \text{(b)} \tag{2.14}$$

2.4.4 Light curve model fitting

General

Modelling the observed eclipse profiles allows, in principle, the determination of the binary's inclination angle i, as well as both the stellar radii. However, there are some caveats to be taken into account.

Let us assume a (detached) binary consisting of a WD and a MS star. Fitting the primary eclipse (the occultation of the WD by the MS star) provides a relation between i, $R_{\rm WD}$ and $R_{\rm sec}$[5]. There is a degeneracy in this relation, in the sense that different combinations of $(i, R_{\rm WD}, R_{\rm sec})$ can yield similarly good fits, in terms of χ^2, because a change in the radii can be exactly compensated by a change in inclination [Ritter & Schroeder, 1979]. This is shown in Figure 2.10.

On the other hand, this means that a given inclination angle value corresponds to a unique pair of $R_{\rm WD}$ and $R_{\rm sec}$. The most secure way of lifting this degeneracy is the detection of the secondary eclipse (effectively, the transit of the WD in front of the MS star). Simultaneously fitting both eclipses provides a unique solution of $(i, R_{\rm WD}, R_{\rm sec})$. The main problem here is the difficulty in detecting the secondary eclipse, as the problem is equivalent to performing ground-based observations of an Earth-sized planet transiting an M-dwarf star. In general, we need $R_{\rm WD}/R_{\rm sec}$ to be

[5] To be exact, eclipses yield the radii scaled by the binary separation $R_{\rm WD}/a$ and $R_{\rm sec}/a$.

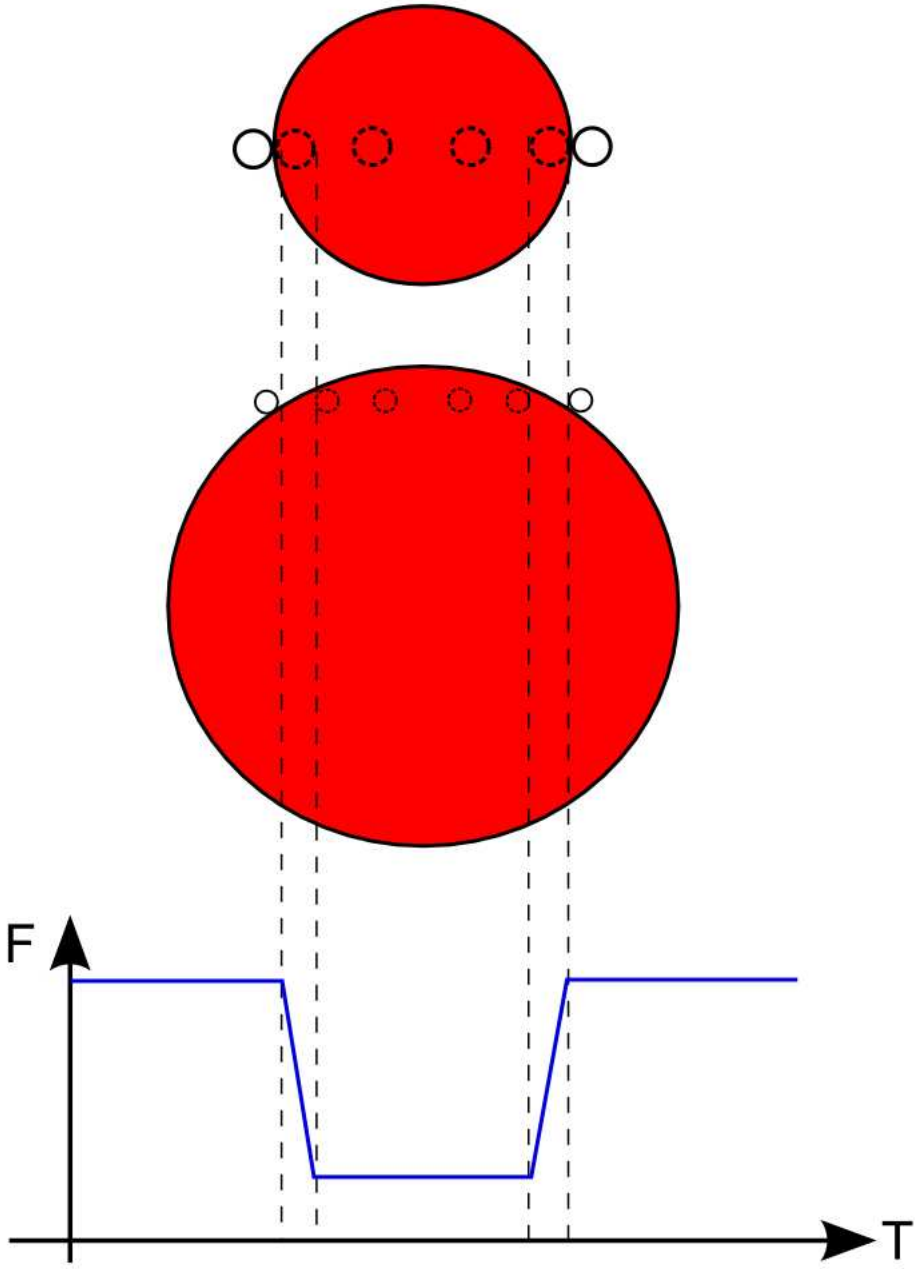

Figure 2.10: Geometry of a primary eclipse in a PCEB. A change in the ratio of $R_{\rm WD}/R_{\rm sec}$ can be exactly compensated by a change in inclination angle i, resulting in the same eclipse profile. Figure courtesy of Steven Parsons.

as large as possible, which requires large white dwarf radii (i.e. low-mass white dwarfs) and small secondary radii (i.e. very late-type MS stars). Hence, this powerful geometric constraint can only be applied in very few cases.

One additional, independent constraint that can be used during the fitting process is *ellipsoidal modulation*, a variation of the out-of-eclipse brightness, arising from the fact that the secondary is tidally distorted and presents a different area (and hence we observe varying flux) during the orbital cycle, which gives a relation between i and $R_{\rm sec}$. Examples of ellipsoidal modulation can be seen in Figure 4.1.

Knowledge of $K_{\rm WD}$ and $K_{\rm sec}$ can provide the *gravitational redshift* of the white dwarf. Fits to the radial velocities provide the systemic velocities γ for both stars; the difference in systemic velocities $\gamma_{\rm WD} - \gamma_{\rm sec}$ is usually interpreted as the gravitational redshift of the WD. According to general relativity, the gravitational redshift of the white dwarf is given by $z \simeq 0.635\,(M_{\rm WD}/{\rm M}_\odot)\,(R_{\rm WD}/{\rm R}_\odot)$ [km/s] [Koester, 1987]. Thus, for a *given* inclination angle i, Equation 2.9 gives a specific WD mass (the mass ratio is known from the radial velocities), and through the light curve modelling a *specific* WD radius. The gravitational redshift for this combination of parameters can then be calculated and its value can be compared to the value of z obtained from spectroscopy. Hence, the gravitational redshift provides an additional constraint.

Unfortunately, as explained previously, radial velocities for white dwarfs are difficult to obtain. Thus, in most cases, the photometric and spectroscopic observational data set consists of a light curve, showing only the primary eclipse and the radial velocity measurements for the secondary star alone. In this case, the mass ratio is also unknown, and the system cannot be solved fully. Masses and radii can only be obtained as a range of possible values with large uncertainties (accuracy of the order of 20%) and M-R relations need to be invoked in the process.

LCURVE

Model fits to light curves presented in this thesis have been performed using Tom Marsh's LCURVE code [see Copperwheat et al., 2010, for an account]. In addition to the two stars, the code offers the option to include accretion components (disc, bright spot) for the analysis of cataclysmic variables. The program treats each star as a sphere and sub-divides it into small elements, the number of which is controlled by the user. Each sphere has its geometry fixed by its radius, which is measured along the line of centres and towards the other star[6]. The code allows for the distortion of Roche geometry (departures from spherical symmetry) and for irradiation of the main-sequence star using the approximation $\sigma T_{\rm sec}^{\prime 4} = \sigma T_{\rm sec}^4 + F_{\rm irr}$, where $T'_{\rm sec}$ is the modified temperature and $T_{\rm sec}$ the temperature of the unirradiated companion, σ is the Stefan-Boltzmann constant and $F_{\rm irr}$ is the irradiating flux, accounting for the angle of incidence and distance from the white dwarf. The white dwarf is treated as a point source in this calculation and no backwarming of the white dwarf is included. The latter is invariably negligible, while the former is a necessary refinement given the approximation inherent in treating the irradiation in this simple manner.

The code computes a model based on input system parameters supplied by the user. The physical parameters, which define the models, are the mass ratio $q = M_{\rm sec}/M_{\rm WD}$, the orbital in-

[6]This treatment effectively scales the radii by the binary separation

clination i, the stellar radii scaled by the binary separation $r_{WD} = R_{WD}/a$ and $r_{sec} = R_{sec}/a$, the unirradiated stellar temperatures of the white dwarf and the secondary star T_{WD} and T_{sec}(assuming black body spectra), the "velocity scale" V_S defined in Equation 2.10, the time of mid-eclipse of the white dwarf T_0 and the distance d. The code accounts for the distance simply as a scaling factor that can be calculated very rapidly for any given model, and so it does not enter the optimisation process. The code also includes limb darkening (up to four coefficients for each star) and gravity darkening parameters. The user has full flexibility as to which parameters will be optimised by the fit, and which ones will be kept fixed at the initial value. However, typically, the light curve of a given system does not contain enough information to constrain all of the parameters simultaneously. For instance, for systems with negligible irradiation, fitting T_{WD} and T_{sec} simultaneously is degenerate, since a change in the temperatures can be exactly compensated by a change in distance.

The accretion disc is modelled as a symmetric, flattened disc with user-defined inner and outer radii scaled by the binary separation. In between these radii, the height of the disc follows a power-law in radius, i.e. $h(R) = h_0 R^b$, with both h_0 and b being parameters of the model and both scaled by the binary separation. The surface brightness of the disc is also treated as a power-law in radius, with the overall level defined by the temperature at the outermost disc radius, translated into a surface brightness assuming a blackbody spectrum. Strictly speaking, this is just a way of normalising the overall flux contribution of the disc, but it is more convenient to think of it in temperature terms.

The bright spot is modelled as a series of elements which lie along a line in the orbital plane. The length l of this line (in units of binary separation) is a model parameter. The geometry of the elements is defined by three angles: the angle ϕ, made by the line of elements of the spot, measured in the direction of binary motion, relative to the rim of the disc ($\phi = 0$ indicates that the line of elements is tangential to the disc); the angle ψ, defined as the angle away from the perpendicular to the line of elements, at which the light from the bright spot is beamed ($\psi = 0$ indicates perpendicular beaming); and the angle ω, which allows the spot to be other than perpendicular to the disc ($\omega = 90$ means a perpendicular spot, while $\omega < 90$ means that the spot is visible for more than half a cycle). The surface brightness of the spot elements scales as $S \propto (x/l)^{\beta} exp[-(x/l)]^{\gamma}$, where x is the distance along the line defining the bright spot, and β and γ are two power-law exponents included as model parameters. The distance between the white dwarf and the point of maximum surface brightness (occurring at $x = l\,(\beta/\gamma)^{1/\gamma}$) is used to define the bright spot position within the binary and is a model parameter.

Fitting routines

Starting from the parameter set, model light curves are fitted to the data using the "downhill"-SIMPLEX (SIM) and LEVENBERG-MARQUARDT (LMQ) methods [Press, 2002].

As its name suggests, SIM uses the notion of a simplex, a geometrical figure consisting, in N dimensions, of N+1 points (or vertices) and all their interconnecting line segments, polygonal faces etc, e.g. a triangle is a simplex in a 2-D parameter space. In a N-dimensional parameter space the minimisation is achieved iteratively by evaluation of a function $f(x)$ defined by the simplex. At each step one point x of the simplex, where the function $f(x)$ is the largest, is moved around the

parameter space, and the function is re-evaluated with the aim $f'(x) < f(x)$ (downhill direction). An appropriate series of such steps will converge to a minimum. This method requires only function evaluations, not the calculation of function derivatives, and it is, therefore, a quick way to get a fit going. However, SIM does not provide any insight on the type of the minimum (local or global).

LMQ is a standard non-linear least squares fitting algorithm, interchanging between the inverse-Hessian algorithm (which requires calculation of the Hessian matrix i.e. the square matrix of second-order partial derivatives of a function) and the method of steepest descent (which requires the calculation of the gradient of a function). The latter is used far from the minimum, switching continuously to the former as the minimum is approached. Two drawbacks of LMQ is that convergence might be very slow - or not reached at all - if the starting point (the initial model parameters) is too far away from a minimum and that, if a minimum is reached, it offers no insight on whether the minimum is a local or the global one. On the other hand, LMQ can provide both a first estimate of parameter uncertainties and a covariance matrix, with the correlations between the various parameters.

Markov Chain Monte Carlo

The usual work-flow is a three stage process and entails starting the fitting process with SIM to locate a minimum in the parameter space and use this result as the starting point for LMQ. LMQ will then explore the parameter space around the minimum and provide uncertainties and correlations on the parameters, which are in turn fed to a *Markov-Chain-Monte-Carlo* (MCMC) process, used for final minimisation (as MCMC is more likely to converge to the global minimum than LMQ) and a robust calculation of uncertainties.

MCMC [see e.g. Ford, 2006, and references therein for a review] is a random walk process, where at each step (jump) a set of model parameter values is drawn from a normal, multi-variate distribution. The selection is governed by the covariance array of the parameters. Each jump is multiplied by a scale factor, and it is either accepted or rejected based on a transition probability. Roberts et al. [1997] have shown that for multi-variate chains, the scale factor is optimally tuned when the acceptance rate is around 0.23. The correct scaling of the jump distribution is very crucial, as one needs to find the balance between adequately sampling the parameter space, converging to a solution and keeping the acceptance rate near the optimal value. The key to this is to obtain an accurate covariance array. Starting with the covariances produced by LMQ, one can run repetitive "trial" chains and each time update the covariance array. Once an accurate covariance array (and by extention an accurate jump distribution) has been found[7], one can proceed with the "production" run of final minimisation and the calculation of the values and uncertainties of the model parameters.

The MCMC chains presented in Chapter 5 has been performed with Tom Marsh's LCMCMC code. Jumps in parameter space are accepted or rejected depending upon a posterior probability (in the Bayesian framework, the probability of the model parameters θ, given the data D, $P(\theta|\mathrm{D})$) evaluated through a combination of χ^2 and a prior probability of the model $P(\theta)$, that is based on previous knowledge of the model parameters and is defined by user-supplied code. Using a normal

[7] When the covariance array changes only slightly between consecutive chains, usually achieved after 3-4 trial runs

(Gaussian) probability density function (PDF) with mean μ and variance σ^2 of the form $P\left(\mu,\sigma^2\right) \propto \exp\left[-\left(x-\mu\right)^2/2\sigma^2\right]$, we can define a "prior" as $P_{\rm prior} = -2*\ln\left(P\left(\theta\right)\right) = \left(\left(x-\mu\right)/\sigma\right)^2$, where x is the calculated value from the model, μ is the observed value and σ the error on the observed value. The posterior probability is defined as $P_{\rm post} = -2*\ln\left(P\left(\theta|{\rm D}\right)\right) = \chi^2 + P_{\rm prior}$. Defining $P^i_{\rm post}$ and $P^{i-1}_{\rm post}$ as the posterior probabilities of step i and $i-1$ respectively, then a jump from $i-1$ to i is immediately accepted if $\Delta P = P^i_{\rm post} - P^{i-1}_{\rm post} < 0 \Leftrightarrow \Delta P = -2*\ln\left(P\left(\theta|{\rm D}\right)_i/P\left(\theta|{\rm D}\right)_{i-1}\right) < 0$, or in the equivalent form $\Delta P = \Delta\chi^2 + \Delta P_{\rm prior} = \left(\chi^2_i - \chi^2_{i-1}\right) + \left(P^i_{\rm prior} - P^{i-1}_{\rm prior}\right) < 0$. If $\Delta P > 0$, then the jump might be conditionally accepted, if $u < \exp\left(-\Delta P/2\right)$ with u a random number and $u \in [0,1]$. This treatment of the transition probability (the rule that decides whether or not a jump is accepted) is effectively a modified version of the (standard) Metropolis-Hastings rule, which is based solely on χ^2, $P \propto \exp\left(-\Delta\chi^2/2\right)$.

An implementation of the above discussion of priors in the MCMC code could arise in the case where both radial velocities $K_{\rm WD}$ and $K_{\rm sec}$ have been measured by spectroscopic observations. Thus in the $j-$th step of the MCMC chain, the value of $K_{\rm WD}$ and $K_{\rm sec}$ can be calculated from the corresponding model values $q_j, i_j, V_{{\rm S},j}$ and Equation 2.12 and compared against the observed values and errors of the radial velocities, in a prior of the form $P_{\rm prior} = \left(\left(K^{\rm MOD}_{\rm WD} - K^{\rm OBS}_{\rm WD}\right)/err^{\rm OBS}_{\rm K_{WD}}\right)^2 + \left(\left(K^{\rm MOD}_{\rm sec} - K^{\rm OBS}_{\rm sec}\right)/err^{\rm OBS}_{\rm K_{sec}}\right)^2$.

Similarly, both stellar masses can be calculated at step j from $q_j, V_{{\rm S},j}$ and Equations 2.13 and both stellar radii as well, from $r_{{\rm WD},j}, r_{{\rm sec},j}, V_{{\rm S},j}$ and Equations 2.14. Thus, a prior for the gravitational redshift of the white dwarf or a prior enforcing a mass-radius relation for either star can easily be implemented.

2.4.5 Fourier transforms

Periodic variability detected in light curves, such as light variations due to the presence of WD pulsations, can be studied using time-series analysis techniques based on *Fourier transforms*.

A Fourier transform (FT) decomposes a signal $x(t)$ into sine waves. At a given frequency ω one can find a set of values (α,ϕ) or (A,B) such that the sinusoid $\alpha\cos\left(\omega t - \phi\right) = A\cos\omega t + B\sin\omega t$ best fits the data $x(t)$, where $\alpha = \sqrt{A^2+B^2}$ and $\tan\phi = B/A$. If this process is repeated for a sufficient number of frequencies ω_j, then the signal can be decomposed as

$$x(t) = \frac{1}{N}\sum_j \alpha_j \cos\left(\omega_j t - \phi_j\right) = \frac{1}{N}\sum_j \left(A_j\cos\omega_j t + B_j \sin\omega_j t\right) \tag{2.15}$$

with the Fourier coefficients A_j and B_j computed as

$$A_j = \sum_k x_k \cos\omega_j t_k \qquad \text{and} \qquad B_j = \sum_k x_k \sin\omega_j t_k \tag{2.16}$$

where $x_k = x(t_k)$. The Fourier coefficients are effectively the correlation of the signal x_k with a sine or cosine wave of frequency ω_j - if there is a good correlation then the corresponding Fourier coefficient is high and gives a large contribution to the sum in Equation 2.15.

Discrete Fourier Transforms (DFTs) are used to decompose discrete signals, e.g. time-series photometric or radial velocity measurements. In our case, the discrete signal under scrutiny is

the light curve of an object. The light curve can be viewed as a series of N numbers x_k $(k = 0, \ldots, N-1)$ obtained over a time-span T, so that x_k is the differential magnitude in bin k corresponding to a time point $t_k = kT/N$. The time-step is $\delta t = T/N$, the frequency-step is $\delta f = 1/T$ and the highest frequency needed for a complete description of the signal by the DFT is $f_{N/2} = \frac{1}{2}N/T$. This frequency, equal to half the *sampling* frequency defined by the spacing of the x_k is called the *Nyquist frequency*.

Certain complications arise when dealing with astronomical data, mainly due to the way the data are obtained, which need to be taken into account before any meaningful interpretation of a DFT can be carried out. To better illustrate these complications it is prudent to introduce the *window function*. The window function is essentially the DFT of a single sinusoid (of arbitrary, but given, frequency) sampled in the exact same way our data set is sampled. Next, we will use the window function and construct ("fake") data sets to investigate some of the possible pitfalls of astronomical time-series analysis. For clarity, the whole process is illustrated in Figure 2.11.

The first thing to consider is that objects can only be observed for a finite amount of time - in our case, as long as it's dark and the object is visible! This affects the accuracy in which a frequency can be detected in the DFT. Long data-sets allow more accurate determinations, and the DFT consists of narrow peaks. The shorter the duration of observations, the broader the peak (Figure 2.11, Panels I-A, I-B). This has a direct effect on our ability to resolve closely spaced frequencies (Figure 2.11, Panels II-A, II-B).

Secondly, the sampling of our data set is limited by the duty cycle of the observations, i.e. exposure time plus the read out time of the CCD. Signals with frequencies higher than the (corresponding) Nyquist frequency *cannot* be resolved. The quick-and-easy way to avoid complications would be to restrict the DFT to frequencies up to the Nyquist frequency. However, things are more complicated. It can be shown that, if a frequency is detected at $f = F_{\rm NYQ} + \Delta f$, the DFT will also produce a peak at $f' = F_{\rm NYQ} - \Delta f$, where $F_{\rm NYQ}$ is the Nyquist frequency. Thus, the DFT is mirrored around the Nyquist frequency, which can result in power from high-frequency signals (such as the spin signals of rapidly rotating WDs) being "down-scattered", and introduce "phantom-peaks" in the DFT, which are very easily mis-interpreted (Figure 2.11, Panel III).

Another consideration is the fact that often the light curve of a target is sampled in an uneven way and can contain gaps, e.g. due to clouds or daylight. The amount of data on either side of the gap might only determine a frequency with an accuracy which is not sufficient to count, with certainty, the number of cycles across the gap. This ambiguity introduces an *alias- pattern* in the DFT, i.e. additional peaks with separations in frequency corresponding to one cycle more or fewer across the gap (Figure 2.11, Panel IV).

Real astronomical data can suffer from all the above mentioned cases, resulting in complex DFTs (Figure 2.11, Panel V). The interpretation of such DFTs and the identification of real, periodic signals needs to be approached with care.

On a final note we should mention, that DFTs of sharp, non-sinusoidal features, such as eclipses, in a light curve will produce peaks in the "correct" frequency (in the case of eclipses this would be the orbital frequency), but power might also be detected at integer multiples of the (fundamental) frequency, known as *harmonics*.

The time-series analysis of light curves presented in this thesis includes *power spectra*

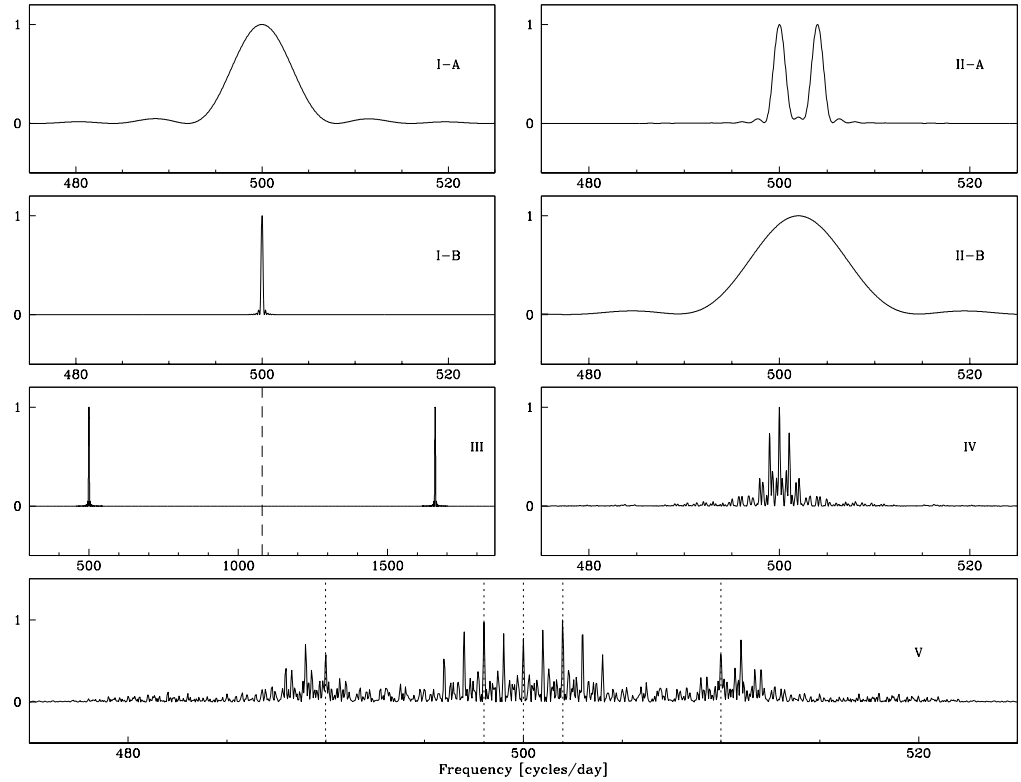

Figure 2.11: Discrete Fourier Transforms of artificial data sets, under various assumptions. Panel I: DFT of a single sinusoid, sampled for 3 h (I-A) and 4 d (I-B). Panel II: DFT of two sinusoids, separated by $4\,\mathrm{d}^{-1}$, sampled for 15 h (II-A) and 2 h (II-B). The DFT in Panel II-B fails to resolve the input frequencies. Panel III: The "real" sinusoid at $f = 1660\,\mathrm{d}^{-1}$ is mirrored at $f' = 500\,\mathrm{d}^{-1}$, due to the Nyquist frequency of observations being $F_{\mathrm{NYQ}} = 1080\,\mathrm{d}^{-1}$ (dashed line). Panel IV: DFT of a single sinusoid sampled over 3 d and the ensuing alias-pattern. The data set also included gaps during the observations due to clouds. Panel V: DFT of five different sinusoids with different amplitudes, irregularly sampled over an interval of 9 d, including gaps due to clouds. Notice how the highest peaks of the DFT do not always correspond to the input frequencies (marked as dotted lines).

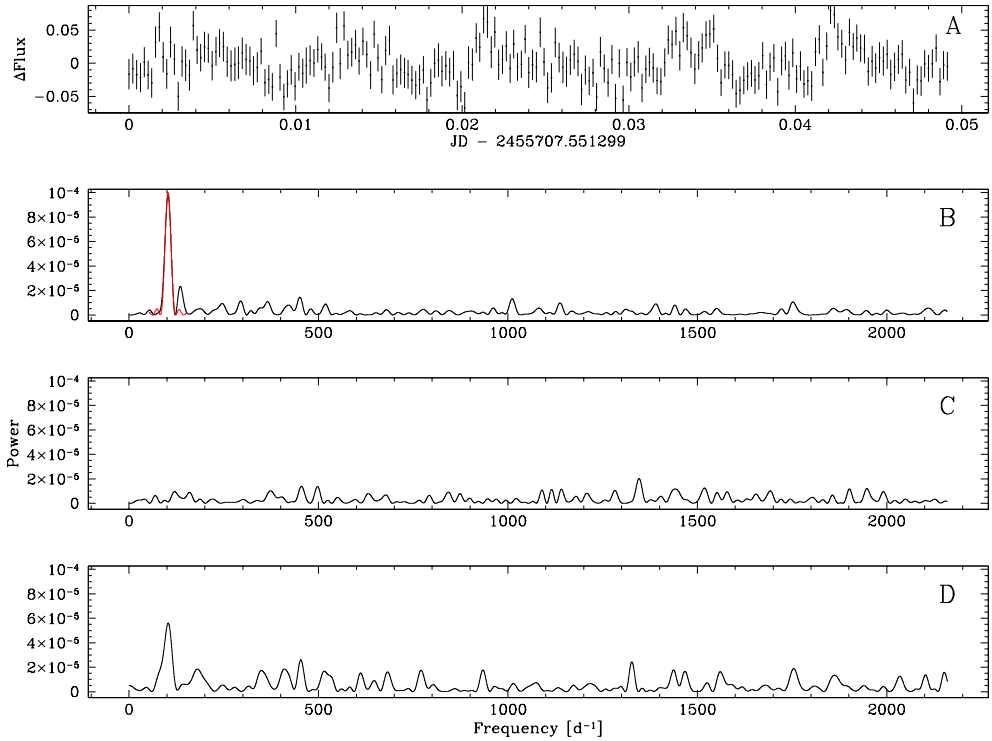

Figure 2.12: Panel A: light curve of a candidate pulsating WD in the detached WD+MS binary SDSSJ 1117-1255. Panel B: the power spectrum (DFT) of the light curve, with the window function (red) scaled to match the highest peak. Panel C: a power spectrum of a simulated light curve, obtained from re-shuffling the flux values of the original, used to estimate the white noise level in the DFT. Panel D: a power spectrum of a simulated light curve obtained from applying a bootstrap method on the original, used for a more robust estimation of the (peak) frequency and error.

(straightforward DFTs) and *Scargle periodograms* [Scargle, 1982] and has been performed using the MIDAS/TSA utility [Schwarzenberg-Czerny, 1993].

We will now take a closer look at the use of time-series analysis techniques through an example, illustrated in Figure 2.12.

In the top panel of Figure 2.12 we plot a light curve of a detached WD+dM binary. The light curve clearly displays variations in the observed flux, although the photometric quality could be considered mediocre. However, we will see that DFTs can detect signals even if the data quality is not the best. We transformed the light curve to a fractional amplitude scale (dividing by the mean and subtracting 1) and calculated a power spectrum (DFT) (Figure 2.12, second panel from the top). The window function (scaled to match the highest peak) is overplotted in red. Indeed, the power spectrum reveals a very strong peak located at frequency $F \sim 103\,\mathrm{d}^{-1}$ corresponding to a period $P \sim 14\,\mathrm{min} \sim 840\,\mathrm{s}$, with the power[8] p being $p = 9.78 \times 10^{-5}$ and the amplitude $A = 2\sqrt{p} = 19.77\,\mathrm{mma}$, where the units [mma] stand for milli-modulation amplitude and correspond to a 0.1%

[8]Power, denoted with lower-case p, should not be confused with period, denoted with upper-case P.

change in intensity (equivalently, A indicates a $\sim 2\%$ change in intensity). Both the frequency and amplitude of this peak are consistent with the values observed in ZZ Ceti-type pulsating WDs.

The DFT shows a number of other peaks, albeit with considerably less power. The most prominent, appearing to be in excess of the window function, is at $F \sim 135\,\mathrm{d}^{-1}$, $P \sim 11\,\mathrm{min}$, $p = 2.33 \times 10^{-5}$, $A = 9.6\,\mathrm{mma}$. The immediate question is whether these peaks represent significant detections. To answer this question, one needs to estimate the noise level of the DFT. This is achieved using a shuffling technique, where each (existing) fractional intensity value f is randomly re-assigned to a different (but existing) time value, thus a pair (t_i, f_i) with $f_i = f(t_i)$ and $i = 0,\ldots,N-1$ is transformed to a pair (t_i, f_j) with $f_j \neq f_i$ and $j = 0,\ldots,N-1$. All time and fractional intensity values are used. This shuffling destroys any coherent signals, but keeps the same time-sampling and noise properties as the original data set. The third-from-the-top panel in Figure 2.12 displays the DFT of one such simulated data set. The differences with the original DFT are obvious. We will examine two different approaches using this technique.

• The *cumulative highest power* (CHP) method - DFTs of simulated data sets are calculated for a large number of sets (in this case, 5000) and the *highest* value of power of each DFT is recorded. We then use a (normalised) cumulative probability distribution to obtain the 68.2%, 95.4% and 99.7% confidence levels of the recorded power values. This is displayed in Figure 2.13. For simplicity, we will sometimes be referring to these confidence levels as 1-, 2- and 3-σ levels, although (strictly speaking) this only applies to a Gaussian distribution, and the power distribution in the DFTs is not necessarily (exactly) Gaussian. The 99.7% confidence level ("3-σ") is considered the detection threshold.

• The *mean of the average power* method (MAP)- DFTs of simulated data sets are calculated for a large number of sets (for our example, again, 5000) and an average (over frequency) DFT is created, that is a frequency F_j in the averaged DFT has an averaged power value of $\bar{p}$, $\bar{p} = \left(\sum_{i=0}^{N} p_i\right)/N$ where N is the number of DFTs and $p_i = p(F_j)$ in each of the N DFTs. Figure 2.14 shows the original DFT with the averaged power spectrum superimposed. In the scale of the original DFT the average spectrum collapses into a "straight" line. The mean power of the average spectrum is then calculated, and three times the mean power is set as the detection threshold.

To have an overview of how the two methods compare to each other, we summarise the results of 4 different applications in Table 2.1. CHP can be viewed as a somewhat conservative estimate of the detection threshold, as it targets the highest value of power *regardless* of the frequency where this power is detected, which could lead to an overestimation of the threshold in our region of interest. This can be seen Table 2.1 in the downward revision of the threshold, when we constrain the DFT in a frequency area around F_1 and F_2. As CHP essentially answers the question "what is the probability that a peak detected at a certain frequency with given power is a spurious detection", it is common to apply the CHP method in a narrow region around the peak under scrutiny. On the other hand, the MAP method retains the frequency information, so it is less sensitive to changes of the DFT range (the mean of the frequency averaged power - and the threshold - is identical in the two MAP applications). However, information on the highest power value in a frequency bin is lost, as (spurious) detections with high power will be averaged out and not have an adverse effect on the mean power, which could lead to an underestimation of the threshold. A combination of the two

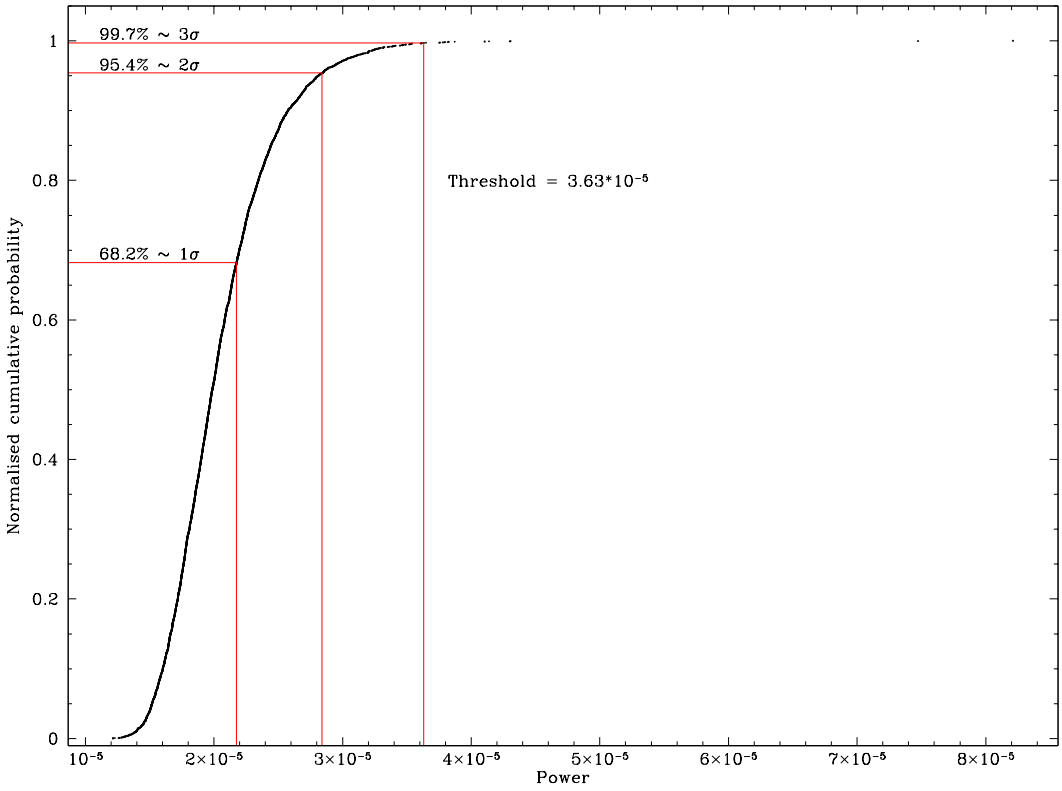

Figure 2.13: 68.2%, 95.4% and 99.7% confidence levels obtained from the *highest* value of power in DFTs, calculated from simulated data sets using the shuffling technique. We refer to these confidence levels as 1-, 2- and 3-σ levels, without necessarily suggesting that the power distribution is Gaussian. The 99.7% confidence level ("3-σ") is considered the detection threshold.

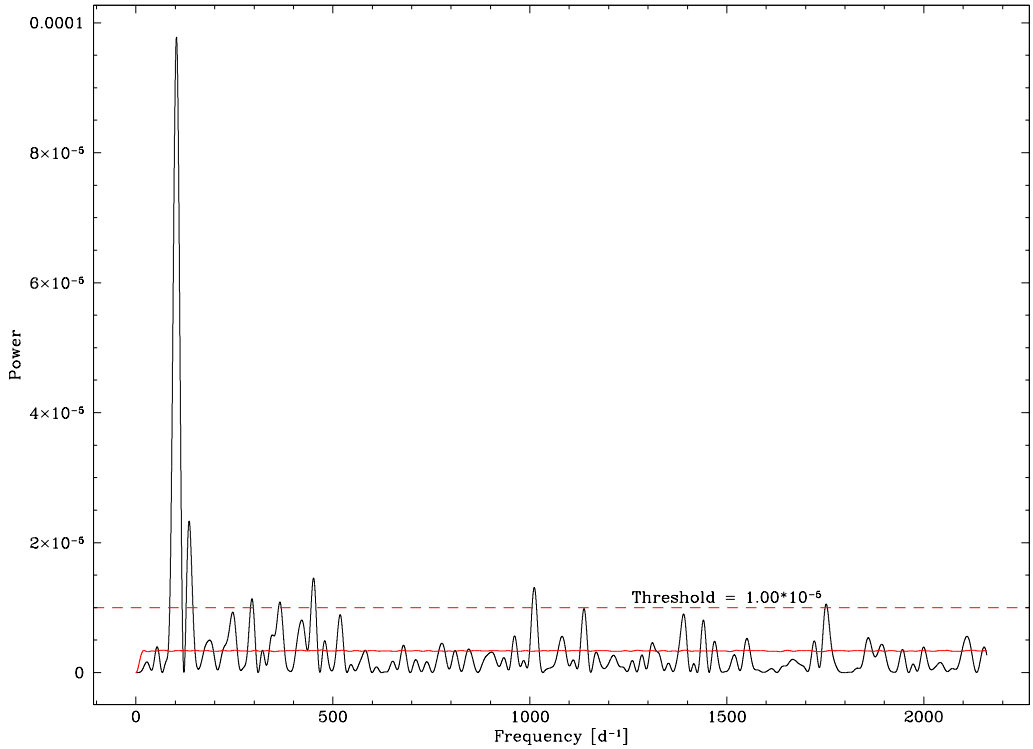

Figure 2.14: The average DFT, calculated from simulated data sets using the shuffling technique and overplotted on the original DFT. Three times the mean of the average power is set as the detection threshold.

Table 2.1: A comparison between the cumulative highest power (CHP) and the mean of average power (MAP) methods. Given are the frequency range of the DFT, the number of shufflings N, the mean M and standard deviation STD of either the highest power (CHP) or the average power (MAP), the value $V = M + 3 \times STD$, the detection threshold (99.7% confidence level for CHP, $3 \times M$ for MAP) and whether the two most prominent peaks $F_1 = 103\,d^{-1}$ and $F_2 = 135\,d^{-1}$ are considered significant detections.

Method	Range [d^{-1}]	N	M	STD	V	Threshold	F_1	F_2
CHP	0 - 2160	5000	2.1×10^{-5}	4.2×10^{-6}	3.3×10^{-5}	3.6×10^{-5}	Y	N
CHP	50 - 150	5000	9.9×10^{-6}	5.2×10^{-6}	2.5×10^{-5}	2.9×10^{-5}	Y	N
MAP	0 - 2160	5000	3.3×10^{-6}	1.9×10^{-7}	3.9×10^{-6}	1.0×10^{-5}	Y	Y
MAP	50 - 150	5000	3.3×10^{-6}	5.1×10^{-8}	3.5×10^{-6}	1.0×10^{-5}	Y	Y

methods could be a reasonable approach, i.e. identifying peaks that pass the threshold limit obtained through MAP and subsequently applying CHP in narrow areas around these peaks. In any case, the "golden rule" before attributing physical status to any detection in a DFT is *multiple detections* over many observations.

As is seen in Table 2.1 the characterisation of $F_2 = 135\,d^{-1}$ in our example as a significant detection is ambiguous and depends on the method used. Another technique that is often employed is to subtract the strongest signal of a DFT (in our case $F_1 = 103\,d^{-1}$) and calculate a new DFT of the residuals. This is achieved by fitting and subtracting a sine wave with the characteristics (F and p/A) of the strongest peak from our data. The process is called *pre-whitening* and is illustrated in Figure 2.15.

It is clear that the pre-whitening process removes a significant amount of power from the peak at $F_2 = 135\,d^{-1}$, while the rest of the DFT remains largely unaffected. This could be an indication that the peak at F_2 is a combination of the window function with another low-amplitude component. We will once again refer to the golden rule, multiple observations are needed before any safe conclusions can be drawn about F_2.

The final step in our analysis is to obtain a robust estimation of the frequency (period) of the signal and the associated error. This is usually achieved using the *bootstrap* method [Press, 2002]. From a light curve containing N pairs of time and flux values (t_i, f_i) we create a simulated data set by *randomly* selecting a *subset* of the (t_i, f_i) pairs. To keep the number of points N constant, some pairs of the original light curve get selected more than once, while others do not get selected at all. The DFT of the simulated data set is then calculated (an example is shown in Figure 2.12, bottom panel) and the position of the peaks under scrutiny noted. Straightforward statistics, mean and standard deviation, are then used to obtain an accurate value of the frequency (taken to be the mean) and its error (taken to be the standard deviation). The results of 5000 bootstrap iterations for our example are presented in Figure 2.16. In the Figure, we indicate the positions where the peaks F_1 and F_2 were detected in each of the bootstrap iterations. Statistics yields the following results: $F_1 = 102.95 \pm 1.39\,d^{-1}$ and $F_2 = 135.51 \pm 2.64\,d^{-1}$, corresponding to $P_1 = 839.2 \pm 11.3\,s$ and $P_2 = 637.6 \pm 12.4\,s$.

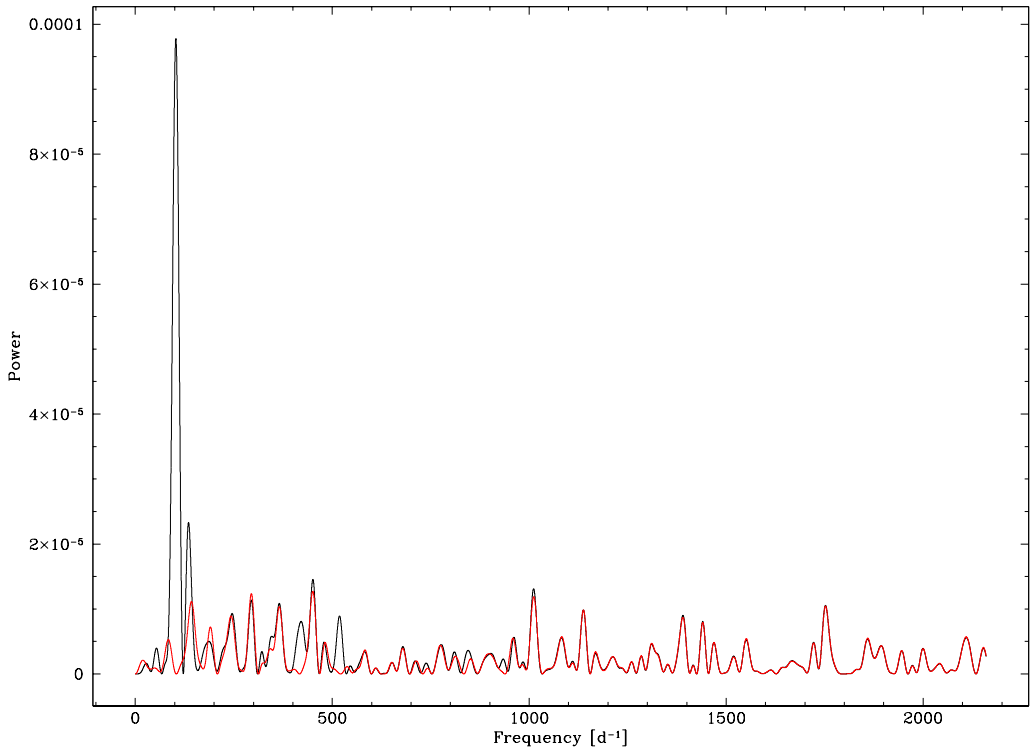

Figure 2.15: Original DFT (black) and re-calculated DFT (red) after pre-whitening the data with a sine wave matching the characteristics of the highest peak.

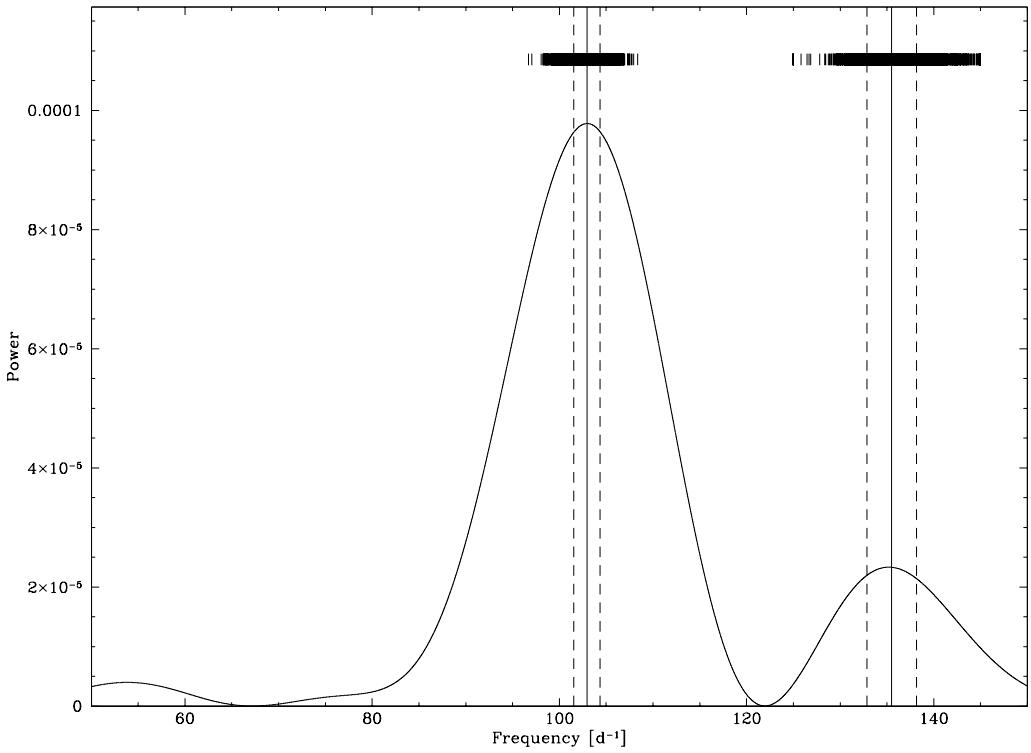

Figure 2.16: The DFT of the original data set, focused around F_1 and F_2. The small tick-marks above the peaks indicate the position where the peaks were detected during the bootstrap tests. For each peak, we indicate the mean value (solid line) and the standard deviation (dashed line).

We now have a full arsenal of methods and techniques, which will be employed in the coming chapters to measure stellar and binary parameters.

Chapter 3

Observational Data set

3.1 Introduction

In this Chapter, I will collect all the photometric and spectroscopic observations that will be presented in the thesis.

3.2 Telescopes

The photometric and spectroscopic data have been collected at the following telescopes (in alphabetical order):

- **APO:** 3.50 m Telescope, Apache Point Observatory, New Mexico, US
- **BR:** 0.40 m Telescope, Braeside Observatory, prev. in Flagstaff, Arizona, now in Orderville, Utah, US
- **CA2.2:** 2.20 m Calar Alto Telescope, Calar Alto, CAHA, Almeria, Spain
- **FTN:** 2.00 m Faulkes Telescope North, Haleakala Observatory, Hawaii, US
- **HT:** 2.40 m Hiltner Telescope, MDM Observatory, Kitt Peak, Arizona, US
- **IAC80:** 0.80 m Telescope, Observatorio del Teide, Tenerife, Spain
- **KY:** 1.20 m Kryoneri Telescope, Korinth, Greece
- **LO:** 1.52 m Loiano Telescope, Bologna, Italy
- **LT:** 2.00 m Liverpool Telescope, Observatorio del Roque de los Muchachos, La Palma, Spain
- **MCD:** 2.10 m Otto Struve Telescope, McDonald Observatory, Fort Davis, Texas, US
- **MER:** 1.20 m Mercator Telescope, Observatorio del Roque de los Muchachos, La Palma, Spain
- **MLO:** 1.00 m Telescope, Mount Laguna Observatory, San Diego, California, US

- **NOT:** 2.50 m Nordic Optical Telescope, Observatorio del Roque de los Muchachos, La Palma, Spain
- **OGS:** 1.00 m Optical Ground Station, Tenerife, Spain
- **OLT:** 1.20 m Oscar Lühning Telescope, Hamburg, Germany
- **RTT:** 1.50 m Russian-Turkish Telescope, Bakyrlytepe, Turkey
- **SPM:** 2.10 m Telescope, San Pedro Martir, Baja California, Mexico
- **USNO:** 1.55 m Telescope, Naval Observatory Flagstaff Station, Flagstaff, Arizona, US
- **WHT:** 4.20 m William Herschel Telescope, Observatorio del Roque de los Muchachos, La Palma, Spain
- **WS:** 0.80 m Wendelstein Telescope, University Observatory Munich, Germany

3.3 Observations

Table 3.1 collects all the observations of the seven systems presented in this thesis. These include data pre-dating the start of my PhD in May 2007, as well as data collected afterwards either by myself or by collaborators. The telescope acronyms are those defined in the previous Section. The vast majority of KY data after Sep. 2004 have been obtained by myself, with the exception of the 2009 and 2010 data. Furthermore I have obtained the Aug. 2007 CA2.2 data on SDSS 0110 and SDSS 0303; the Oct. 2007 MER data on SDSS 0110 and SDSS 0303; the Jul. 2008 WHT data on SDSS 1548; the May 2010 WHT data on SDSS 1210; and the Sep. 2010 WHT data on V 455.

Table 3.1: Log of all the photometric and spectroscopic observations. Given are an ID number, the date of observation, the telescope, the filter (photometry) or grating (spectroscopy), the duration of observations, the exposure time and the number of frames collected.

ID	Date	Obs.	Filter/Grating	Duration [h]	Exp. [s]	Frames
SDSS 0110 - Chapter 4						
01	2006 Aug 04	IAC80	*I*	2.92	420	25
02	2006 Aug 05	IAC80	*I*	3.77	60	170
03	2006 Aug 10	IAC80	*I*	1.47	420	13
04	2006 Aug 15	IAC80	*I*	1.71	420	15
05	2006 Aug 16	IAC80	*I*	1.47	420	12
06	2006 Sep 15	CA2.2	*I*	3.49	60	130
07	2006 Sep 16	CA2.2	*I*	8.15	45–55	312
08	2006 Sep 17	CA2.2	*I*	8.08	25–60	582
09	2006 Sep 26	WHT	R600B/R316R	0.67	1200	2

continued on the next page...

Table 3.1: (. . . continued)

ID	Date	Obs.	Filter/Grating	Duration [h]	Exp. [s]	Frames
10	2006 Sep 27	WHT	R600B/R316R	0.67	600	4
11	2006 Sep 29	WHT	R600B/R316R	0.34	600	2
12	2007 Aug 20	CA2.2	*BV*	1.94	25	159
13	2007 Aug 21	CA2.2	*BV*	1.19	25	101
14	2007 Sep 03	WHT	R1200B/R600R	0.56	1000	2
15	2007 Sep 04	WHT	R1200B/R600R	1.12	1000	4
16	2007 Oct 09	MER	clear	2.75	40	150
SDSS 0303 - Chapter 4						
01	2006 Sep 12	CA2.2	clear	4.91	15–35	443
02	2006 Sep 14	CA2.2	clear	0.87	45–60	63
03	2006 Sep 15	CA2.2	clear	0.87	60	44
04	2006 Sep 18	CA2.2	*R*	3.34	50–60	165
05	2006 Sep 26	WHT	R600B/R316R	0.67	600	4
06	2006 Sep 27	WHT	R600B/R316R	3.00	600	18
07	2007 Aug 22	CA2.2	*BV*	0.82	30	63
08	2007 Aug 26	CA2.2	*BV*	1.24	35	84
09	2007 Oct 15	MER	clear	1.35	55	60
SDSS 1210 - Chapter 5						
01	2009 Apr 01	LT	V+R	1.00	5	708
02	2009 Apr 02	LT	V+R	1.00	5	1416
03	2009 Apr 03	LT	V+R	1.00	5	1416
04	2009 Apr 04	LT	V+R	1.00	5	1416
05	2009 Apr 05	LT	V+R	1.00	5	2124
06	2009 Apr 06	LT	V+R	1.00	5	708
07	2009 Apr 29	WHT	R600B/R1200R	0.25	900	1
08	2009 May 02	WHT	R600B/R1200R	0.75	900	3
09	2010 Apr 23	WHT	R600B/R1200R	0.17	600	1
10	2010 May 18	WHT	R600B/R600R	3.00	900	12
11	2011 Feb 06	LT	V+R	1.00	5	720
12	2011 Mar 02	LT	V+R	1.00	5	720
13	2011 Apr 02	LT	V+R	1.00	5	720
14	2011 May 08	LT	V+R	1.00	5	720
15	2011 Jul 03	LT	V+R	1.00	5	720
SDSS 1435 - Chapter 4						
01	2006 Jul 04	WHT	R1200B/R600R	0.20	720	1

continued on the next page...

Table 3.1: (. . . continued)

ID	Date	Obs.	Filter/Grating	Duration [h]	Exp. [s]	Frames
02	2006 Jul 05	WHT	R1200B/R600R	0.25	900	1
03	2007 Feb 16	IAC80	*I*	1.34	90	451
04	2007 Feb 17	IAC80	*I*	4.90	90	162
05	2007 Feb 18	IAC80	*I*	5.64	70	226
06	2007 May 18	CA2.2	*V*	0.18	15	9
07	2007 May 19	CA2.2	*BV*	0.40	12	48
08	2007 May 19	CA2.2	clear	0.22	12-15	27
09	2007 Jun 23	WHT	R1200B/R600R	1.67	1200	5
10	2007 Jun 24	WHT	R1200B/R600R	0.67	1200	2
SDSS 1548 - Chapter 4						
01	2006 Jul 02	WHT	R1200B/R600R	0.34	1200	1
02	2006 Jul 03	WHT	R1200B/R600R	0.42	1500	1
03	2007 Jun 19	WHT	R1200B/R600R	1.00	1200	3
04	2007 Jun 20	WHT	R1200B/R600R	0.67	1200	2
05	2007 Jun 21	WHT	R1200B/R600R	1.34	1200	4
06	2007 Jun 22	WHT	R1200B/R600R	1.34	1200	4
07	2007 Jun 23	WHT	R1200B/R600R	0.34	1200	1
08	2007 Jun 24	WHT	R1200B/R600R	0.67	1200	2
09	2008 May 08	IAC80	*V*	5.99	300	71
10	2008 May 10	IAC80	*R*	5.47	300	64
11	2008 May 12	IAC80	*R*	0.34	300	5
12	2008 Jun 26	NOT	clear	3.50	90	140
13	2008 Jun 29	NOT	clear	0.95	115	30
14	2008 Jul 05	WHT	*R*	0.95	5	247
HS 2325 - Chapter 6						
01	2003 Sep 05	KY	clear	6.31	30	646
02	2004 Jun 10	KY	clear	0.80	30	75
03	2004 Jun 11	KY	clear	4.32	30	390
04	2004 Jun 12	KY	clear	2.82	30	270
05	2004 Jul 25	KY	clear	3.70	30	380
06	2004 Jul 27	KY	clear	6.60	30	650
07	2004 Oct 21	KY	clear	6.75	20	988
08	2004 Oct 22	KY	clear	6.35	20	850
09	2004 Oct 23	KY	clear	5.82	20	803
10	2005 Sep 05	CA22	clear	10	572	1
11	2005 Sep 11	HT	600 l/mm	2.00	360/480	17

continued on the next page...

Table 3.1: (. . . continued)

ID	Date	Obs.	Filter/Grating	Duration [h]	Exp. [s]	Frames
12	2005 Sep 12	HT	600 l/mm	3.62	360/480	31
13	2005 Sep 15	NOT	clear	1.65	4	564
14	2005 Sep 16	NOT	clear	3.97	4	1308
15	2006 Aug 23	KY	clear	7.21	30	711
16	2006 Oct 28	KY	clear	6.14	30	578
17	2007 Jan 24	HT	600 l/mm	0.24	360/480	2
V 455 - Chapter 7						
01	2000 Sep 25	BR	*R*	7.65	54	510
02	2000 Sep 28	BR	*R*	5.21	89	211
03	2001 Nov 21	BR	clear	3.75	89	152
04	2001 Nov 22	BR	clear	4.94	59	302
05	2002 Oct 15	KY	clear	3.30	35	340
06	2002 Oct 16	KY	clear	3.60	30	432
07	2003 Aug 14	KY	clear	3.71	13	1029
08	2003 Aug 15	KY	clear	3.65	13	1012
09	2003 Aug 16	KY	clear	3.53	13	980
10	2003 Aug 17	KY	clear	3.42	13	948
11	2003 Aug 18	KY	clear	4.51	13	1249
12	2003 Aug 19	KY	clear	4.73	13	1311
13	2003 Aug 20	KY	clear	5.17	13	1432
14	2003 Oct 12	BR	clear	9.35	61	552
15	2003 Oct 13	BR	clear	8.88	59	542
16	2003 Oct 15	BR	clear	7.30	59	446
17	2004 Aug 24	OGS	clear	6.30	16	1419
18	2004 Aug 25	USNO	clear	3.66	52	254
19	2004 Aug 26	USNO	clear	5.11	52	354
20	2004 Aug 27	OGS	clear	3.80	16	856
21	2004 Aug 27	USNO	clear	5.14	52	356
22	2004 Aug 28	OGS	clear	7.22	16	1626
23	2004 Aug 28	USNO	clear	5.41	52	375
24	2004 Aug 29	OGS	clear	5.31	16	1196
25	2004 Aug 29	WS	clear	1.09	30	131
26	2004 Aug 30	OGS	clear	7.87	16	1772
27	2004 Aug 30	OLT	clear	2.05	22	337
28	2004 Aug 31	OGS	clear	6.39	15	1534
29	2004 Aug 31	USNO	clear	8.62	52	597
30	2004 Sep 01	OGS	clear	7.33	16	1650

continued on the next page...

Table 3.1: (. . . continued)

ID	Date	Obs.	Filter/Grating	Duration [h]	Exp. [s]	Frames
31	2004 Sep 01	OLT	clear	3.04	22	498
32	2004 Sep 02	OLT	clear	3.86	22	633
33	2004 Sep 06	WS	clear	7.36	30	884
34	2004 Sep 10	OLT	clear	4.16	22	682
35	2004 Sep 10	WS	clear	8.51	30	1022
36	2004 Sep 11	LO	clear	6.38	21	1094
37	2004 Sep 11	MLO	clear	3.57	6	2147
38	2004 Sep 11	WS	clear	2.04	30	245
39	2004 Sep 12	LO	clear	2.50	21	430
40	2004 Sep 12	MLO	clear	4.94	6	2969
41	2004 Sep 12	OLT	clear	6.61	22	1083
42	2004 Sep 12	SPM	*V*	3.19	18	638
43	2004 Sep 13	KY	clear	4.06	14	1046
44	2004 Sep 13	LO	clear	7.06	21	1211
45	2004 Sep 13	MLO	clear	5.88	6	3532
46	2004 Sep 13	OLT	clear	3.06	22	501
47	2004 Sep 13	SPM	*V*	7.81	18	1563
48	2004 Sep 14	KY	clear	7.98	14	2053
49	2004 Sep 14	MLO	clear	5.69	6	3417
50	2004 Sep 14	OLT	clear	7.46	22	1222
51	2004 Sep 14	SPM	*V*	7.49	18	1498
52	2004 Sep 15	KY	clear	7.61	14	1958
53	2004 Sep 15	LO	clear	1.27	22	208
54	2004 Sep 15	MLO	clear	4.12	6	2476
55	2004 Sep 15	OLT	clear	2.78	22	456
56	2004 Sep 15	SPM	*V*	6.21	19	1177
57	2004 Sep 16	KY	clear	7.68	14	1977
58	2004 Sep 16	MLO	clear	6.39	6	3837
59	2004 Sep 16	OLT	clear	7.05	21	1209
60	2004 Sep 16	SPM	*V*	7.75	19	1470
61	2004 Sep 17	MLO	clear	4.95	6	2974
62	2004 Sep 17	OLT	clear	2.34	22	383
63	2004 Sep 17	RTT	clear	8.08	21	1386
64	2006 Aug 20	KY	clear	6.93	14	1783
65	2006 Aug 21	KY	clear	7.00	10	2521
66	2006 Aug 22	KY	clear	8.10	20	1458
67	2006 Sep 14	KY	clear	3.48	10	1255
68	2006 Oct 27	KY	clear	6.14	17	1302

continued on the next page...

Table 3.1: (. . . continued)

ID	Date	Obs.	Filter/Grating	Duration [h]	Exp. [s]	Frames
69	2006 Oct 29	KY	clear	4.53	17	961
70	2006 Nov 21	KY	clear	4.52	20	815
71	2009 Oct 07	KY	clear	3.85	14	965
72	2009 Oct 09	KY	clear	9.12	11	2938
73	2010 Sep 07	APO	*BG*40	9.77	5	6831
74	2010 Sep 12	WHT	*V*	8.63	7	4262
75	2010 Sep 12	MCD	*BG*40	4.08	5	2938
76	2010 Sep 13	WHT	*V*	5.21	7	2590
77	2010 Oct 11	FTN	*g*	4.87	40	433
78	2010 Oct 13	FTN	*g*	4.52	30	536
79	2010 Oct 14	MCD	*BG*40	6.44	5	4623

HS 2325 photometric monitoring

In addition to the data gathered at professional telescopes, intensive observations of HS 2325 (Chapter 6) using small aperture telescopes were carried out by some amateur astronomer collaborators of my supervisor Prof. Boris Gänsicke. These observations were collected as part of a dedicated photometric monitoring campaign, which was organised and coordinated by myself. Data reductions were performed by the respective observers. These observations are summarised in Table 3.2.

Table 3.2: Observers, telescope information and reduction software used in the photometric campaign for HS 2325.

Obs.	Type	Aper.	f/	CCD	FOV	Reduction
David Boyd	SCT	14”	5.3	SXV-H9	$16' \times 12'$	`AIP4WIN`
Steve Brady	Newtonian	16”	4.5	ST8-XME	$26' \times 17'$	`MaximDL`
Ian Miller	SCT	14”	10	SXVF-H16	$15' \times 15'$	`AIP4WIN`
Yenal Ögmen	SCT	14”	5.2	DSI Pro II	$11.5' \times 9.2'$	`MaximDL`
Joachim Pietz	SCT	11”	6.5	ST8-XME	$26' \times 17'$	`Muniwin`
Bart Staels	SCT	11”	6.3	MX716	$12' \times 9'$	`MaximDL`

3.4 Data Reduction

3.4.1 Photometry

The large majority of the photometric data have been reduced by myself, in the manner described in Section 2.3.2 using the pipeline described in Gänsicke et al. [2004], which performs bias- and

dark-current subtraction and flat-fielding within ESO/MIDAS and carries out aperture photometry in SEXTRACTOR [Bertin & Arnouts, 1996]. This excludes the following:

- All the IAC80 data, which are courtesy of and were reduced by Dr. Pablo Rodríguez-Gil in the standard fashion within IRAF[1]
- The SPM data of V 455, which are courtesy of and were reduced by Prof. Gagik Tovmassian in the standard fashion within IRAF
- The APO, FTN and MCD data of V 455, which are courtesy of and were reduced by Dr. Anjum Mukadam in the standard fashion within IRAF

In addition, the NOT data of HS 2325 are courtesy of Dr. Jorge Casares, but have been reduced by myself; the LT data of SDSS 1210 are automatically de-biased and flat-fielded by the LT data reduction pipeline, but photometry was carried out by myself using SEXTRACTOR.

System by system specifics

SDSS 0110

- IAC80: SI 2k x 2k E2V CCD, FOV 10.25′ x 10.25′, binned 2 x 2 and windowed to reduce readout time to 11 s
- CA2.2: Calar Alto Faint Object Spectrograph (CAFOS), 2k x 2k pixel SITe CCD, FOV 16′ x 16′, windowed to reduce readout time to 10 s
- MER: MERcator Optical Photometric imagEr (MEROPE) 2k x 2k EEV CCD, FOV 6.5′ x 6.5′), binned 3 x 3 to reduce readout time to about 8 s

SDSS 0303

- CA2.2: Calar Alto Faint Object Spectrograph (CAFOS), 2k x 2k pixel SITe CCD, FOV 16′ x 16′, windowed to reduce readout time to 10 s
- MER: MERcator Optical Photometric imagEr (MEROPE) 2k x 2k EEV CCD, FOV 6.5′ x 6.5′), binned 3 x 3 to reduce readout time to about 8 s

SDSS 1210

- LT: RISE [Steele et al., 2004], Andor DW485 using an E2V CCD47-20 frame transfer chip, unvignetted circular FOV of 11′ in diameter, binned 2 x 2

[1] IRAF is distributed by the National Optical Astronomy Observatory, which is operated by the Association of Universities for Research in Astronomy, Inc., under contract with the National Science Foundation, http://iraf.noao.edu

SDSS 1435

- IAC80: SI 2k x 2k E2V CCD, FOV 10.25′ x 10.25′, binned 2 x 2 and windowed to reduce readout time to 11 s
- CA2.2: Calar Alto Faint Object Spectrograph (CAFOS), 2k x 2k pixel SITe CCD, FOV 16′ x 16′, windowed to reduce readout time to 10 s

SDSS 1548

- IAC80: SI 2k x 2k E2V CCD, FOV 10.25′ x 10.25′, binned 2 x 2 and windowed to reduce readout time to 11 s
- NOT: Andalucia Faint Object Spectrograph and Camera (ALFOSC), 2k x 2k pixel E2V CCD42-40, FOV 6.5′ x 6.5′, binned 2 x 2
- WHT: AUX-port imager, 2148 x 4200 pixel E2V CCD44-82, unvignetted circular FOV of 2.2′ in diameter, binned 4 x 4 to reduce readout time to 4 s

HS 2325

- CA2.2: Calar Alto Faint Object Spectrograph (CAFOS), 2k x 2k pixel SITe CCD, FOV 16′ x 16′, binned 3 x 3 and windowed to reduce readout time to 10 s
- KY: 516 x 516 pixel SI-502 chip, FOV 2.5′ x 2.5′
- NOT: Andalucia Faint Object Spectrograph and Camera (ALFOSC), 2k x 2k pixel E2V CCD42-40, FOV 6.5′ x 6.5′, binned 2 x 2 and windowed to reduce readout time to about 6 s

3.4.2 Spectroscopy

The reduction of the spectroscopic data was carried out in the manner described in Section 2.3.2 using the STARLINK[2] packages KAPPA and FIGARO. The spectra were optimally extracted [Horne, 1986] using Tom Marsh's algorithms as implemented in PAMELA [Marsh, 1989] and the wavelength calibration was performed with Tom Marsh's MOLLY[3].

The WHT data of SDSS 0110, SDSS 0303, SDSS 1435 and SDSS 1548 were reduced by Dr. John Taylor (Southworth). For the WHT data of SDSS 1210 I performed preliminary on-the-fly reduction at the telescope. The final reduction and calibration was performed by Dr. Elmé Breedt.

The spectroscopic data of HS 2325 are courtesy of and have been reduced by Dr. John Thorstensen. The data reduction was performed with standard IRAF routines, using an original implementation of the optimal extraction algorithm detailed by Horne [1986].

[2]The Starlink Software can be found at `http://starlink.jach.hawaii.edu/`

[3]PAMELA and MOLLY were written by Tom Marsh and can be found at http://www.warwick.ac.uk/go/trmarsh

System by system specifics

SDSS 0110, SDSS 0303, SDSS 1435, SDSS 1548

WHT using the dual-arm Intermediate dispersion Spectrograph and Imaging System (ISIS). For all observations the blue-arm detector was an EEV 2k x 4k CCD. In 2006 July and September the red-arm detector was a Marconi 2k x 4k CCD, and in later observing runs a high-efficiency RED+ 2k x 4k CCD was used. In all cases the CCDs were binned spectrally by a factor of 2 and spatially by factors of 2–4, to reduce readout noise, and windowed in the spatial direction to decrease the readout time.

Wavelength calibrations were obtained in a standard fashion using spectra of copper-argon and copper-neon arc lamps. For SDSS 0303, arc lamp exposures were obtained during the spectroscopic observations and the wavelength solutions were interpolated from the two arc spectra bracketing each spectrum. For the other objects dedicated arc spectra were not obtained, to increase the time efficiency of the observations. The spectra were wavelength-calibrated using arc exposures taken at the beginning of each night, and drift in the wavelength solution was removed using measurements of the positions of the λ7913 and λ6300 night-sky emission lines. In the blue arm, a reliable correction of the wavelength zero-point was not possible as only one (moreover weak) sky-line Hg I λ 4358 is available, and consequently, these spectra were not suitable for velocity measurements. The reciprocal dispersion and resolution for the R316R grating are approximately $1.7\,\text{Å}\,\text{px}^{-1}$ and 3.3 Å, and for the R600R grating are $0.89\,\text{Å}\,\text{px}^{-1}$ and 1.5 Å, respectively.

SDSS 1210

WHT using ISIS. Both the EEV12 CCD on the blue arm and the RED+ CCD on the red arm were binned by a factor of three in the spatial direction and a factor of two in the spectral direction. This setup resulted in an average dispersion of 0.88 Å per binned pixel over the wavelength range 3643 – 5137 Å (blue arm) and 0.99 Å per binned pixel over the wavelength range 7691 – 9184 Å (red arm, R600). From measurements of the full width at half maximum of arclines and strong skylines, the resolution was determined to be 1.4 Å.

The wavelength scale was derived from Copper-Neon and Copper-Argon arc lamp exposures taken every hour during the observations, which were interpolated to the middle of each of the science exposures. For the blue arm the calibration was determined from a 5th order polynomial fit to 25 lines, with a root mean square (RMS) of 0.029 Å. The red arm was also fitted with a 5th order polynomial, to 17 arclines. The RMS was 0.032 Å.

HS 2325

HT using the modular spectrograph and a SiTe 2048^2 pixel CCD, yielding 2 Å/pixel and from 4210 to 7500 Å but with decreased sensitivity toward the ends of the wavelength range. The spectral resolution was $\sim$ 3.5 Å full width at half maximum (FWHM).

For wavelength calibration, a dispersion curve derived from lamp exposures in twilight was used, shifted for each nighttime exposure to force the apparent velocity of the λ 5577 night-sky line to be zero. Standard stars were observed in twilight whenever the sky permitted, and these observations were used to flux-calibrate the data. The scatter of the standard stars typically suggested that the flux

calibration is uncertain by several tenths of a magnitude, probably due to uncalibrated losses at the spectrograph slit.

3.5 Contributions by collaborators

- The evolutionary calculations presented in Section 4.9 were performed by Dr. Matthias Schreiber
- The grid of DAZ models used throughout Chapter 5 was calculated by Prof. Detlev Koester
- The spectroscopic analysis presented in Section 5.5 was performed by Prof. Boris Gänsicke
- The white dwarf limb darkening coefficients used in Section 5.7 were calculated by Steven Parsons
- The evolutionary calculations presented in Section 5.9 were performed by Dr. Monica Zorotovic
- The distance calculation presented in Section 6.6 was performed by Dr. John Thorstensen

Chapter 4

Four new eclipsing PCEBs from SDSS

4.1 Introduction

In this Chapter, I begin the study of eclipsing white dwarf binaries by presenting four new eclipsing post-common-envelope binaries identified in the SDSS. I will apply the techniques described in Chapter 2 to measure the orbital periods and radial velocities of all four systems. I will then focus on the light curve modelling, employed to measure the masses and radii of the binary components. Finally, the past and future evolution of the four stars will be briefly explored.

4.2 Target information

The four new eclipsing systems presented in this Chapter are:

- SDSSJ 011009.09+132616.1 (henceforth SDSS 0110)
- SDSSJ 030308.35+005444.1 (henceforth SDSS 0303)
- SDSSJ 143547.87+373338.5 (henceforth SDSS 1435)
- SDSSJ 154846.00+405728.8 (henceforth SDSS 1548).

Full coordinates and SDSS u,g,r,i,z magnitudes of the four systems are given in Table 4.1.

These systems have been selected as candidates in our search for eclipsing SDSS WDMS binaries (Section 2.2.1). SDSS 0303 and SDSS 1435 exhibited the largest secondary star radial velocities among ~ 1150 WDMS binaries, which have SDSS spectra of sufficiently good quality, an indicator of potentially high inclination. For SDSS 0110 two SDSS spectra were available, which differed substantially in the strength of the emission lines detected in the spectra. Emission lines are a result of a *reflection effect*, i.e. heating of the companion star by a hot WD primary, as is the case for SDSS 0110. At short orbital periods, the companion is expected to be tidally locked, so that the heated side always points towards the WD. A variation of the strength of the emission

Table 4.1: Full coordinates and u, g, r, i, z magnitudes of the four systems presented in this Chapter.

SDSS J	Coordinates [J2000]	u	g	r	i	z
0110+1326	01 10 09.09 +13 26 16.1	16.51	16.53	16.86	17.02	16.94
0303+0054	03 03 08.35 +00 54 44.1	19.14	18.60	18.06	16.89	16.04
1435+3733	14 35 47.87 +37 33 38.5	17.65	17.14	17.25	16.98	16.66
1548+4846	15 48 46.00 +40 57 28.8	18.79	18.32	18.41	18.17	17.68

lines indicates that we do not always see the inner hemisphere, implying a high inclination. In the case of SDSS 1548, the available information on the radial velocity of the secondary and the initial estimate for $M_{\rm WD}$ and $M_{\rm sec}$ suggested $i \sim 85^{\circ}$ (Equation 2.8). Subsequent time-series photometric observations revealed white dwarf eclipses in all four objects. We should note that SDSS 1435 has been independently identified by Steinfadt et al. [2008].

4.3 Observations and data reduction

The observational data set and information on the data reduction procedures are summarised in Chapter 3. Figure 4.1 shows phase-folded (using the ephemerides derived in the next Section) light curves and radial velocity curves of all four systems.

4.4 Orbital Periods and Ephemerides

Mid-eclipse times for all systems were obtained with the mirroring method (Section 2.4.1). These mid-eclipse times are listed in the Appendix. For SDSS 1435 we have also used the mid-eclipse times provided by Steinfadt et al. [2008].

Following the procedure outlined in Section 2.4.1 we obtained the orbital periods and ephemerides of the four systems. The resulting ephemerides, on a UTC timescale, with numbers in parenthesis indicating the error on the last digit, are

$$T_0(\mathrm{HJD}) = 2453994.44787(9) + 0.3326873(1)\mathrm{E} \tag{4.1}$$

for SDSS 0110, that is $P_{\rm orb} = 7.984495(3)$h

$$T_0(\mathrm{HJD}) = 2453991.6164(1) + 0.13443772(7)\mathrm{E} \tag{4.2}$$

for SDSS 0303, that is $P_{\rm orb} = 3.226505(1)$h

$$T_0(\mathrm{HJD}) = 2454148.70361(6) + 0.1256311(1)\mathrm{E} \tag{4.3}$$

for SDSS 1435, that is $P_{\rm orb} = 3.015144(2)$h and

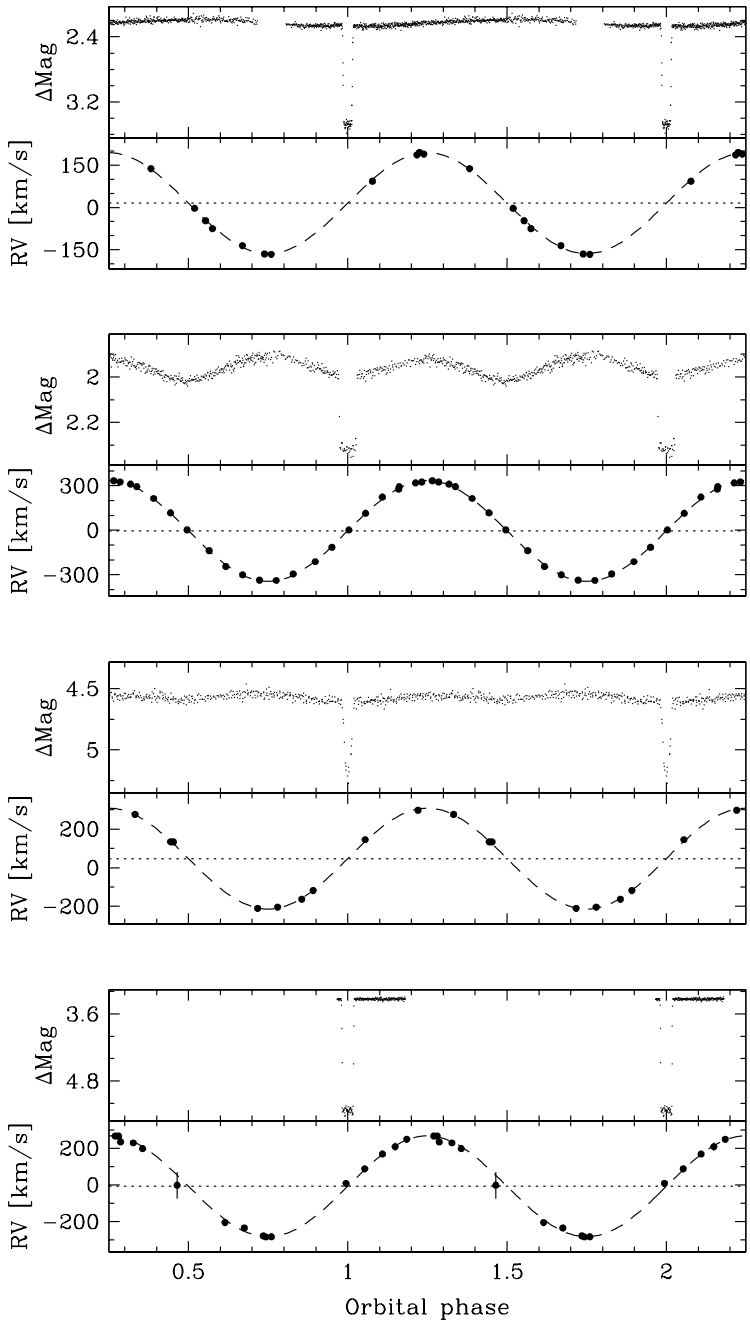

Figure 4.1: Phase-folded light- and radial velocity curves of the four systems. From top to bottom (two panels for each system): CA2.2 *I*-band light curve and Ca II radial velocity curve of SDSS 0110, CA2.2 filterless light curve and Na I radial velocity curve of SDSS 0303, IAC80 *I*-band light curve and Na I radial velocity curve of SDSS 1435 and WHT *R*-band light curve and Na I radial velocity curve of SDSS 1548.

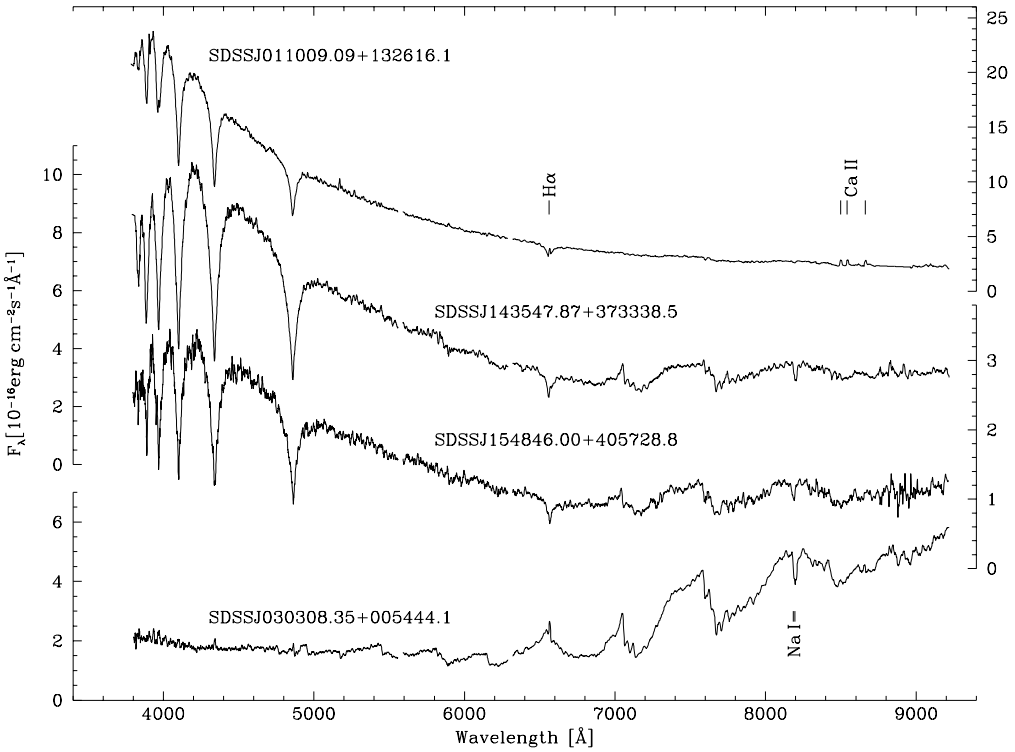

Figure 4.2: SDSS spectra of the four systems. Top to bottom: SDSS 0110, SDSS 1435 SDSS 1548 and SDSS 0303. The radial velocity of the companion star in SDSS0110+1326 was measured from the Hα and Ca II emission lines, whereas for the other three systems, we used the Na I absorption doublet

$$T_0(\mathrm{HJD}) = 2454592.57135(6) + 0.18551774(4)\mathrm{E} \tag{4.4}$$

for SDSS 1548, that is $P_{\mathrm{orb}} = 4.45242576(4)$h.

These ephemerides were then used to fold both the photometric and the spectroscopic data over phase (Figure 4.1).

4.5 Radial velocities of the secondary stars

Figure 4.2 shows the SDSS spectra of our four targets. Radial velocity measurements and the subsequent sine fits were performed for the secondary stars only, following the procedure outlined in Section 2.4.2. The resulting radial velocity amplitudes are reported in Table 4.2

4.5.1 The secondary in SDSS 0110

The spectrum of SDSS 0110 displays the Ca II λλ 8498.02,8542.09,8662.14 triplet in emission, as well as the Hα line also in emission. We determined the velocities of the Hα emission line by fitting

Table 4.2: Secondary star radial velocity measurements for all four systems

System	Line	$K_{\rm sec}$ [km s^{-1}]	Error [km s^{-1}]	γ [km s^{-1}]	Error [km s^{-1}]
SDSS 0110	Ca II	178.8	2.4	15.2	2.4
	Hα	200.1	4.8	19.4	4.1
SDSS 0303	Na I	339.7	1.9	-4.0	1.4
SDSS 1435	Na I	260.9	2.9	47.4	2.2
SDSS 1548	Na I	274.7	2.6	-7.4	2.2

a second-order polynomial plus a Gaussian to the spectra. For the Ca II triplet, we fitted a second-order polynomial plus three Gaussians with identical width and whose separations were fixed to the corresponding laboratory values.

The Hα and Ca II radial velocities were then separately phase-folded using the corresponding orbital ephemeris, and fitted with a sine wave. The phasing of the radial velocity curves agreed with that expected from an eclipsing binary (i.e. red-to-blue crossing at orbital phase zero) within the errors (see also Figure 4.1).

We decided to investigate whether the emission lines originate predominantly on the illuminated hemisphere of the secondary star. If that is the case (keeping in mind that we see the system almost edge-on) we expect a significant variation of the line strength with orbital phase, reaching a maximum around phase $\phi = 0.5$ (superior conjunction of the secondary) and almost disappearing around $\phi = 0.0$. Figure 4.3 shows average spectra of SDSS 0110, focused on the Hα line and the Ca II triplet for $\phi = 0.0$ and $\phi = 0.5$.

It is apparent that the Hα and Ca II emission lines are very strong near $\phi = 0.5$. The Hα emission line is very weak near $\phi = 0.0$, and Ca II is seen in absorption. The equivalent width (EW) of the blue-most component of the Ca II triplet is shown in Figure 4.4 (top panel) as a function of orbital phase. Given the spectral resolution and quality of our data, measuring the EW of the Hα emission line is prone to substantial uncertainties, as it is embedded in the broad Hα absorption of the white dwarf photosphere, but it generally follows a similar pattern as the one seen in the Ca II triplet.

This analysis supports our assumption that the emission lines originate on the irradiated, inner hemisphere of the secondary star. Hence, the centre of light of the secondary star is displaced towards the Lagrangian point L_1, with respect to the centre of mass. The emission lines trace, therefore, the movement of the centre of light and not the centre of mass and as a result, the $K_{\rm sec}$ values measured from either the Hα or the Ca II emission lines are very unlikely to represent the true radial velocity amplitude of the secondary star, but instead give a lower limit to it.

4.5.2 The secondaries in SDSS 0303, SDSS 1435, and SDSS 1548

The Na I $\lambda\lambda$ 8183.27,8194.81 absorption doublet is a strong feature in the spectra of SDSS 0303, SDSS 1435, and SDSS 1548. We measured the radial velocity variation of the secondary stars in all three systems by fitting this doublet with a second-order polynomial plus two Gaussian lines of common width and a separation fixed to the corresponding laboratory value. A sine-fit to each of

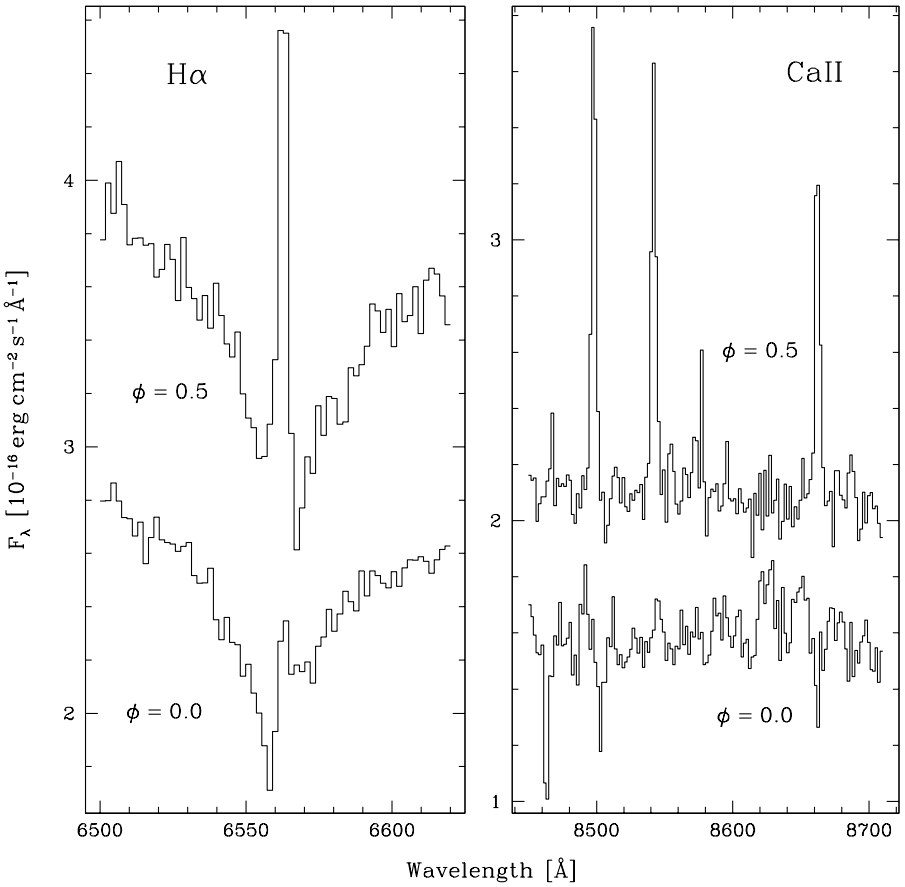

Figure 4.3: Average spectra of SDSS 0110. Left panel: Hα line, right panel: Ca II triplet. The binary phase of each spectrum is clearly marked. Prior to averaging, each spectrum was shifted to the restframe of the secondary, using the measured $K_{\rm sec}$ and γ values. For each line and binary phase, three spectra were averaged.

the radial velocities data sets, phase-folded using the corresponding orbital ephemerides gives the radial velocity of the secondary star, $K_{\rm sec}$, and the systemic velocity γ for each system. The results of the radial velocity measurements are summarised in Table 4.2.

No significant variation in the strength of the Na I doublet was observed as a function of orbital phase, and we hence assume that $K_{\rm sec}$ measured from this doublet reflects the true radial velocity amplitudes of the secondary stars in SDSS 0303, SDSS 1435, and SDSS 1548. This is illustrated in Figure 4.4, where we plot the equivalent widths against orbital phase.

4.6 Spectroscopic stellar parameters

The spectral decomposition/fitting method described in detail in Rebassa-Mansergas et al. [2007] was employed to estimate the white dwarf effective temperatures $T_{\rm eff}$ and surface gravities $\log g$, as well as the spectral types of the companion stars, for all four systems, using their SDSS spectroscopy.

Briefly, the method employed is the following: as a first step a two-component model is fitted to the WDMS binary spectrum using a grid of observed M-dwarf and white dwarf templates. This step determines the spectral type and flux contribution of the M-dwarf component. After subtracting the best-fit M-dwarf, the residual white dwarf spectrum is fitted with a grid of white dwarf model spectra from Koester et al. [2005]. The fits are performed to the normalised Hβ to Hε line profiles, omitting Hα, which is most severely contaminated by the continuum and/or Hα emission from the companion star. Balmer line profile fits can lead to degeneracy in the determination of $T_{\rm eff}$ and $\log g$, as their equivalent widths (EWs) go through a maximum at $T_{\rm eff} \simeq 13000\,{\rm K}$, which means that fits of similar quality can be achieved for a "hot" and "cold" solution. In order to select the physically correct solution, an additional fit to the continuum plus Balmer lines is performed over the range 3850–7150 Å. The resulting $T_{\rm eff}$ and $\log g$ are less accurate than those from line profile fits, but sensitive to the slope of the spectrum, and hence allow in most cases to break the degeneracy between the hot and cold solutions. Figure 4.5 illustrates this procedure.

Once $T_{\rm eff}$ and $\log g$ are determined, the white dwarf mass and radius can be estimated using an updated version of the tables from Bergeron et al. [1995a]. The results, after applying this method to our four systems, are summarised in Table 4.3. The preferred solution ("hot" or "cold") is highlighted in bold fond.

In the case of SDSS 0303, which contains a DC white dwarf, the spectral decomposition results in ${\rm Sp}(2) = {\rm M4.5} \pm 0.5$ for the secondary star. The subsequent fit to the residual white dwarf spectrum is not physically meaningful, as the white dwarf in SDSS 0303 does not exhibit Balmer lines. The fit to the overall spectrum, which is purely sensitive to the continuum slope, suggests $T_{\rm eff} < 8000\,{\rm K}$, which is consistent with the DC classification of the white dwarf. In this case we can use Equation 2.6b to get a rough, first estimate of the white dwarf mass.

In Figure 4.6, we have plotted Equation 2.6b for $i = 90^{\circ}$ and $i = 78^{\circ}$. For lower inclinations no eclipses occur for $K_{\rm sec} = 339.7\,{\rm km\,s^{-1}}$ and $P_{\rm orb} = 0.134\,{\rm d}$. For a given choice of the inclination angle, Equation 2.6b defines a unique relation $M_{\rm sec}\,(M_{\rm WD})$. If we further assume a mass for the secondary, we can investigate the possible range of the white dwarf mass for SDSS 0303. For an extremely conservative lower limit of $M_{\rm sec} \geq 0.08\,{\rm M}_{\odot}$ (the lower mass limit for an M-dwarf, e.g. Dorman et al. [1989], with the spectrum of SDSS 0303 clearly identifying the companion as a

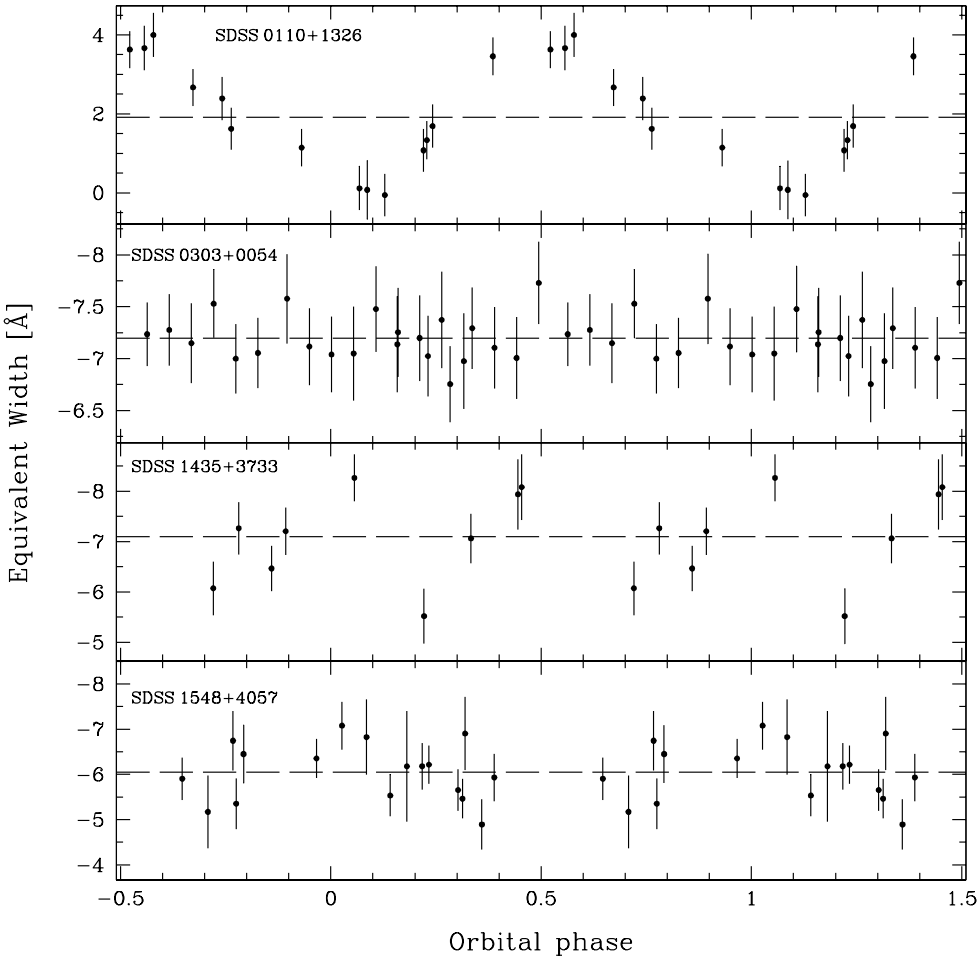

Figure 4.4: Equivalent widths of the lines used to measure radial velocities in all four systems with respect to the orbital phase. Top panel: blue-most component of the Ca II emission triplet in SDSS 0110. Lower three panels: blue-most component of the Na I absorption doublet in SDSS 0303, SDSS 1435 and SDSS 1548 respectively. The dashed lines indicate the mean EW. The strong variation of the EW of the Ca II emission line is obvious. No significant variation as a function of phase is observed for the other three systems. A full orbital cycle has been duplicated for clarity.

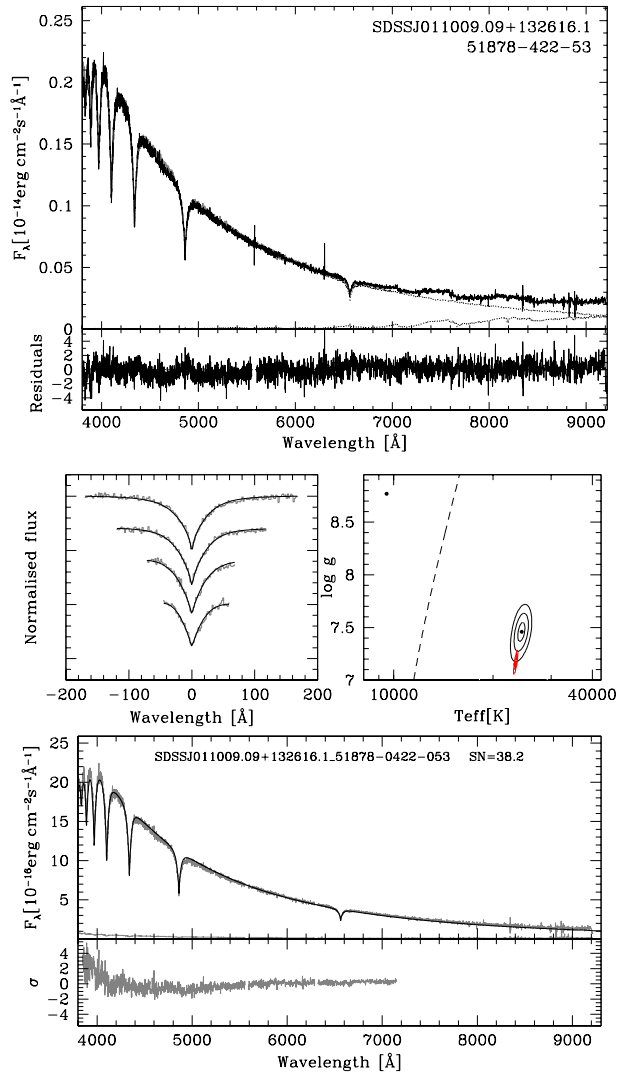

Figure 4.5: Two-component fit to the spectrum of SDSS 0110. The top panel shows the spectrum of the object as a solid black line and the two templates, white dwarf and M-dwarf, as dotted lines. The residuals from the fit are shown directly below. Middle left panel: best-fit (black lines) to the observed Hβ to Hε (grey lines, top to bottom) WD line profiles, after subtracting the best-fit M-dwarf template. The model spectra and observations have been normalised in the same way. Middle right panel: 1, 2 and 3 σ contour plots in the $T_{\rm eff} - \log g$ plane. The black contours refer to the best line profile fit, the red ones (collapsing into a dot on the scale of the plot) to the fit of the spectral range 3850–7150 Å. The dashed line indicates the occurrence of maximum Hβ equivalent width. The best "hot" and "cold" line profile solutions are indicated by black dots, while the best fit to the whole spectrum by a red one. Bottom panel: the residual white dwarf spectrum resulting from the spectral decomposition and their flux errors (grey lines) along with the best-fit white dwarf model (black line) in the 3850–7150 Å wavelength range (upper part) and the residuals of the fit (grey line, lower part).

Table 4.3: Summary of the results obtained for SDSS 0110, SDSS 1435 and SDSS 1548 from our spectral decomposition technique. The preferred set of parameters for each system is highlighted in bold fond.

Solution	$M_{\rm WD}[{\rm M}_\odot]$	$\log g$	$T_{\rm eff}$ [K]	Sp(2)
SDSS 0110				
Hot	**0.47±0.02**	**7.65±0.05**	**25891±427**	**M4±1**
Cold	1.2 ± 0.03	9 ± 0.04	9619 ± 23	M4 ± 1
SDSS 1435				
Hot	0.40 ± 0.05	7.58 ± 0.11	12536 ± 438	M4.5 ± 0.5
Cold	**0.41±0.05**	**7.62±0.12**	**12536±488**	**M4.5±0.5**
SDSS 1548				
Hot	0.43 ± 0.16	7.64 ± 0.31	14899 ± 1300	M6 ± 0.5
Cold	**0.62±0.28**	**8.02±0.44**	**11699±820**	**M6±0.5**

main-sequence star), we get a WD mass of $M_{\rm WD} \geq 0.68\,{\rm M}_\odot$. Even under this extreme assumption for the companion star, the white dwarf in SDSS 0303 has to be more massive than the average field white dwarf [e.g. Koester et al., 1979; Liebert et al., 2005]. If we assume Sp(2) = M4, the upper limit of the spectral type according to our spectral decomposition of the SDSS spectrum, and use the spectral type-mass relation of Rebassa-Mansergas et al. [2007], we find $M_{\rm sec} \simeq 0.32\,{\rm M}_\odot$, and hence $M_{\rm WD} \geq 0.96\,{\rm M}_\odot$. These estimates assume $i = 90^\circ$, for lower inclinations the respective $M_{\rm WD}$ values become larger, as illustrated in Figure 4.6. In summary, based on $K_{\rm sec}$, $P_{\rm orb}$, and a generous range in possible $M_{\rm sec}$ we expect the white dwarf in SDSS 0303 to be fairly massive, $0.7\,{\rm M}_\odot \lesssim M_{\rm WD} \lesssim 1.0\,{\rm M}_\odot$.

4.7 Light Curve model fitting

Ultimately, our aim is to combine the information from the $K_{\rm sec}$ radial velocity amplitudes determined in Section 4.5, the information contained in the light curve, and the white dwarf effective temperature determined from the spectral fit in Section 4.6 to establish a full set of stellar parameters for the four eclipsing PCEBs. The adopted method is described in the next two subsections, where SDSS 0110 requires a slightly broader approach, as a correction needs to be applied to the $K_{\rm sec}$ velocity determined from the emission lines. In all cases, LCURVE has been used to model the light curves (with the accretion disc and bright spot components switched off) and minimisation was obtained using the SIMPLEX and LEVENBERG-MARQUARDT methods (Section 2.4.4).

4.7.1 SDSS 0303, SDSS 1435 and SDSS 1548

Our approach is to fit a light curve model to the data for a selected grid of points in the $M_{\rm WD} - M_{\rm sec}$ plane. Each point in the $M_{\rm WD} - M_{\rm sec}$ plane defines a mass ratio q, and, using $K_{\rm sec}$ and $P_{\rm orb}$, a binary inclination i (Equation 2.8). Hence, a light curve fit for a given ($M_{\rm WD}$, $M_{\rm sec}$) combination will have

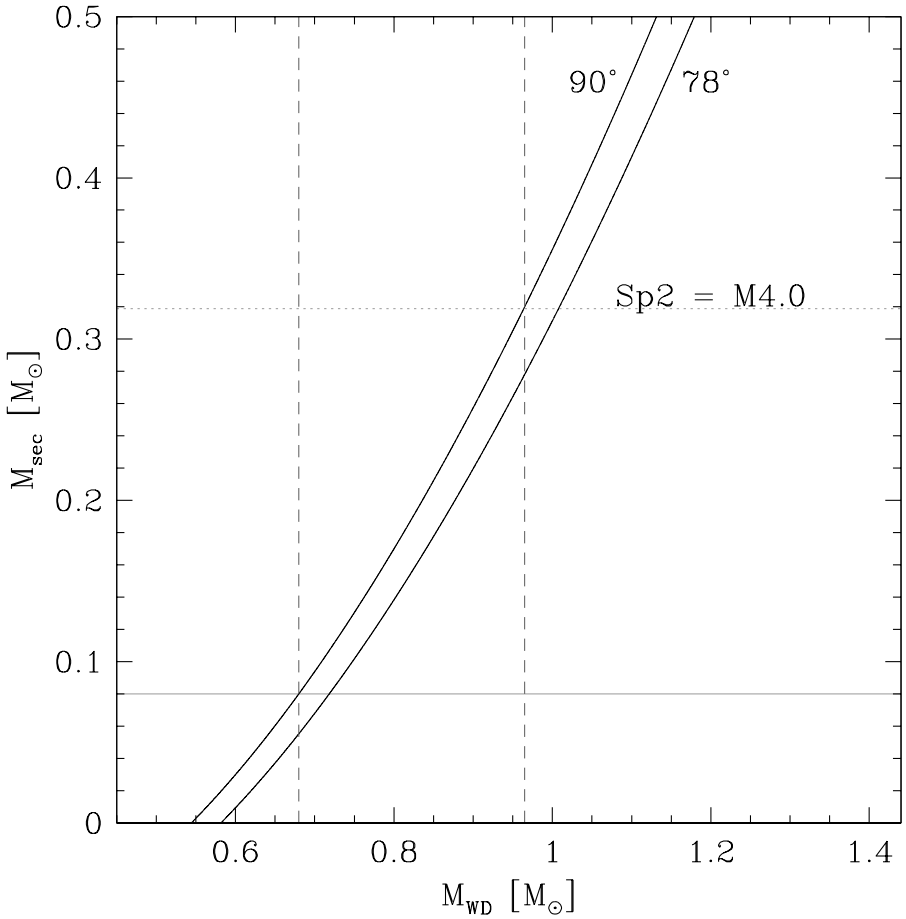

Figure 4.6: Mass function plot for SDSS 0303, for $i = 78°$ and $i = 90°$. The grey horizontal line corresponds to a lower mass limit for M-dwarfs. The dotted horizontal line is the value of $M_{\rm sec}$, corresponding to a secondary spectral type of $\mathrm{Sp}(2) = \mathrm{M4}$, assuming a $\mathrm{Sp}(2) - M_{\rm sec}$ relation. The dashed vertical lines indicate the corresponding range for the white dwarf mass.

$M_{\rm WD}$, $M_{\rm sec}$, q, and i fixed, whereas $R_{\rm WD}$, $R_{\rm sec}$, $T_{\rm WD}$, $T_{\rm sec}$, and T_0 are in principle free parameters. In practice, we fix $T_{\rm WD}$ to the value determined from the spectroscopic fit, which is sufficiently accurate, hence only $R_{\rm WD}$, $R_{\rm sec}$, $T_{\rm sec}$, and T_0 are free parameters in the light curve fits. We leave T_0 free to vary to account for the $O-C$ errors in each individual light curve. The fitted values of T_0 were of the order of 10 s, consistent with the $O-C$ values quoted in Table A.1.

Each light curve fit in the $M_{\rm WD}-M_{\rm sec}$ plane requires some initial estimates of $R_{\rm WD}$, $R_{\rm sec}$, $T_{\rm sec}$. For $R_{\rm WD}$ we adopt the theoretical white dwarf mass-radius relation interpolated from the tables of Bergeron et al. [1995a]. For $R_{\rm sec}$ we use the mass-radius relation of Baraffe et al. [1998], adopting an age of 5 Gyr. For $T_{\rm sec}$, we use the spectral type of the secondary star as determined from the spectral decomposition combined with the spectral type-temperature relation from Rebassa-Mansergas et al. [2007]. $R_{\rm WD}$ and $R_{\rm sec}$ are then scaled by the binary separation, obtained through Kepler's law, Equation 2.1.

We defined large and densely covered grids of points in the $M_{\rm WD}-M_{\rm sec}$ plane which generously bracket the initial estimates for $M_{\rm WD}$ and $M_{\rm sec}$ based on the spectral decomposition/fitting. For SDSS 0303, where no spectral fit to the white dwarf is available, we bracket the range in $M_{\rm WD}$ illustrated in Figure 4.6. Points for which (formally) $\sin i > 1$ were discarded from the grid, for all other points a light curve fit was carried out, recording the resulting $R_{\rm WD}$, $R_{\rm sec}$, and $T_{\rm sec}$. The number of light curve fits performed for each system was between 7000 and 10000, depending on the system.

4.7.2 SDSS 0110

In the case of SDSS 0110 the inclination angle cannot readily be calculated through Equation 2.8, as we measured $K_{\rm sec}$ from either the Hα or Ca II emission lines, which do not trace the motion of the secondary's centre of mass, but the centre of light in the given emission line. The general approach in this case is to apply a correction to the observed $K_{\rm sec}$, where the motion of the secondary star's centre of mass, $K_{\rm sec,cor}$ is expressed according to Wade & Horne [1988] as

$$K_{\rm sec,\,cor} = \frac{K_{\rm sec}}{1-(1+q)\,(\Delta R/a)} \tag{4.5}$$

where $K_{\rm sec}$ is the measured radial velocity, q is the mass ratio of the system, a the binary separation and ΔR is the displacement of the centre of light from the centre of mass of the secondary. ΔR can have a minimum value of zero, i.e. the two centres coincide and no correction is needed and a maximum value of $R_{\rm sec}$, i.e. all light comes from a small region of the secondary star closest to the primary.

An assumption often used in the literature is that the emission due to irradiation is distributed uniformly over the inner hemisphere of the secondary star, and is zero on its unirradiated side, in which case $\Delta R = (4/3\pi)R_{\rm sec}$ [e.g. Wade & Horne, 1988; Wood et al., 1995; Orosz et al., 1999; Vennes et al., 1999].

A more physical model of the distribution of the irradiation-induced emission line flux can be derived from the analysis of the orbital variation of the equivalent width of the emission line. A fine example of this approach is the detailed study of the Ca II $\lambda\lambda$ 8498.02, 8542.09,8662.14 emission in the WDMS binary HR Cam presented by Maxted et al. [1998]. However, given the small number

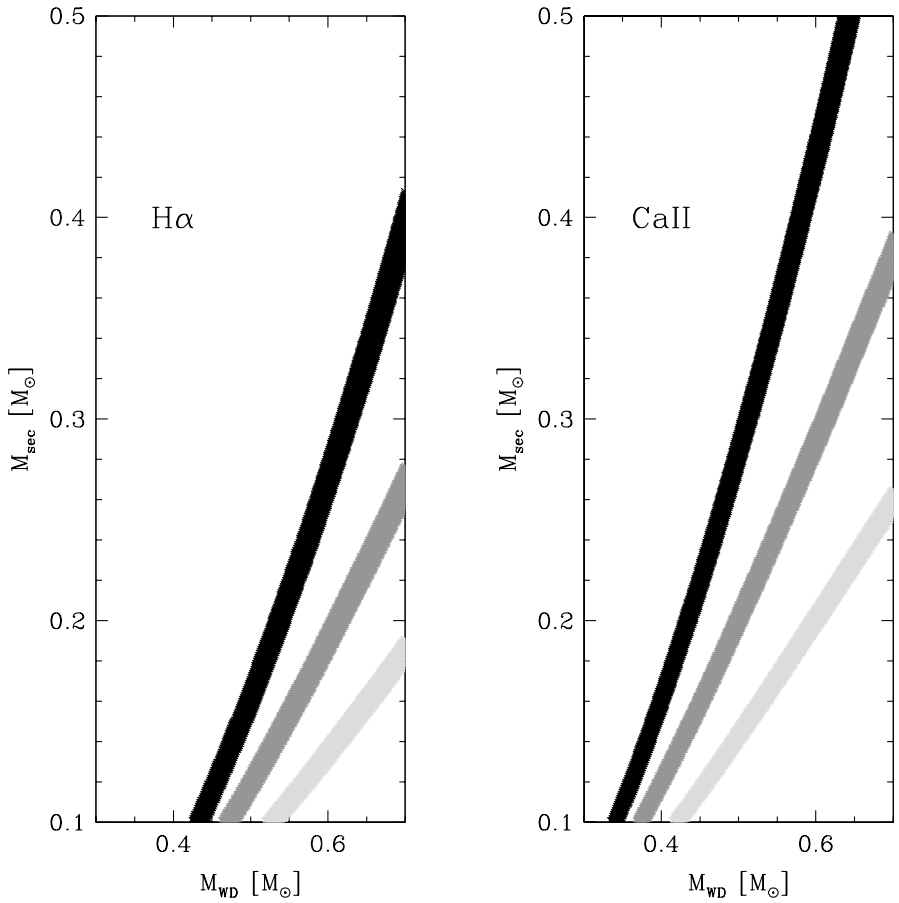

Figure 4.7: Grid of $(M_{\rm WD}, M_{\rm sec})$ points for which the light curve of SDSS 0110 has been fitted. Different assumptions for the K-correction were made: $\Delta R = 0$ (black strip), $\Delta R = (4/3\pi)R_{\rm sec}$ (dark grey strip) and $\Delta R = R_{\rm sec}$ (light grey strip). Left panel: ($M_{\rm WD}$,$M_{\rm sec}$) grid for $K_{\rm sec} = K_{\rm sec,H\alpha} = 200.1\,{\rm km\,s^{-1}}$. Right panel: ($M_{\rm WD}$,$M_{\rm sec}$) grid for $K_{\rm sec} = K_{\rm sec,CaII} = 178.8\,{\rm km\,s^{-1}}$.

of spectra, it is currently not possible to apply this method to SDSS 0110.

Our approach for modelling SDSS 0110 was to calculate the binary separation from Equation 2.1 for each pair of $(M_{\rm WD}, M_{\rm sec})$ of the initial grid and then, using Equation 4.5, calculate various possible $K_{\rm sec,cor}$ values for this $(M_{\rm WD}, M_{\rm sec})$ point, assuming various forms of ΔR. We adopted the following three different cases: (i) $\Delta R = 0$, i.e. the centre of light coincides with the centre of mass, (ii) $\Delta R = (4/3\pi)R_{\rm sec}$, i.e. the uniform distribution case and (iii) $\Delta R = R_{\rm sec}$, i.e. the maximum possible displacement of the centre of light. This was done for both the Hα and the Ca II lines. Having attributed a set of corrected radial velocity values to each point of the grid, we could now make use of Equation 2.8 to calculate the corresponding inclination angles. Again, points with a (formal) $\sin i > 1$ were eliminated from the grid. The allowed $(M_{\rm WD}, M_{\rm sec})$ pairs for both lines and all three ΔR cases are shown in Figure. 4.7.

The first of the three ΔR cases, $\Delta R = 0$, is obviously not a physically correct approach, as

Table 4.4: Corrected values of the radial velocity of the secondary star in SDSS 0110, after assuming a form of ΔR, for both the cases of the Hα and the Ca II emission lines.

ΔR	mean [km s^{-1}]	std.dev.	range [km s^{-1}]
Hα			
0	200.1	-	-
$(4/3\pi)\,R_{\rm sec}$	213.1	2.7	207.9-218.2
$R_{\rm sec}$	225.2	3.5	218.5-232.1
Ca II			
0	178.8	-	-
$(4/3\pi)\,R_{\rm sec}$	195.1	4.2	186.6-202.7
$R_{\rm sec}$	209.1	6.1	197.2-219.9

it implies that no correction is necessary. However, we did use it as a strict lower limit of the radial velocity of the secondary. In this sense, the third case, $\Delta R = R_{\rm sec}$, is a strict upper limit for $K_{\rm sec}$. Table 4.4 lists the ranges $K_{\rm sec,cor}$ corresponding to our adopted grid in the $(M_{\rm WD}, M_{\rm sec})$ plane shown in Figure 4.7.

We should note that, although reasonable as assumptions, it is quite possible that neither the $\Delta R = (4/3\pi)R_{\rm sec}$ nor the $\Delta R = R_{\rm sec}$ corrections correspond to the true distributions of the Hα and/or the Ca II emission lines on the secondary. Furthermore, it is not necessary that the distribution of Hα emission is the same with the distribution of Ca II emission. This means that the centre of light of Hα and the centre of light of Ca II have different displacements, i.e. it is possible that different forms of ΔR need to be applied to Hα and Ca II [see e.g. Parsons et al., 2010a, for further examples of different emission velocity values]. These facts could explain the actual differences between the radial velocity values of Hα and Ca II (measured and/or corrected) as shown in Table 4.4.

4.8 Results

Our light curve fitting procedure yields fitted values for $R_{\rm WD}$, $R_{\rm sec}$, and $T_{\rm sec}$ for a large grid in the $M_{\rm WD} - M_{\rm sec}$ plane, where each $(M_{\rm WD}, M_{\rm sec})$ point is defined by q and i of the corresponding model, through $K_{\rm sec}$ and $P_{\rm orb}$. However, as detailed in Section 2.4.4 the information available (in the form of the secondary star's radial velocity and the primary eclipse) is not enough to fully constrain the system and models with different parameter values give equally good fits. Analysing the results of the fitting was done in the following fashion.

In a first step, we applied a cut in the quality of the light curve fits, where we considered three different degrees of "strictness" by culling all models whose χ^2 was more than 1, 2 or 3σ above the best-fit value. This allowed us to retain only the good fits, but typically left us with a relatively large degeneracy in the parameter space.

In a second step, we had to select among the various equally good light curve fits those that are physically plausible. This was done using the mass-radius relations of Bergeron et al. [1995a] for the white dwarf, and the 5.0 Gyr model of Baraffe et al. [1998] for the M-dwarf. We then calculated

for each model the relative difference between the theoretical value of the radius and the value of the radius from the fit,

$$\delta R = \left| \frac{R_{\rm fit} - R_{\rm th}}{R_{\rm th}} \right| \tag{4.6}$$

where $R_{\rm fit}$ and $R_{\rm th}$ are the radius obtained from the light curve fit, and the radius from the mass-radius relation, respectively.

Assuming that the binary components obey, at least to some extent, a theoretical mass-radius relation, we defined cut-off values of $\delta R = 5\%$, 10%, and 15%, above which light curve models will be culled. The maximum of $\delta R = 15\%$ was motivated by the radius excess over theoretical main-sequence models observed in eclipsing low-mass binaries [Ribas et al., 2008], and by the current observational constraints on the white dwarf mass-radius relation [Provencal et al., 1998]. This cut in radius was applied individually for the white dwarf, ($\delta R_{\rm WD}$) and the companion star ($\delta R_{\rm sec}$).

Combining both the χ^2 and δR cuts left us in general with a relatively narrow range of system parameters that simultaneously satisfy the radial velocity amplitude and the morphology of the light curve. In a final step, we examined how well the stellar masses determined from the light curve/radial velocity analysis agreed with those derived from the spectral decomposition.

4.8.1 SDSS 0303

Modelling the light curve of SDSS 0303 involved the following two problems. Firstly, the time resolution of our data set poorly resolves the white dwarf ingress and egress phases, and consequently the white dwarf radius can only be loosely constrained. We decided therefore to fix the white dwarf radius in the light curve fits to the value calculated from the adopted white dwarf mass-radius relation of Bergeron et al. [1995a]. Secondly, the light curve displays a strong, but slightly asymmetric ellipsoidal modulation, with the two maxima being of unequal brightness (Figure 4.1). Similar light curve morphologies have been observed in the WDMS binaries BPM 71214 [Kawka & Vennes, 2003] and LTT 560 [Tappert et al., 2007], and have been attributed to star spots on the secondary star. By design, our light curve model cannot provide a fit that reproduces the observed asymmetry. Having said this, the presence of ellipsoidal modulation provides an additional constraint on $R_{\rm sec}$ that is exploited by the light curve fit.

A number of models passed the strictest configuration of our cut-offs, i.e. 1σ and $\delta R_{\rm sec} = 5\%$ (no cut was used in $\delta R_{\rm WD}$, as $R_{\rm WD}$ has been fixed during the fits). The possible range of solutions in the $M_{\rm WD} - M_{\rm sec}$ plane is shown in Figure 4.8.

Gray dots designate those light curve fits making the 1σ cut, black dots those that satisfy both the 1σ and $\delta R_{\rm sec} = 5\%$ cuts. The resulting ranges in white dwarf masses and secondary star masses are $M_{\rm WD,lcfit} = 0.88 - 0.95\,{\rm M}_{\odot}$ and $M_{\rm sec,lcfit} = 0.23 - 0.28\,{\rm M}_{\odot}$, respectively, corresponding to a white dwarf radius of $R_{\rm WD} = 0.008 - 0.009\,{\rm R}_{\odot}$ and a secondary radius of $R_{\rm sec} = 0.25 - 0.27\,{\rm R}_{\odot}$. Figure 4.9 shows one example of the light curve fits within this range for the model parameters $M_{\rm WD} = 0.91\,{\rm M}_{\odot}$, $R_{\rm WD} = 0.009\,{\rm R}_{\odot}$, $M_{\rm sec} = 0.25\,{\rm M}_{\odot}$, $R_{\rm sec} = 0.26\,{\rm R}_{\odot}$ and $i = 82.6^{\circ}$.

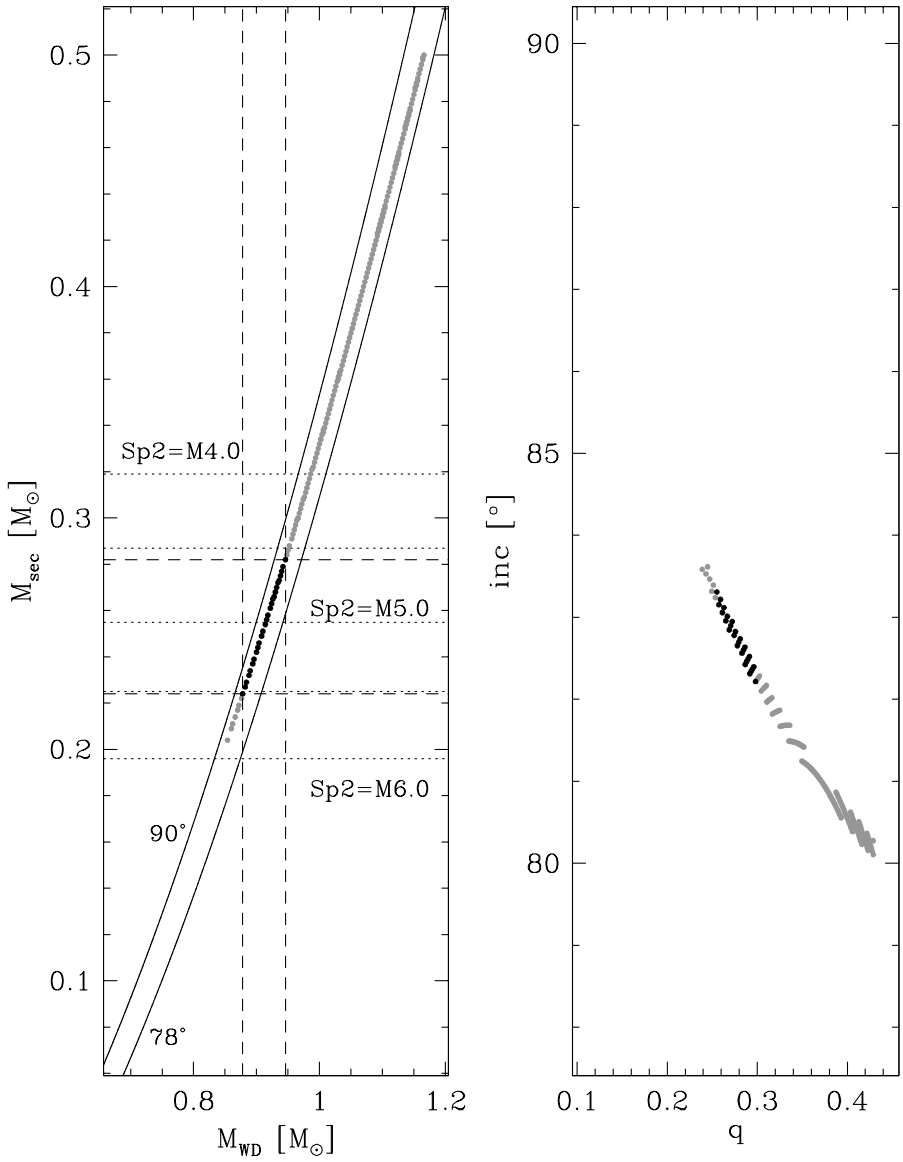

Figure 4.8: Light curve model fitting results for SDSS 0303. Left panel: $M_{\rm WD}$ and $M_{\rm sec}$ values corresponding to fits with χ^2 values within 1σ of the minimum value (grey points) and, simultaneously, with $\delta R_{\rm sec} \leq 0.05$ (black points). Right panel: the same, only in the $q-i$ plane. Also depicted in the left panel are curves corresponding to the mass function (solid black lines, $i = 90^\circ$ and 78°) which (by definition) bracket the possible solutions, $\mathrm{Sp}(2) - M_{\rm sec}$ relations (dotted, horizontal, black lines) and the range of possible $(M_{\rm WD}, M_{\rm sec})$ values (dashed, horizontal and vertical, black lines)

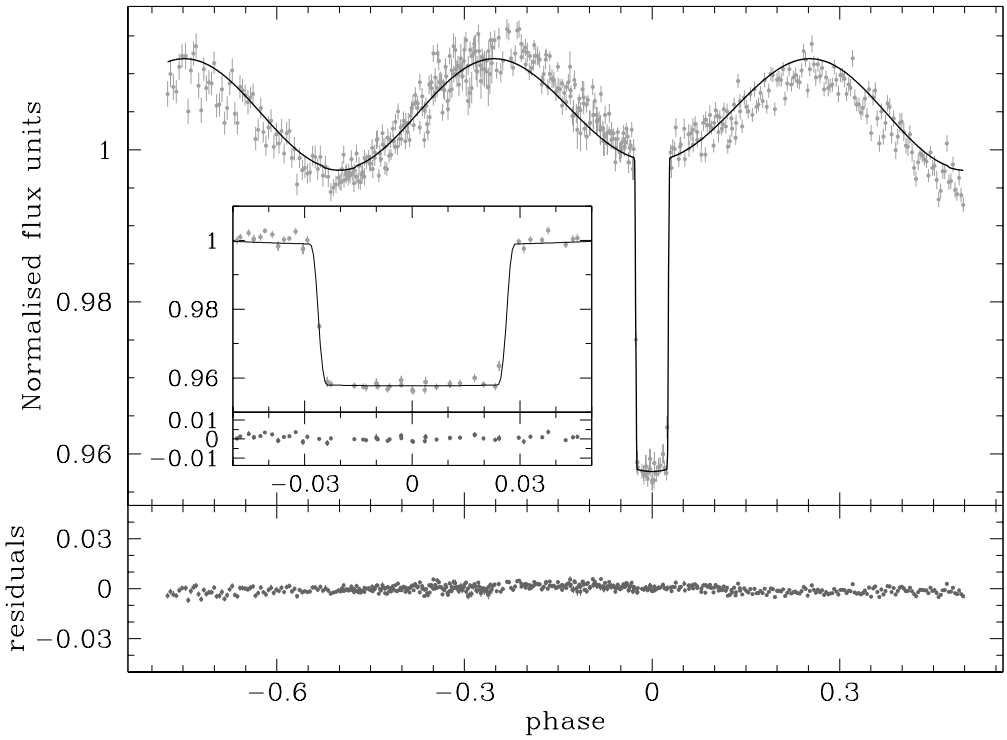

Figure 4.9: Model fit to the CA2.2 filterless light curve of SDSS 0303, for $M_{\rm WD} = 0.91\,{\rm M}_{\odot}$, $R_{\rm WD} = 0.009\,{\rm R}_{\odot}$, $M_{\rm sec} = 0.25\,{\rm M}_{\odot}$, $R_{\rm sec} = 0.26\,{\rm R}_{\odot}$ and $i = 82.6^{\circ}$. The model meets both our χ^2 (within 1σ) and the δR (within 5%) cut-offs. The residuals from the fit are shown at the bottom of the panel. Inset panel: data points and model fit focused around the eclipse.

To check the consistency of our light curve fits with the results from the spectral decomposition, we indicate in Figure 4.8 the radii of M-dwarfs with spectral types $\mathrm{Sp}(2) = \mathrm{M4} - \mathrm{M6}$ in steps of 0.5, based on the spectral type-mass relation given by Rebassa-Mansergas et al. [2007]. The secondary star mass from the light curve fit, $M_{\mathrm{sec,lcfit}} = 0.23 - 0.28\,\mathrm{M}_{\odot}$, corresponds to a secondary spectral type of $\mathrm{Sp}(2)_{\mathrm{lcfit}} = \mathrm{M4.5} - \mathrm{M5.5}$. The expected spectral type of the secondary from the spectral decomposition was $\mathrm{Sp}(2)_{\mathrm{spfit}} = \mathrm{M4.5} \pm 0.5$, hence, both methods yield consistent results.

4.8.2 SDSS 1435

For SDSS 1435, which is partially eclipsing, our temporal resolution, although again not ideal, was nevertheless deemed to be adequate to constrain the white dwarf radius from the light curve fits. Thus, a δR_{WD} cut was also applied. We applied again our strictest cuts on the light curve models, 1σ and $\delta R_{\mathrm{WD}} = \delta R_{\mathrm{sec}} = 5\%$, and the parameters of the surviving models are shown in Figure 4.10, where the meaning of the symbols is the same as in Figure 4.8.

These fits imply a white dwarf mass and radius of $M_{\mathrm{WD}} = 0.48 - 0.53\,\mathrm{M}_{\odot}$ and $R_{\mathrm{WD}} = 0.014 - 0.015\,\mathrm{R}_{\odot}$, respectively, and a secondary star mass and radius of $M_{\mathrm{sec}} = 0.19 - 0.25\,\mathrm{M}_{\odot}$ and $R_{\mathrm{sec}} = 0.22 - 0.25\,\mathrm{R}_{\odot}$, respectively. A sample fit that obeyed all three constraints is shown in Fig. 4.11. The model parameters are $M_{\mathrm{WD}} = 0.5\,\mathrm{M}_{\odot}$, $R_{\mathrm{WD}} = 0.015\,\mathrm{R}_{\odot}$, $M_{\mathrm{sec}} = 0.21\,\mathrm{M}_{\odot}$, $R_{\mathrm{sec}} = 0.23\,\mathrm{R}_{\odot}$ and $i = 77.6^{\circ}$.

Comparing the white dwarf masses from the spectroscopic decomposition/fit, $M_{\mathrm{WD,spfit}} = 0.41 \pm 0.08\,\mathrm{M}_{\odot}$, with the range of white dwarf masses allowed by the light curve fitting, $M_{\mathrm{WD,lcfit}} = 0.48 - 0.53\,\mathrm{M}_{\odot}$, reveals a reasonable agreement. Regarding the spectral type of the secondary star, we indicate in Figure 4.10 again the masses of M-dwarfs in the range M4 - M6, in steps of 0.5 spectral classes, following the $\mathrm{Sp}(2) - M_{\mathrm{sec}}$ relation of Rebassa-Mansergas et al. [2007]. This illustrates that the light curve fits result in a $\mathrm{Sp}(2)_{\mathrm{lcfit}} = \mathrm{M5} - \mathrm{M6}$, whereas the spectral decomposition provided $\mathrm{Sp}(2)_{\mathrm{spfit}} = \mathrm{M4.5} \pm 0.5$. Hence, also the results for the secondary star appear broadly consistent.

Steinfadt et al. [2008] independently reported the eclipsing nature of SDSS 1435, and estimated $M_{\mathrm{WD}} = 0.35 - 0.58\,\mathrm{M}_{\odot}$, $R_{\mathrm{WD}} = 0.0132 - 0.0178\,\mathrm{R}_{\odot}$, $M_{\mathrm{sec}} = 0.15 - 0.35\,\mathrm{M}_{\odot}$ and $R_{\mathrm{sec}} = 0.17 - 0.32\,\mathrm{R}_{\odot}$. The parameter ranges determined from our analysis are fully consistent with Steinfadt et al.'s work. In Figure 4.12 we overplot on the photometry of Steinfadt et al. [2008] the light curve model shown in Figure 4.11, illustrating that our solution is consistent with their data.

While the temporal resolution of our photometry is worse than that of Steinfadt et al. [2008], our analysis benefited from two additional constraints, firstly the mass function determined from our spectroscopy, and secondly the detection of a weak ellipsoidal modulation in our *I*-band light curve. While the observations of Steinfadt et al. [2008] covered the entire binary orbit, their data were obtained through a BG-39 filter, centred at 4800 Å, where the flux contribution of the companion star is negligible.

4.8.3 SDSS 1548

For SDSS 1548, we follow a very similar approach as for SDSS 1435, adopting a 1σ cut in χ^2 but a slightly less strict cut on the radii, $\delta R_{\mathrm{WD}} = \delta R_{\mathrm{sec}} = 10\%$. Figure 4.13 shows the solutions of

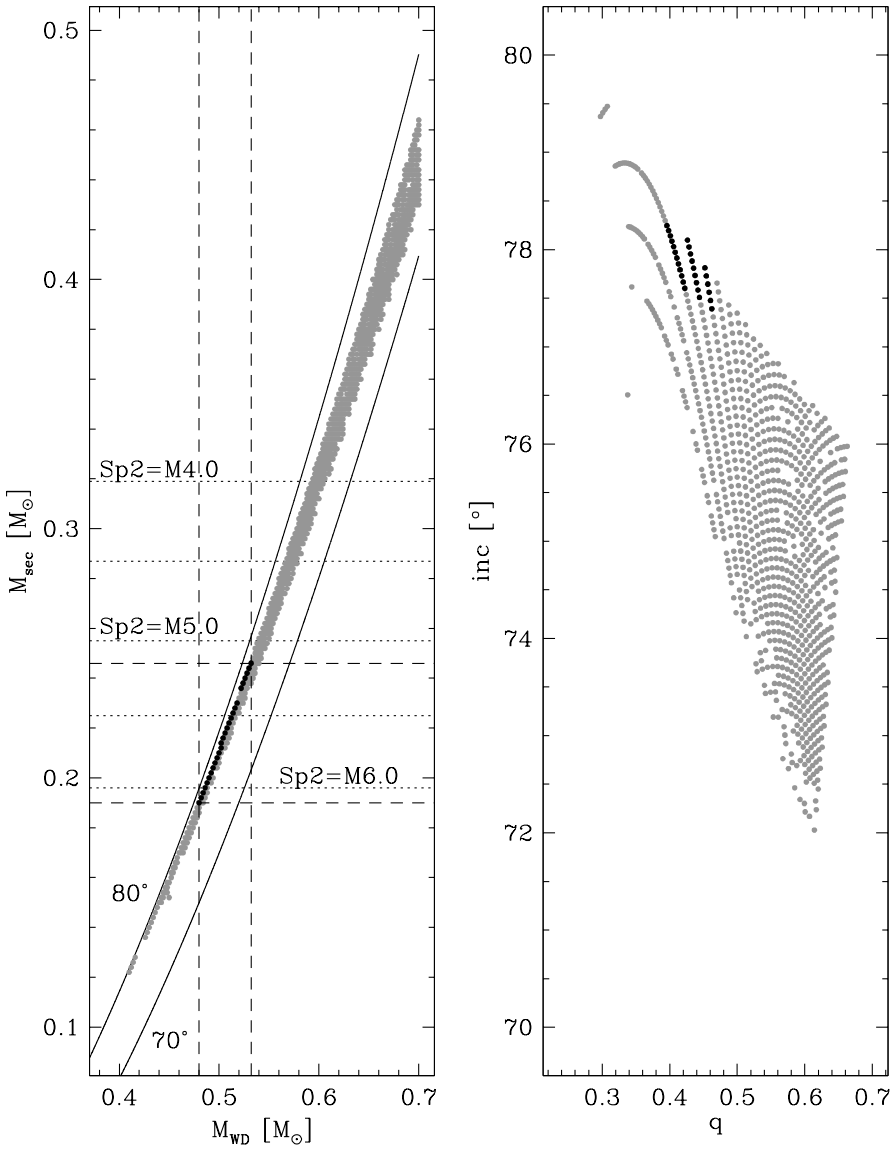

Figure 4.10: Light curve model fitting results for SDSS 1435. Left panel: $M_{\rm WD}$ and $M_{\rm sec}$ values corresponding to fits with χ^2 values within 1σ of the minimum value (grey points) and, simultaneously, with $\delta R_{\rm sec} \leq 0.05$ (black points). Right panel: the same, only in the $q-i$ plane. Also depicted in the left panel are curves corresponding to the mass function (solid black lines, $i = 70^\circ$ and 80°) which (by definition) bracket the possible solutions, $\mathrm{Sp}(2) - M_{\rm sec}$ relations (dotted, horizontal, black lines) and the range of possible $(M_{\rm WD}, M_{\rm sec})$ values (dashed, horizontal and vertical, black lines)

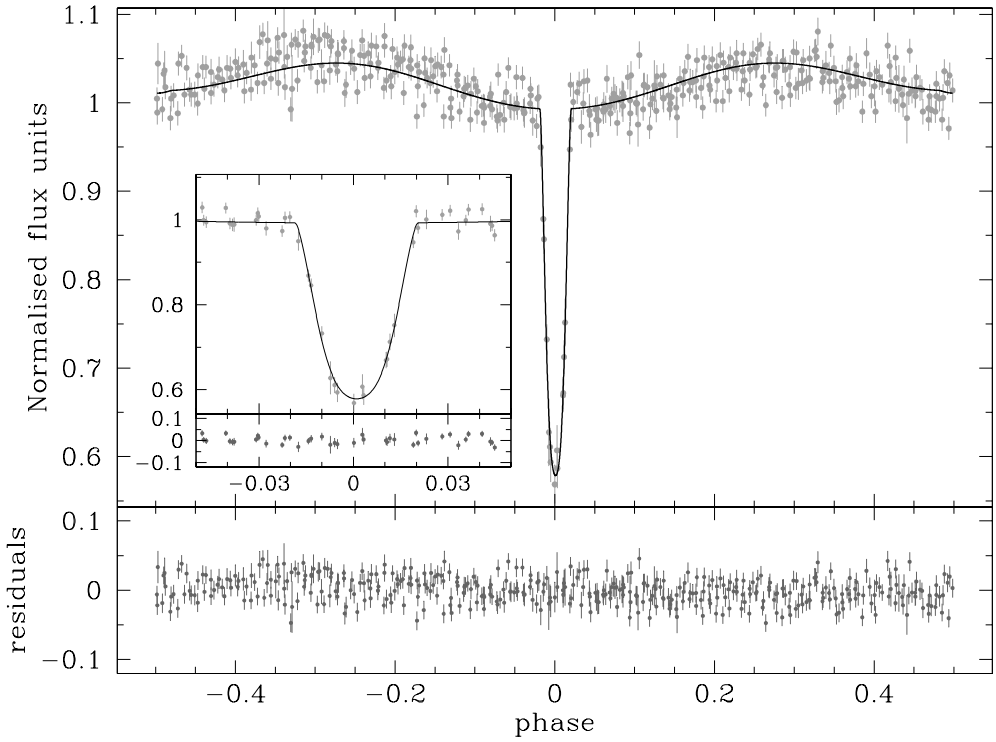

Figure 4.11: Model fit to the IAC80 *I*-band light curve of SDSS 1435, for $M_{\rm WD} = 0.5\,{\rm M}_{\odot}$, $R_{\rm WD} = 0.015\,{\rm R}_{\odot}$, $M_{\rm sec} = 0.21\,{\rm M}_{\odot}$, $R_{\rm sec} = 0.23\,{\rm R}_{\odot}$ and $i = 77.6^{\circ}$. The model meets both our χ^2 (within 1σ) and the δR (for both the WD and the secondary star, within 5%) cut-offs. The residuals from the fit are shown at the bottom of the panel. Inset panel: data points and model fit focused around the eclipse.

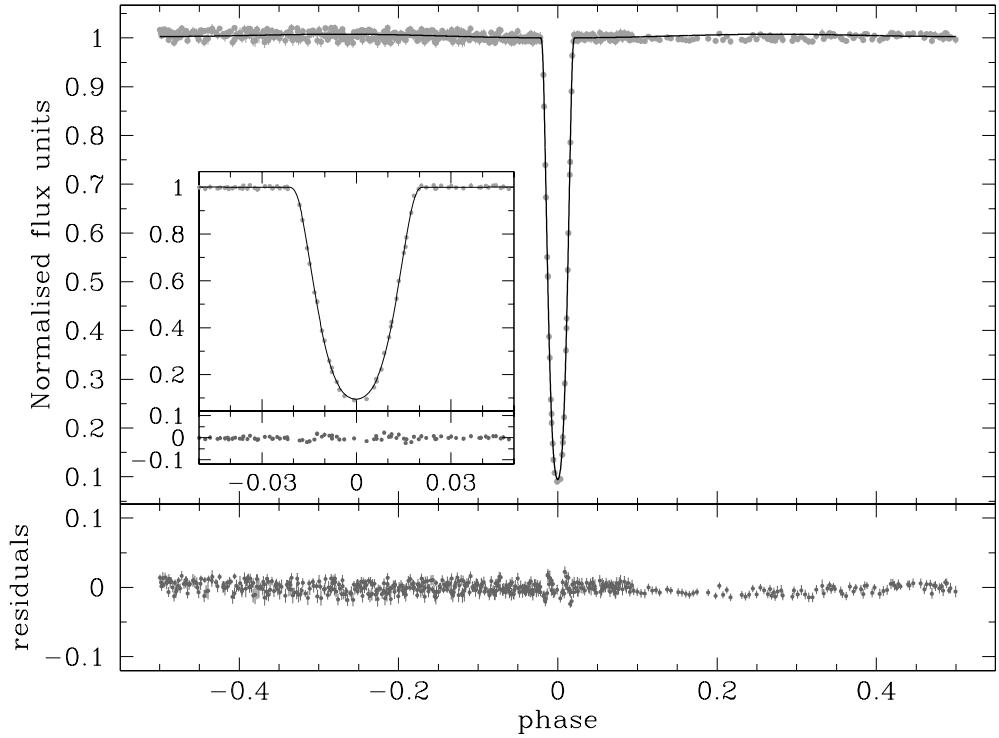

Figure 4.12: Our light curve model for SDSS 1435, as determined from fitting our IAC80 *I*-band photometry and shown in Figure 4.11, along with the data from Steinfadt et al. [2008], illustrating a high degree of consistency.

Table 4.5: Summary of the fitting results of SDSS 0110, for all three ΔR prescriptions, for both the cases of the Hα and the Ca II emission lines. In all cases we applied 3σ and $\delta R = 15\%$ cut-offs. A ($\surd$) means some models passed the cut-off, whereas a (-) means no models passed.

K-correction	Hα	**Ca II**
$\Delta R = 0$	$\surd$	$\surd$
$\Delta R = (4/3\pi)\,R_{\rm sec}$	-	$\surd$
$\Delta R = R_{\rm sec}$	-	-

our light curve fits that survived those criteria, where plot symbols have the same meaning as in Figures 4.8 and 4.10.

The models satisfying both cuts imply a white dwarf mass and radius of $M_{\rm WD} = 0.61 - 0.68\,{\rm M}_{\odot}$ and $R_{\rm WD} = 0.010 - 0.011\,{\rm R}_{\odot}$ respectively, and a secondary mass and radius of $M_{\rm sec} = 0.15 - 0.20\,{\rm M}_{\odot}$ and $R_{\rm sec} = 0.17 - 0.20\,{\rm R}_{\odot}$ respectively. A sample fit that obeyed all three constraints is shown in Figure 4.14. The model parameters are $M_{\rm WD} = 0.65\,{\rm M}_{\odot}$, $R_{\rm WD} = 0.011\,{\rm R}_{\odot}$, $M_{\rm sec} = 0.18\,{\rm M}_{\odot}$, $R_{\rm sec} = 0.18\,{\rm R}_{\odot}$ and $i = 85.6^{\circ}$.

The white dwarf parameters obtained from the light curve fitting are in full agreement with those derived from the spectral decomposition. The former give a possible range of white dwarf masses of $M_{\rm WD,lcfit} = 0.61 - 0.68\,{\rm M}_{\odot}$, while the latter yield a value of $M_{\rm WD,spfit} = 0.62 \pm 0.28\,{\rm M}_{\odot}$. In Figure 4.13, we indicate the masses corresponding to secondary spectral types M6, M6.5, and M7. The spectral fitting points to a ${\rm Sp(2)}_{\rm spfit} =$ M6 secondary. Our models indicate ${\rm Sp(2)}_{\rm lcfit} =$ M6 $-$ M7 again consistent with the spectroscopic result.

4.8.4 SDSS 0110

Because of the uncertainty in the true $K_{\rm sec}$ velocity of the secondary star, we inspected a total of six different grids of light curve fits for SDSS 0110 (three K-corrections for each of the observed $K_{\rm sec,\,H\alpha}$ and $K_{\rm sec,\,CaII}$ (Table 4.4), and consequently, this star needs a slightly more extensive discussion compared to the other three systems.

In a first exploratory step, we applied our least strict cut-offs, adopting a 3σ cut on the fit quality, and a $\delta R = 15\%$ cut for both the white dwarf and the secondary star radii. Even with these loose constraints, the $\Delta R = R_{\rm sec}$ case, i.e. assuming that the emission is concentrated on the surface of the secondary closest to the white dwarf, does not produce any solutions that meet the cut-off criteria. For the uniform illumination case, $\Delta R = (4/3\pi)\,R_{\rm sec}$, there were no solutions for $K_{\rm sec} = K_{\rm sec,\,H\alpha}$, but a few solutions for the $K_{\rm sec} = K_{\rm sec,\,CaII}$. Finally, a number of solutions existed for the case $\Delta R = 0$, i.e. assuming no K-correction, for both Hα and Ca II. Table 4.5 summarises this analysis, and the models that survived the culling defined ranges of ($M_{\rm WD}$,$M_{\rm sec}$) pairs which are illustrated in Figure 4.15. Keeping in mind the uncertainties in our simplistic approach for a K-correction (see again the discussion at the end of Section 4.7.2) the apparent discrepancy between the Hα and the Ca II grids is not surprising.

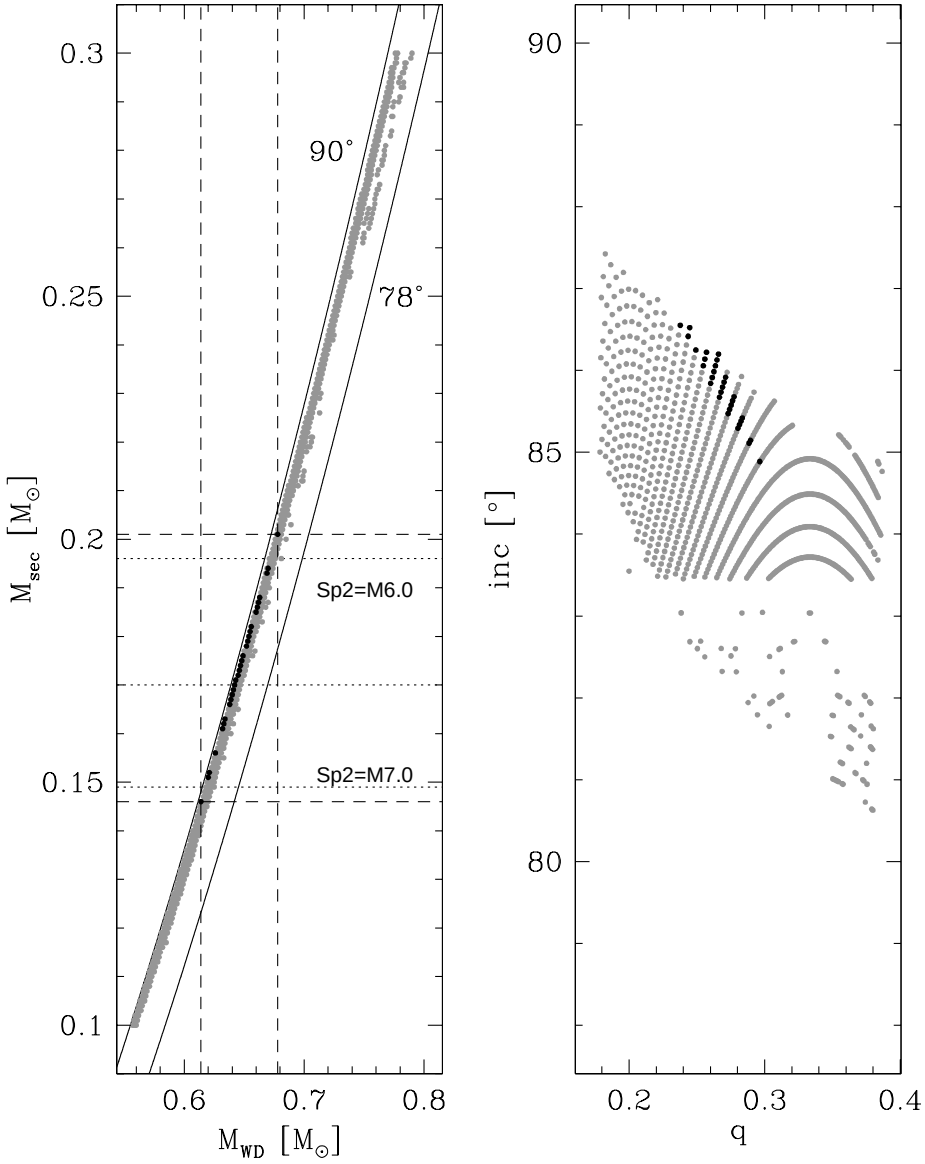

Figure 4.13: Light curve model fitting results for SDSS 1548. Left panel: $M_{\rm WD}$ and $M_{\rm sec}$ values corresponding to fits with χ^2 values within 1σ of the minimum value (grey points) and, simultaneously for both white dwarf and secondary radii, with $\delta R \leq 0.1$ (black points). Right panel: the same, only in the $q-i$ plane. Also depicted in the left panel are the mass function for $i = 78^\circ$ and $i = 90^\circ$ (solid black lines), $\mathrm{Sp}(2) - M_{\rm sec}$ relations for spectral types M6, 6.5, and 7 (dotted, horizontal, black lines) and the range of possible $(M_{\rm WD}, M_{\rm sec})$ values (dashed, horizontal and vertical, black lines).

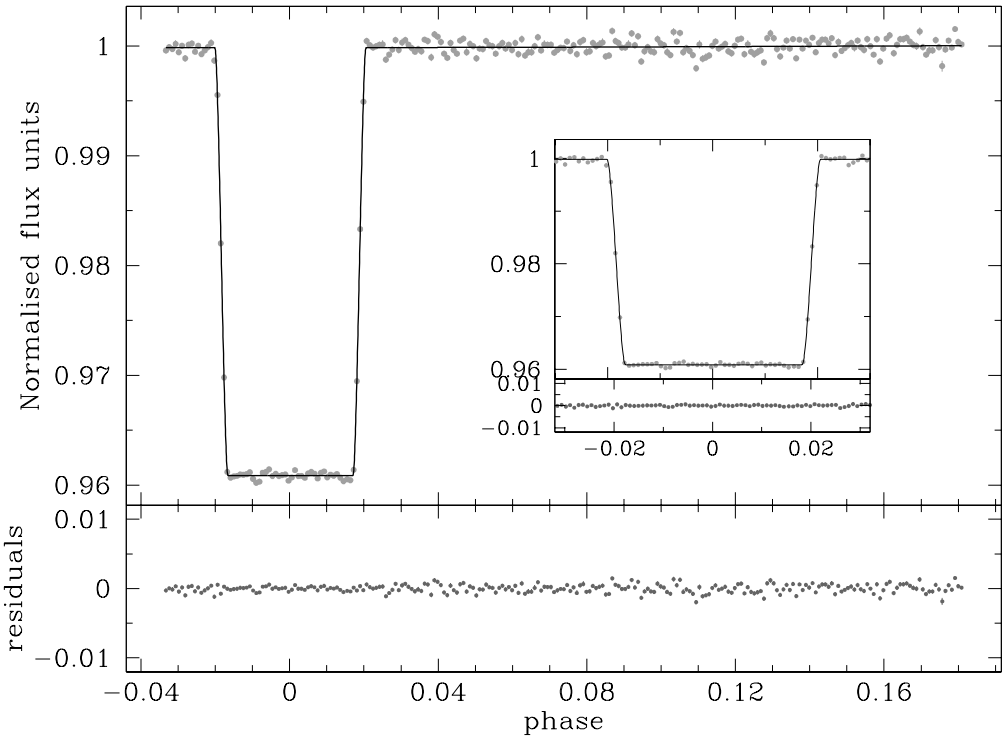

Figure 4.14: Model fit to the WHT/*R*-band light curve of SDSS 1548, for $M_{\rm WD} = 0.65\,{\rm M}_{\odot}$, $R_{\rm WD} = 0.011\,{\rm R}_{\odot}$, $M_{\rm sec} = 0.18\,{\rm M}_{\odot}$, $R_{\rm sec} = 0.18\,{\rm R}_{\odot}$ and $i = 85.6^{\circ}$. The model meets both a $1\sigma\,\chi^2$ cut-off, and the $\delta R \leq 0.10$, cut-off, for both the white dwarf and the secondary radii. The residuals from the fit are shown at the bottom of the panel. Inset panel: data points and model fit focused around the eclipse.

Given that the uniform irradiation prescription, $\Delta R = (4/3\pi)\,R_{\rm sec}$ represents a mid-way between the two extreme assumptions $\Delta R = R_{\rm sec}$ and $\Delta R = 0$, and that a reasonably large range of possible solutions was found for the Ca II velocities, we decided to explore tighter χ^2 constraints for this case. While a number of light curve models are found within 1σ of the minimum χ^2 value, both $\delta R_{\rm WD}$ and $\delta R_{\rm sec}$ were $\sim 15\%$ in all cases. No models survived if we reduced the value of δR in addition to the tighter χ^2 constraint.

As an illustration of the quality of the light curve fits achieved, Figure 4.16 shows a fit with $M_{\rm WD} = 0.59\,{\rm M}_{\odot}$, $R_{\rm WD} = 0.015\,{\rm R}_{\odot}$, $M_{\rm sec} = 0.28\,{\rm M}_{\odot}$, $R_{\rm sec} = 0.32\,{\rm R}_{\odot}$, $i = 85^{\circ}$ and $K_{\rm sec} = 197\,{\rm km\,s^{-1}}$. The mass of the secondary corresponds to a spectral type of ${\rm Sp}(2) = {\rm M4.5}$. We stress, however, that we do not adopt this model as a final solution for the parameters of SDSS 0110, but rather consider it as a physically plausible set of parameters.

Taking the 1σ confidence levels of the light curve fits at face value, they imply a white dwarf mass of $M_{\rm WD,lcfit} = 0.59 - 0.7\,{\rm M}_{\odot}$ and a secondary mass of $M_{\rm sec,lcfit} = 0.28 - 0.38\,{\rm M}_{\odot}$. For the white dwarf, these numbers are in contrast with the results from the spectral decomposition, $M_{\rm WD,spfit} = 0.47 \pm 0.02\,{\rm M}_{\odot}$. The errors in the spectroscopic white dwarf parameters are purely of statistical nature. However, even assuming a reasonably large systematic error of 0.2 dex in $\log g$ (implying $M_{\rm WD,spfit} = 0.39 - 0.55\,{\rm M}_{\odot}$) the white dwarf masses implied by the light curve fit and the spectroscopic fit appear to be inconsistent.

Regarding the secondary, adopting $M_{\rm sec,lcfit} = 0.28 - 0.38\,{\rm M}_{\odot}$ and the ${\rm Sp}(2) - M_{\rm sec}$ relation of Rebassa-Mansergas et al. 2007 suggests a spectral type of ${\rm Sp}(2)_{\rm lcfit} = {\rm M3 - M4.5}$, which is consistent with the results of the spectral decomposition, ${\rm Sp}(2)_{\rm spfit} = {\rm M4 \pm 1}$.

While our analysis of the light curve fits demonstrates that the data can be modelled well, it is clear that the lack of a reliable value for $K_{\rm sec}$ prevents the choice of the physically most meaningful solution. Consequently, a definite determination of the stellar parameters of SDSS 0110 is not possible on the basis of the currently available data, and we adopt as a first cautious estimate the values of our spectral decomposition fit. As mentioned before, a physically motivated K-correction can be modelled once a larger set of spectra covering the entire binary orbit are available.

4.9 Post common envelope evolution

Considering their short orbital periods, the four new eclipsing systems discussed in this Chapter must have formed through common envelope evolution (Section 1.2.3). As shown by Schreiber & Gänsicke [2003], if the binary and stellar parameters are known, it is possible to reconstruct the past and predict the future evolution of PCEBs for a given angular momentum loss prescription. Assuming the classical disrupted magnetic braking scenario of [Rappaport et al., 1983] (Section 1.3.4), for fully convective stars gravitational radiation is assumed to be the only angular momentum loss mechanism, which applies to all the four systems. The current ages of the PCEBs are determined by interpolating the cooling tracks from Wood [1995]. Table 4.6 lists the evolutionary parameters for our four eclipsing WDMS binaries.

The calculated evolutionary tracks of the four systems are shown in Figure 4.17. The present position of each binary is indicated by an asterisk. The grey-shaded region indicates the $2-3$ h orbital period gap. Given that the four binaries contain low-mass secondary stars, all of them are

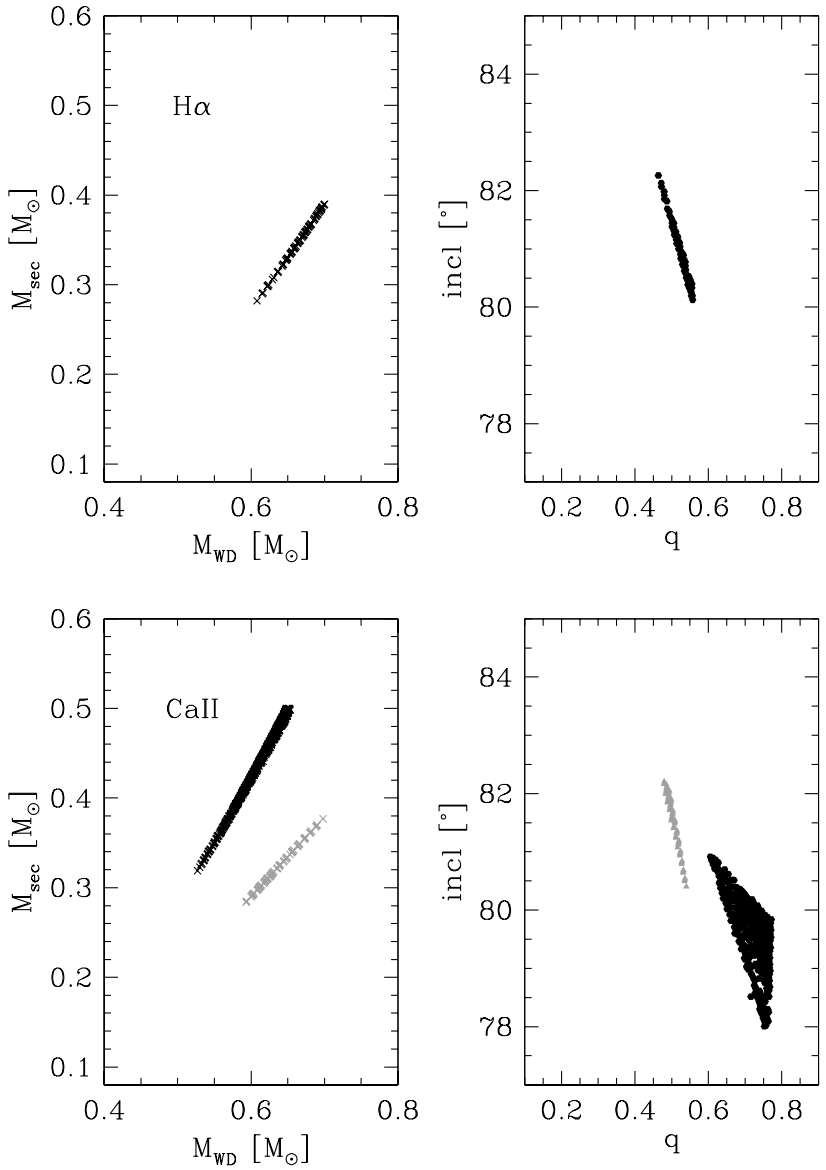

Figure 4.15: Results of the model fitting of SDSS 0110 for Hα (top panels) and Ca II (bottom panels), for a 3σ confidence level and $\delta R < 0.15$. Black points correspond to $\Delta R = 0$, grey to $\Delta R = (4/3\pi)\, R_{\rm sec}$ (where applicable, see text for details). Left panels show the $(M_{\rm WD}, M_{\rm sec})$ plane, right panels the $q - i$ plane.

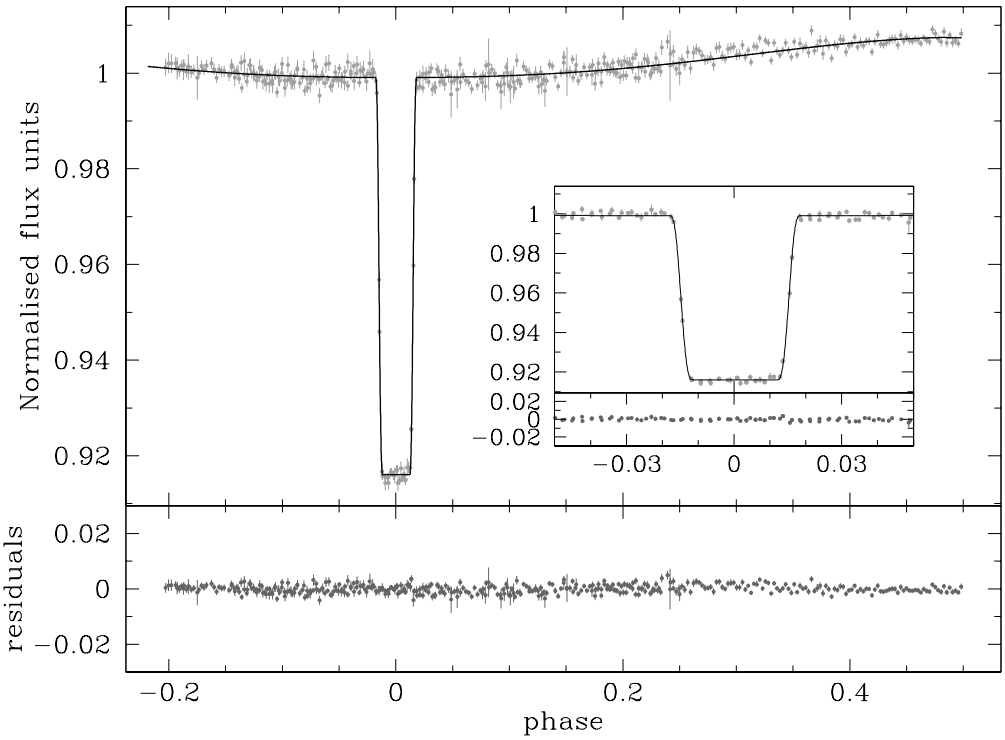

Figure 4.16: Model fit to the CA2.2 *I*-band light curve of SDSS 0110, for $M_{\rm WD} = 0.59\,{\rm M}_{\odot}$, $R_{\rm WD} = 0.015\,{\rm R}_{\odot}$, $M_{\rm sec} = 0.28\,{\rm M}_{\odot}$, $R_{\rm sec} = 0.32\,{\rm R}_{\odot}$, $i = 85^{\circ}$ and $K_{\rm sec} = 197\,{\rm km\,s^{-1}}$. The model radii agree with the theoretically predicted ones within 15%, for both the white dwarf and the secondary star. The residuals from the fit are shown at the bottom of the panel. Inset panel: data points and model fit focused around the eclipse.

Table 4.6: Reconstructed and predicted orbital periods as well as expected evolutionary times for the four new eclipsing PCEBs. The cooling age of the white dwarfs is $t_{\rm cool}$ while $P_{\rm CE}$ and $P_{\rm sd}$ are the orbital periods at the end of the common envelope phase and at the onset of mass transfer, respectively. The time still needed to enter the semi-detached CV configuration is $t_{\rm sd}$.

SDSS J	$t_{\rm cool}$ [yr]	$P_{\rm sd}$ [d]	$P_{\rm CE}$ [d]	$t_{\rm sd}$ [yr]
0110+1326	1.41e+07	0.097	0.332	1.78e+10
0303+0050	3.23e+09	0.097	0.228	5.95e+08
1435+3733	2.53e+08	0.088	0.132	9.50e+08
1548+4057	3.91e+08	0.069	0.191	4.23e+09

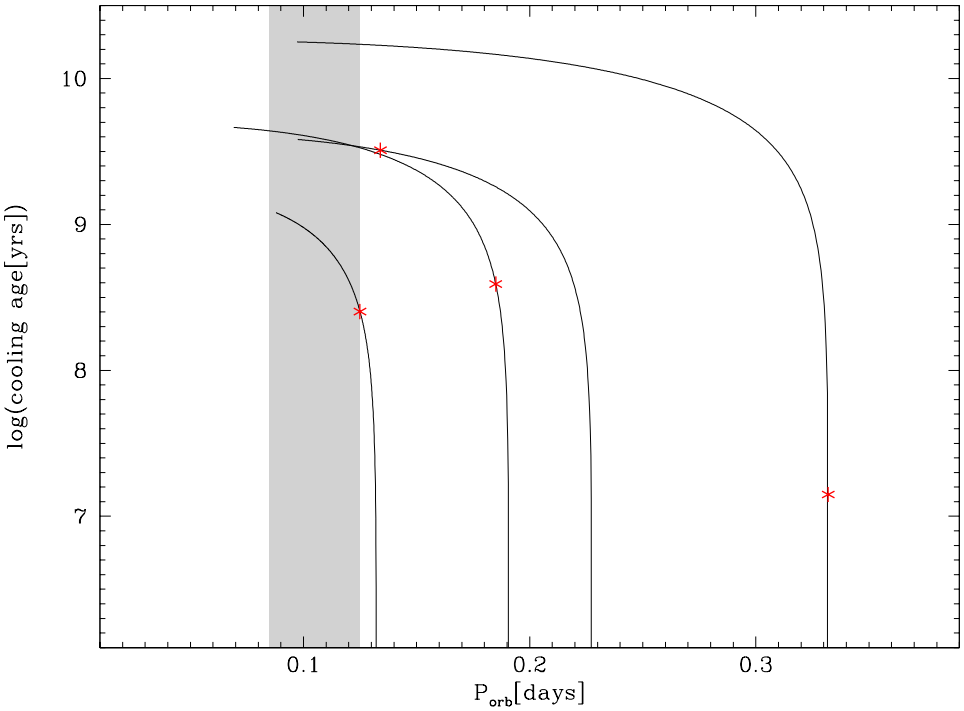

Figure 4.17: Evolutionary post common envelope tracks for our four eclipsing binaries. From left to right: SDSS 1435, SDSS 1548, SDSS 0303 and SDSS 0110. The current position of the systems is indicated by an asterisk. We assumed only gravitational wave radiation as angular momentum loss agent, as all four systems are thought to contain fully convective secondary stars. The orbital period gap of CVs is highlighted in grey – all four systems will start mass transfer in, or shortly below the gap.

expected to start mass transfer in or below the period gap. This underlines the fact first noticed by Schreiber & Gänsicke [2003] that only very few progenitors of long-period CVs are known. SDSS 0303+0050 has passed most of its PCEB lifetime and its current orbital period differs significantly from the reconstructed value at the end of the CE phase. The other three systems are rather young PCEBs with a current orbital period close to $P_{\rm CE}$.

4.10 Discussion

The four systems presented in this Chapter served as a "proof-of-concept" for our dedicated search for eclipsing PCEBs, showing that our candidate selection criteria can indeed identify eclipsing systems. We have also illustrated how straightforward photometric and spectroscopic observations can provide information on the stellar and binary properties, and seen the techniques discussed in Chapter 2 applied in practice.

The amount of available observations, coupled with the poor time-resolution of our light curves and the lack of spectroscopic information on the radial velocities of the white dwarfs in all four systems, leads to a largely unconstrained parameter space. This is mirrored in the large

uncertainties and the need to invoke mass-radius relations and is also the reason why no MCMC optimisation was carried out, as it would not be particularly enlightening.

On an individual basis, SDSS 1435 is the first confirmed partially eclipsing PCEB and its WD seems to be less massive than the average field-WD in agreement with predictions from the CE evolution theory. On the other hand, SDSS 0303 seems to harbour an unusually massive (and in fact the most massive so far in a PCEB) white dwarf. Recent observations (S.Parsons, priv. comm.) indicate a potential magnetic nature of the WD primary in SDSS 0303. The white dwarf in SDSS 1548 is an all-in-all "normal" WD, but we should note that the $T_{\rm eff} - \log g$ values place it inside the ZZ Ceti instability strip, a fact worthy of future investigation. SDSS 0110 is the least constrained system of the four, owing to the difficulties in correcting the emission-line radial velocity value. All systems have secondaries that are of later type than M4.

Assembling a larger data set (especially spectroscopic observations fully covering the orbit, see again Figure 4.1) and of higher quality (high signal-to-noise spectroscopy, high temporal resolution photometry to fully resolve the white dwarf ingress/egress) could significantly improve the current parameter determinations and provide valuable observational input both for the CE models and for testing and calibrating M-R relations of WD and low-mass stars.

Chapter 5

Precise parameters for a low-mass white dwarf and a low-mass main-sequence star

5.1 Introduction

In this Chapter, another eclipsing PCEB from SDSS will be presented. The main difference with Chapter 4 is the amount of available observational information, namely the measurement of the radial velocity of the white dwarf. This measurement fixes the mass ratio q and provides strict constraints on the stellar masses and the binary inclination. As a result, a different approach to modelling will be presented. Masses and radii can be determined without the need to invoke either the χ^2- or the δR-cut of the previous Chapter. In addition to that, the quality of the spectroscopy allows proper treatment of limb-darkening, and the high-time resolution photometry fully resolves the eclipse profile, in contrast to the data set of the previous Chapter. Hence, this system warrants optimisation through MCMC and this method will be demonstrated in practice.

5.2 Target information

The system presented here is SDSSJ 121010.1+334722.9 (henceforth SDSS 1210), also identified in our search for eclipsing PCEBs from SDSS. It was listed by Rebassa-Mansergas et al. [2010] as a WDMS binary dominated by the flux of a low-mass companion with a spectral type M5V, suggesting that the white dwarf must be very cool. Inspecting the Na I $\lambda\lambda$ 8183.27,8194.81 doublet in the six SDSS sub-spectra[1], with exposure times of 15–30 min taken over the course of three nights, we found large radial velocity variations that strongly suggested an orbital period of a few hours. Time-series photometry soon revealed the eclipsing nature of the system. Full coordinates and SDSS

[1] Sub-spectra is the common name for the individual sub-exposures that are co-added to produce one SDSS spectrum with high signal-to-noise ratio

Table 5.1: Full coordinates, g, r, i magnitudes and $g-r$, $r-i$ colours of SDSS 1210 and the three comparison stars used in the analysis presented in this Chapter.

Star	Coordinates [J2000]	g	r	i	$g-r$	$r-i$
SDSS 1210	12 10 10.13 +33 47 22.88	16.94	16.16	14.92	0.78	1.24
C1	12 10 13.13 +33 46 05.95	15.98	15.33	15.11	0.65	0.22
C2	12 10 10.15 +33 44 02.61	17.33	16.01	15.33	1.32	0.68
C3	12 10 30.28 +33 46 53.07	15.80	15.46	15.34	0.34	0.12

u, g, r, i, z magnitudes of the target and the three comparison stars used in the analysis are given in Table 5.1. We note that that SDSS 1210 also has a GALEX near-ultraviolet (NUV) detection of NUV $= 20.82$, but no far-ultraviolet (FUV) detection.

5.3 Observations and data reduction

The observational data set and information on the data reduction procedures are summarised in Chapter 3. Note that all the LT observations were carried out in one-hour-long observing blocks. Multiple blocks during one night were not consecutive, but had time-gaps between them. A sample light curve is shown in Figure 5.1. The out-of-eclipse variation is ellipsoidal modulation, arising from the tidally deformed secondary.

5.4 Orbital period and ephemeris

We have determined the orbital period and ephemeris of SDSS 1210 through mid-eclipse timings using the mirroring method. This provided a preliminary ephemeris.

Subsequently, we phase-folded our data set with the preliminary ephemeris and proceeded with the light curve model fitting (see Section 5.7). Having an accurate model at hand, we re-fitted each light curve individually. This provides a more accurate mid-eclipse time and a robust estimation of the error, as the light curve fitting code includes the time of mid-eclipse T_0 as a parameter.

Repeating the cycle count determination and the linear ephemeris fitting, as done in the mirroring method, we obtained the following ephemeris calculated on a Modified Julian Date-timescale and corrected to the solar system barycentre

$$\mathrm{MJD\,(BTDB)} = 54923.033686(6) + 0.124489764(1)\,E \tag{5.1}$$

with the numbers in parentheses indicating the error on the last digit. Thus, SDSS 1210 has an orbital period of $P_{\mathrm{orb}} = 2.987754336(24)$ h. The mid-eclipse times are listed in the Appendix.

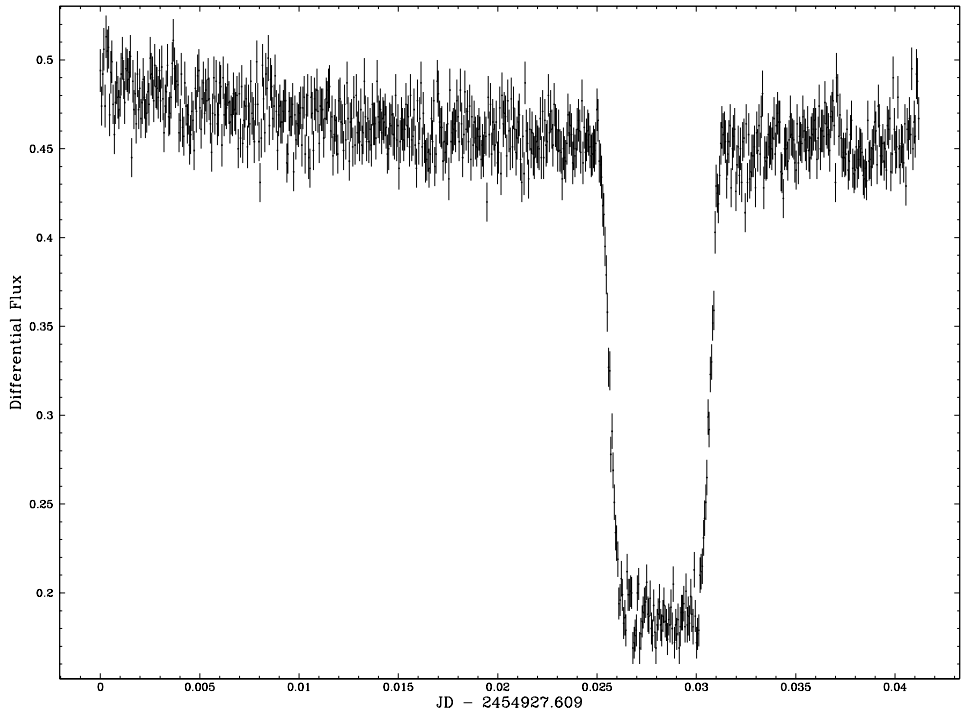

Figure 5.1: Sample light curve of SDSS 1210 obtained at the LT on April 05, 2009.

5.5 Spectroscopic analysis

Whereas the SDSS spectrum of SDSS 1210 remained inconclusive with respect to the nature of the white dwarf [Rebassa-Mansergas et al., 2010], our blue-arm WHT spectroscopy immediately revealed a host of narrow metal lines that exhibit radial velocity variations anti-phased with respect to those of the M-dwarf. The 18 WHT spectra obtained in May 2010, averaged in the white dwarf restframe and continuum-normalised, are shown in Figure 5.2 and illustrate the wealth of absorption lines from Mg, Al, Si, Ca, Mn, and Fe. Similar metal lines have been detected in the optical spectra of a few other cool PCEBs, e.g. RR Cae [Zuckerman et al., 2003] or LTT 560 [Tappert et al., 2007], and indicate accretion of mass via a wind from the M-dwarf.

We have analysed the blue WHT spectra using hydrogen-dominated but metal-polluted (DAZ) spectra calculated with the stellar atmosphere code described by Koester [2010]. We fixed the surface gravity to $\log g = 7.70$, as determined from the fits to the LT light curve (Section 5.8). The model grid covered effective temperatures $5400\,\mathrm{K} \leq T_{\rm eff} \leq 7400\,\mathrm{K}$ in steps of 200 K and metal and He abundances of $\log[\mathrm{Z/H}] = -3.0, -2.3, -2.0, -1.3, -1.0$, with all relevant elements up to zinc included, and fixed their relative abundances ratios to the respective solar values. We then fitted the model spectra to the average WHT spectrum in the range 3645–3930 Å, where the contribution of the M-dwarf is entirely negligible. A good fit is found for $T_{\rm WD} \simeq 6000\,\mathrm{K}$ and metal abundances at $\simeq 0.01$ their solar values, however, the effective temperature and the metal abundances are strongly correlated (Figure 5.3).

This degeneracy is lifted by including the GALEX detection of SDSS 1210, as the predicted

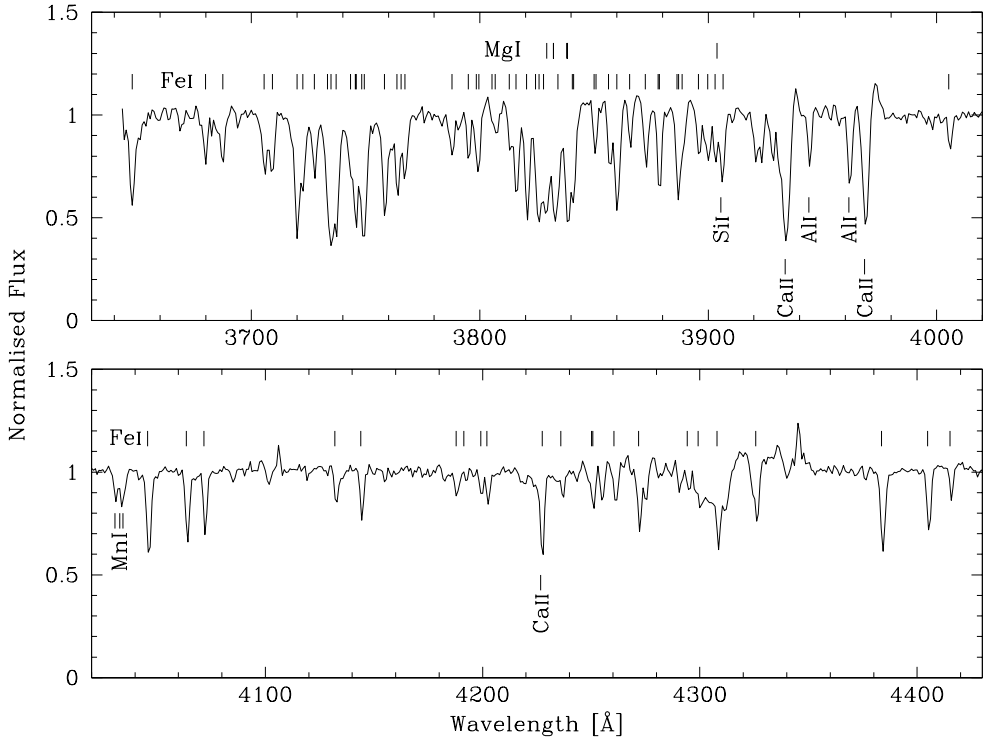

Figure 5.2: The normalised average WHT spectrum in the white dwarf restframe, along with line identifications for absorption lines originating in the white dwarf photosphere.

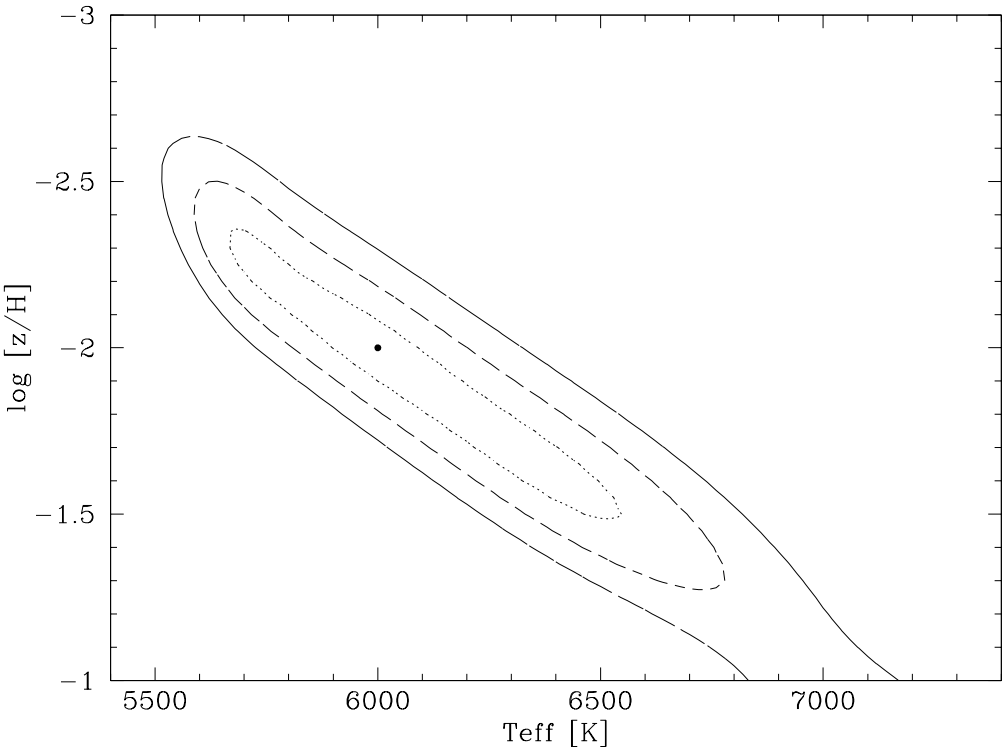

Figure 5.3: Results of model spectra fitting to the average WHT spectrum. The single point indicates the best fit solution. The contours indicate the regions where the χ^2 of the fit is within 1, 2 and 3σ (dotted, short-dashed and long-dashed lines respectively) of the minimum.

near-UV flux is a strong function of the effective temperature. The uncertainty in the absolute flux calibrations of our WHT spectra and the GALEX observations introduces a small systematic uncertainty on the final result, and we settle for $T_{\rm WD} = 6000 \pm 200\,{\rm K}$ and $\log[{\rm Z/H}] = -2.0 \pm 0.3$. Independently, the weakness of the Balmer lines in the WHT spectrum also requires that $T_{\rm WD} \lesssim 6400\,{\rm K}$. The spectral modelling of SDSS 1210 is shown Figure 5.4.

Adopting the white dwarf radius from the light curve fit (Section 5.7 and 5.8), $R_{\rm WD} = 0.0159\,{\rm R}_{\odot}$, the flux-scaling factor of the best-fit spectral model implies a distance of $d \simeq 50 \pm 5\,{\rm pc}$, which is in good agreement with $d \sim 66 \pm 34\,{\rm pc}$ estimated by Rebassa-Mansergas et al. [2010] from fitting the M-dwarf.

The detection of metals in the photosphere of the white dwarf allows an estimate of the accretion rate [e.g. Dupuis et al., 1993; Koester & Wilken, 2006], as long as the system is in accretion-diffusion equilibrium. In the temperature regime of this white dwarf, the diffusion time scales of the metals detected in the WHT spectrum vary by a factor 2, and are, for $T_{\rm WD} = 6000\,{\rm K}$, in the range 30000-60000 years. For completeness, we note that because we have adopted solar abundance ratios for the metals, these small differences in diffusion time scales imply slightly non-solar ratios in the accreted material. In principle, the individual metal-to-metal ratios can be determined from the observed spectrum of the white dwarf, and hence allow to infer the abundances of the companion star, however, this requires data with substantially higher spectral resolution to resolve the line blends. It is plausible to assume that the average accretion rate over the diffusion time scales involved is constant, as the binary configuration (separation of the two stars, Roche-lobe filling factor of the companion) changes on much longer time scales. Summing up the mass fluxes at the bottom of the convective envelope, and taking into account the uncertainties in $T_{\rm WD}$ and the metal abundances, gives $\dot{M} \simeq (5 \pm 2) \times 10^{-15}\,{\rm M}_{\odot}\,{\rm yr}^{-1}$. There are now three PCEBs with similar stellar components that have measured accretion rates, RR Cae ($\dot{M} \simeq 4 \times 10^{-16}\,{\rm M}_{\odot}\,{\rm yr}^{-1}$; Debes 2006), LTT 560 ($\dot{M} \simeq 5 \times 10^{-15}\,{\rm M}_{\odot}\,{\rm yr}^{-1}$; Tappert et al. 2011), and SDSS 1210 ($\dot{M} \simeq 5 \times 10^{-15}\,{\rm M}_{\odot}\,{\rm yr}^{-1}$).

Whereas SDSS 1210 and LTT 560 have similar orbital periods, the period of RR Cae is roughly twice as long, suggesting that the efficiency of wind-accretion decreases as the binary separation and Roche-lobe size of the companion increase, as expected. A more systematic analysis of the wind-loss rates of M-dwarfs and the efficiency of wind accretion in close binaries would be desirable, but will require a much larger sample of systems.

5.6 The spectroscopic orbit

Radial velocities of the binary components have been measured from the Fe I λλ 4045.813,4063.594, 4071.737,4132.058,4143.869 absorption lines for the white dwarf and the Na I λλ 8183.27,8194.81 absorption doublet for the secondary star.

The Fe I lines were simultaneously fitted with a second-order polynomial plus five Gaussians of common width and a separation fixed to the corresponding laboratory values. A sine fit to the radial velocities, phase-folded using the orbital ephemeris yields $K_{\rm WD} = 95.3 \pm 2.1\,{\rm km\,s}^{-1}$ and $\gamma_{\rm WD} = 24.2 \pm 1.4\,{\rm km\,s}^{-1}$.

The Na I doublet was fitted with a second-order polynomial plus two Gaussians of common width and a separation fixed to the corresponding laboratory value. A sine fit to the ra-

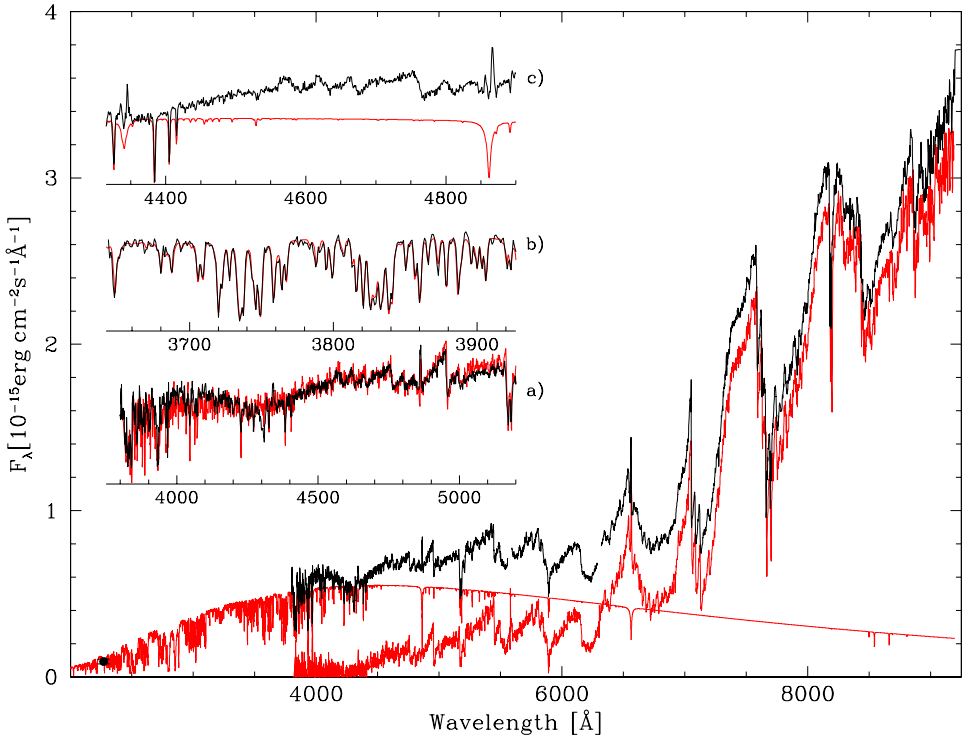

Figure 5.4: Spectral modelling of SDSS1210. Main panel: the SDSS spectrum and the GALEX NUV flux (black), along with the best-fit white dwarf model (red, $T_{\rm WD} = 6000$ K, $\log g = 7.70$, $\log[{\rm Z/H}] = -2.0$) and the best-fit M-dwarf template for the companion (red, Sp2=M5). Inset (a): The sum of the white dwarf model and M-dwarf template provide a good match to the blue end of the SDSS spectrum (black), with the low flux of the M-dwarf template being the dominant limitation. Inset (b): Best-fit white dwarf model (red) and the average WHT spectrum for $\lambda < 3930$ Å, where the M-dwarf contributes practically nothing to the observed flux. Inset (c): Best-fit white dwarf model (red) and the average WHT spectrum (black) illustrating the weakness of the Hβ and Hγ lines of the white dwarf. Increasing the temperature very rapidly results in Balmer lines and/or a NUV flux that are inconsistent with the observations.

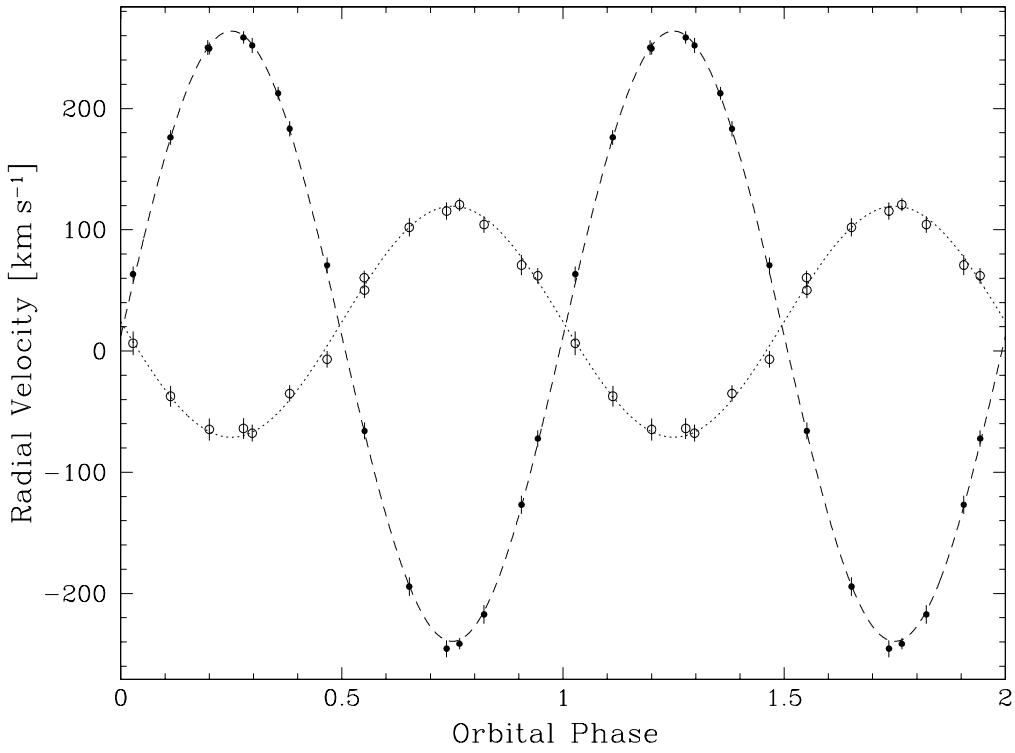

Figure 5.5: Phase-folded radial velocity curves of the secondary star (filled circles) and the white dwarf (open circles), with their respective errors. Also shown are the sine fits to the velocities of both components. A full cycle is repeated for clarity.

dial velocities, phase-folded using the orbital ephemeris yields $K_{\rm sec} = 251.7 \pm 2.0\,{\rm km\,s^{-1}}$ and $\gamma_{\rm sec} = 12.2 \pm 0.9\,{\rm km\,s^{-1}}$.

Knowledge of both radial velocities allows us to obtain the mass ratio q of the binary, namely $q = K_{\rm WD}/K_{\rm sec} = 0.379 \pm 0.009$. We tentatively interpret the difference between $\gamma_{\rm WD}$ and $\gamma_{\rm sec}$ as the gravitational redshift of the white dwarf $z_{\rm WD,spec}$, which yields $z_{\rm WD,spec} = 11.9 \pm 1.7\,{\rm km\,s^{-1}}$.

Figure 5.5 shows the measured radial velocities phase-folded on the orbital period and the corresponding sine-fits.

5.7 Light curve modelling

As per usual, model light curves were fitted to the data using LCURVE. Initial minimisation was carried out with the SIMPLEX and LEVENBERG-MARQUARDT methods. In contrast to the four systems of Chapter 4, the available photometric and spectroscopic information on SDSS 1210 provide strong constraints on the parameter space, which warrants an MCMC process for final optimisation and estimation of uncertainties. This was achieved with LCMCMC.

During the MCMC minimisation, we kept $T_{\rm WD}$ fixed at $T_{\rm WD} = 6000\,{\rm K}$ and the gravity darkening of the secondary fixed at 0.08 (the usual value for a convective atmosphere). Limb dark-

ening coefficients were also held fixed. For the white dwarf we calculated quadratic limb darkening coefficients from a white dwarf model with $T_{\rm WD} = 6000\,{\rm K}$ and $\log g = 7.7$. The corresponding values were found to be a$= 0.174$ and $b = 0.421$ for $I(\mu)/I(1) = 1-{\rm a}(1-\mu) - b\,(1-\mu)^2$, with μ being the cosine of the angle between the line of sight and the surface normal. For the secondary star we used the Tables of Claret & Bloemen [2011]. We interpolated between the values of V and R (as the observations were obtained through a V+R filter) for a $T = 3000\,{\rm K}$ and $\log g = 5$ star, to obtain quadratic limb darkening coefficients ${\rm a}' = 0.62$ and $b' = 0.273$. All other parameters were allowed to vary. A Gaussian prior, similar to that discussed in Section 2.4.4, was implemented for the measured radial velocities $K_{\rm WD}$ and $K_{\rm sec}$.

It quickly became apparent that the way the photometric data were acquired would present a hurdle in the analysis. Our data set consisted of many one-hour observing blocks. While the sum of all blocks covers the whole orbital cycle, each observing block individually covers only a third of it, and each block was not necessarily centred around the eclipse. The blocks were obtained over many nights and under varying conditions, including seeing, sky brightness, extinction and airmass.

The varying conditions will have different effects on stars of different colour. Complications arise when we consider the very broad V+R filter of our observations. Figure 5.6 shows the Sloan g,r,i-filter curves, with RISE's V+R curve superimposed. It is clear that the latter is effectively spread over all three of the Sloan filters. From the available comparison stars (see again Table 5.1), C1 has a $g-r$ colour similar to SDSS 1210, C2 is rather red, while C3 is quite blue. However, none of the three come close to the $r-i$ index of SDSS 1210.

The direct result of the above discussion is that the observing blocks suffer from variations in the overall flux level, which means that, in the absence of a flux standard, the photometry cannot be calibrated in absolute terms. Combining all observing blocks into one phase-folded light curve results in significant scattering between points obtained at similar orbital phase, as relative flux variations cannot be accounted for. In turn, this introduces a systematic uncertainty in the determination of the stellar parameters. This effect is more pronounced in the phase-folded light curve produced using C3 as comparison, as illustrated in Figure 5.7.

While it is true that light curves produced with C1 or C2 will suffer less variations, the systematic uncertainties will remain and affect the determination of binary parameters. To gauge the effect of these systematic uncertainties we worked in the following fashion: each observing block has been reduced thrice, using all three comparison stars. The data were then phase-folded together and two phase-folded light curves were produced from each comparison star. One containing all the photometric points (excluding only some isolated and obvious outliers) and one where observing blocks with a large intrinsic scatter were omitted. Thus, we ended up with six phase-folded light curves. A dedicated MCMC optimisation was calculated for each light curve. We will use the following notation when referring to these chains: C1A denotes a light curve produced with comparison star C1 and all data points, C2E denotes a light curve produced with comparison star C2 excluding some of the observing blocks, and so on.

For the determination of stellar and binary properties, q and i are fitted parameters and are obtained directly from the MCMC result, the binary separation is calculated using the fitted parameter $V_{\rm S}$ and Equation 2.11, the two masses $M_{\rm WD}$ and $M_{\rm sec}$ are calculated from q, $V_{\rm S}$ and Equations 2.13 a,b and the two radii $R_{\rm WD}$ and $R_{\rm sec}$ from the fitted parameters $r_{\rm WD}$, $r_{\rm sec}$, $V_{\rm S}$ and

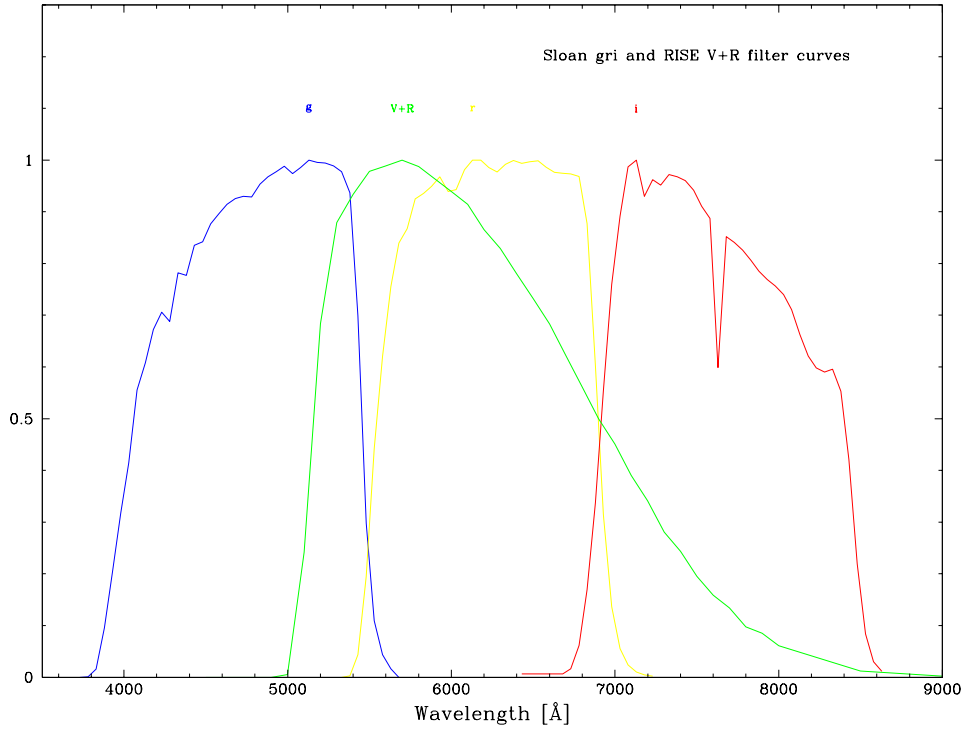

Figure 5.6: The filter curves of Sloan *g* (blue), *r* (yellow) and *i* (red), together with the V+R (green) filter of RISE.

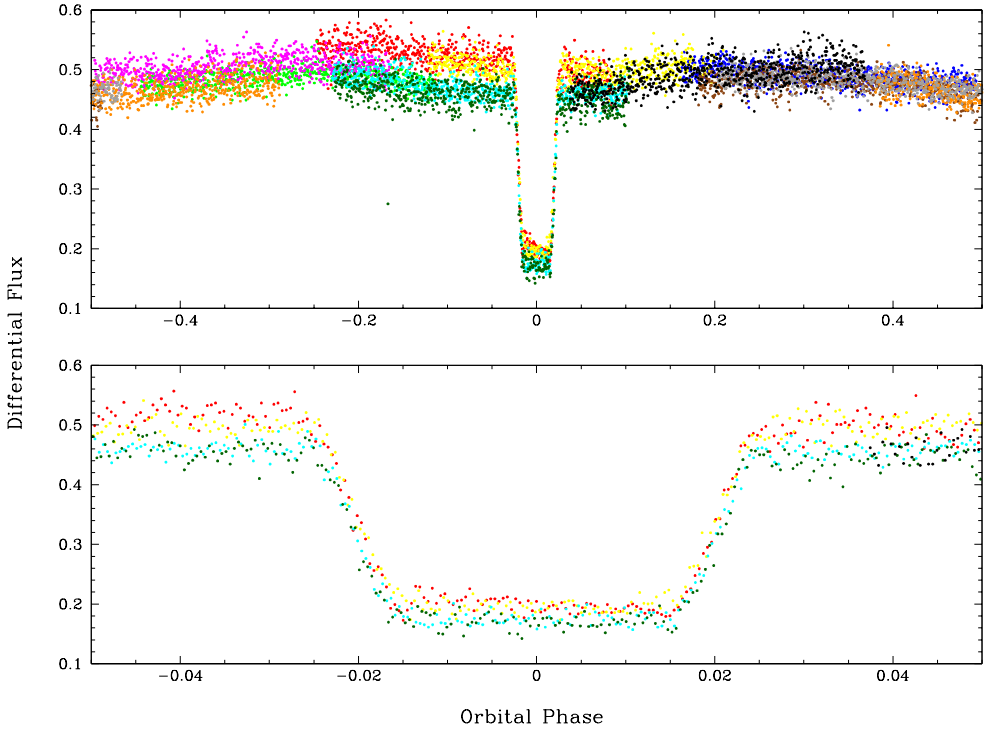

Figure 5.7: Intrinsic scattering of the phase-folded light curve of SDSS 1210, introduced due the combination of various observing blocks and the lack of absolute flux calibration. Each colour corresponds to a different observing block

Equations 2.14 a,b.

5.8 Results

The results of the six MCMC processes are summarised in Table 5.2. The quoted values and errors represent the mean and root mean square (RMS) of the posterior distribution of each parameter. The radius of the secondary, as determined by Equation 2.14b is measured along the line connecting the centres of the two stars and, due to the tidal distortion, its value is larger than the average radius. Therefore, on Table 5.2 we also report the more representative value of the volume-averaged radius $R_{\rm sec,vol.aver.}$.

To illustrate the achieved quality of the fits, we plot models C1A and C1E in Figure 5.8. While the overall quality of the fit is very satisfactory, the model seems to slightly overpredict the flux at the wings of the ellipsoidal modulation. This discrepancy could be data related, due to the intrinsic scattering of points; system related, e.g. due to the presence of starspots affecting the modulation; model related, due to the treatment of stellar temperatures as a black body spectrum, assuming a specific (filter-related) wavelength; or due to a combination of these factors.

With regard to the binary and stellar parameters, the MCMC results indicate the following: as expected for a detached system, the light curves depend very weakly on q and its value is well constrained by the radial velocities. All six chains give inclination angle values just above 79°, consistent with each other within the errors. There is a slight shift upwards, when excluding blocks from the phase-folded light curve.

This behaviour of q and i, together with the tight spectroscopic constraints, mean that the component masses are, more or less, independent of the model used. Thus, the white dwarf in SDSS 1210 has a mass of $M_{\rm WD} = 0.415 \pm 0.010\,{\rm M}_{\odot}$ and the secondary star has a mass of $M_{\rm sec} = 0.158 \pm 0.006\,{\rm M}_{\odot}$.

The quantity most seriously affected from systematics is the white dwarf radius. This is especially evident when considering models C3A and C3E. However, such a discrepancy is expected, since C3 is a considerably blue star and is more susceptible to airmass/colour effects, leading to large intrinsic scattering. The values for $R_{\rm WD}$ as obtained from C1A, C1E, C2A and C2E are consistent within their errors, indicating a systematic uncertainty comparable to the statistical one. This is illustrated in Figure 5.9.

The secondary star radius is affected in a similar, albeit less pronounced, way. All six models lead to values broadly consistent within their statistical errors and a systematic uncertainty of the same order as the statistical one. Figure 5.10 shows the six different values of the volume-averaged secondary star radius overplotted on a M-R relation for MS stars. Taken at face value, the results of the MCMC optimisation indicate that the secondary is $\sim$ 10 percent larger than theoretically predicted. As can be seen in Figure 5.10, this discrepancy drops to $\sim$ 5 percent, if magnetic activity of the secondary is taken into account.

Regarding the gravitational redshift of the white dwarf, the values obtained using the mass and radius measurements from Table 5.2, correcting for the redshift of the secondary star, the difference in transverse Doppler shifts and the potential at the secondary star owing to the white dwarf, are $z_{\rm WD} = 15.9 \pm 0.4\,{\rm km\,s^{-1}}$ from C1E and $z_{\rm WD} = 15.8 \pm 0.4\,{\rm km\,s^{-1}}$ from C2E. Both values are

Table 5.2: Stellar and binary parameters obtained from MCMC optimisation. The quoted errors are statistical uncertainties. See text for details on the notation of models.

Parameter	Model Values	
	C1A	C1E
q	0.380 ± 0.010	0.380 ± 0.010
i [°]	79.05 ± 0.15	79.28 ± 0.15
$M_{\rm WD}$ [$M_\odot$]	0.415 ± 0.010	0.414 ± 0.010
$R_{\rm WD}$ [$R_\odot$]	0.0157 ± 0.0003	0.0159 ± 0.0003
WD $\log g$	7.664 ± 0.015	7.652 ± 0.016
$M_{\rm sec}$ [$M_\odot$]	0.158 ± 0.006	0.157 ± 0.006
$R_{\rm sec}$ [$R_\odot$]	0.217 ± 0.003	0.212 ± 0.003
$R_{\rm sec,vol.aver.}$ [$R_\odot$]	0.202 ± 0.003	0.199 ± 0.003
a [$R_\odot$]	0.871 ± 0.008	0.870 ± 0.008
	C2A	C2E
q	0.381 ± 0.010	0.380 ± 0.010
i [°]	79.03 ± 0.15	79.13 ± 0.15
$M_{\rm WD}$ [$M_\odot$]	0.415 ± 0.010	0.415 ± 0.010
$R_{\rm WD}$ [$R_\odot$]	0.0161 ± 0.0003	0.0159 ± 0.0003
WD $\log g$	7.641 ± 0.015	7.649 ± 0.017
$M_{\rm sec}$ [$M_\odot$]	0.158 ± 0.006	0.158 ± 0.006
$R_{\rm sec}$ [$R_\odot$]	0.217 ± 0.003	0.215 ± 0.003
$R_{\rm sec,vol.aver.}$ [$R_\odot$]	0.203 ± 0.003	0.201 ± 0.003
a [$R_\odot$]	0.871 ± 0.008	0.871 ± 0.008
	C3A	C3E
q	0.378 ± 0.010	0.379 ± 0.010
i [°]	79.36 ± 0.18	79.29 ± 0.16
$M_{\rm WD}$ [$M_\odot$]	0.414 ± 0.010	0.414 ± 0.010
$R_{\rm WD}$ [$R_\odot$]	0.0138 ± 0.0003	0.0150 ± 0.0003
WD $\log g$	7.773 ± 0.023	7.700 ± 0.019
$M_{\rm sec}$ [$M_\odot$]	0.156 ± 0.007	0.157 ± 0.006
$R_{\rm sec}$ [$R_\odot$]	0.210 ± 0.004	0.211 ± 0.003
$R_{\rm sec,vol.aver.}$ [$R_\odot$]	0.197 ± 0.003	0.198 ± 0.003
a [$R_\odot$]	0.869 ± 0.008	0.870 ± 0.008

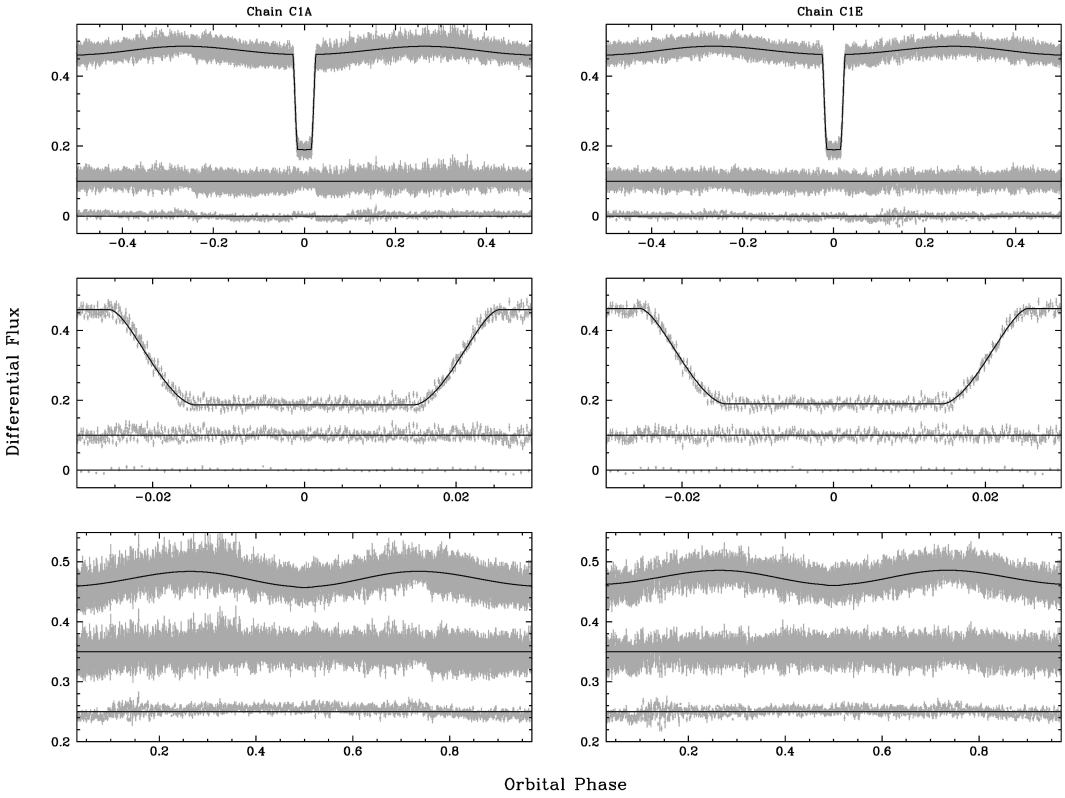

Figure 5.8: Light curve fitting results for models C1A (left) and C1E (right). In each of the six panels we plot the phase-folded light curve with the model superimposed (top trace), the residuals of the fit (middle trace, offset from 0 for clarity) and a binned version of the residuals (bottom trace). Shown are the entire light curve (top panels), a zoom around the eclipse (middle panels) and the out-of-eclipse ellipsoidal modulation (bottom panels).

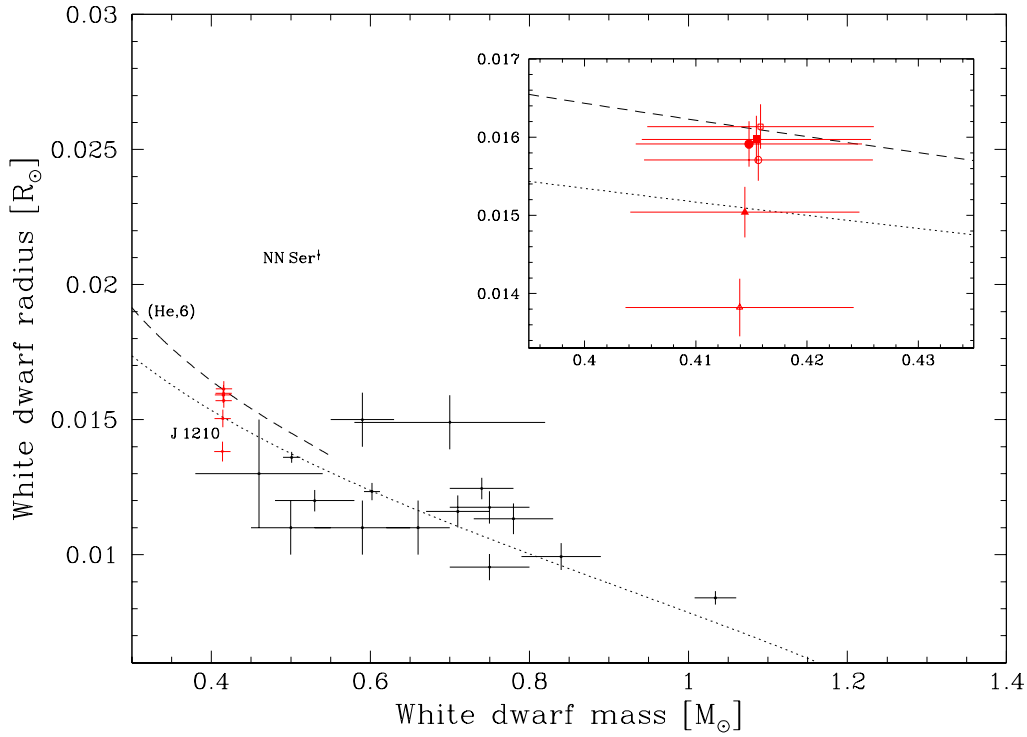

Figure 5.9: Mass-radius plot for white dwarfs. Black points are data from Provencal et al. [1998], Provencal et al. [2002] and Casewell et al. [2009]. The dotted line is the zero-temperature mass-radius relation of Eggleton as quoted in Verbunt & Rappaport [1988]. The dashed line, marked as (He,6) is a M-R relation for a $T_{\rm WD} = 6000$ K, He-core WD, with a hydrogen layer of $M(H)/M_{\rm WD} = 3 \times 10^{-4}$, interpolated from the models of Althaus & Benvenuto [1997]. NN Ser [Parsons et al., 2010a] is marked, indicating the accuracy achieved in eclipsing PCEBs. The results of the six chains for SDSS 1210 are plotted in red. Inset panel: zoom-in on the values of SDSS 1210. The points are C1A: open circle; C1E: filled circle; C2A: open square; C2E: filled square; C3A: open triangle; C3E: filled triangle.

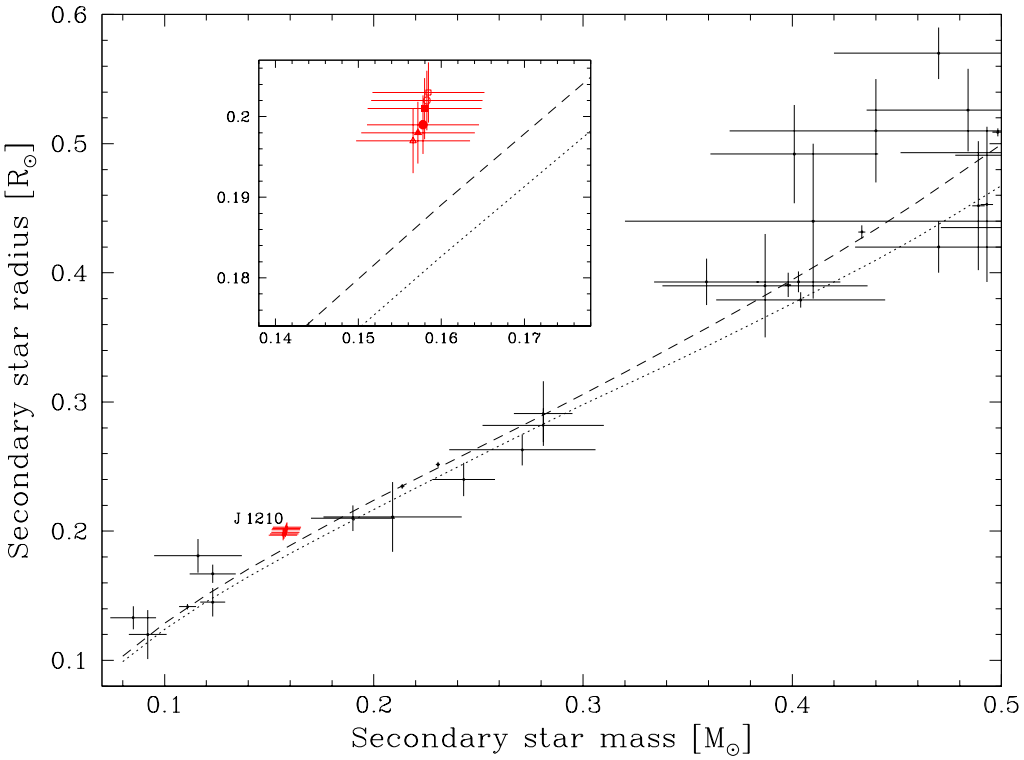

Figure 5.10: Mass-radius plot for low-mass stars. Black points are data from López-Morales [2007] and Beatty et al. [2007], where the masses of single stars were determined using mass-luminosity relations. The dotted line is the 5.0-Gyr isochrone from Baraffe et al. [1998]. The dashed line is a 5.0-Gyr model including effects of magnetic activity from Morales et al. [2010]. The results of the six chains for the volume-averaged radius of the secondary in SDSS 1210 are plotted in red. Inset panel: zoom-in on the values of SDSS 1210. The points are C1A: open circle; C1E: filled circle; C2A: open square; C2E: filled square; C3A: open triangle; C3E: filled triangle.

consistent within $\sim 2\sigma$ with the spectroscopic value of $z_{WD,spec} = 11.9 \pm 1.7\,km\,s^{-1}$.

5.9 Past and future evolution

Following the exact same procedure as described in Section 4.9 we have reconstructed the past and predicted the future evolution of SDSS 1210. Given the low mass of the secondary, the only angular momentum loss mechanism for SDSS 1210 is gravitational radiation. Based on the temperature and the mass of the white dwarf we interpolate the cooling tracks of Althaus & Benvenuto [1997] and obtain a cooling age of $t_{cool} = 3.54\,Gyr$. This corresponds to the time that passed since the binary left the common-envelope. We calculate the period it had when it left the common envelope to be $P_{CE} = 4.24h$. Following the same method as in Zorotovic et al. [2010] and based on their results we reconstructed the initial parameters of the binary using a common-envelope efficiency of $\alpha_{CE} = 0.25$ and the same fraction of internal energy [see Zorotovic et al., 2010, for more details]. We found an initial mass of $M_{prog} = 1.33\,M_\odot$ for the progenitor of the white dwarf, which filled its Roche lobe when its radius was $R_{prog} = 91.31\,R_\odot$. At that point, the orbital separation was $a = 162.67\,R_\odot$, and the age of the system was $t_{sys} = 4.44\,Gyr$, since it was formed. Using the radius of the secondary[2] we calculate that the system will reach a semi-detached configuration and become a cataclysmic variable (CV) at an orbital period of $P_{sd} = 2.01\,h$ in $t_{sd} = 1.51\,Gyr$.

Given that the current P_{orb} places SDSS 1210 right at the upper edge of the CV orbital period gap, and that the calculated P_{sd}, when SDSS 1210 will start mass-transfer, is right at the lower edge of the period gap, we are tempted to speculate whether SDSS 1210 is in fact a detached CV entering (or just having entered) the period gap. Davis et al. [2008] have shown that a large number of detached WD+MS binaries with orbital periods between 2-3 hours are in fact CVs that have switched off mass-transfer and are crossing the period gap. This could in principle explain the apparently over-sized secondary in SDSS 1210, as expected from the disrupted magnetic braking theory [e.g. Rappaport et al., 1983]. However, the temperature of the WD in SDSS 1210 seems to be uncomfortably low for a WD that has recently stopped accreting [Townsley & Gänsicke, 2009].

5.10 Discussion

Comparing the parameter determinations of SDSS 1210 with the four systems presented in Chapter 4, it becomes evident how one additional piece of information (in this case K_{WD}) can vastly improve the accuracy of measurements by providing tight constraints on the parameter space. The masses of both components in SDSS 1210 have been determined independent of any theoretical mass-radius relation, while the radii suffer from systematic uncertainties in our data.

With a mass of $M_{WD} = 0.415 \pm 0.010\,M_\odot$ and a temperature of $T_{WD} \sim 6000\,K$, the DAZ white dwarf in SDSS 1210 pushes the boundaries in a hitherto unexplored region of the WD parameter space. The M-R results from the four Chains C1 and C2 are consistent with a He-core WD, assuming a hydrogen layer of $M(H)/M_{WD} = 3 \times 10^{-4}$. However, due to lack of observational con-

[2] We assume a representative value of $R_{sec,vol.aver.} = 0.200\,R_\odot$ for the volume-averaged radius of the secondary

straints for the H-layer thickness and the uncertainty in the radii, we will defer identifying the WD as a definite He-core and simply emphasise the strong candidacy.

The secondary star, with a mass of $M_{\rm sec} = 0.158 \pm 0.006\,{\rm M}_{\odot}$, illustrates once more the excellent opportunity that PCEBs give us, for testing and calibrating the M-R relations of low-mass stars. Taking the radius measurements at face value, the secondary star seems to be $\sim$ 10 percent larger than the theoretical values, although this drops to $\sim$ 5 percent, if magnetic activity is taken into consideration. Kraus et al. [2011] found that low-mass stars in short period binaries appear to be overinflated (although their analysis was restricted to $M > 0.3\,{\rm M}_{\odot}$), which seems to be the case for SDSS 1210. We should note however, that the mass and radius of the secondary star in the eclipsing PCEB NN Ser (with $M_{\rm sec} = 0.111 \pm 0.004\,{\rm M}_{\odot}$ and comparable orbital period to SDSS 1210) is consistent with theoretical M-R predictions, if the irradiation by the hot WD primary is taken into account [Parsons et al., 2010a].

We have speculated whether SDSS 1210 is in fact a detached CV entering the period gap, which could explain the large radius of the secondary. This hypothesis could be tested by measuring the rotational velocity of the white dwarf. This can be achieved through high-resolution spectroscopy of the Fe I absorption lines in the WD photosphere [see e.g. Tappert et al., 2011].

The parameter determinations of SDSS 1210 could benefit from longer duration observations, spanning more than one orbital cycle, preferentially in the SDSS-filters and using a standard star for absolute flux calibration. In this way, the systematic uncertainties affecting our data could be reduced.

Chapter 6

HS 2325+8205 - an ideal laboratory for accretion disc physics

6.1 Introduction

The post-common-envelope binaries presented in Chapters 4 and 5 will eventually evolve into the semi-detached, mass-transferring configuration of a cataclysmic variable. The presence of an accretion disc, as a result of mass-transfer, makes any analysis of such systems significantly more complicated. In this Chapter an eclipsing dwarf nova above the period gap will be presented. The system is an example where, despite the presence of an eclipse, high signal-to-noise ratio data are needed to obtain stellar parameters.

6.2 Target information

The system under study, HS 2325+8205 (RA = 23:26:50.4, Dec = +82:22:12, henceforth HS 2325), was one of the systems spectroscopically identified as a CV candidate within the HQS (Section 2.2.2). Interestingly, it is possible that this was not the first time HS 2325 attracted attention, as Morgenroth [1936] mentioned short-term variability of HS 2325, which correspondingly was included in the New Catalogue of Suspected Variable Stars as NSV 14581 (though with rather uncertain coordinates). Information on the comparison stars used in photometry is provided in Table 6.1.

6.3 Observations and data reduction

The observational data set and information on the data reduction procedures, both for data collected at professional telescopes and for those collected using small aperture telescopes, are summarised in Chapter 3. Figure 6.1 shows three sample light curves, during the rise to outburst, in an intermediate state and in quiescence, respectively. HS 2325 has been found to vary in brightness between $\sim 17^{\rm th}$ and $\sim 14^{\rm th}$ magnitude. In addition to eclipses, the light curve of HS 2325 displays additional features: short-term, random, out-of-eclipse variations, usually termed "flickering" [e.g. Bruch, 1992,

Table 6.1: The four comparison stars employed in the photometry of HS 2325. Their USNO-A2.0 and GSC2.3 identifiers are given, along with *B*, *V* and *R* magnitudes. The *B* and *R* magnitudes are taken from the USNO, and *V* from the GSC catalogue.

Star	USNO ID	GSC ID	*B*	*V*	*R*
C1	1650-02769321	N0TQ000055	15.40	13.81	13.60
C2	1650-02774158	N0TQ000054	14.80	14.05	14.30
C3	1650-02775103	N0TQ009686	15.60	14.90	14.80
C4	1650-02770392	N0TQ009847	16.70	16.44	16.30

2000], and an "orbital hump", a brightening before the start of the eclipse attributed to the bright spot coming into view [e.g. Krzeminski, 1965].

The mean quiescent spectrum is shown in Figure 6.2. The flux level of the observed spectrum implied a *V*-magnitude near 17.0, subject to the calibration uncertainties.

6.4 Orbital Period and Ephemeris

The orbital ephemeris of HS 2325 was determined from an analysis of the mid-eclipse times, which were measured using the mirroring method. The resulting ephemeris was

$$T_0(\mathrm{HJD}) = 2452888.42554(3) + 0.194334535(3)\,\mathrm{E} \tag{6.1}$$

with mid-eclipse times calculated on a UTC timescale. Equation 6.1 gives an orbital period of $P_{\mathrm{orb}} = 279.841731(5)\,\mathrm{min}$ for HS 2325, with numbers in parenthesis indicating the error on the last digit. The mid-eclipse times are listed in the Appendix.

6.5 Secondary spectral type and radial velocities analysis

As is typical for quiescent dwarf novae, the Balmer lines in emission are the most prominent features in the spectrum of HS 2325 with equivalent widths of $\simeq 30$ and $\simeq 54$ Å for Hβ and Hα respectively. He I emission is detected at 4921, 5015, and 5876 Å, and Fe II λ5169 as well. The absorption bands of an M-dwarf companion are conspicuous. To quantify the M dwarf contribution, archival spectra of M dwarfs taken with the same instrumental setup were subtracted. The archival spectra were classified by Boeshaar [1976]. The spectral type and scaling were varied until the M-dwarf features were cancelled as well as possible. The lower two traces in Figure 6.2 show the best decomposition. From this exercise, the estimated spectral type of the companion is M3.0 $\pm$ 0.75 subclasses, and its flux corresponds to $V = 19.0 \pm 0.4$ (external error, including calibration uncertainties).

Radial velocities of the Hα emission line were measured using a double-Gaussian convolution method outlined by Schneider & Young [1980]; the centres of the Gaussians were separated by $1280\,\mathrm{km\,s^{-1}}$, and each individual Gaussian had a FWHM of $270\,\mathrm{km\,s^{-1}}$, comparable to the spectral resolution. This emphasised the outer wings of the line profile. To measure the velocity of the M-

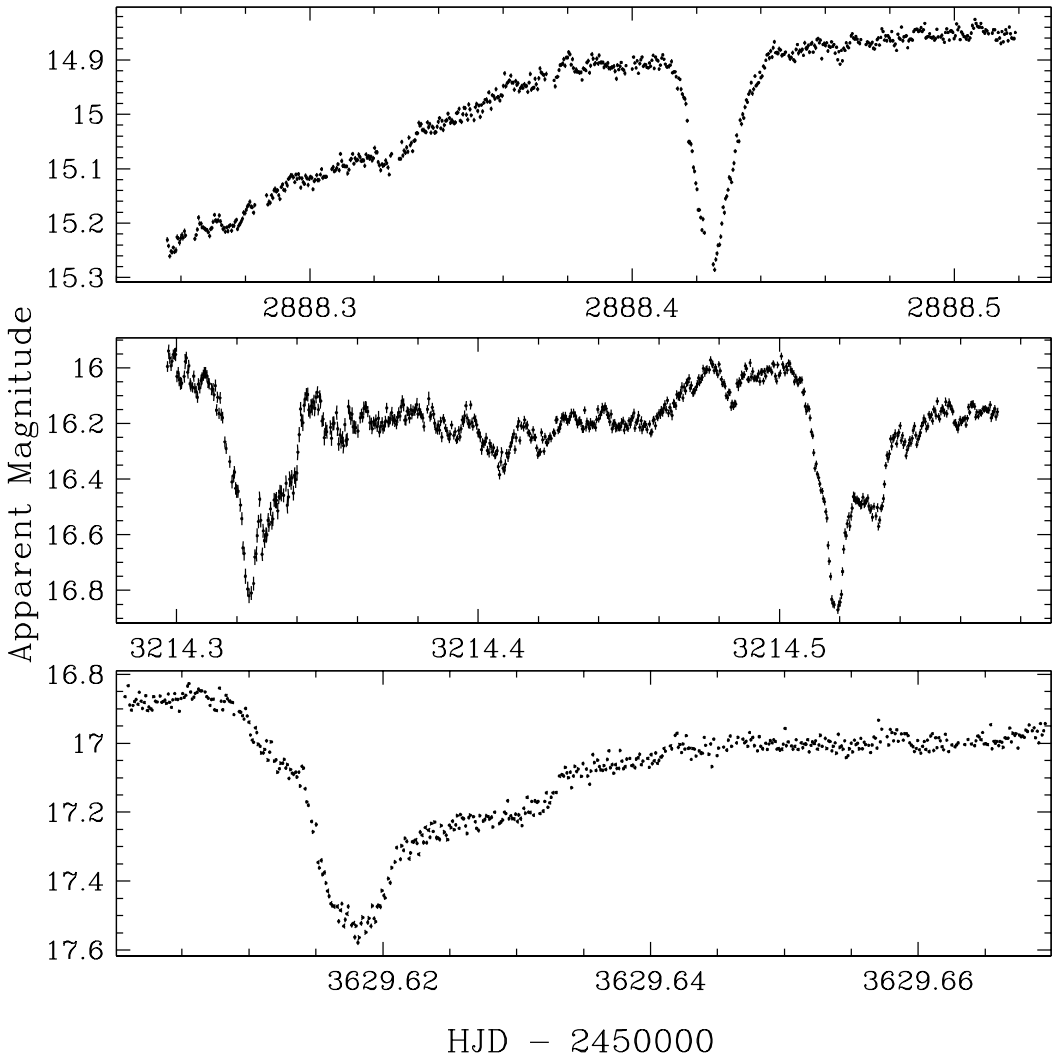

Figure 6.1: Sample light curves of HS 2325. Top panel: filterless KY observations, from September 5, 2003, with the system on the rise to outburst. Middle panel: filterless KY observations, from July 27, 2004, with the system in an intermediate state, where more than one orbital cycle was covered. Bottom panel: filterless NOT observations, from September 15, 2005, with the system in quiescence. The difference in the eclipse profiles, between the three light curves, even during one night, is evident.

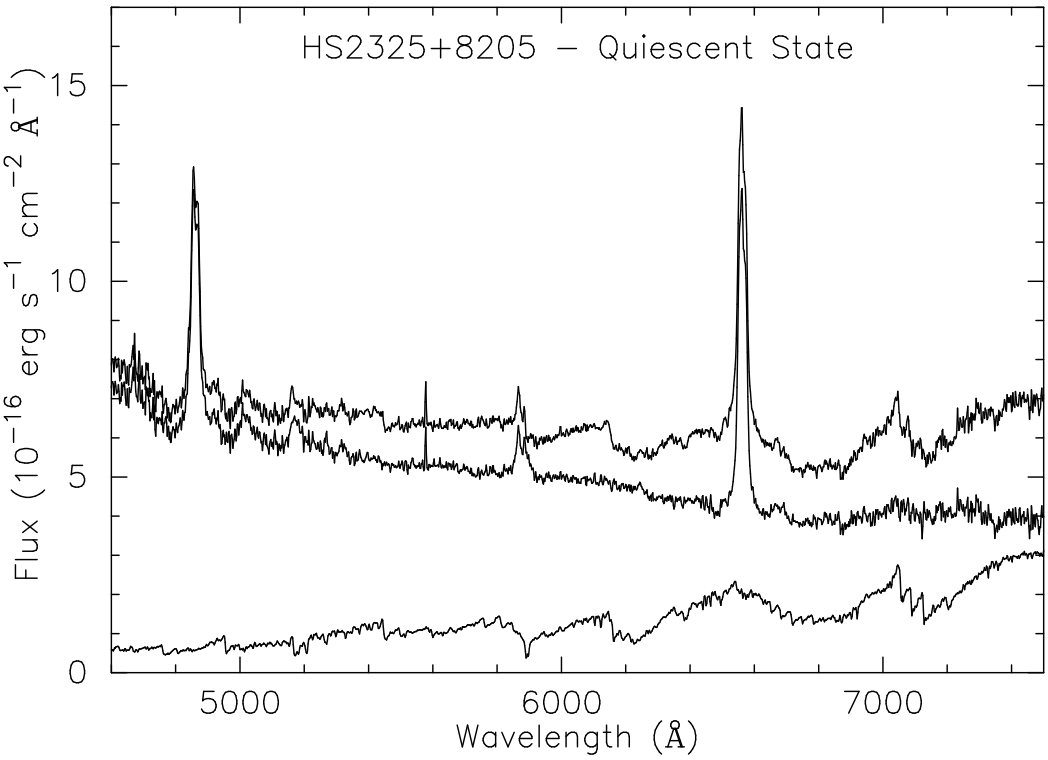

Figure 6.2: (Top trace): Mean quiescent spectrum of HS 2325. (Bottom trace): A library spectrum of the M3 dwarf Gliese 436, scaled so that it has an apparent V-band magnitude of $\sim$ 19.0. (Middle trace): The HS 2325 spectrum minus the scaled M-dwarf.

Table 6.2: Fits to the absorption and emission radial velocities. K is the semi-amplitude, N the number of different measurements and σ is an estimate in the uncertainty in an individual data point (the RMS residual around the best fit). Numbers in square brackets indicate that the corresponding parameter was held fixed during the fit.

Data set	T_0^a	$P_{\rm orb}$[d]	K [km s^{-1}]	γ [km s^{-1}]	N	σ [km s^{-1}]
Absorption	[3168.46177]	[0.19433453]	237(28)	$-19(20)$	24	71
Hα emission	3625.8335(18)	[0.19433453]	145(9)	$-42(6)$	50	32

[a] Blue-to-red crossing, HJD $-$ 2450000.

dwarf component, the cross-correlation program `rvsao` was used, written by Kurtz & Mink [1998]. For the template, a velocity-compensated composite M-dwarf spectrum was used, composed by summing the spectra of a large number of M dwarfs for which Marcy et al. [1987] tabulate precise velocities. The cross-correlation region was from 6000 to 6500 Å; this was chosen to include some strong atomic and TiO features, while avoiding emission lines. Not all the spectra gave usable cross-correlation velocities; we limited the analysis to those for which the formal velocity error was less than 35 km s^{-1}.

Table 6.2 lists fits to the radial velocities, of the form $v(t) = \gamma + K \sin[(t - T_0)/P_{\rm orb}]$. The orbital period $P_{\rm orb}$ was held fixed to the value derived from eclipses. Because of the modest number of absorption velocities and their limited phase coverage, and because the absorption should trace the motion of the secondary star fairly well, we fixed T_0 to the mid-eclipse ephemeris when fitting the absorption velocities. Figure 6.3 shows the emission and absorption velocities as a function of orbital phase.

6.6 Distance

The distance to HS 2325 can be estimated using the secondary star's contribution to the spectrum and our knowledge of the orbital period $P_{\rm orb}$.

For a secondary star of mass $M_{\rm sec}$ at a fixed $P_{\rm orb}$, the Roche lobe radius R_2 is proportional to ${M_{\rm sec}}^{1/3}$, and is almost independent of the primary mass $M_{\rm WD}$ [Beuermann et al., 1998]. We do not know $M_{\rm sec}$, but we can estimate it using evolutionary models tabulated by Baraffe & Kolb [2000]; these suggest that the secondary is between 0.23 M$_\odot$ and 0.56 M$_\odot$. At this $P_{\rm orb}$, Equation 1 of Beuermann et al. [1998] then implies $R_2 = 0.47 \pm 0.07$ R$_\odot$. Beuermann et al. [1999] tabulate absolute magnitudes and radii for late type dwarfs as a function of spectral class, which implies a surface brightness for each star. In the range of spectral type we see here, these correspond to $M_V = 8.8 \pm 0.7$ for a 1R$_\odot$ star, where the uncertainty includes both the spectral type uncertainty and the scatter among the tabulated points. Combining this with the radius yields an estimate of $M_V = 10.4 \pm 0.8$ for the secondary.

The Galactic coordinates of HS 2325 are $(l, b) = (120^\circ, 20^\circ)$; at this location, Schlegel et al. [1998] estimate $E(B-V) = 0.19$ to the edge of the Galaxy. Assuming that our object lies outside most of the dust, and taking the M-dwarf contribution to the spectrum as $V = 19.0 \pm 0.4$, then yields

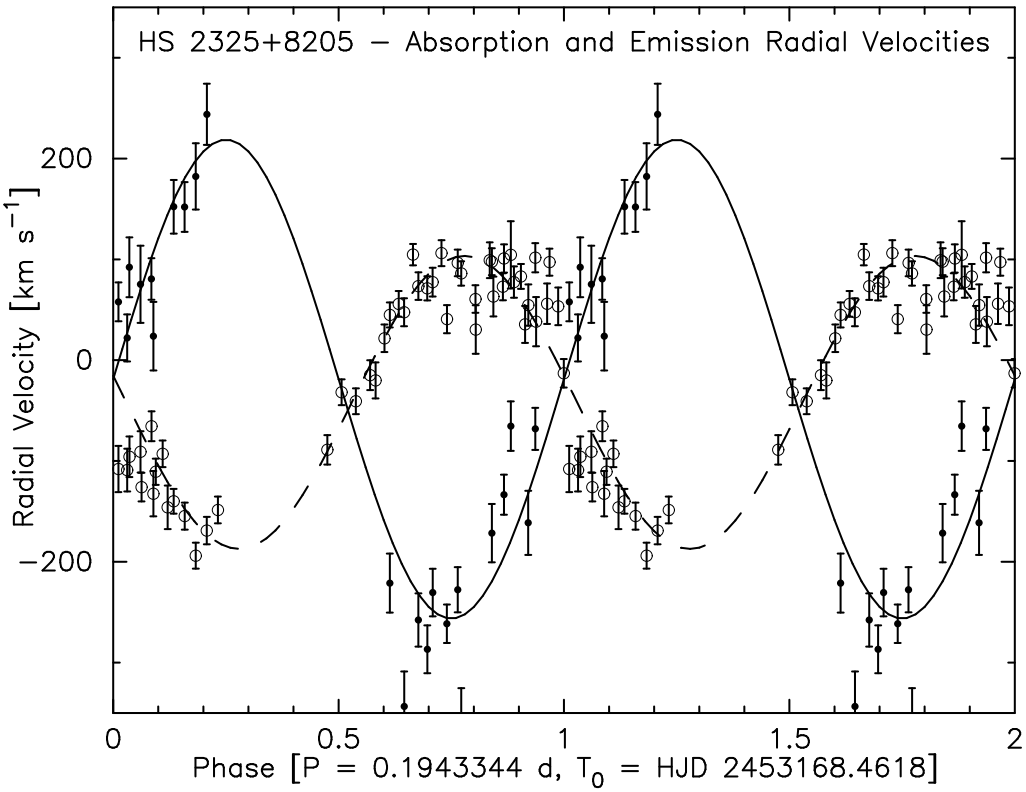

Figure 6.3: Radial velocities of HS 2325 in the quiescent state, plotted as a function of orbital phase. The open circles show the Hα emission and their formal uncertainties, and the solid dots show the cross-correlation velocities of the M dwarf. There is a gap in coverage at $0.25 < \phi < 0.42$, and only some of the spectra yielded usable absorption velocities. The dashed curve shows the best fit to the emission velocities, with $P_{\rm orb}$ fixed but T_0, K, and γ allowed to vary. For the absorption velocity fit (solid line), T_0 was held fixed to the eclipse phase, K and γ were adjusted.

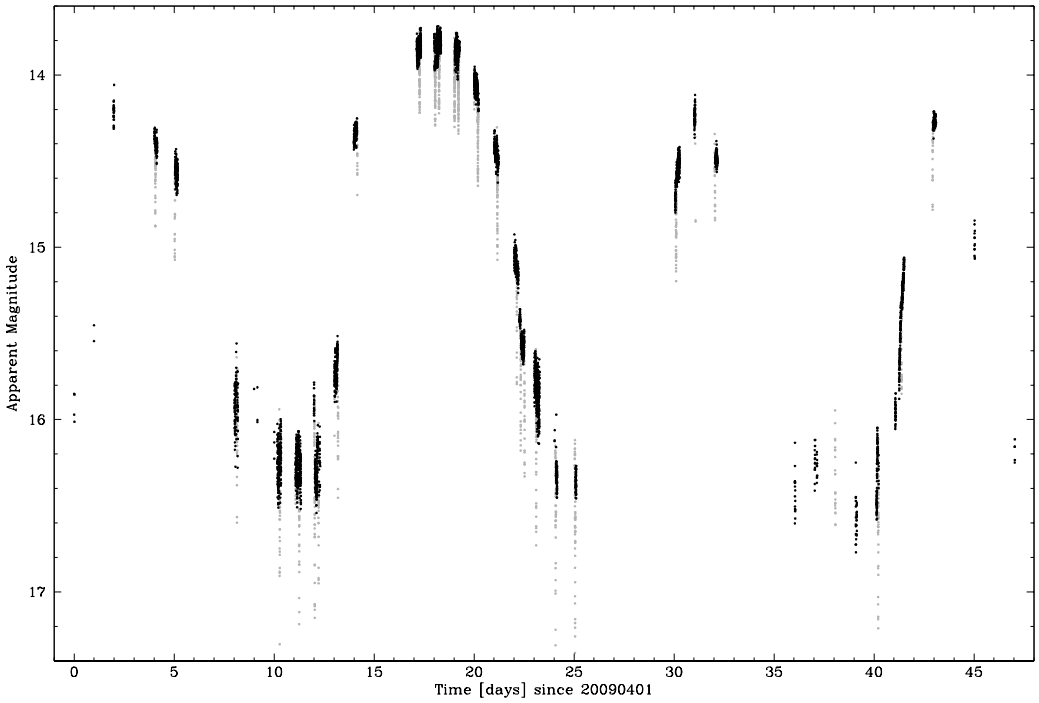

Figure 6.4: The result of the outburst monitoring campaign for HS 2325. Four outbursts have been recorded in 50 days. Points in light grey indicate the system being in eclipse

an extinction-corrected distance modulus of $(m-M)_0 = 8.0 \pm 0.9$, corresponding to a distance of $400(+200,-140)$ pc. Note carefully that this estimate makes no assumption that the secondary follows a main-sequence mass-radius relation; it assumes only that the secondary's spectral type is a reliable guide to its surface brightness, and that it fills its Roche lobe.

6.7 Outburst behaviour

HS 2325 was monitored intensively for about 50 days, starting from the 1st of April 2009 using small aperture telescopes. Depending on the availability of observers and weather conditions, the observing runs spanned a wide range, from nights with only a few points, to nights with time-series photometry for more than one orbital cycle and from multiple observers. The resulting light curve is shown in Figure 6.4.

Four outbursts have been recorded during this period, indicating a recurrence time of $\sim 12-14$ d. Prominent is a "long" outburst, lasting $\sim 11-12$ d. It is difficult to judge whether the rise to and the decline from outburst are asymmetric. This "long" outburst seems to be followed by a "short" outburst, for which we only have data points around the assumed maximum. This could be a hint towards a bimodal distribution of the duration of the outbursts, observed in many dwarf novae [see e.g. Szkody & Mattei, 1984; Ak et al., 2002]. Further observations are required to establish a more accurate recurrence time and to check the consistency of the "long" and "short" outburst succession.

We have inspected v7.12 (2009) of the Ritter and Kolb catalogue [Ritter & Kolb, 2003] and compiled a list of U Gem-type dwarf novae (UG) and Z Cam-type stars (ZC) (see again Section 1.3.6) that are found in the range $4\,\mathrm{h} < P_{\mathrm{orb}} < 5\,\mathrm{h}$. Only systems with confirmed UG/ZC status and with a quoted outburst recurrence period were considered. This left us with a list of 22 systems (out of the 39 listed in R&K in this P_{orb} range). ZC systems dominate the short end of the outburst recurrence period distribution, while UG systems tend to have longer intervals between outbursts. Our inferred outburst recurrence period of $\sim 12-14\,\mathrm{d}$ for HS 2325 places the system in the ZC region. However, as there has been no recorded standstill for HS 2325 (the hallmark of ZC systems), its identification as either a UG or a ZC remains ambiguous.

6.8 Eclipse morphology

In a (non-magnetic) eclipsing CV the shape of the eclipse depends on which of the white dwarf, bright spot and accretion disk (or combination) is being eclipsed and also on which of these components is the dominant light source for a given brightness level. If the inclination of the system is sufficiently high, all three components can be eclipsed, resulting in a complex eclipse, such as the one in Z Cha [e.g. Wood et al., 1986]. An example for lower inclination is U Gem, where only the bright spot and the accretion disc are eclipsed, resulting in a different profile [e.g. Zhang & Robinson, 1987].

Figure 6.5 displays a close-up of different eclipses of HS 2325. The eclipses in the bright state exhibit a symmetric V-shape, typical for an accretion disc-dominated system. During quiescence the eclipse morphology becomes more complicated and reveals breaks in slope, indicative of different components coming in and out of eclipse. The overall behaviour is reminiscent of that of OY Car [see e.g. Rutten et al., 1992, their Fig. 2a-f] and EM Cyg [Mumford & Krzeminski, 1969].

The eclipses are shallow with a typical depth of ~ 0.8 magnitudes, changing to ~ 0.4 around the outburst maximum. It is interesting to note that the eclipse depth remains almost constant, while the system is rising in brightness, and that the two available eclipses near quiescence (Run IDs 13 and 14) seem to be slightly shallower than those in an intermediate level (e.g. run IDs 03 and 05).

A consistent feature seen in the eclipse profiles is the break in slope near orbital phase ~ 0.08, which can be explained as the egress of the bright spot (for comparison, see Z Cha, Wood et al. 1986, and OY Car, Wood et al. 1989). The corresponding ingress phase of the bright spot is difficult to discern, but it could be situated between phases -0.04 and -0.03. The contact points (ingress and/or egress) for the white dwarf cannot be unambiguously determined.

The nature of the deepest part of the eclipse, between phases ~ -0.02 to ~ 0.02, is intriguing. Its depth follows the trend of the eclipses, varying between 0.2 - 0.4 magnitudes, with a typical depth of ~ 0.3 magnitudes. Its U-shaped, symmetrical shape is puzzling - both in high inclination systems (where the WD and the bright spot are fully eclipsed) and in systems with a lower inclination, where the WD is not eclipsed, but the bright spot is, the eclipse is expected to be "flat-bottomed" (while the WD and/or bright spot are fully occulted) and/or display significant asymmetries (see Savoury et al. [2011] for various examples of eclipse profiles). A symmetric, U-shape like the one observed in HS 2325 could be attributed to a partial eclipse of the WD (see again the light curve of SDSS 1435in Chapter 3). A further complication is the fact that the depth of this

feature remains roughly constant, independent of the brightness of the accretion disc.

It is uncertain whether the eclipse profiles in quiescence are a result of poor time resolution/quality of our data or there is an underlying physical reason.

6.9 Estimates of the binary properties

The standard work-flow in an eclipsing CV [see e.g. Wood et al., 1986, 1989, 1992; Littlefair et al., 2006a,b] involves the identification of "contact points", i.e. the exact moments of the ingress and egress of the white dwarf, the bright spot and the accretion disc. These contact points (and the corresponding phase-widths of eclipse) are used to place firm (geometrical) constraints on the mass ratio q and the inclination angle i [e.g. Bailey, 1979; Horne, 1985] and deduce information about the size of the bright spot and the accretion disc. Flickering can complicate the situation, making the contact phases difficult to discern. A technique often employed to tackle this problem is averaging together many light curves to drive down the intrinsic scattering introduced by flickering [see e.g. Copperwheat et al., 2010, for the case of IP Peg].

Although breaks in slope are seen in the light curve of HS 2325, the available data set is not of sufficient quality and time-resolution to unambiguously identify the various contact points, taking the strong effects of flickering into account as well. The constant brightness variations in our ensemble of light curves make any averaging attempt difficult. Hence, it remains unclear whether the white dwarf in HS 2325 is fully or partially eclipsed or if it is not eclipsed at all.

We can, however, find a relation between q and i by determining the size of the accretion disc, following a method similar to that of Dhillon et al. [1991]. The phase half-width of eclipse at maximum intensity (essentially timing the first and last contacts of eclipse and dividing by two) $\Delta\phi$ is related to the disc radius through

$$\frac{R_{\rm D}}{a} = \sin i \sin\left(2\pi\Delta\phi\right) - \frac{R_{\rm C}}{a} \tag{6.2}$$

where $R_{\rm C}$ is the half-cord of the secondary and is given by

$$\frac{R_{\rm C}}{a} = \sqrt{\left(\frac{R_2}{a}\right)^2 - \cos^2 i} \tag{6.3}$$

[see e.g. Sulkanen et al., 1981]. The volume radius R_2/a is given in Equation 1.2.

The distance between the primary and the inner Lagrangian point L_1 is given by

$$\left(\frac{R_{L_1}}{a}\right) = \left(1.0015 + q^{0.4056}\right)^{-1} \tag{6.4}$$

[Silber, 1992], so that the disc radius can be expressed in units of L_1 simply by dividing Equations 6.2 and 6.4.

The mean phase half-width of eclipse at maximum intensity was determined by eye, from light curves around outburst maximum when the disc is expected to be at its largest, to be $\Delta\phi = 0.1 \pm 0.02$. The large error is due to the fact that the exact beginning and end of the eclipse are uncertain because of flickering, and because in some cases there is a distinct slope in the out of

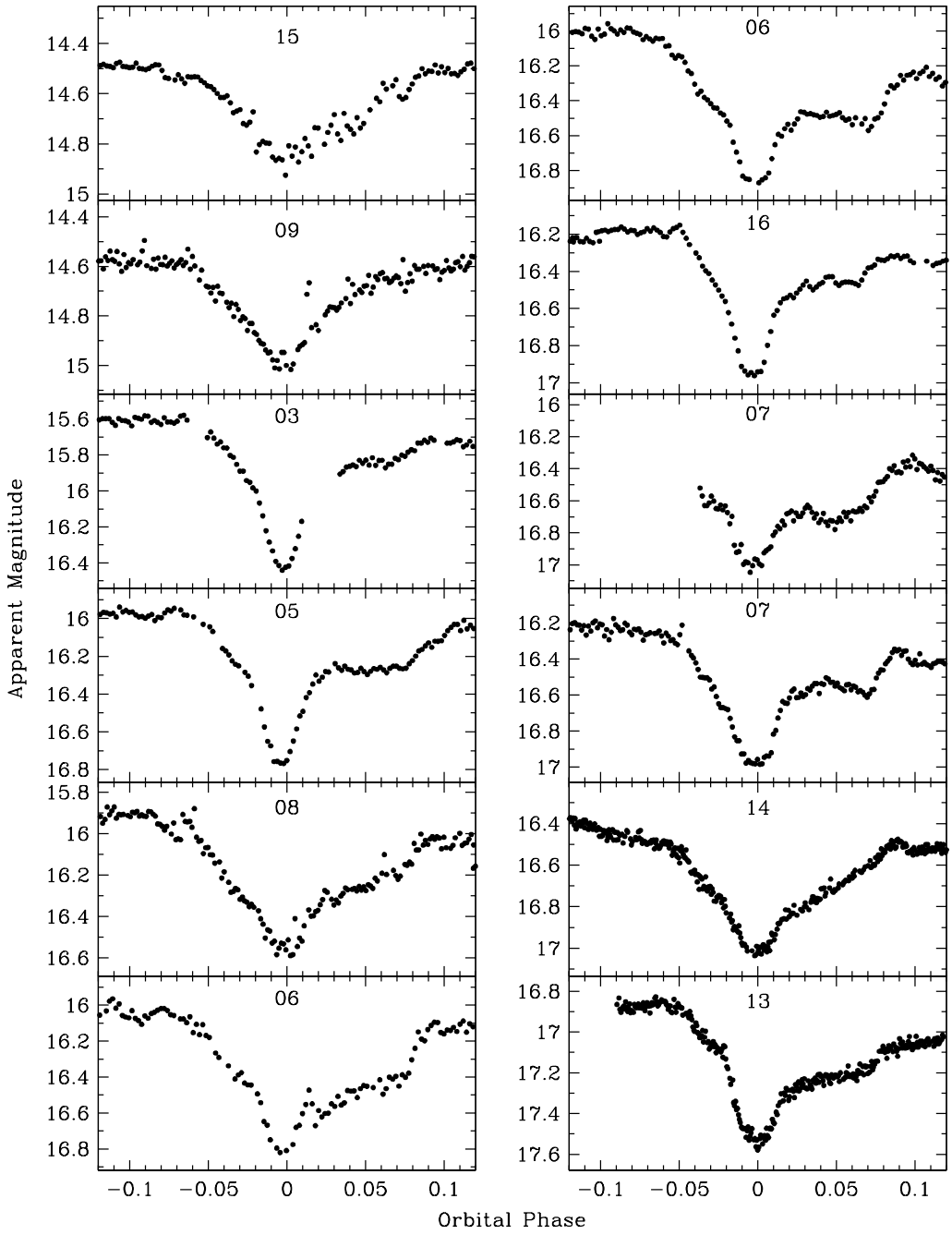

Figure 6.5: Eclipse profiles of HS 2325, sorted by out-of-eclipse brightness (from top to bottom and from left to right; top left being the brightest, bottom right the faintest). The light curves have been phase-folded using the ephemeris given in Equation 6.1 and are shown for the phase interval $-0.12 < \phi < 0.12$. The numbers in each panel correspond to the run ID listed in Table 3.1.

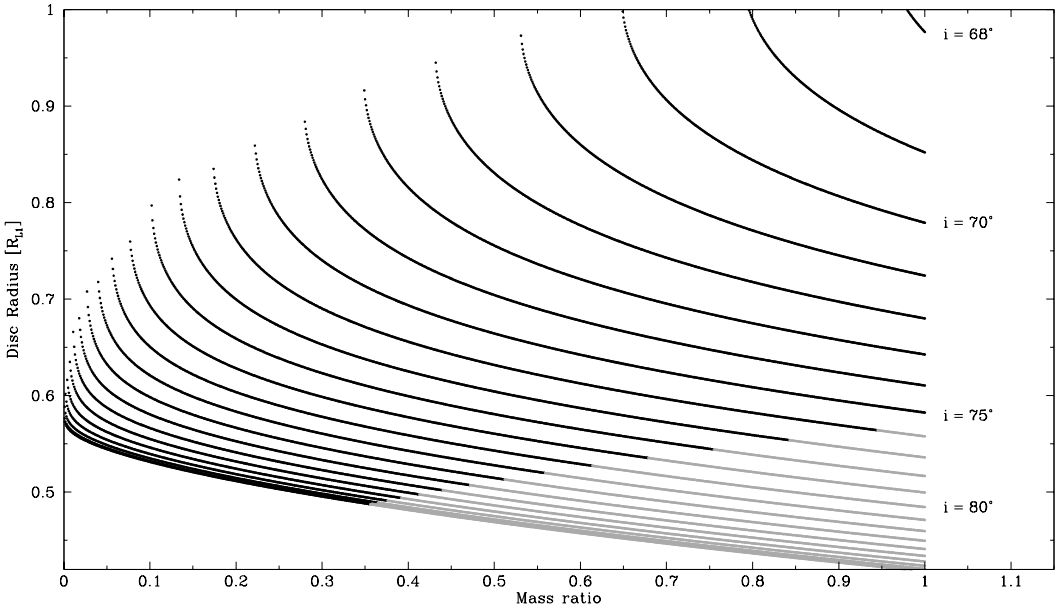

Figure 6.6: Accretion disc radius, in units of $[L_1]$, as a function of q and i. The curves are bound below - grey coloured - by the requirement of a partial disc eclipse.

eclipse part of the light curve, as the system rises in outburst (see e.g. Figure 6.1, top panel).

Figure 6.6 shows the disc radius calculated for $0 \leq q \leq 1$ and various inclination angles using the above set of equations. The curves are bound above by the requirement that $R_{\rm D} \leq L_1$ and below by the requirement that $R_{\rm D} > R_{\rm C}$ for a partial disc eclipse, which is shown by the change in line colour. This allows us to place a strict lower limit for the inclination angle to be $i_{\rm min} = 68^{\circ}$. However, the upper limit of i and the possible values of q remain unconstrained.

Using the mass function, Equation 2.6b, we can transform a given (q,i) pair to a given $(M_{\rm WD}, M_{\rm sec})$ pair. Figure 6.7 shows Equation 2.6b calculated for $i_{\rm min} = 68^{\circ}$ and $i_{\rm max} = 90^{\circ}$, over a wide range in secondary mass, $0.1 \leq M_{\rm sec}[{\rm M}_{\odot}] \leq 0.6$. Allowed $(M_{\rm WD}, M_{\rm sec})$ pairs are located between the two dash-dot curves. We can further narrow down the parameter space, by making two assumptions:

1. The secondary follows the mass-period relation of Smith & Dhillon [1998], which yields $M_{\rm sec} = 0.47 \pm 0.07\,{\rm M}_{\odot}$ (Figure 6.7, dashed, horizontal lines)
2. The radial velocity variation of the emission lines tracks the motion of the white dwarf, so $K_{\rm em} = K_{\rm WD} = 145 \pm 9\,{\rm km\,s^{-1}}$ and, therefore, $q_{\rm spec} = K_{\rm WD}/K_{\rm sec} = 0.61 \pm 0.08$ (Figure 6.7, dotted lines).

In order to gauge how realistic these assumptions are, we turn to the statistical properties of the known CV population.

For the former assumption, the spectral type of the secondary (M3.0 $\pm$ 0.75) suggests $M_{\rm sec} = 0.23 - 0.56\,{\rm M}_{\odot}$, adopting the evolutionary models of Baraffe & Kolb [2000]. The mass-period relation of Smith & Dhillon [1998] gives $M_{\rm sec} = 0.47 \pm 0.07\,{\rm M}_{\odot}$, while the semi-empirical

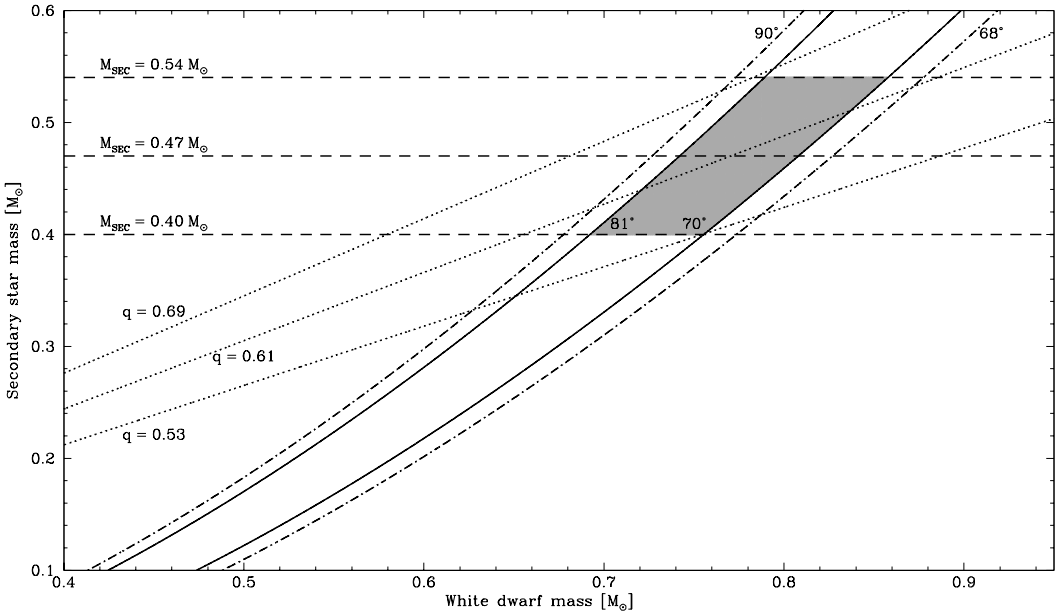

Figure 6.7: Constraints on the masses of the binary components. Solid curves: Equation 2.6b plotted for $i = 68^\circ, 90^\circ$ (dash-dot curves) and $i = 70^\circ, 81^\circ$ (solid curves). Dashed lines: constraints on the secondary mass, assuming the mass-period relation of Smith & Dhillon [1998]. Dotted lines: constraints on the mass ratio q assuming $K_{\rm em} = K_{\rm WD}$. Shaded in grey is the allowed parameter space, under the previous assumptions (see text for details).

donor star sequence of Knigge [2006] gives $M_{\rm sec} = 0.43\,{\rm M}_\odot$. In both cases, the mass of the secondary is at the high-mass end of the range estimated from the spectral type, in agreement with the results of Beuermann et al. [1998], that CV secondaries above the gap are generally cooler than ZAMS stars with the same mean mass density.

The latter assumption is a frequently adopted one in CV research, but it must be viewed with a certain amount of caution [see e.g. Shafter, 1983; Thorstensen, 2000]. An encouraging fact in the case of HS 2325 is that the phasing of the emission lines is consistent with the eclipse ephemeris. Several studies regarding the mass of the white dwarf primaries in CVs above the period gap, point towards a canonical value of $\sim 0.8\,{\rm M}_\odot$ ($< M_{\rm WD} >= 0.81 \pm 0.04\,{\rm M}_\odot$ Webbink 1990; $< M_{\rm WD} > = 0.80 \pm 0.22\,{\rm M}_\odot$, Smith & Dhillon 1998; $< M_{\rm WD} >= 0.75 \pm 0.16\,{\rm M}_\odot$, Knigge 2006; $< M_{\rm WD} > = 0.78 \pm 0.19\,{\rm M}_\odot$, Southworth et al. 2009). Adopting $< M_{\rm WD} >= 0.78 \pm 0.19\,{\rm M}_\odot$ and $M_{\rm sec} = 0.47 \pm 0.07\,{\rm M}_\odot$, the mass ratio expected for HS 2325 on the base of these empirical evidence is $q_{\rm emp} = 0.60 \pm 0.17$. The agreement of $q_{\rm emp}$ and $q_{\rm spec}$ is comforting, though the closeness of the match is probably coincidental, considering the large error on $q_{\rm emp}$.

If the assumptions on $M_{\rm sec}$ and q are indeed correct, and we underline again that, especially, $q_{\rm spec}$ should be treated as a rough estimate, then the allowed inclination angle range becomes $70^\circ \leq i \leq 81^\circ$ (Figure 6.6) and the allowed $(M_{\rm WD}, M_{\rm sec})$ pairs are indicated as the grey shaded area in Figure 6.7.

Finally, we also made a preliminary attempt to model the observed light curve profile of HS 2325, to check whether our constraints lead to a plausible model. We employed LCURVE to

model the 2005 Sep. 15 light curve taken at the NOT, which has the highest observing cadence and the system was found to be in quiescence. The bright spot and accretion disc model parameters were switched on (Section 2.4.4). The results are shown in Figure 6.8. Three cases need to be considered.

Case 1: No eclipse of the white dwarf

The red model in Figure 6.8 was computed for $q = 0.6$ and $i = 71°$, corresponding to $M_{\rm WD} = 0.81\,{\rm M}_{\odot}$ and $M_{\rm sec} = 0.48\,{\rm M}_{\odot}$. Both q and i were held fixed during the fitting process. In this combination the white dwarf is not eclipsed at all. While this model reproduces the ingress and egress phases well, it fails completely to fit the deepest part of the eclipse, indicating that an additional component is occulted.

Case 2: Grazing eclipse of the white dwarf

The blue model in Figure 6.8 was computed for $q = 0.6$ and $i = 71.45°$, corresponding to $M_{\rm WD} = 0.80\,{\rm M}_{\odot}$ and $M_{\rm sec} = 0.48\,{\rm M}_{\odot}$. We see that the morphology of the grazing eclipse of the white dwarf is reminiscent of the observed central dip in the eclipse profile, however, the particular model is too narrow to reproduce the deepest part of the eclipse. To properly fit this part (black model, $q = 0.6$, $i = 71.2°$, $M_{\rm WD} = 0.80\,{\rm M}_{\odot}$ and $M_{\rm sec} = 0.48\,{\rm M}_{\odot}$) requires a white dwarf radius of $R_{\rm WD} = 0.0372\,{\rm R}_{\odot}$, which is in complete disagreement with the radius of $R_{\rm WD} = 0.0105\,{\rm R}_{\odot}$, calculated from the models of Bergeron et al. [1995a] for a white dwarf of the adopted mass.

Since a larger white dwarf radius seems to be required to properly fit the deepest part of the eclipse, we repeated the fitting, following the exact same procedure as above, with the lowest plausible white dwarf mass of $M_{\rm WD} = 0.62\,{\rm M}_{\odot}$ (corresponding to $q = 0.43$ and $i = 72°$). The fitting process resulted in the same inconsistency regarding the radius of the white dwarf.

Thus, a grazing eclipse alone cannot fully account for the deepest part of the eclipse.

Case 3: Total eclipse of the white dwarf

A total eclipse of the white dwarf cannot be, securely and unambiguously, excluded with the present data set. However, as there are no clear signatures of the white dwarf ingress/egress contact points, the light curve does not provide enough constraints to test this case, and we did not try to fit any model that had a high enough inclination to imply a total WD eclipse.

A plausible scenario that could account for the fitting results is the presence of an additional, physically larger, bright component in the central part of the accretion disc. This component could be, for example, an enhanced boundary layer [see e.g. Wood et al., 1989; Wood & Horne, 1990] that is a dominant light source and outshines the white dwarf. The deepest part of the eclipse could then be attributed to a partial eclipse of this component. Unfortunately, this alternative does not offer more insight on whether the white dwarf is eclipsed or not, something that can only be answered with an improved data set, namely high-cadence and high-photometric accuracy observations at quiescence for more than one orbital cycles.

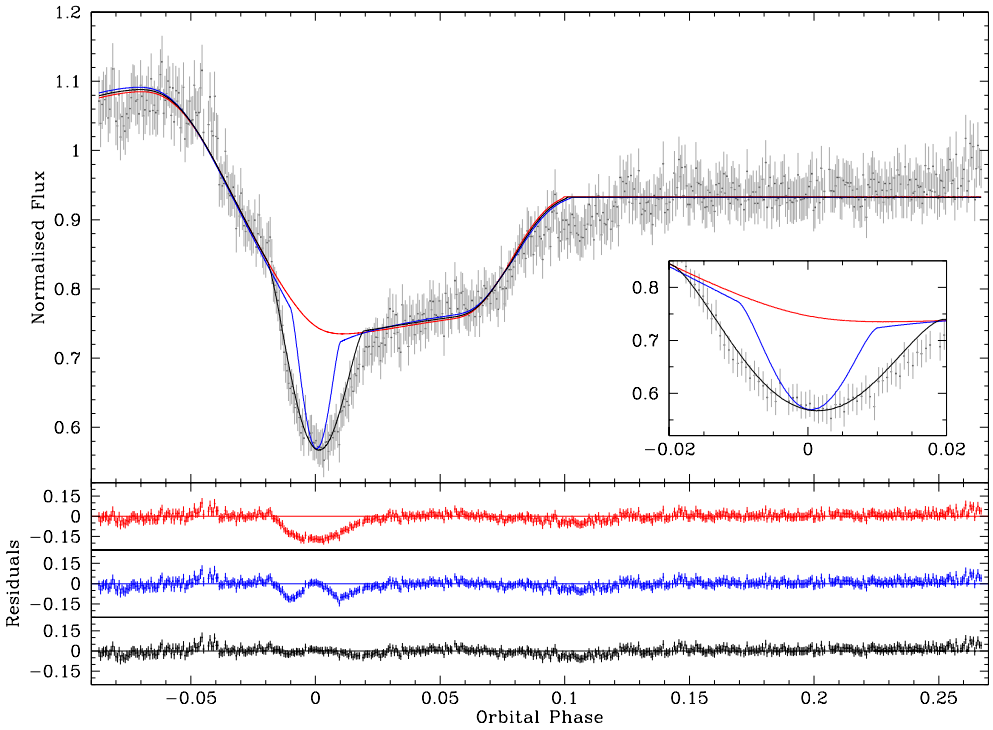

Figure 6.8: Model fits to the clear-filter, Sep. 15 2005 NOT light curve of HS 2325. Top panel: the light curve with three different models, using different q and i assumptions, over-plotted. Bottom three panels: the residuals of the fits of each different model. Inset panel: zoom-in around the deepest part of eclipse. See text for details.

6.10 Discussion

The exact geometry of HS 2325 and the components contributing in the eclipse profile remain unknown, and no safe conclusion can be drawn. The shallowness of the eclipses could be used as an argument against a total eclipse of the white dwarf; however, it could be that the white dwarf has (unusually) lower surface brightness and its signature in the light curve is not as strong [see e.g. Copperwheat et al., 2010, for the case of the cool white dwarf in IP Peg].

The boundary layer scenario cannot be readily tested using LCURVE, where the accretion disc is modelled as a symmetric, flattened disc, and a simple radial power law variation for its surface brightness is assumed. Thus, any component similar to a boundary layer (or a more complicated structure of the accretion disc) cannot be accounted for. If that were true, the parameter values established in the fit could not be fully trusted. This is because the fit would try to compensate e.g. for the variations due to the boundary layer, by radically changing other parameters, such as the white dwarf radius.

The current lack of observational constraints makes the uniqueness of the fits, presented previously, difficult to judge. All the above examined cases and assumptions could be rendered void, if a future high-quality, high time-resolution light curve clearly displays eclipse contact points of the white dwarf. However, the analysis based on the size of the accretion disc is independent of the white dwarf eclipse. Furthermore, high signal-to-noise spectroscopic observations could confirm, through use of *diagnostic diagrams* [e.g Shafter, 1983; Thorstensen, 2000; Southworth et al., 2010], whether HS 2325 belongs to the handful of systems where measurements of the radial velocity of the WD are possible. Additional observations are of paramount importance for the study of HS 2325.

Having said that, HS 2325 presents us with an unparallelled opportunity for "hands-on" study of accretion processes. Its modest brightness range makes it a suitable target for 2m - 4m-class telescopes and also, as we have demonstrated, accessible with the small aperture telescopes of amateur astronomers. Its high declination means it is circumpolar and observable all-year-round from the Northern hemisphere, while its short outburst interval practically guarantees that a (modest) observational run of a few days will record either the rise to or the decline from outburst. This will enable "real-time" studies of the evolution and structural changes of the accretion disc to be carried out, through the means of *eclipse mapping* [Horne, 1985] and *Doppler tomography* [Marsh & Horne, 1988].

Chapter 7

V455 And - searching for white dwarf pulsations

7.1 Introduction

Angular momentum loss inexorably drives the evolution of cataclysmic variables to shorter orbital periods, until the period minimum is reached and the system bounces back to longer $P_{\rm orb}$ (Section 1.3.4). The final stop along the evolutionary line of a (post-common-envelope) white dwarf binary will be a cataclysmic variable below the period gap. In the previous Chapters I have presented new systems, I have measured orbital periods and radial velocities and I have used light curve modelling to obtain system parameters. This Chapter is somewhat different. The system presented here has been previously identified and had its $P_{\rm orb}$ determined and radial velocities measured. Although the system is eclipsing, I will not apply the usual modelling techniques. Instead, I will focus on a different kind of photometric variability present in the system, which is believed to arise from pulsations of the WD primary. Thus, I will here employ the techniques of time series analysis, through Fourier transforms, as presented in Section 2.4.5, in an attempt to confirm the nature of the variability.

7.2 Target background

This Chapter is devoted to V 455 Andromedae (henceforth V 455) also known as HS 2331+3905 (RA = 23:34:01.6, Dec = +39:21:41.4). It was originally identified as a CV candidate from the HQS survey and studied by Araujo-Betancor et al. [2005] (henceforth AB05). The light curve of V 455 is shown in Figure 7.1.

V 455 in a nutshell

In AB05 V 455 is, rightfully, described as "the cataclysmic variable that has it all". Indeed the system is eclipsing, albeit partially; it has an orbital period of $P_{\rm orb} = 81.08\,$min, placing it very

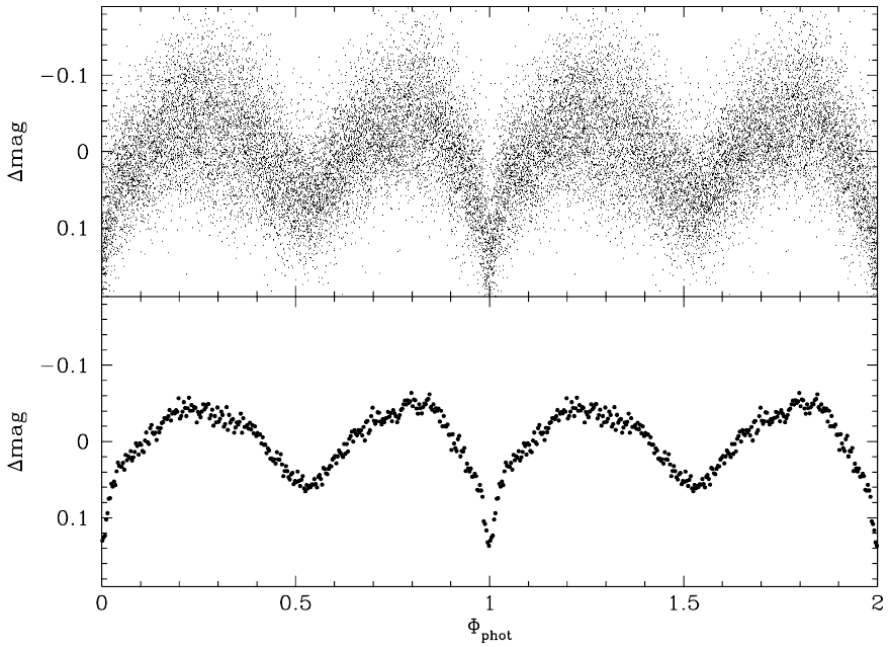

Figure 7.1: The phase-folded light curve of V 455 as shown in AB05. Top panel: the entire data set. Bottom panel: the same, but re-sampled into bins of 100 points. A full cycle is repeated for clarity.

close to the period minimum; it shows evidence for a permanent superhump with $P_{\rm sh} = 83.38\,{\rm min}$, associated with a precessing, elliptical accretion disc; and it most likely contains a brown-dwarf donor, making it a good candidate for a post-bounce system. The most striking feature is the fact that the radial velocities (measured from Balmer and Helium lines) are predominantly modulated at a spectroscopic period of $P_{\rm spec} \sim 3.5\,{\rm h}$ and *not* the orbital period. This period is not at all related to $P_{\rm orb}$, it does not show up directly on photometric data and it was found to drift in period and/or phase on timescales of a few days [see Araujo-Betancor et al., 2005, for a more detailed discussion].

In addition to the above, time-series analysis performed on the photometric data set, through power spectra and Scargle periodograms, revealed a number of significant signal detections. These were

- A signal at the orbital frequency, $F_{\rm orb} = 17.76\,{\rm d}^{-1}$
- A dominant signal at double the orbital frequency, $F_{\rm dh} = 35.52\,{\rm d}^{-1}$, resulting from the "double-hump" shaped light curve
- A combination of signals at $200\,{\rm d}^{-1} < F_{\rm puls} < 300\,{\rm d}^{-1}$, attributed to non-radial (g-mode) white dwarf pulsations
- Two signals at $F = 1277.76\,{\rm d}^{-1}$ and $F = 1284.75\,{\rm d}^{-1}$, the latter attributed to the white dwarf spin and the former to a sideband (beat) frequency between the spin signal and the $P_{\rm spec} \sim 3.5\,{\rm h}$ spectroscopic period

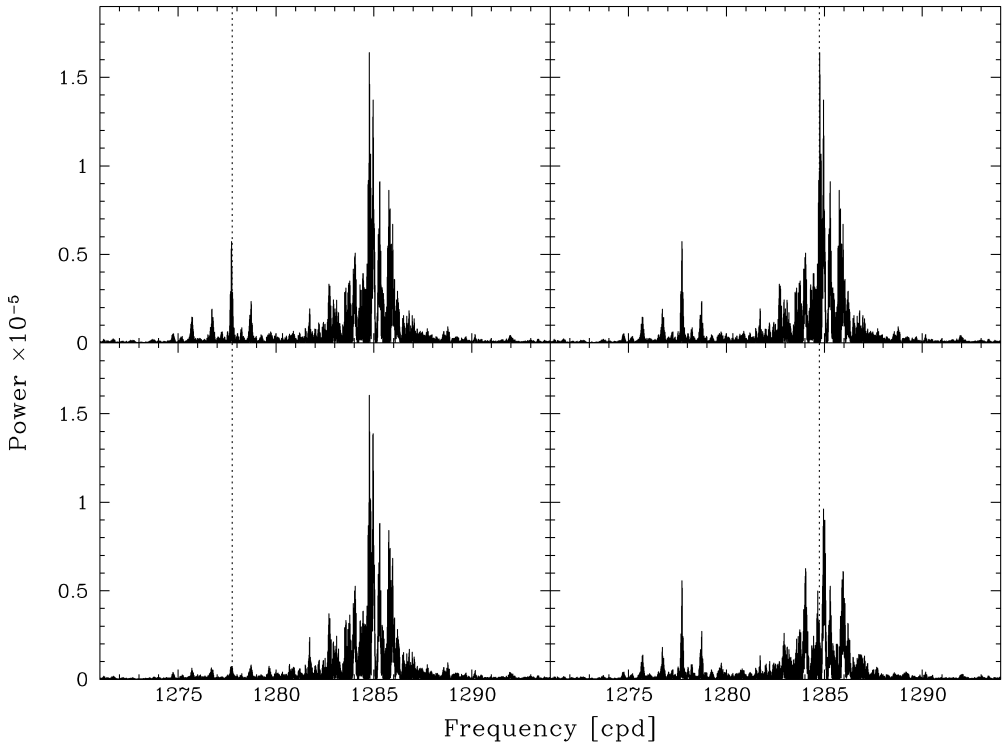

Figure 7.2: Identification of the WD $F_{\rm spin}$ in V 455. Top panels: the DFT calculated from data collected in the 2004 campaign. Bottom left panel: pre-whitening with $F = 1277.76\,\mathrm{d}^{-1}$ removes the signal completely, indicating long term stability and coherence. Bottom right panel: pre-whitening with $F = 1284.75\,\mathrm{d}^{-1}$ leaves considerable residual power, indicating that this signal is not stable on long-timescales.

- Two signals at $F = 2555.5\,\mathrm{d}^{-1}$ and $F = 2569.25\,\mathrm{d}^{-1}$, believed to be the first harmonics of the white dwarf spin and the sideband frequencies.

The 2004 photometric campaign

During August - September 2004, a multi-site photometric campaign of V 455 was conducted. The purpose was to study the signals at $200\,\mathrm{d}^{-1} < F_{\rm puls} < 300\,\mathrm{d}^{-1}$ and determine if they are indeed a result of WD pulsations. Such campaigns provide uninterrupted, alias-free observations, which are very useful for studying white dwarf pulsations [e.g. Kepler et al., 2003; Mukadam et al., 2010]. This data set has immediately led to an important discovery, albeit not related to pulsations. In AB05 the signal at $F = 1284.75\,\mathrm{d}^{-1}$ was attributed to the white dwarf spin and the one at $F = 1277.76\,\mathrm{d}^{-1}$ was thought to be the beat frequency between the spin and the $\sim 3.5\,\mathrm{h}$ spectroscopic period. Power spectra calculated from the data set collected during the campaign show that the signal at $F = 1277.76\,\mathrm{d}^{-1}$ is coherent and stable over the course of two months (pre-whitening with this frequency removes the signal completely from the power spectrum), whereas the signal at $F = 1284.75\,\mathrm{d}^{-1}$ is not (pre-whitening leaves residual power). This is illustrated in Figure 7.2.

Based upon this evidence, coupled with evidence from fast spectroscopy (D.Steeghs, priv. comm.) and X-Ray observations (P.Wheatley, priv. comm.), we identify the white dwarf spin frequency to be $F_{\rm spin} = 1277.76\,{\rm d}^{-1}$ and the sideband frequency to be $F_{\rm beat} = 1284.75\,{\rm d}^{-1}$. The fact that $F_{\rm beat} > F_{\rm spin}$ implies that the region where the beat signal originates from, moves in a *retrograde* direction with regard to the white dwarf rotation. Such a retrograde motion is predicted by simulations [Foulkes et al., 2006, 2010] of accretion discs that are *warped*, due to a pressure torque induced by irradiation from a central X-ray source [e.g. Wijers & Pringle, 1999]. On a similar note, Tovmassian et al. [2007] have studied a scenario including the precession of the rotational axis of the WD. A combination of these models might be able to explain the 3.5 h spectroscopic period, but the answer remains elusive.

The 2007 superoutburst

One of the features missing from V 455 at the time of publication of AB05 was any kind of dwarf nova activity. The system did not disappoint and in September 04, 2007 it underwent a spectacular 8-mag superoutburst, confirming that it belongs to the WZ Sge sub-class[1] of CVs, as hypothesised in AB05. I was extremely lucky to have an observing run around that time at the 1.2m Kryoneri telescope in Greece focused on V 455 as part of the investigation for pulsations, so I was able to record the superoutburst from its very early stages. In the previous night, the system was observed to still be in quiescence ($V \approx 16.4$). Figure 7.3 shows these observations, overplotted on AAVSO[2] observations prompted after a VSNET-alert[3]. In the last observation, obtained at October 14, 2010, the system was found at $V \approx 16.1$, still not fully back to quiescence, more than 3 years after the superoutburst.

7.3 Scope of the work

In AB05 the signals detected in the power spectra at a range $200\,{\rm d}^{-1} < F_{\rm puls} < 300\,{\rm d}^{-1}$ were tentatively attributed to g-mode pulsations. This was done on the basis that the corresponding periods of the observed signals, $288\,{\rm s} < {\rm P} < 432\,{\rm s}$ matched the observed range of white dwarf pulsations both in single ZZ Ceti stars (see again Section 1.4.3) and in the CV GW Lib [van Zyl et al., 2004]. While this interpretation is wholly plausible, no definite proof that these signals are indeed pulsations has yet been provided. Proof can come through use of power spectra and comprehensive time-series analysis, in order to establish the repeated occurance of signals at specific frequencies, indicative of a stable mechanism, i.e. g-mode pulsations of the white dwarf (remember again the "golden rule", Section 2.4.5). The purpose of my work was to perform such a study of V 455. To this end, I have re-analysed the light curves presented in AB05 (collected from 2000 to 2003), together with the light curves from the photometric campaign of 2004 (which up to this point have not been properly

[1] WZ Sge systems are a type of SU UMa dwarf novae, which only show rare superoutbursts and almost no normal outbursts

[2] The American Association of Variable Star Observers, Alert Notice 357

[3] Variable Star NETwork, alert 9530, http://ooruri.kusastro.kyoto-u.ac.jp/pipermail/vsnet-alert/2007-September/001152.html

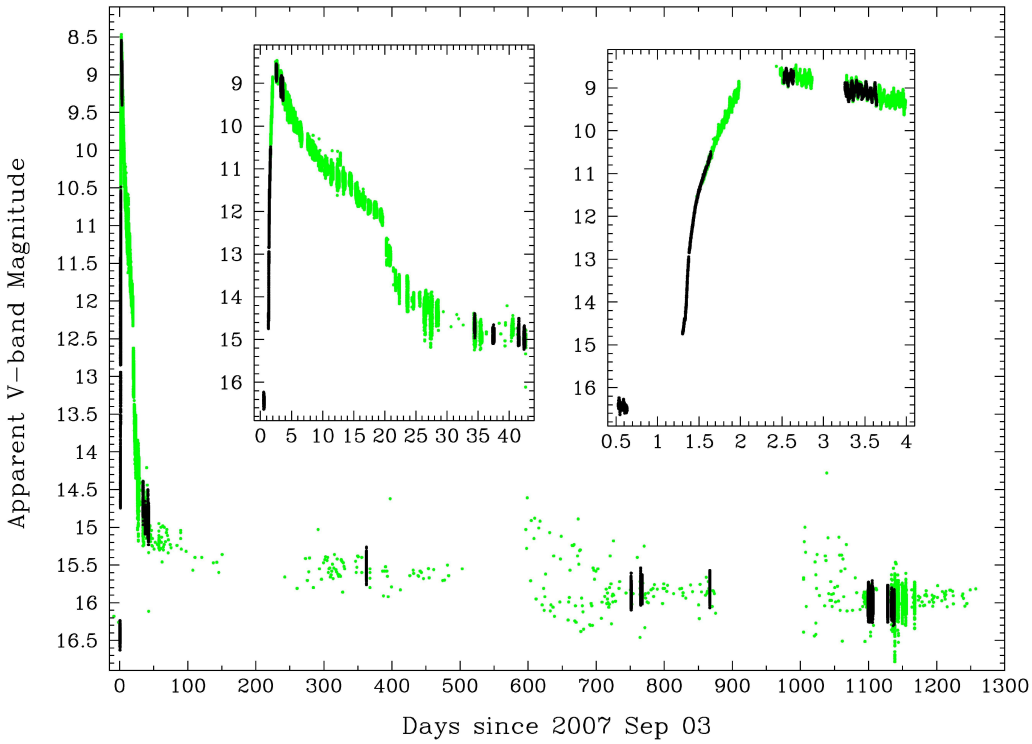

Figure 7.3: Onset and evolution of the 2007 superoutburst of V 455 as recorded by the AAVSO (green points) and by our own observations (black points). On the night of Sep. 03, the system was still in quiescence, while the observations on Sep. 04 (the onset of the superoutburst) started independently of the VSNET alert, barely a minute after the official confirmation. Left inset panel: a close-up on the evolution of the superoutburst during the first $\sim$ 45 days. Right inset panel: a close-up on the evolution of the superoutburst during the first $\sim$ 4 days.

analysed), as well as light curves obtained in subsequent years (from 2005 to 2010, see Table 3.1 for details).

7.4 Analysis

The analysis has been carried out with power spectra (DFTs) calculated in the frequency range $150\,\mathrm{d}^{-1} < F < 450\,\mathrm{d}^{-1}$. In what follows I will refer to this range as *region of interest* (ROI).

7.4.1 Light curve selection

For the analysis, I have selected light curves that met two criteria: (i) the observations had more than 3 hours pure on-target time (to ensure that closely spaced frequencies can be resolved, see again Figure 2.11, Panels II-A, II-B), and (ii) the sampling of the data corresponded to a Nyquist frequency of $F_{\mathrm{Nyq}} > 450\,\mathrm{d}^{-1}$, which translates into a duty-cycle (exposure time plus readout time) of $t_{\mathrm{dc}} < 96\,\mathrm{s}$. These light curves are reported in Table 3.1.

7.4.2 Light curve preparation

All light curve have been processed in the following fashion:

(1) Each individual light curve was first converted from the V-band magnitude to V-band flux through $f_V = c \times f_{\mathrm{Vega}} \times 10^{-0.4 m_V}$, where m_V is the V magnitude, f_{Vega} is the flux of Vega in the V-band and c is a normalisation constant, so that the quiescent flux is normalised to 1.

(2) The light curves were then smoothed using a box-car filter. The number of points, n_{p}, of the box-car varied for every light curve and was chosen according to the corresponding duty cycle t_{dc}, so that the actual width (in time) of the filter would always be $n_{\mathrm{p}} \times t_{\mathrm{dc}} = 5760\,\mathrm{s}$ (corresponding to $15\,\mathrm{d}^{-1}$). The smoothed light curve was then subtracted from the original, effectively removing any power below $15\,\mathrm{d}^{-1}$. In CVs, accretion-driven flickering results in low-frequency, high-amplitude signals appearing in the DFTs. When re-shuffling the data (e.g. when we estimate the noise level of the DFT, Section 2.4.5), these signals can leak into higher frequencies and lead to an overestimate of the noise level. Use of the box-car filtering removes this unwanted low-frequency power.

(3) The light curves were then pre-whitened with the white dwarf spin at $F_{\mathrm{spin}} = 1277.76\,\mathrm{d}^{-1}$ and the sideband signal F_{beat}[4] and their associated harmonics, to avoid possible down-scattering of power from these signals in the ROI, when reflected around the Nyquist frequency (see again Figure 2.11, Panel III), as such down-scattered signals would only make matters more complicated.

After this step I calculated a power spectrum in the ROI, from all the light curves prior to 2007, which is shown in the top panel of Figure 7.4. An inspection of the power spectrum reveals the

[4] as this signal is not coherent, each light curve was pre-whitened with the frequency where the beat signal was detected (in the particular light curve).

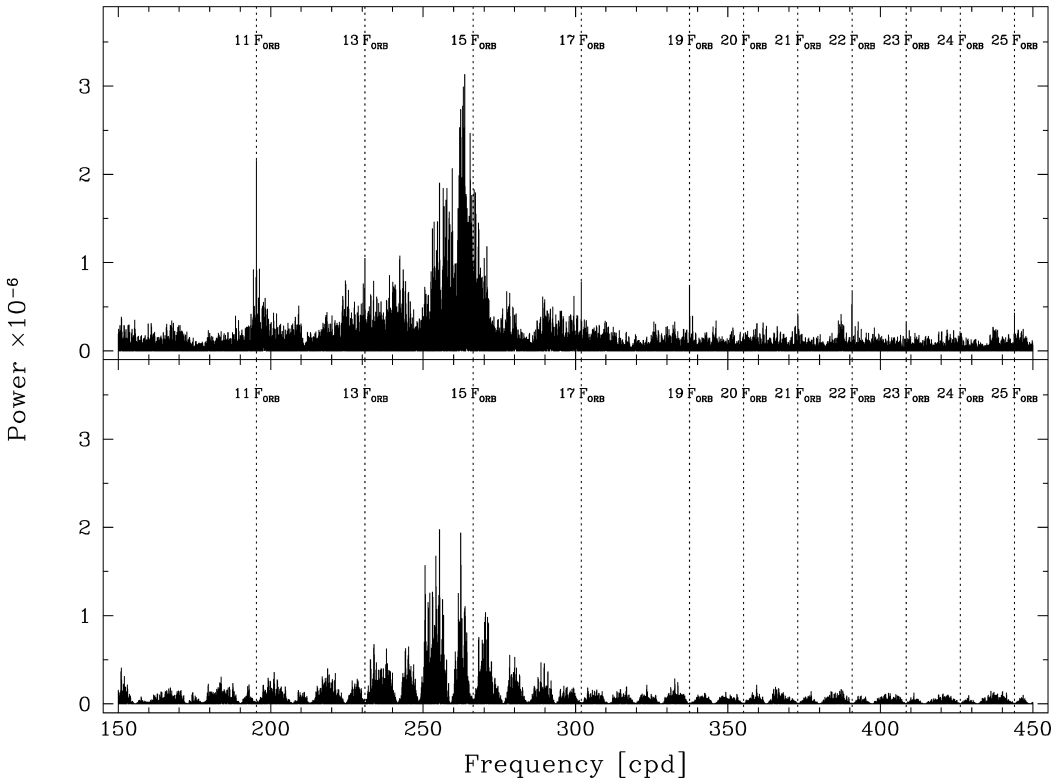

Figure 7.4: Top panel: A power spectrum of the ROI $150 - 450\,\mathrm{d}^{-1}$ calculated from all available data prior to 2007, after step-3 of light curve preparation. A significant amount of excess power in the ROI can be attributed to very high order harmonics of the orbital frequency and/or the double-hump frequency. Bottom panel: a re-calculated power spectrum after pre-whitening the high order harmonics (step-4 of light curve preparation). Excess power remains in the ROI.

presence of high-order harmonics of the orbital and/or double-hump frequencies, up to $25 \times F_{\mathrm{orb}}$, a direct result of the very sharp V-shaped eclipses in V 455.

(4) Thus, all, the light curves were also pre-whitened with the signals $F_{\mathrm{orb}} = 17.76\,\mathrm{d}^{-1}$ and $F_{\mathrm{dh}} = 35.52\,\mathrm{d}^{-1}$, as well as their harmonics up to the 24^{th} order, again to avoid having signals with known origin in the ROI. The re-calculated DFT is shown in the bottom panel of Figure 7.4 and indicates that, despite the significant pre-whitening, there is excess power remaining in the ROI, indicative of additional sources of signals. These signals were the subject of further analysis.

7.4.3 Combining light curves

During the 2004 photometric campaign, a large number of the light curves overlapped in time. After the initial processing stage, I merged together all those light curves that overlapped, to increase the duration of observations and, thus, the resolving power of the DFT.

7.4.4 Signal detection thresholds

In order to determine the significance of a signal detection, the overall noise level of the data needed to be estimated. This was achieved through the cumulative highest power method (CHP) described in Section 2.4.5. The ROI was divided into thirty $10\,\mathrm{d}^{-1}$-wide windows. In each window, the 99.7%-confidence level was calculated using the CHP method. The detection threshold for the ROI was taken to be the average of the 99.7%-confidence levels in each window.

In each power spectrum I then looked for signals in the ROI that are detected above the corresponding threshold. The frequencies and the uncertainties of these signals were subsequently determined using a bootstrap method, in the manner described in Section 2.4.5.

7.5 Results

7.5.1 Yearly data sets

I will first examine power spectra calculated on a yearly basis, i.e. calculating a DFT of all the light curves collected in a year. The resulting power spectra are shown in Figure 7.5.

The DFTs from the years prior to the superoutburst (top three panels in Figure 7.5) appear to be very similar in structure, implying the long-term presence of signals in the ROI. The latest DFT, obtained from data gathered three years after the superoutburst, shows a different picture, with the strongest clusters of excess power detected in higher (shorter) frequencies (periods).

The overall behaviour is consistent with attributing (at least some of) the power excess to white dwarf pulsations. Pulsation periods of ZZ Ceti stars show a distinct trend with temperature [e.g. Clemens, 1993; Kanaan et al., 2002; Mukadam et al., 2006], with the hotter DAVs showing shorter pulsation periods ($100 - 300\,\mathrm{s}$) than their cooler counterparts ($600 - 1000\,\mathrm{s}$).

Thus, this shift to shorter periods in the power spectra is expected, as the white dwarf in V 455 has been heated, potentially outside the instability strip, from enhanced accretion during the superoutburst, and the system is now cooling down back to its quiescent state.

7.5.2 Signal detection on a nightly basis

I now turn my attention to the various 3σ-significant signals detected on a run-to-run basis, in an attempt to identify repeating occurrences indicative of pulsation modes of the white dwarf.

The results of this search are presented in Figure 7.6. Notice that the X-axis is now period, instead of frequency. Each line represents a single light curve identified in the Y-axis, through a combination of observing date and telescope acronym. Light curves that have more than one telescope acronyms are those obtained during the 2004 campaign and were merged together. To aid the identification of a signal detection over multiple nights, I plot each signal as a straight line, extending in the Y-direction. Errors in the period of the detected signals are given as error-bars along the X-axis and, in some cases, are not readily visible in the scale of the plot.

At a first glance Figure 7.6 shows a rather complicated detection pattern, with a large number of significant signals detected in most nights. Although signals are found in the entire range, it is worth noting that there seem to be *preferred periods*, as most signals can be grouped in multiple

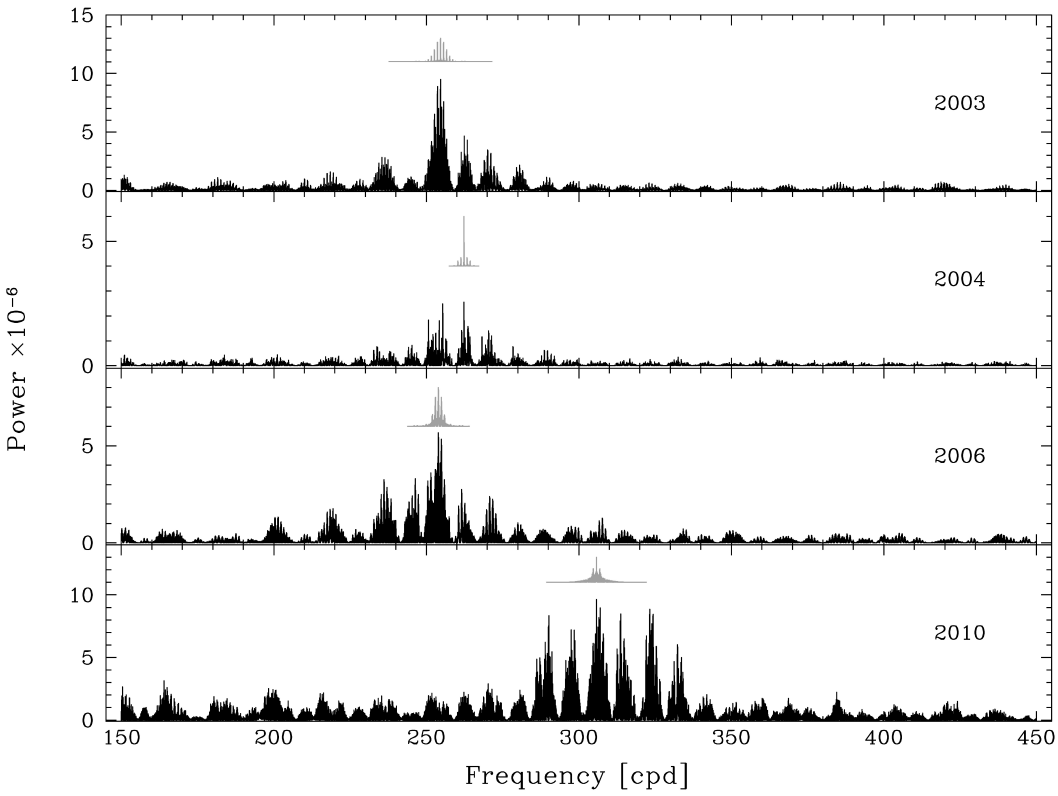

Figure 7.5: Power spectra of V 455 calculated by combining all data that have been collected in a year (indicated in each panel). I also plot the corresponding window functions (grey) shifted to the highest peak. The similarities in the DFTs of the pre-superoutburst years (top three panels) are obvious, as well as the shift of power to higher frequencies in the post-superoutburst data set (bottom panel). Notice the different limits on the Y-axes.

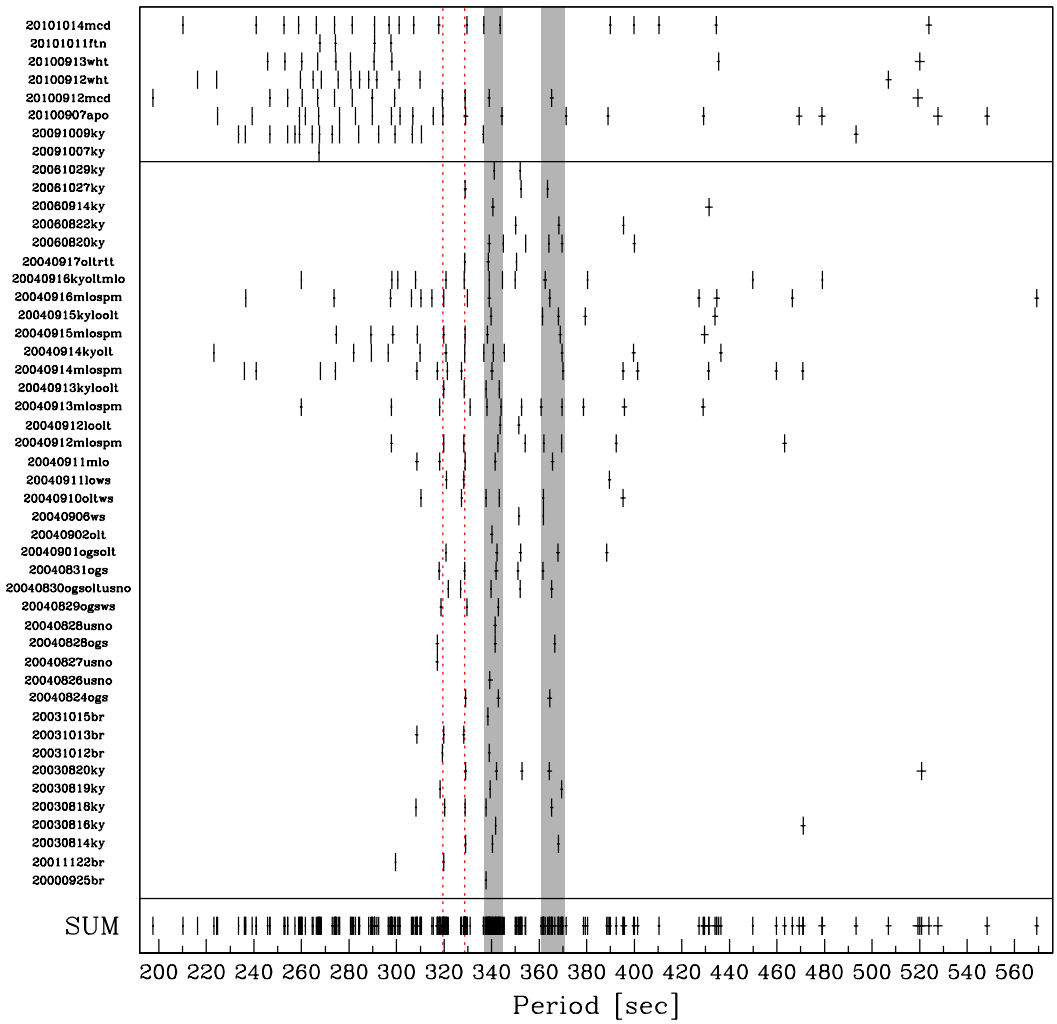

Figure 7.6: Nightly signal detections in DFTs of V 455. Notice that the X-axis is period, not frequency. Each row corresponds to one light curve, given on the Y-axis as a "DATE-OBSERVATORY" code. Light curves with more than one observatory acronym have been obtained during the multi-longitude photometric campaign. A line is used to separate data sets prior to and after the superoutburst of 2007. Each signal is plotted as a line (along the Y-axis) to aid the eye in the alignment of periods in different nights. Error-bars along the X-axis are the errors on the determined periods, with some being too small for the scale of the plot. The grey shaded regions and the two red lines are discussed in detail in the text.

(> 2) detections, clearly illustrated at the bottom panel in Figure 7.6. Similarly rich power spectra have been observed both in cool, single pulsating WDs [e.g. G 29-38; Kleinman et al., 1998] and in WDs in CVs [e.g. GW Lib; van Zyl et al., 2004, albeit much simpler than V 455]. The shift from longer to shorter periods observed in the yearly data sets is mirrored in the detections on an individual basis, as the bulk of signals in light curves obtained after 2007 (top part of Figure 7.6) is clearly shifted to shorter periods with respect to the those from light curves prior to 2007.

All detections of Figure 7.6 are summarised in Table 7.1. Frequencies (periods) were grouped together if their values were consistent within the errors. The quoted frequency/period values and errors were obtained as follows: for single detections, I report the formal values as obtained from the bootstrap method; for $N = 2$ detections I report the mean value, while the error is obtained from summing the constituent errors in quadrature; for $N \geq 3$ I again report the mean value, while the error is obtained by comparing (i) the standard deviation of the constituent frequencies, (ii) the mean of the constituent errors and (iii) the range-half-width $(F_{\rm max} - F_{\rm min})/2$ of the constituent frequencies of one group; the largest value is the reported error.

There are 4 cases with $N > 20$ detections: two signals at $P_1 = 319.39 \pm 2.32\,$s and $P_2 = 328.64 \pm 1.40\,$s, marked by red lines in Figure 7.6); and two *regions of activity* (ROA), i.e. regions were significant signals are consistently detected, albeit with some variation in their periods, at $P_{\rm ROA1} = 340.87 \pm 3.83\,$s and $P_{\rm ROA2} = 365.70 \pm 4.59\,$s, indicated by the grey-shaded areas in Figure 7.6). These regions could be a result of closely spaced periods, that are unresolved in the data sets at hand. If the amplitudes of the constituent signals change with time, then the unresolved, single detection in the DFTs will be shifted towards the largest amplitude component. This is also the reason for the conservative approach in the error estimation of multiple detections. Such "fine structure" of closely spaced frequencies could arise because of the rapid rotation of the WD or from *oblique pulsations*, due to the alignment of pulsations with a precessing magnetic axis [e.g. Montgomery et al., 2010].

On a final note, linear combinations of frequencies are detected in individual nights. For example, in the night 20030820ky the frequencies $F1 = 165.89\,{\rm d}^{-1}$, $F2 = 237.17\,{\rm d}^{-1}$, $F3 = 244.96\,{\rm d}^{-1}$ and $F4 = 252.65\,{\rm d}^{-1}$ are detected. However, $F3 = 3 \times F1 - F4$ and $F2 = 2 \times F3 - F4$, so not all significant detections are independent. Linear combinations are a very common occurrence in pulsating WDs [e.g. Brassard et al., 1995; Wu, 2001, and references therein].

7.6 Discussion

The analysis presented in this Chapter lends further support to the idea that the power detected in the DFTs of V 455 in the range $150 - 450\,{\rm d}^{-1}$ is a result of non-radial (g-mode) pulsations of the WD primary. Hot white dwarf pulsators generally excite shorter period (higher frequency) modes compared to cold ones [Clemens, 1993]; as the WD in V 455 has been heated during the superoutburst, one would expect a shift in the detected power towards higher frequencies, which is indeed observed (Figure 7.5). Furthermore, the analysis of the power spectra on an individual-night-basis clearly reveals clustering of signals, i.e. there are preferred frequencies inside the $150 - 450\,{\rm d}^{-1}$ range where signals are consistently detected, indicating a stable physical mechanism at work. In other words, the behaviour of the detected signals is exactly the one expected, if these

Table 7.1: The frequencies, periods and corresponding errors of all significant signal detections from Figure 7.6. See text for details on the quoted values. The number of detections is also indicated.

F [d^{-1}]	P [s]	#	F [d^{-1}]	P [s]	#
151.77 ± 0.25	569.28 ± 0.93	1	286.85 ± 0.31	301.21 ± 0.33	3
157.56 ± 0.34	548.38 ± 1.17	1	287.50 ± 0.25	300.52 ± 0.26	1
163.73 ± 0.61	527.71 ± 1.98	1	289.87 ± 1.49	298.07 ± 1.54	13
165.83 ± 0.74	521.04 ± 2.33	4	295.48 ± 0.23	292.41 ± 0.23	1
170.42 ± 0.40	506.98 ± 1.18	1	297.70 ± 1.22	290.23 ± 1.19	8
175.16 ± 0.33	493.26 ± 0.93	1	299.64 ± 0.22	288.35 ± 0.21	1
180.36 ± 0.58	479.04 ± 1.55	2	303.93 ± 0.35	284.28 ± 0.33	2
183.66 ± 0.41	470.43 ± 1.05	3	305.60 ± 0.29	282.72 ± 0.27	1
185.18 ± 0.29	466.58 ± 0.75	1	306.91 ± 0.35	281.51 ± 0.33	3
186.53 ± 0.38	463.19 ± 0.94	1	307.80 ± 0.46	280.70 ± 0.42	2
187.93 ± 0.29	459.74 ± 0.70	1	313.04 ± 0.28	276.00 ± 0.25	2
192.06 ± 0.18	449.87 ± 0.43	1	313.74 ± 0.24	275.39 ± 0.21	1
199.76 ± 1.72	432.55 ± 3.73	10	315.30 ± 0.96	274.03 ± 0.84	8
202.26 ± 0.35	427.16 ± 0.75	1	322.71 ± 0.65	267.73 ± 0.54	6
210.53 ± 0.33	410.39 ± 0.64	1	323.77 ± 0.25	266.85 ± 0.20	2
215.22 ± 0.39	401.45 ± 0.73	1	324.40 ± 0.25	266.34 ± 0.21	1
216.07 ± 0.34	399.88 ± 0.64	3	326.34 ± 0.34	264.76 ± 0.28	2
218.48 ± 0.45	395.46 ± 0.82	4	330.31 ± 0.36	261.57 ± 0.28	1
220.17 ± 0.28	392.42 ± 0.50	1	332.78 ± 0.93	259.63 ± 0.73	8
221.96 ± 0.42	389.25 ± 0.74	4	335.74 ± 0.18	257.34 ± 0.14	1
227.70 ± 0.56	379.44 ± 0.93	3	339.90 ± 0.50	254.19 ± 0.37	2
232.70 ± 0.36	371.29 ± 0.57	1	341.69 ± 0.60	252.86 ± 0.44	2
236.28 ± 2.97	365.70 ± 4.59	28	350.18 ± 0.65	246.73 ± 0.46	2
243.94 ± 0.30	354.19 ± 0.43	2	351.57 ± 0.58	245.75 ± 0.40	1
245.79 ± 0.99	351.52 ± 1.42	12	358.60 ± 0.81	240.94 ± 0.54	2
253.48 ± 2.84	340.87 ± 3.83	42	360.99 ± 0.20	239.34 ± 0.13	1
256.69 ± 0.21	336.59 ± 0.28	3	365.64 ± 0.42	236.30 ± 0.27	3
261.00 ± 0.26	331.03 ± 0.33	1	369.94 ± 0.38	233.55 ± 0.24	1
262.90 ± 1.12	328.64 ± 1.40	23	384.39 ± 0.34	224.77 ± 0.20	1
270.52 ± 1.96	319.39 ± 2.32	25	385.24 ± 0.27	224.27 ± 0.16	1
274.20 ± 0.35	315.10 ± 0.41	2	387.22 ± 0.46	223.13 ± 0.27	1
278.59 ± 0.29	310.13 ± 0.32	5	399.56 ± 0.28	216.24 ± 0.15	1
280.13 ± 0.45	308.42 ± 0.50	6	411.28 ± 0.45	210.08 ± 0.23	1
281.66 ± 0.42	306.76 ± 0.46	4	437.37 ± 0.67	197.54 ± 0.30	1

signals are the result of pulsations.

However, I should stress that I do not claim that *every one* of the signals reported in Table 7.1 is a different pulsation mode. Spurious signals in the region of interest can be a result of *quasi-periodic oscillations* [QPOs; Patterson et al., 1977], which are observed at periods of a few hundred seconds with amplitudes of a few percent [e.g. Warner et al., 2003, and references therein]. Hence, while these multiple detections are encouraging, final confirmation of white dwarf pulsations will have to wait for more data.

If (some of) the signals are indeed pulsations, the analysis of the power spectra reveals a very complicated behaviour. Given the accreting nature of V 455 and taking into account other observed properties of the system (rapidly rotating and magnetic WD; the bizarre ~ 3.5 h spectroscopic period), such complexity is probably to be expected. V 455 illustrates the need for long-lasting, multi-site campaigns. A data set consisting of day-long uninterrupted observations is required, to unravel the mysteries of the period spectrum.

Towards this end, another photometric campaign has been scheduled for September 2011. Given that a year has passed since the last observations, and the WD has been cooling in the meantime, a shift in the detected signals is expected, moving again to lower (longer) frequencies (periods) and possibly returning to the state indicated by data prior to 2007. Such a behaviour will confirm that these signals are indeed pulsations.

The next step involves a secure and unambiguous mode identification: pulsation modes are described using the *spherical harmonics* Y_m^ℓ; mode identification involves assigning ℓ and m values to the observed frequencies. A model for the white dwarf is required, based on measured (or assumed) values of $M_{\rm WD}$, $T_{\rm WD}$, atmospheric composition, element abundances, thickness of H- or He-layers etc. Pulsation models are then employed, and the frequencies $F_{\rm model}$ of the (exited) pulsation modes ℓ, m are computed and compared to the observed frequencies $F_{\rm obs}$. If a match is found, then a frequency $F_{\rm obs}$ represents the ℓ, m-mode [see Townsley et al., 2004, for an application on GW Lib].

Chapter 8

Discussion and Conclusions

8.1 Summary

In this thesis, I have studied seven eclipsing white dwarf binary systems. The systems presented in Chapters 4 to 7 could be, somewhat liberally, viewed as the story of a white dwarf and its companion captured at different snapshots along its evolutionary history.

In Chapters 4 and 5 I have identified SDSS 0110, SDSS 0303, SDSS 1435, SDSS 1548 and SDSS 1210 as new eclipsing post-common-envelope binaries from the SDSS. This was the first time that eclipsing PCEBS have been identified by a dedicated search, and not by mere coincidence. Subsequently, I presented the follow-up photometric and spectroscopic observations and have used them to measure the orbital periods and radial velocities of the binary components in each system. I then fitted the light curves of each system and, using spectroscopic constraints, I measured the masses and radii of the WD primary and the MS secondary stars. The juxtaposition of Chapters 4 and 5 highlighted the limitations which are sometimes imposed by the data in obtaining the desired accurate measurements. In particular, I showed that in cases where either $K_{\rm WD}$ or $K_{\rm sec}$ are absent no accurate measurements can be achieved, and invoking a mass-radius relation is necessary in order to obtain a solution. I also clearly illustrated the different approach in methodology and the large improvement on parameter determinations that can be achieved, when additional observational constraints are available (measurement of $K_{\rm WD}$ in Chapter 5).

In Chapter 6 I have identified HS 2325 as an eclipsing cataclysmic variable from the HQS. Following the same pattern as the previous two Chapters, I presented the follow-up photometric and spectroscopic observations, which were used to measure the orbital period of the system (placing HS 2325 above the CV orbital period gap) and the radial velocity of the secondary star, while I indicated the possibility that the radial velocity of the white dwarf might also be measurable in this system, an uncommon fact in CVs. While it was not possible to obtain accurate measurements of the stellar parameters, mainly due to the fact that the eclipse profile is not fully resolved with the data at hand, I combined the available observational information together with theoretical predictions and empirical evidence from the known CV population to obtain a first, broad estimate of their values. Finally, I have also presented the outcome of a photometric monitoring campaign using small aperture telescopes, which revealed the very frequent occurrence of dwarf nova outbursts,

marking HS 2325 as an ideal candidate for long-term monitoring.

In Chapter 7 I revisited V 455 And, identified as HS 2331+3905 in the HQS, and conducted the first comprehensive analysis of its power spectra in order to determine whether the significant excess of power detected in the region $150\,\mathrm{d}^{-1} < f < 450\,\mathrm{d}^{-1}$ could indeed be attributed to non-radial white dwarf pulsations. Towards this end, I analysed 10-years-worth of photometric observations, obtained both before and after the only recorded superoutburst of V 455. I have examined power spectra on a night-to-night basis, i.e. calculated from one light curve at a time, as well as on a year-to-year basis, i.e. calculated from a combined set of light curves obtained over a year. This analysis revealed an extremely complex behaviour of the power spectra, indicating the necessity for further intensive observations. However, the results of this study, namely the presence of preferred frequencies/periods through multiple detections, the shift of the detected signals from longer to shorter periods after the superoutburst, and the identification of linear combinations between the detected signals are all very strong indicators that non-radial pulsations are the cause for (at least some) of the excess power.

In what follows, I will put this work into a broader astrophysical context and describe the future outlook.

8.2 Observational constraints on the common-envelope phase

For the better part of 40 years, since the discovery of V 471 Tau [Nelson & Young, 1970], eclipsing PCEBs have been rather neglected and overlooked. The known population consisted of only seven systems, most of which were chance discoveries. The theoretical understanding of the common-envelope phase predicted a large number of low-mass, $M_{\mathrm{WD}} \lesssim 0.4\,\mathrm{M}_{\odot}$, white dwarf primaries in these systems [Willems & Kolb, 2004]. This was further supported by studies of the mass distribution of large white dwarf samples [e.g. Liebert et al., 2005; Rebassa-Mansergas et al., 2010]. However, with the exception of RR Cae [$M_{\mathrm{WD}} = 0.44\,\mathrm{M}_{\odot}$; Maxted et al., 2007], the sample contained moderately massive, $M_{\mathrm{WD}} > 0.5\,\mathrm{M}_{\odot}$, white dwarfs. Furthermore, these systems were chance discoveries and the sample suffered from the bias that affected the general known population of PCEBs [Schreiber & Gänsicke, 2003], containing mainly hot, $T_{\mathrm{WD}} > 10000\,\mathrm{K}$, white dwarfs.

Lately, the field of PCEBs has been revolutionised by the SDSS. With data from the SDSS becoming publicly available, my collaborators and I have undertaken the first dedicated search for eclipsing PCEBs. So far, the search has been very prolific: results from seven systems have already been published (Pyrzas et al. 2009; Nebot Gómez-Morán et al. 2009; Parsons et al. 2011b; and this work) doubling the known sample in a few years of observations. Another 16 systems have been confirmed as eclipsing and 18 more await confirmation, i.e. bringing the total number of systems up to several dozens is entirely feasible. What is more, initial indications suggest that a large number of the primaries in these eclipsing systems are indeed low-mass white dwarfs [and see Rebassa-Mansergas et al., 2011, for PCEBs from SDSS in general]. All the systems are reported in Table 8.1.

Table 8.1: The current roster of eclipsing PCEBs. We list the known population prior to the SDSS, the systems identified in the SDSS and already published, the systems identified in the SDSS and confirmed as eclipsing but not yet published, and candidate eclipsing systems identified in the SDSS. Some of the systems were also identified in the Catalina Sky Survey [Drake et al., 2010]. Given are the masses and radii for the WD and the secondary star. The masses for the confirmed and candidate systems, where follow-up observations are lacking, are obtained through spectral fitting of the WD and a spectral type-mass relation for the secondary, as described in Rebassa-Mansergas et al. [2010]. Thus, these mass values should only be considered preliminary. For these systems, no light curve modelling has been performed and values of radii are therefore not available.

System	$M_{\rm WD}$ [$M_\odot$]	$R_{\rm WD}$ [$R_\odot$]	$M_{\rm sec}$ [$M_\odot$]	$R_{\rm sec}$ [$R_\odot$]
Known eclipsing PCEBs (7)				
V471 Tau[1]	0.84 ± 0.05	0.0107 ± 0.0007	0.93 ± 0.07	0.96 ± 0.04
RXJ 2130.6+4710[2]	0.554 ± 0.017	0.0137 ± 0.0014	0.555 ± 0.023	0.534 ± 0.017
DE CVn[3]	$0.51^{+0.06}_{-0.02}$	$0.0136^{+0.0008}_{-0.0002}$	0.41 ± 0.06	$0.37^{+0.06}_{-0.007}$
GK Vir[4]	0.51 ± 0.04	0.016	0.1	0.15
RR Cae[5]	0.44 ± 0.022	0.015 ± 0.0004	0.183 ± 0.013	0.188-0.23
QS Vir[6]	0.78 ± 0.04	0.011 ± 0.01	0.43 ± 0.04	0.42 ± 0.02
NN Ser[7]	0.535 ± 0.0012	0.0211 ± 0.0002	0.111 ± 0.004	0.1415 ± 0.002
Published new eclipsing PCEBs (7)				
SDSS 0110+1326[8]	0.47 ± 0.2	0.0163-0.0175	0.255-0.38	0.262-0.36
SDSS 0303+0054[8]	0.878-0.946	0.0085-0.0093	0.224-0.282	0.246-0.27
SDSS 0857+0342[9]	0.51 ± 0.05	0.0247 ± 0.0008	0.09 ± 0.01	0.110 ± 0.004
SDSS 1210+3347[10]	0.415 ± 0.010	$0.0157 - 0.0161$	0.158 ± 0.006	$0.197 - 0.203$
SDSS 1212–0123[11]	0.46-0.48	0.016-0.018	0.26-0.29	0.28-0.31
SDSS 1435+3733[8]	0.48-0.53	0.0144-0.0153	0.19-0.246	0.218-0.244
SDSS 1548+4057[8]	0.614-0.678	0.0107-0.0116	0.146-0.201	0.166-0.196
Confirmed eclipsing PCEBs (16)				
SDSS 0106–0014[12]	0.37	-	0.12	-
SDSS 0138–0016[14,15]	-	-	-	-
SDSS 0259–0044[14,15]	-	-	-	-
SDSS 0308–0054[14,15]	-	-	-	-
SDSS 0814+4059[12,13]	0.86	-	0.255	-
SDSS 0838+1914[12,13]	0.39	-	0.255	-

continued on the next page...

Table 8.1: (. . . continued)

System	M_{WD} [$M_\odot$]	R_{WD} [$R_\odot$]	M_{sec} [$M_\odot$]	R_{sec} [$R_\odot$]
SDSS 0908+0604[12,13]	0.37	-	0.319	-
SDSS 0957+2342[12,13]	0.43	-	0.431	-
SDSS 1223–0056[12]	0.39	-	0.255	-
SDSS 1329+1230[12]	0.35	-	-	-
SDSS 1348+1834[12,13]	0.59	-	0.319	-
SDSS 1423+2409[12,13]	0.41	-	0.255	-
SDSS 1648+2811[12]	0.63	-	0.319	-
SDSS 2208–0115[13,14]	-	-	-	-
SDSS 2235+1428[12]	0.45	-	-	-
SDSS 2348+0029[12,14]	0.25	-	0.38	-
Candidate eclipsing PCEBs (18)				
SDSS 0238–0005[12]	0.48	-	0.38	-
SDSS 0320–0638[12]	0.79	-	0.255	-
SDSS 0935+2251[13]	-	-	-	-
SDSS 0939+3258[12,13]	0.52	-	0.319	-
SDSS 1021+1744[12]	1.06	-	0.319	-
SDSS 1244+1017[12,13]	0.4	-	0.319	-
SDSS 1143+0009[12]	0.6	-	0.319	-
SDSS 1410–0202[12,13]	0.47	-	0.38	-
SDSS 1434+5335[12]	0.49	-	0.319	-
SDSS 1452+2045[12]	-	-	0.319	-
SDSS 1456+1611[12,13]	0.37	-	0.196	-
SDSS 1506–0120[12]	0.45	-	0.319	-
SDSS 1510+0041[12]	0.79	-	0.149	-
SDSS 1529+0020[12]	0.38	-	0.255	-
SDSS 2132+0031[12]	0.39	-	0.319	-
SDSS 2208+0037[12]	-	-	0.255	-
SDSS 2318–0935[12]	0.5	-	0.38	-
SDSS 2320+0110[12]	0.28	-	0.431	-

[1]O'Brien et al. [2001]; [2]Maxted et al. [2004]; [3]van den Besselaar et al. [2007]; [4]Fulbright et al. [1993]; [5]Maxted et al. [2007]; [6]O'Donoghue et al. [2003]; [7]Parsons et al. [2010a]; [8]Pyrzas et al. [2009]; [9]Parsons et al. [2011b]; [10]this work; [11]Nebot Gómez-Morán et al. [2009]; [12]Rebassa-Mansergas et al. [2010]; [13]Drake et al. [2010]; [14]SDSS Stripe 82 data; [15]Becker et al. [2011]

The list reported in Table 8.1 is not exhaustive; many more systems should still be "hidden" in the SDSS data, awaiting identification; ongoing and future surveys, such as the Palomar Transient Factory (PTF), the Panoramic Survey Telescope & Rapid Response System (Pan-STARRS) and

the space-based mission GAIA, are expected to be at least as successful as SDSS in identifying large numbers of eclipsing WD+MS binaries; in addition the first short period, eclipsing WD+WD binaries (which must have evolved through two CE-phases) have recently been discovered [Steinfadt et al., 2010; Parsons et al., 2011a; Brown et al., 2011].

The aim is to exploit the emerging large and homogeneous sample of eclipsing PCEBs, as well as the emerging class of eclipsing WD+WD binaries, and obtain accurate measurements of the masses and radii of the binary components. This sample will provide strict observational constraints on the common-envelope ejection efficiency and the value of α_{ce} and will help us take a decisive step towards a unified treatment of the CE phase. Furthermore, this large number of accurate masses and radii measurements will play a crucial role in the calibration and testing of the mass-radius relations of white dwarfs and low-mass stars and in improving our understanding of stellar structure.

Future work needs to be carried out on several fronts. These include obtaining higher quality data to improve the accuracy of the stellar parameters of the known systems; confirming suspected eclipsing systems and carrying out intensive follow-up observations; fully exploiting the new Data Releases of SDSS (and data releases of the time-domain surveys mentioned above) to identify more systems; and expanding our search to identify PCEBs with earlier (K-, G-, F-) type companions.

8.3 Studying accretion in real time

Accretion is one of the most fundamental astrophysical processes, playing a key role in e.g. star and planet formation, in supernovae Type Ia explosions and in powering quasars. Interacting binaries offer the best chance of studying accretion discs and the mechanism of accretion in detail. Due to their large numbers, cataclysmic variables are at the forefront of such efforts.

HS 2325 with the detection of eclipses and the very short outburst recurrence time, is an ideal laboratory for accretion disc studies. Eclipsing dwarf novae above the period gap are relatively rare [$\sim$ 20 systems; Ritter & Kolb, 2003, v7.12] and even fewer have accurately determined parameters [Southworth et al., 2009]. A comparison with well-known and well-studied dwarf novae above the period gap quickly reveals the advantages of HS 2325: U Gem is also eclipsing [e.g. Warner & Nather, 1971], but undergoes outbursts only 2-3 times a year [Ak et al., 2002]; SS Cyg [see e.g. Sion et al., 2010, for a recent study] undergoes outbursts $\sim$ once a month [Ak et al., 2002], but it is *not* eclipsing. Z Cam systems have outburst recurrence times comparable to HS 2325 [Ak et al., 2002], however, only two eclipsing Z Cam systems are currently known: EM Cyg [e.g. North et al., 2000, and references therein] and AY Psc [e.g. Gülsecen et al., 2009, and references therein].

HS 2325 has the additional advantages of being observable throughout the year from the northern hemisphere and, due to its magnitude range, being observable even with small aperture telescopes equipped with CCDs. Future work should be carried out in two directions. On one hand, a concentrated campaign at large aperture (2-4m-class) telescopes, aiming to provide high-time resolution, simultaneous photometric and spectroscopic observations, preferably covering at least one outburst cycle. In quiescence, this data set will allow the determination of the exact eclipse morphology, while also providing a unique opportunity for tracking the structural evolution of the accretion disc during the rise to and/or the decline from outburst. On the other hand, the attention of amateur astronomer communities, such as the AAVSO, should be drawn to HS 2325 so that a long-

term monitoring of the system can commence. Given enough time, this will lead to the accumulation of data on a very large number of outbursts, which can then be directly tested against the predictions of the disk instability theory. This monitoring will also be able to confirm the possible Z Cam nature of HS 2325, if standstills are observed.

8.4 White dwarf pulsations in extreme conditions

V 455 And is a truly intriguing system, combining virtually all features that can be detected in a CV. Intensive studies of V 455 could hold the key to investigate the effects of accretion and rapid rotation on g-mode pulsations.

As the WD in V 455 is still cooling down after the 2007 superoutburst, we can track the evolution of pulsations and, thus, have the opportunity to study almost in real time a process that otherwise takes place over millions of years. Furthermore, V 455 offers us a unique advantage, as the signature of the WD spin is readily detected in the light curve. This allows us to study the detected pulsation modes in conjunction with the *known* value of the WD's rotation. Potential changes in the long-term stability of the WD spin signal ("spin-up" or "spin-down"), could be an indication of fluctuations in the accretion rate, which in turn could be compared with the long-term stability of pulsation frequencies, providing insight on the effects of enhanced or reduced accretion on pulsations.

Future work involves two types of observations. On one hand, UV spectroscopic observations are needed to accurately measure the temperature of the white dwarf[1] and track its cooling rate. On the other hand, multi-longitude photometric campaigns are of paramount importance for the study of the power spectra of V 455. In fact, both HST observations and a multi-longitude campaign have been scheduled for September 2011. Preferably, these campaigns should be conducted every year, with a global coverage that allows the uninterrupted monitoring of the system on timescales longer than a day, and with high temporal cadence so that the WD spin signal is also resolved in each light curve. Finally, future work should definitely involve efforts on pulsation mode identification: matching observed frequencies to ℓ, m-values will be the ultimate proof that the signals are indeed pulsations, but also having a large collection of ℓ, m-values from observed frequencies will allow detailed asteroseismological studies of V 455 and provide insight in the physics of pulsation excitation mechanisms in accreting white dwarfs.

As this thesis reaches its end, I can only hope that I have managed to capture and convey some of the many interesting aspects of white dwarf binary research and that I have convinced the reader that such systems are worthy of our attention and study.

[1] Currently this is only achieved with the HST

Appendix A

Mid-eclipse times

Table A.1: Mid-eclipse times, observed minus calculated values and cycle count for all systems

T_0	$O-C$ [s]	Cycle	T_0	$O-C$ [s]	Cycle
SDSS 0110: HJD(UTC) - 2 450 000					
3994.447919	+4	0	3996.444139	+12	+6
3995.445757	-16	3	4383.692048	0	+1170
SDSS 0303: HJD(UTC) - 2 450 000					
3991.616630	+20	0	4339.675049	-12 2559	2559
3993.498445	-1	14	4335.642243	-26 2589	2589
3994.708508	-2	23	4389.552460	+33 2960	2960
3997.531505	-12	44			
SDSS 1210: MJD(BTDB) - 50 000					
4923.0336744	-1	0	5623.0396100	-1	5623
4925.0255324	+1	16	5654.0375754	-0	5872
4926.1459281	-0	25	5690.0151216	+1	6161
4927.1418460	-0	33	5745.9109933	-2	6610
5599.1376175	+3	5431			
SDSS 1435: HJD(UTC) - 2 450 000					
4148.703460	-13	0	4240.414150	-10	730
4149.708650	-1	8	4240.665530	-1	732
4150.588020	-5	15	4249.711030	+5	804
4150.713970	+22	16	4251.721130	+6	820

continued on the next page...

Table A.1: (. . . continued)

T_0	$O-C$ [s]	Cycle	T_0	$O-C$ [s]	Cycle
4239.409160	-6	722	4252.851790	+4	829
SDSS 1548: HJD(UTC) - 2 450 000					
4592.572220 +71	0	4644.516130	-11	280	
4597.395910	+92	26	4647.484710	+15	296
4597.577710	-230	27	4653.421220	+11	328
4599.621800 +185	38				
HS 2325: HJD(UTC) - 2 450 000					
2888.425480	-6	0	4524.527990	-1	8419
3168.461560	-4	1441	4544.544400	-5	8522
3212.575440	-9	1668	4560.479940	5	8604
3214.324580	2	1677	4927.383490	0	10492
3214.518890	-0	1678	4933.602120	-6	10524
3300.220510	7	2119	4934.573920	4	10529
3300.414840	7	2120	4935.351320	10	10533
3301.386470	3	2125	4935.545640	8	10534
3302.357990	-10	2130	4940.598350	10	10560
3619.512060	-1	3762	4941.375690	10	10564
3629.617580	10	3814	4941.569840	-6	10565
3630.589230	8	3819	4942.347170	-7	10569
3971.452040	11	5573	4942.541460	-11	10570
4037.331340	2	5912	4943.513250	-0	10575
4289.577510	-3	7210	4944.485020	8	10580
4312.508950	-6	7328	4945.456530	-6	10585
4320.476770	3	7369	4945.650900	-3	10586
4335.440630	12	7446	4945.845190	-7	10587
4358.371920	-4	7564	4946.428210	-6	10590
4379.360110	1	7672	4947.399870	-7	10595
4393.352210	2	7744	4948.371720	8	10600
4451.458200	-1	8043	4963.529620	-8	10678
4510.535910	0	8347	4964.695730	0	10684

Bibliography

Abazajian, K. N., et al., 2009, ApJS, 182, 543

Aihara, H., et al., 2011, ApJS, 193, 29

Ak, T., Ozkan, M. T., Mattei, J. A., 2002, A&A, 389, 478

Allen, C. W., 1976, Astrophysical Quantities

Althaus, L. G., Benvenuto, O. G., 1997, ApJ, 477, 313

Althaus, L. G., Córsico, A. H., Miller Bertolami, M. M., 2007, A&A, 467, 1175

Andersen, J., 1991, ARA&A, 3, 91

Araujo-Betancor, S., et al., 2005, A&A, 430, 629

Arras, P., Townsley, D. M., Bildsten, L., 2006, ApJ Lett., 643, L119

Aungwerojwit, A., Gänsicke, B. T., 2009, in S. J. Murphy & M. S. Bessell, ed., The Eighth Pacific Rim Conference on Stellar Astrophysics, vol. 404 of *ASP Conference Series*, p. 276

Aungwerojwit, A., et al., 2005, A&A, 443, 995

Aungwerojwit, A., et al., 2006, A&A, 455, 659

Bailey, J., 1979, MNRAS, 187, 645

Baraffe, I., Kolb, U., 2000, MNRAS, 318, 354

Baraffe, I., Chabrier, G., Allard, F., Hauschildt, P. H., 1998, A&A, 337, 403

Barlow, B. N., Dunlap, B. H., Rosen, R., Clemens, J. C., 2008, ApJ Lett., 688, L95

Bath, G. T., 1969, ApJ, 158, 571

Bath, G. T., 1972, ApJ, 173, 121

Bath, G. T., 1973, Nat, 246, 84

Bayless, A. J., Orosz, J. A., 2006, ApJ, 651, 1155

Beatty, T. G., et al., 2007, ApJ, 663, 573

Becker, A. C., Bochanski, J. J., Hawley, S. L., Ivezić, Ž., Kowalski, A. F., Sesar, B., West, A. A., 2011, ApJ, 731, 17

Berger, D. H., et al., 2006, ApJ, 644, 475

Bergeron, P., Wesemael, F., Beauchamp, A., 1995a, PASP, 107, 1047

Bergeron, P., Wesemael, F., Lamontagne, R., Fontaine, G., Saffer, R. A., Allard, N. F., 1995b, ApJ, 449, 258

Bergeron, P., Fontaine, G., Billères, M., Boudreault, S., Green, E. M., 2004, ApJ, 600, 404

Bertin, E., Arnouts, S., 1996, A&AS, 117, 393

Beuermann, K., Baraffe, I., Kolb, U., Weichhold, M., 1998, A&A, 339, 518

Beuermann, K., Baraffe, I., Hauschildt, P., 1999, A&A, 348, 524

Beuermann, K., et al., 2010, A&A, 521, L60+

Boeshaar, P. C., 1976, The spectral classification of M-dwarf stars, Ph.D. thesis, Ohio State Univ., Columbus.

Brassard, P., Fontaine, G., Wesemael, F., 1995, 96, 545

Brickhill, A. J., 1983, MNRAS, 204, 537

Brown, W. R., Kilic, M., Hermes, J. J., Allende Prieto, C., Kenyon, S. J., Winget, D. E., 2011, ArXiv eprints., 1107.2389

Bruch, A., 1992, A&A, 266, 237

Bruch, A., 2000, A&A, 359, 998

Buat-Ménard, V., Hameury, J.-M., Lasota, J.-P., 2001, A&A, 369, 925

Casewell, S. L., Dobbie, P. D., Napiwotzki, R., Burleigh, M. R., Barstow, M. A., Jameson, R. F., 2009, MNRAS, 395, 1795

Castanheira, B. G., Kepler, S. O., Kleinman, S. J., Nitta, A., Fraga, L., 2010, MNRAS, 405, 2561

Chanmugam, G., 1972, Nat, 236, 83

Claret, A., Bloemen, S., 2011, A&A, 529, A75+

Clemens, J. C., 1993, Baltic Astronomy, 2, 407

Clemens, J. C., 1994, The origin and evolution of the white dwarf stars, Ph.D. thesis, Texas Univ.

Copperwheat, C. M., Marsh, T. R., Dhillon, V. S., Littlefair, S. P., Hickman, R., Gänsicke, B. T., Southworth, J., 2010, MNRAS, 402, 1824

Cropper, M., 1990, Space Sci. Rev., 54, 195

Davis, P. J., Kolb, U., Willems, B., Gänsicke, B. T., 2008, MNRAS, 389, 1563

de Kool, M., 1990, ApJ, 358, 189

de Kool, M., 1992, A&A, 261, 188

de Kool, M., Ritter, H., 1993, A&A, 267, 397

de Kool, M., van den Heuvel, E. P. J., Pylyser, E., 1987, A&A, 183, 47

De Marco, O., Passy, J.-C., Moe, M., Herwig, F., Mac Low, M.-M., Paxton, B., 2011, MNRAS, 411, 2277

Debes, J. H., 2006, ApJ, 652, 636

Dhillon, V. S., Marsh, T. R., Jones, D. H. P., 1991, MNRAS, 252, 342

Dolez, N., Vauclair, G., 1981, A&A, 102, 375

Dorman, B., Nelson, L. A., Chau, W. Y., 1989, ApJ, 342, 1003

Drake, A. J., et al., 2010, ArXiv eprints., 1009.3048

Dreizler, S., Heber, U., 1998, A&A, 334, 618

Dufour, P., Fontaine, G., Liebert, J., Schmidt, G. D., Behara, N., 2008, ApJ, 683, 978

Dufour, P., Béland, S., Fontaine, G., Chayer, P., Bergeron, P., 2011, ApJ Lett., 733, L19+

Dufour, P., et al., 2007, ApJ, 663, 1291

Dunlap, B. H., Barlow, B. N., Clemens, J. C., 2010, ApJ Lett., 720, L159

Dupuis, J., Fontaine, G., Pelletier, C., Wesemael, F., 1993, ApJS, 84, 73

Dziembowski, W., Koester, D., 1981, A&A, 97, 16

Eggleton, P. P., 1976, in P. Eggleton, S. Mitton, & J. Whelan, ed., Structure and Evolution of Close Binary Systems, vol. 73 of *IAU Symposium*, p. 209

Eggleton, P. P., 1983, ApJ, 268, 368

Fleming, T. A., Liebert, J., Green, R. F., 1986, ApJ, 308, 176

Fontaine, G., Brassard, P., 2008, PASP, 120, 1043

Fontaine, G., Brassard, P., Charpinet, S., 2003, Ap&SS, 284, 257

Ford, E. B., 2006, ApJ, 642, 505

Foulkes, S. B., Haswell, C. A., Murray, J. R., 2006, MNRAS, 366, 1399

Foulkes, S. B., Haswell, C. A., Murray, J. R., 2010, MNRAS, 401, 1275

Frank, J., King, A. R., Raine, D. J., 1985, Accretion power in astrophysics, Cambridge University Press, Cambridge

Fukugita, M., Ichikawa, T., Gunn, J. E., Doi, M., Shimasaku, K., Schneider, D. P., 1996, AJ, 111, 1748

Fulbright, M. S., Liebert, J., Bergeron, P., Green, R., 1993, ApJ, 406, 240

Gänsicke, B. T., Hagen, H., Engels, D., 2002, in B. T. Gänsicke, K. Beuermann, & K. Reinsch, ed., The Physics of Cataclysmic Variables and Related Objects, vol. 261 of *ASP Conference Series*, p. 190

Gänsicke, B. T., Araujo-Betancor, S., Hagen, H.-J., Harlaftis, E. T., Kitsionas, S., Dreizler, S., Engels, D., 2004, A&A, 418, 265

Gänsicke, B. T., Szkody, P., Howell, S. B., Sion, E. M., 2005, ApJ, 629, 451

Gänsicke, B. T., et al., 2009, MNRAS, 397, 2170

Gianninas, A., Bergeron, P., Fontaine, G., 2005, ApJ, 631, 1100

Gianninas, A., Bergeron, P., Fontaine, G., 2006, AJ, 132, 831

Gianninas, A., Bergeron, P., Fontaine, G., 2007, in R. Napiwotzki & M. R. Burleigh, ed., 15th European Workshop on White Dwarfs, vol. 372 of *ASP Conference Series*, p. 577

Gülsecen, H., Retter, A., Liu, A., Esenoğlu, H., 2009, New Astronomy, 14, 330

Gunn, J. E., et al., 1998, AJ, 116, 3040

Gunn, J. E., et al., 2006, AJ, 131, 2332

Hōshi, R., 1979, Prog. Theor. Phys., 61, 1307

Hagen, H.-J., Groote, D., Engels, D., Reimers, D., 1995, A&AS, 111, 195

Hansen, B. M. S., et al., 2002, ApJ Lett., 574, L155

Hirose, M., Osaki, Y., 1990, PASJ, 42, 135

Hjellming, M. S., Webbink, R. F., 1987, ApJ, 318, 794

Horne, K., 1985, MNRAS, 213, 129

Horne, K., 1986, PASP, 98, 609

Howell, S. B., Rappaport, S., Politano, M., 1997, MNRAS, 287, 929

Howell, S. B., Nelson, L. A., Rappaport, S., 2001, ApJ, 550, 897

Huang, S., 1966, AnAp, 29, 331

Iben, Jr., I., Tutukov, A. V., 1984, 54, 335

Iben, I. J., 1991, ApJS, 76, 55

Iben, I. J., Livio, M., 1993, PASP, 105, 1373

Kanaan, A., Kepler, S. O., Winget, D. E., 2002, A&A, 389, 896

Kawka, A., Vennes, S., 2003, AJ, 125, 1444

Kawka, A., Vennes, S., Dupuis, J., Chayer, P., Lanz, T., 2008, ApJ, 675, 1518

Kepler, S. O., et al., 2003, A&A, 401, 639

King, A. R., 1988, QJRAS, 29, 1

Kleinman, S. J., et al., 1998, ApJ, 495, 424

Knigge, C., 2006, MNRAS, 373, 484

Knigge, C., 2010, in V. Kologera & M. van der Sluys, ed., American Institute of Physics Conference Series, vol. 1314 of *American Institute of Physics Conference Series*, p. 171

Knigge, C., Baraffe, I., Patterson, J., 2011, ApJS, 194, 28

Koester, D., 1987, ApJ, 322, 852

Koester, D., 2010, MmSAI, 81, 921

Koester, D., Allard, N. F., 2000, BaltA, 9, 119

Koester, D., Wilken, D., 2006, A&A, 453, 1051

Koester, D., Schulz, H., Weidemann, V., 1979, A&A, 76, 262

Koester, D., Napiwotzki, R., Voss, B., Homeier, D., Reimers, D., 2005, A&A, 439, 317

Kolb, U., 1993, A&A, 271, 149

Kolb, U., Baraffe, I., 1999, MNRAS, 309, 1034

Kolb, U., Stehle, R., 1996, MNRAS, 282, 1454

Kraft, R. P., Mathews, J., Greenstein, J. L., 1962, ApJ, 136, 312

Kraus, A. L., Tucker, R. A., Thompson, M. I., Craine, E. R., Hillenbrand, L. A., 2011, ApJ, 728, 48

Krzeminski, W., 1965, ApJ, 142, 1051

Kurtz, M. J., Mink, D. J., 1998, PASP, 110, 934

Landolt, A. U., 1968, ApJ, 153, 151

Lasker, B. M., Hesser, J. E., 1969, ApJ Lett., 158, L171+

Lasker, B. M., Hesser, J. E., 1971, ApJ Lett., 163, L89+

Liebert, J., Bergeron, P., Holberg, J. B., 2005, ApJS, 156, 47

Littlefair, S. P., Dhillon, V. S., Marsh, T. R., Gänsicke, B. T., 2006a, MNRAS, 371, 1435

Littlefair, S. P., Dhillon, V. S., Marsh, T. R., Gänsicke, B. T., Southworth, J., Watson, C. A., 2006b, Sci, 314, 1578

Livio, M., 1989, Space Sci. Rev., 50, 299

Livio, M., Soker, N., 1988, ApJ, 329, 764

López-Morales, M., 2007, ApJ, 660, 732

Marcy, G. W., Lindsay, V., Wilson, K., 1987, PASP, 99, 490

Marsh, T. R., 1989, PASP, 101, 1032

Marsh, T. R., Horne, K., 1988, MNRAS, 235, 269

Maxted, P. F. L., Marsh, T. R., Moran, C., Dhillon, V. S., Hilditch, R. W., 1998, MNRAS, 300, 1225

Maxted, P. F. L., Marsh, T. R., Morales-Rueda, L., Barstow, M. A., Dobbie, P. D., Schreiber, M. R., Dhillon, V. S., Brinkworth, C. S., 2004, MNRAS, 355, 1143

Maxted, P. F. L., Napiwotzki, R., Dobbie, P. D., Burleigh, M. R., 2006, Nat, 442, 543

Maxted, P. F. L., O'Donoghue, D., Morales-Rueda, L., Napiwotzki, R., 2007, MNRAS, 376, 919

McCook, G. P., Sion, E. M., 1999, ApJS, 121, 1

McGraw, J. T., 1977, The ZZ Ceti stars: A new class of pulsating white dwarfs, Ph.D. thesis, Texas Univ., Austin.

McGraw, J. T., Liebert, J., Starrfield, S. G., Green, R., 1979, in H. M. van Horn & V. Weidemann, ed., IAU Colloq. 53: White Dwarfs and Variable Degenerate Stars, p. 377

Mestel, L., 1968, MNRAS, 138, 359

Metcalfe, T. S., 2003, ApJ Lett., 587, L43

Metcalfe, T. S., Salaris, M., Winget, D. E., 2002, ApJ, 573, 803

Meyer, F., Meyer-Hofmeister, E., 1979, A&A, 78, 167

Meyer, F., Meyer-Hofmeister, E., 1981, A&A, 104, L10+

Montgomery, M. H., Williams, K. A., Winget, D. E., Dufour, P., De Gennaro, S., Liebert, J., 2008, ApJ Lett., 678, L51

Montgomery, M. H., et al., 2010, ApJ, 716, 84

Morales, J. C., Ribas, I., Jordi, C., 2008, A&A, 478, 507

Morales, J. C., Gallardo, J., Ribas, I., Jordi, C., Baraffe, I., Chabrier, G., 2010, ApJ, 718, 502

Morgenroth, O., 1936, Astronomische Nachrichten, 258, 265

Mukadam, A. S., Montgomery, M. H., Winget, D. E., Kepler, S. O., Clemens, J. C., 2006, ApJ, 640, 956

Mukadam, A. S., et al., 2004, ApJ, 607, 982

Mukadam, A. S., et al., 2010, ApJ, 714, 1702

Mumford, G. S., Krzeminski, W., 1969, ApJS, 18, 429

Nebot Gómez-Morán, A., et al., 2009, A&A, 495, 561

Nelemans, G., Tout, C. A., 2005, MNRAS, 356, 753

Nelemans, G., Verbunt, F., Yungelson, L. R., Portegies Zwart, S. F., 2000, A&A, 360, 1011

Nelson, B., Young, A., 1970, PASP, 82, 699

North, R. C., Marsh, T. R., Moran, C. K. J., Kolb, U., Smith, R. C., Stehle, R., 2000, MNRAS, 313, 383

O'Brien, M. S., Bond, H. E., Sion, E. M., 2001, ApJ, 563, 971

O'Donoghue, D., Koen, C., Kilkenny, D., Stobie, R. S., Koester, D., Bessell, M. S., Hambly, N., MacGillivray, H., 2003, MNRAS, 345, 506

Orosz, J. A., Wade, R. A., Harlow, J. J. B., Thorstensen, J. R., Taylor, C. J., Eracleous, M., 1999, AJ, 117, 1598

Osaki, Y., 1974, PASJ, 26, 429

Paczyński, B., 1967, Acta Astron., 17, 287

Paczyński, B., 1971, ARA&A, 9, 183

Paczynski, B., 1976, in P. Eggleton, S. Mitton, & J. Whelan, ed., Structure and Evolution of Close Binary Systems, vol. 73 of *IAU Symposium*, p. 75

Paczynski, B., 1981, Acta Astron., 31, 1

Paczynski, B., Sienkiewicz, R., 1981, ApJ Lett., 248, L27

Panei, J. A., Althaus, L. G., Benvenuto, O. G., 2000, A&A, 353, 970

Parsons, S. G., Marsh, T. R., Copperwheat, C. M., Dhillon, V. S., Littlefair, S. P., Gänsicke, B. T., Hickman, R., 2010a, MNRAS, 402, 2591

Parsons, S. G., Marsh, T. R., Gänsicke, B. T., Drake, A. J., Koester, D., 2011a, ApJ Lett., 735, L30+

Parsons, S. G., et al., 2010b, MNRAS, 407, 2362

Parsons, S. G., et al., 2011b, MNRAS, submitted

Patterson, J., 1984, ApJS, 54, 443

Patterson, J., 1994, PASP, 106, 209

Patterson, J., 1998, PASP, 110, 1132

Patterson, J., 2001, PASP, 113, 736

Patterson, J., Robinson, E. L., Nather, R. E., 1977, ApJ, 214, 144

Pickering, E. C., Fleming, W. P., 1896, ApJ, 4, 369

Podsiadlowski, P., Rappaport, S., Han, Z., 2003, MNRAS, 341, 385

Pogson, N., 1857, MNRAS, 17, 200

Politano, M., 1996, ApJ, 465, 338

Politano, M., Weiler, K. P., 2006, ApJ Lett., 641, L137

Politano, M., Weiler, K. P., 2007, ApJ, 665, 663

Press, W. H., 2002, Numerical recipes in C++ : the art of scientific computing, Cambridge Univ. Press, Cambridge

Pretorius, M. L., Knigge, C., O'Donoghue, D., Henry, J. P., Gioia, I. M., Mullis, C. R., 2007, MNRAS, 382, 1279

Pringle, J. E. & Wade, R. A., ed., 1985, Interacting binary stars, Cambridge University Press, Cambridge

Provencal, J. L., Shipman, H. L., Hog, E., Thejll, P., 1998, ApJ, 494, 759

Provencal, J. L., Shipman, H. L., Koester, D., Wesemael, F., Bergeron, P., 2002, ApJ, 568, 324

Pyrzas, S., Gänsicke, B. T., Rebassa-Mansergas, A., Schreiber, M., Rodríguez-Gil, P., Marsh, T. R., Gomez-Moran, A. N., Koester, D., 2010, in K. Werner & T. Rauch, ed., 17th European White Dwarf Workshop, vol. 1273 of *AIP Conference Series*, p. 372

Pyrzas, S., et al., 2009, MNRAS, 394, 978

Quirion, P., Fontaine, G., Brassard, P., 2007, ApJS, 171, 219

Rappaport, S., Joss, P. C., Webbink, R. F., 1982, ApJ, 254, 616

Rappaport, S., Verbunt, F., Joss, P. C., 1983, ApJ, 275, 713

Rebassa-Mansergas, A., Gänsicke, B. T., Rodríguez-Gil, P., Schreiber, M. R., Koester, D., 2007, MNRAS, 382, 1377

Rebassa-Mansergas, A., Gänsicke, B. T., Schreiber, M. R., Koester, D., Rodríguez-Gil, P., 2010, MNRAS, 402, 620

Rebassa-Mansergas, A., Nebot Gómez-Morán, A., Schreiber, M. R., Girven, J., Gänsicke, B. T., 2011, MNRAS, 413, 1121

Rebassa-Mansergas, A., et al., 2008, MNRAS, 390, 1635

Ribas, I., 2006, Ap&SS, 304, 89

Ribas, I., Morales, J. C., Jordi, C., Baraffe, I., Chabrier, G., Gallardo, J., 2008, MmSAI, 79, 562

Ricker, P. M., Taam, R. E., 2008, ApJ Lett., 672, L41

Ritter, H., Kolb, U., 2003, A&A, 404, 301

Ritter, H., Schroeder, R., 1979, A&A, 76, 168

Roberts, G. O., Gelman, A., Gilks, W. R., 1997, Annals of Applied Probability, 7, 110

Rutten, R. G. M., Kuulkers, E., Vogt, N., van Paradijs, J., 1992, A&A, 265, 159

Savoury, C. D. J., et al., 2011, MNRAS, 415, 2025

Scargle, J. D., 1982, ApJ, 263, 835

Schlegel, D. J., Finkbeiner, D. P., Davis, M., 1998, ApJ, 500, 525

Schneider, D. P., Young, P., 1980, ApJ, 238, 946

Schreiber, M. R., Gänsicke, B. T., 2003, A&A, 406, 305

Schreiber, M. R., Gänsicke, B. T., Mattei, J. A., 2002, A&A, 384, L6

Schreiber, M. R., Gänsicke, B. T., Southworth, J., Schwope, A. D., Koester, D., 2008, A&A, 484, 441

Schreiber, M. R., et al., 2010, A&A, 513, L7

Schwarzenberg-Czerny, A., 1993, in P. Grosbol & R. de Ruijsscher, ed., 5. ESO/ST-ECF Data Analysis Workshop, vol. 47 of *ESO Conference and Workshop Proceedings*, p. 149

Shafter, A. W., 1983, ApJ, 267, 222

Shafter, A. W., 1992, ApJ, 394, 268

Shafter, A. W., Wheeler, J. C., Cannizzo, J. K., 1986, ApJ, 305, 261

Silber, A. D., 1992, Studies of an X-Ray Selected Sample of Cataclysmic Variables., Ph.D. thesis, MASSACHUSETTS INSTITUTE OF TECHNOLOGY.

Sion, E. M., Cheng, F. H., Long, K. S., Szkody, P., Gilliland, R. L., Huang, M., Hubeny, I., 1995, ApJ, 439, 957

Sion, E. M., Godon, P., Myzcka, J., Blair, W. P., 2010, ApJ Lett., 716, L157

Smith, D. A., Dhillon, V. S., 1998, MNRAS, 301, 767

Soker, N., Livio, M., Harpaz, A., 1984, MNRAS, 210, 189

Southworth, J., Clausen, J. V., 2007, A&A, 461, 1077

Southworth, J., Hickman, R. D. G., Marsh, T. R., Rebassa-Mansergas, A., Gänsicke, B. T., Copperwheat, C. M., Rodríguez-Gil, P., 2009, A&A, 507, 929

Southworth, J., Marsh, T. R., Gänsicke, B. T., Steeghs, D., Copperwheat, C. M., 2010, A&A, 524, A86

Steele, I. A., et al., 2004, in J. M. Oschmann Jr., ed., Society of Photo-Optical Instrumentation Engineers (SPIE) Conference Series, vol. 5489 of *Presented at the Society of Photo-Optical Instrumentation Engineers (SPIE) Conference*, p. 679

Steinfadt, J. D. R., Bildsten, L., Howell, S. B., 2008, ApJ Lett., 677, L113

Steinfadt, J. D. R., Kaplan, D. L., Shporer, A., Bildsten, L., Howell, S. B., 2010, ApJ Lett., 716, L146

Sulkanen, M. E., Brasure, L. W., Patterson, J., 1981, ApJ, 244, 579

Szkody, P., Mattei, J. A., 1984, PASP, 96, 988

Szkody, P., Gänsicke, B. T., Howell, S. B., Sion, E. M., 2002a, ApJ Lett., 575, L79

Szkody, P., Gänsicke, B. T., Sion, E. M., Howell, S. B., 2002b, ApJ, 574, 950

Szkody, P., et al., 2010, ApJ, 710, 64

Taam, R. E., Bodenheimer, P., 1989, ApJ, 337, 849

Taam, R. E., Ricker, P. M., 2006, ArXiv Astrophysics e-prints

Taam, R. E., Sandquist, E. L., 2000, ARA&A, 38, 113

Tappert, C., Gänsicke, B. T., Schmidtobreick, L., Aungwerojwit, A., Mennickent, R. E., Koester, D., 2007, A&A, 474, 205

Tappert, C., Gänsicke, B. T., Schmidtobreick, L., Ribeiro, T., 2011, A&A, in press,arXiv:1107.3586

Taylor, J. H., Fowler, L. A., McCulloch, P. M., 1979, Nat, 277, 437

Thorstensen, J. R., 2000, PASP, 112, 1269

Torres, G., 2007, ApJ Lett., 671, L65

Tovmassian, G. H., Zharikov, S. V., Neustroev, V. V., 2007, ApJ, 655, 466

Townsley, D. M., Gänsicke, B. T., 2009, ApJ, 693, 1007

Townsley, D. M., Arras, P., Bildsten, L., 2004, ApJ Lett., 608, L105

Tutukov, A., Yungelson, L., 1979, in P. S. Conti & C. W. H. De Loore, ed., Mass Loss and Evolution of O-Type Stars, vol. 83 of *IAU Symposium*, p. 401

van den Besselaar, E. J. M., et al., 2007, A&A, 466, 1031

van Zyl, L., Warner, B., O'Donoghue, D., Sullivan, D., Pritchard, J., Kemp, J., 2000, BaltA, 9, 231

van Zyl, L., et al., 2004, 350, 307

Vennes, S., Thorstensen, J. R., Polomski, E. F., 1999, ApJ, 523, 386

Verbunt, F., Rappaport, S., 1988, ApJ, 332, 193

Verbunt, F., Zwaan, C., 1981, A&A, 100, L7

Vogt, N., 1982, ApJ, 252, 653

Wade, R. A., Horne, K., 1988, ApJ, 324, 411

Warner, B., 1995, Cataclysmic Variable Stars, Cambridge University Press, Cambridge

Warner, B., Nather, R. E., 1971, MNRAS, 152, 219

Warner, B., Robinson, E. L., 1972, Nat, 239, 2

Warner, B., van Zyl, L., 1998, in F.-L. Deubner, J. Christensen-Dalsgaard, & D. Kurtz, ed., New Eyes to See Inside the Sun and Stars, vol. 185 of *IAU Symposium*, p. 321

Warner, B., Woudt, P. A., Pretorius, M. L., 2003, MNRAS, 344, 1193

Webbink, R. F., 1977, ApJ, 211, 486

Webbink, R. F., 1984, ApJ, 277, 355

Webbink, R. F., 1990, in C. W. Mauche, ed., Accretion-Powered Compact Binaries, p. 177

Webbink, R. F., 2008, in E. F. Milone, D. A. Leahy, & D. W. Hobill, ed., Astrophysics and Space Science Library, vol. 352 of *Astrophysics and Space Science Library*, p. 233

Weber, E. J., Davis, Jr., L., 1967, ApJ, 148, 217

Werner, K., Herwig, F., 2006, PASP, 118, 183

Whitehurst, R., 1988, MNRAS, 232, 35

Wijers, R. A. M. J., Pringle, J. E., 1999, MNRAS, 308, 207

Willems, B., Kolb, U., 2004, A&A, 419, 1057

Winget, D. E., 1982, Gravity Mode Instabilities in DA White Dwarfs., Ph.D. thesis, THE UNIVERSITY OF ROCHESTER.

Winget, D. E., Kepler, S. O., 2008, ARA&A, 46, 157

Winget, D. E., van Horn, H. M., Hansen, C. J., 1981, ApJ Lett., 245, L33

Winget, D. E., Robinson, E. L., Nather, R. D., Fontaine, G., 1982a, ApJ Lett., 262, L11

Winget, D. E., van Horn, H. M., Tassoul, M., Fontaine, G., Hansen, C. J., Carroll, B. W., 1982b, ApJ Lett., 252, L65

Winget, D. E., Kepler, S. O., Kanaan, A., Montgomery, M. H., Giovannini, O., 1997, ApJ Lett., 487, L191+

Wood, J., Horne, K., Berriman, G., Wade, R., O'Donoghue, D., Warner, B., 1986, MNRAS, 219, 629

Wood, J. H., Horne, K., 1990, MNRAS, 242, 606

Wood, J. H., Horne, K., Berriman, G., Wade, R. A., 1989, ApJ, 341, 974

Wood, J. H., Horne, K., Vennes, S., 1992, ApJ, 385, 294

Wood, J. H., Robinson, E. L., Zhang, E.-H., 1995, MNRAS, 277, 87

Wood, M. A., 1995, in D. Koester & K. Werner, ed., White Dwarfs, vol. 443 of *Lecture Notes in Physics, Berlin Springer Verlag*, p. 41

Wu, Y., 2001, MNRAS, 323, 248

York, D. G., et al., 2000, AJ, 120, 1579

Zhang, E.-H., Robinson, E. L., 1987, ApJ, 321, 813

Zorotovic, M., Schreiber, M. R., Gänsicke, B. T., Nebot Gómez-Morán, A., 2010, A&A, 520, A86+

Zorotovic, M., Schreiber, M. R., Gänsicke, B. T., 2011, ArXiv eprints., 1108.4600

Zuckerman, B., Koester, D., Reid, I. N., Hünsch, M., 2003, ApJ, 596, 477